NON-LINEAR FLUID DYNAMICS IN OSCILLATORY CYLINDRICAL CAVITIES

CARLES PANADÈS I GUINART

SUPERVISED BY DR. FRANCISCO MARQUÈS AND DR. ALVARO MESEGUER

Dissertation submitted for the Degree of

Doctor of Philosophy

(Computational and Applied Physics)

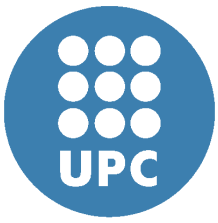

UNIVERSITAT POLITÈCNICA DE CATALUNYA

DEPARTAMENT DE FÍSICA APLICADA

May 2013

A mons pares per donar-me la vida,
a la Mireia per donar-li sentit

Stilicidi casus lapidem cavat
Lucretius, *De Rerum Natura*
La caiguda de l'aigua gota a gota forada la pedra
Lucreci, *De la natura de les coses*

NON-LINEAR FLUID DYNAMICS IN OSCILLATORY CYLINDRICAL CAVITIES

Carles Panadès i Guinart

Supervised by Dr. Francisco Marquès and Dr. Alvaro Meseguer

Universitat Politècnica de Catalunya 2013

Even though the transition to turbulence has been studied for over a century, its complete comprehension still remains unclear even for the simplest flows and continues to be a daunting challenge for the scientific community. Among these, there is the transition from the von Kármán vortex street to turbulent wakes. The complexity of this problem poses a series of difficulties that leaves little room for manoeuvre, so other ways to tackle this question have to be sought. A reasonable option is the analysis of the instability phenomena that other flows with the same symmetry group undergo. Despite being really different, an example of such flow is the one generated in a cylindrical cavity subjected to an oscillatory shear.

The purpose of the present thesis has been to provide a deeper understanding of the mechanisms that are responsible for the transition in oscillatory cylindrical cavities. Besides the potential implications of studying such systems for the transitions in wake flows, the system under consideration might be useful for any investigation involving a periodic forcing. Accurate spectral computations of the incompressible Navier-Stokes equations have been combined with equivariant bifurcation and normal form theories in an attempt to achieve our goal from different, yet complementary, perspectives.

The utilisation of these techniques has produced positive results in the field under consideration. The linear stability analysis has resulted in three types of different bifurcations expected by normal form theory and previous results. The evolution in time of these bifurcating modes yield the non-linear saturated states, which can be synchronous with the forcing or acquire an additional frequency (quasiperiodic). Furthermore, the exploration of regions where two synchronous modes become unstable at the same time, has provided a wide variety of novel states that are not necessarily synchronous. The description of these phenomena via bifurcation theory and dynamical systems techniques is in accordance with the numerical simulations, despite not having an absolute quantitative agreement between them.

The research focused on the study of viscoelastic fluids in periodically driven cylindrical cavities is a natural extension of the main topic of this thesis. Although this part has to be considered in a preliminary stage, there are some evidences suggesting that the system is always linearly stable and the only possibility to break the basic state is

via a subcritical finite-amplitude bifurcation. The transition recalls in a great deal the instabilities in Newtonian plane Couette and pipe Poiseuille, thus resulting in a much more difficult instability scenario that the one that was initially expected.

ACKNOWLEDGEMENTS

Sovint, mentre estava escrivint, em dispersava tot imaginant-me a mi mateix en aquest precís instant redactant uns agraïments catàrtics fruit de l'emoció d'haver enllestit finalment la tesi. Se'm va fer molt difícil no escriure'ls abans d'hora i van ser diverses les vegades que vaig haver de refrenar-me. El motiu per esperar pot semblar tan absurd com senzill: volia que el moment de posar en escrit els meus sentiments d'agraïment fos completament genuí i, per tant, havia de ser *a posteriori* de l'escriptura del cos central de la tesi. Ara és el moment, abans no m'envaeixi el tedi d'aquell que s'acosta al final de la seva empresa.

Amb la típica boirina que enterenyina els records, recordo la primera trobada amb el Paco i l'Àlvar. Va ser al despatx d'aquest primer i no sé si fou deliberat o no però hi havia bastants membres, no me'n recordo ben bé de quins, del que és el Grup de Dinàmica No Lineal de Fluids per tal d'esbossar les seves línies de treball. La majoria de les tècniques que vau anomenar m'eren completament desconegudes però encara tinc a la memòria l'entusiasme del Paco per totes les coses que pensava que podríem fer plegats en el transcurs de la tesi. Us vull agrair de tot cor, Paco i Àlvar, la dedicació i paciència que heu tingut amb mi; només espero haver estat a l'alçada de les expectatives, moltes gràcies, de debò. També vull donar les gràcies a la Isabel, l'Oriol i l'Arantxa per tenir sempre la porta oberta i permetre'm assaltar-los amb preguntes sobre el codi o de qualsevol altre caire. Agrair-li també al Niels, al Calvete, a la Marta i al Jordi, la seva amistat. Ja per acabar amb el Grup de Dinàmica No Lineal de Fluids, us vull agrair tots aquests anys de companyonia a la resta (Fernando, Ferran, Vicente, David, Roland, Albert, Cesca, José, Odalys, Jaime, Àngels, etc). Al llistat de gent del Departament de Física Aplicada, m'agradaria afegir el Toni per haver evitat de manera constant la rebel·lió de les màquines, i l'Anna, l'Anna Maria, l'Alícia i la Roser per la seva constant ajuda des d'administració. També m'agradaria donar les gràcies a la UPC per l'oportunitat que em va donar concedint-me una beca FPU-UPC.

Deixant de banda la gran amistat que ens uneix i l'estimació que els hi tinc a tots, també vull agrair l'interés que tant els meus amics de física (Ausiàs, Cerni, Ferran, Guillem, Manolo, Miguel, Gerard, Pol, Nacho, Míriam, Puig, Alessandro, Bigas, Josep, Salinas, Adrià, Ricci, Xavi...) com els amics de FEN (Riccardo, Jonàs...) com també els de la colla Bar Bodega Javier Crew (Andratx, Tomeu, Néstor, Joan...) han mostrat cap a la feina que he anat realitzant al llarg d'aquests anys.

Gràcies també a l'Ignasi Pagonabarraga per haver-me ensenyat els principis de la física de fluids i haver-me tutelat durant el meu Treball Final de Màster. Vull correspondre amb gratitud l'oportunitat que vaig tenir de fer els meus primers passos en el

món de la recerca de la mà del Grup de Nanomagnetisme dirigit per en Javier Tejada i les seves dues mans dretes, el Joan Manel Hernàndez i el Toni Garcia, així com els bons moments que vaig passar amb tots els companys (Diego, Guillem, Saul i tota la resta). Li estic molt agraït al Jordi Ortín per haver-me posat en contacte amb els que serien els meus directors, així com també per les interessants discussions que inicialment vam mantenir, juntament amb la Laura Casanellas. I would like to thank Juan M. Lopez for his guidance in part of the work and the fruitful results that has produced our collaboration. I feel that I am indebted with Alexander Morozov for his kind advice and sincerity in our meetings too.

També vull agrair als meus companys de córrer la gran diversió de generar turbulència al nostre voltant, així com als amics del F.S.Tricamp la demostració pràctica que no cal saber-ne de fluids per passar-s'ho be xutant una pilota. Moltes gràcies als meus bons amics de Tarragona (Albert, Hèctor, Hugo, Marc, Reina, Torrents, Tarek, Tomàs, Torrell, Eli, Mari, Ignasi...) per ser tots inseparables i pels reiterats intents d'escoltar en què he estat treballant tots aquests anys.

Pel que fa a la família, en som un bon munt i la mar de ben avinguts. Tot i que no aparegui en els articles, sóc tan Panadès com Guinart i us vull agrair a tots, amics i familiars de les dues bandes, els bons moments que hem passat entaulats durant les nostres trobades. Per família també entra la banda de tipus polític, Albert, Dolors, moltes gràcies per tot.

Al meu germà. Un germà no el tries, és per sempre i jo he tingut la sort de tenir el millor que podia demanar. La Graciela, la seva fantàstica dona que amb la seva veu és capaç d'animar els moments de màxima desesperació. El Joan Pol, el meu fillol que tantes alegries ens ha donat aquest any, sé que fa poc que ens coneixm però tinc la certesa que ens l'estimarem molt.

A mons pares. No sabeu com us n'estic d'agraït per la vida que m'heu donat, el suport que he rebut per part vostra en les meves decisions i, per damunt de tot, el fet que sempre m'hagueu fet costat i animat a fer allò que més m'agradès. Espero que estigueu tan orgullosos de mi com jo ho estic de vosaltres.

Ja per acabar, la Mireia, el meu amor. Escriure aquesta tesi ha estat tot un repte que de ben segur no hagués pogut assolir sense tu. Ha estat un camí molt llarg i dur per mi, però sé que també ho ha estat per tu. T'estic infinitament agraït per la teva comprensió i, per damunt de tot, pel teu amor. T'estimo.

TABLE OF CONTENTS

CHAPTER 1

INTRODUCTION

From the fluid dynamics point of view, the flow engendered in a periodically driven cylindrical cavity is a problem of fundamental interest whose study has not been deeply addressed yet, though it may have some far-reaching implications. The oscillatory forcing induced in the cylindrical cavity generates a two-dimensional axisymmetric flow that is invariant under a group of symmetries composed by some purely spatial and spatio-temporal symmetries (i.e. a spatial symetry composed with a temporal evolution). Computational fluids mechanics, dynamical systems analysis and bifurcation theory are combined together in this document to shed some light on the intricate issue of oscillatory cylindrical cavities.

Besides the *per se* appealing interest of the instability phenomena, the transition from the two-dimensional flow to three-dimensional states is also crucial in unraveling the mechanisms that destabilise systems that are invariant under the action of the same symetries. Such systems include the classical example of the two-dimensional von Kármán vortex street in the wake of a cylinder and a variety of periodically forced flows. Let us first introduce these flows as a motivation for the present work.

1.1 The von Kármán vortex street

The von Kármán vortex street is a well-known pattern that arises in the wakes of high-speed flows past objects, such as cylinders. Wakes are generated immediately behind a solid body because of the motion of the surrounding fluid. In the cylinder setting, the geometry of the object and the fluid properties allow us to define a sole dimensionless magnitude, the Reynolds number Re. For relatively small velocities, the flow is perfectly laminar after the cylinder. As the velocity increases, the streamlines become more distorted little by little and this distortion eventually evolves into vortical structures. At some point, these structures become a repeating pattern of vortices that are shed from the alternating sides of the object, a cylinder in Figure 1.1, the von Kármán vortex street. This succession of swirling structures develops not only in our human scale, but in a variety of imaginable scenarios. For instance, in the atmospheric scale, it has been reported by the Landsat7 satellite how the flow of the wind past an island is able to create a von Kármán vortex street around the Alejandro Selkirk Island (Figure 1.2).

As a matter of fact, the shedding of vortices from the different sides of the cylinder

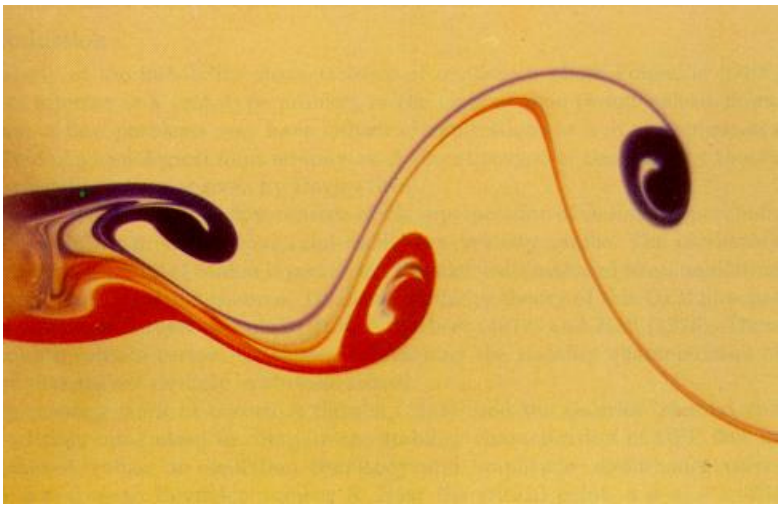

Figure 1.1: Two-dimensional wake of a circular cylinder (taken from Perry *et al.* (1982)).

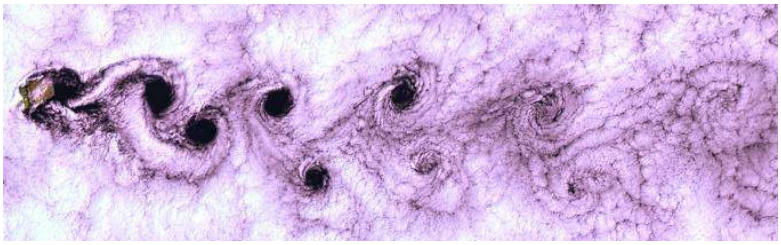

Figure 1.2: Von Kármán vortex street created by the wake of the wind flowing around the Alejandro Selkirk Island (taken from Landsat7).

introduces a new characteristic time, the Strouhal period, T, which depends on the Reynolds number. Due to this period, the von Kármán vortex street possesses some unique symmetries that other wake structures do not. Figure 1.3 exhibits the streamwise flow of the von Kármán vortex street at time $t = t_0$ and after evolving half of the Strouhal period $t = t_0 + T/2$. The flow is clearly reflected respect to the $y = 0$ plane after advancing in time $T/2$. In addition to this spatio-temporal symmetry, since the von Kármán vortex street does not possess any velocity in z, the flow is also invariant to translations and reflections in the spanwise direction.

By means of increasing the velocity, this two-dimensional flow breaks into the spanwise direction. Mode A is the first three-dimensional instability to emerge ($Re \approx 200$) from the cylinder wake, and preserves the spatio-temporal symmetry; in contrast, mode B breaks the spatio-temporal symmetry and bifurcates at $Re \approx 270$ from a state that is already unstable to a mode A (Williamson, 1988, 1996). Thus, in the experiments, the unstable mode cannot be selected because there is only one dimensionless control-

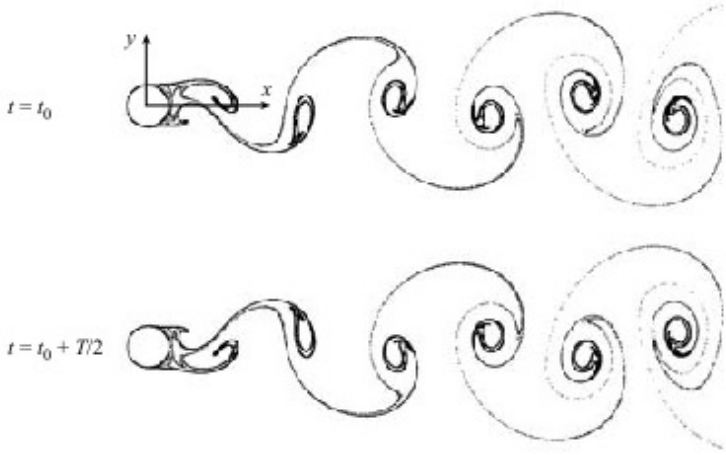

Figure 1.3: Illustration of the spatio-temporal symmetry of a two-dimensional circular cylinder wake for $Re = 188.5$ at times t_0 and $t_0 + T/2$, where t_0 is arbitrary and T is the Strouhal period (adapted from Blackburn *et al.* (2005)).

ling parameter, the Reynolds number. The numerical computations of cylindrical wake flows impose a periodicity in the z direction, so a non-dimensional wave number β is introduced straightforwardly. The Floquet analysis performed in Barkley & Henderson (1996) demonstrated that the most unstable mode could be selected tuning β for a fixed Re, thus infering the long-wave/short-wave character of mode A/B. Further numerical studies showed the presence of a quasiperiodic three-dimensional mode that can manifest either as standing waves or spanwise travelling waves (Blackburn & Lopez, 2003*a*; Blackburn *et al.*, 2005). Further studies, based on bifurcation theory (Barkley *et al.*, 2000) have corroborated the existance of all these unstable modes in the wake of a circular cylinder. Consequently, coming back to the experiments, traces of mode B and the quasiperiodic modes only appear as secondary bifurcations from the first bifurcation, mode A.

1.2 Periodically driven flows

Periodically driven flows, such as the one in a periodically driven cavity, are of great relevance to attain further properties of the two-dimensional time-periodic wakes because they share the same symmetry group. Figure 1.4 represents a schematic of the cavity exhibiting the coordinate system and the instantaneous isosurfaces of the spanwise z-vorticity of a two-dimensional basic state. This system possesses two characteristic lengths (H and ΓH) and one periodic direction with wavelength ΛH. In addition, the

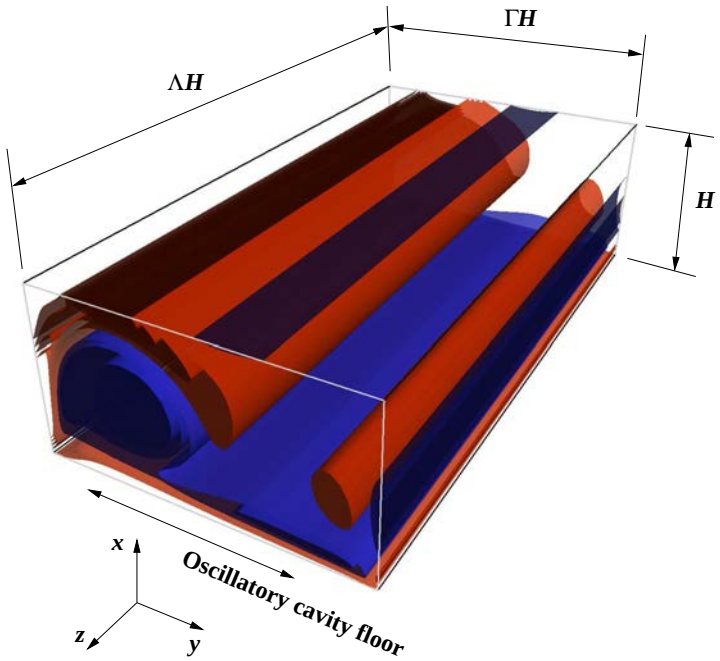

Figure 1.4: Schematic of the periodically driven cavity showing the coordinate system and instantaneous isosurfaces of the spanwise z-vorticity of a basic state (adapted from Blackburn & Lopez, 2003*b*).

wall located at $x = 0$ oscillates periodically in the y direction, whereas the upper one is steady. One important motivation to study periodically driven cavity flows stems from the fact that, with a fixed geometry, the amplitude and frequency of the forcing provide two controlling parameters: the Reynolds number Re and the Stokes number St. While wake flows are autonomous and open, the flow engendered in a periodically driven cavity is non-autonomous and closed. Blackburn & Lopez (2003*b*) showed through Floquet analysis and direct numerical simulations how the basic state lost stability to three-dimensional modes, analogous to the synchronous A and B modes and the quasiperiodic modes, depending on the amplitude and the frequency of the wall (Figure 1.5). In constrast to wake instabilities, mode B preserves the spatio-temporal symmetry and has a short-wave character, while mode A is the opposite: breaks the symmetry and is long-wave. The QP mode can manifest as modulated standing or spanwise travelling waves, but the latter solution is the only stable solution. The agreement between numerics and experiments is more than remarkable (Vogel *et al.*, 2003; Leung *et al.*, 2005). Regrettably, the travelling nature of the QP mode could not be captured in the experiments due to the finite nature of the spanwise direction. Furthermore, the bifurcation theory is very useful to describe the instabilities and adjusts pretty well to the observed phenomena (Marques *et al.*, 2004) too.

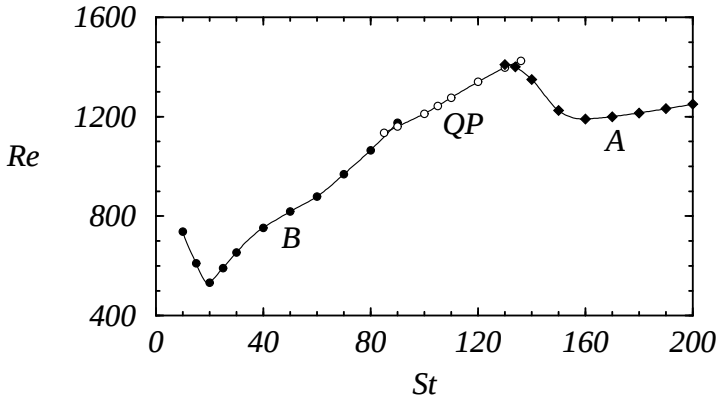

Figure 1.5: Critical Reynolds number, Re_c, as a function of the Stokes number, St, for the transition from the basic state to the different three-dimensional states, B, QP and A, for the periodically forced rectangular cavity flow (adapted from Blackburn & Lopez, 2003*b*; Leung *et al.*, 2005).

The periodically driven cavity is very useful in the sense that all the unstable modes are observable as first bifurcations. However, the periodicity imposed in the z direction prevents the complete agreement between theory and experiments, as well as, the emergence of secondary bifurcations. This drawback can be solved by means of making this coordinate truly periodic through homotopy, therefore converting the former cavity into an enclosed annulus.

Blackburn & Lopez (2011) found that the flow inside the annulus has the same three distinct instabilities: the two synchronous modes (A and B) and the QP mode, which manifests as modulated standing or travelling waves. The curvature of the system, characterised by the radius ratio Ψ, is capable of determining which mode becomes unstable first. Unfortunately, the Fourier numbers of the unstable modes are rather high and the obtaining of pure non-linear states is only possible when running in the appropriate subspaces. Computations in the non-linear regime very close to the onset of three-dimensional instabilities produce inexorably mixed mode states with a really complicated structure, as can be observed from a first glimpse at Figure 1.6. A travelling wave with $k = 33$ was computed in the proper subspace, and then the subspace restrictions were removed at $t = 0$. The mode with $k = 27$ starts to grow exponentially after the perturbations have organised. Upon initial non-linear saturation, there is a competition of these modes that somehow seems regular, but eventually the behaviour appears temporally chaotic.

Therefore, the annular cavity possesses all the symmetries, but the large wave numbers of the instabilities do not allow the simulations to obtain pure mode saturated

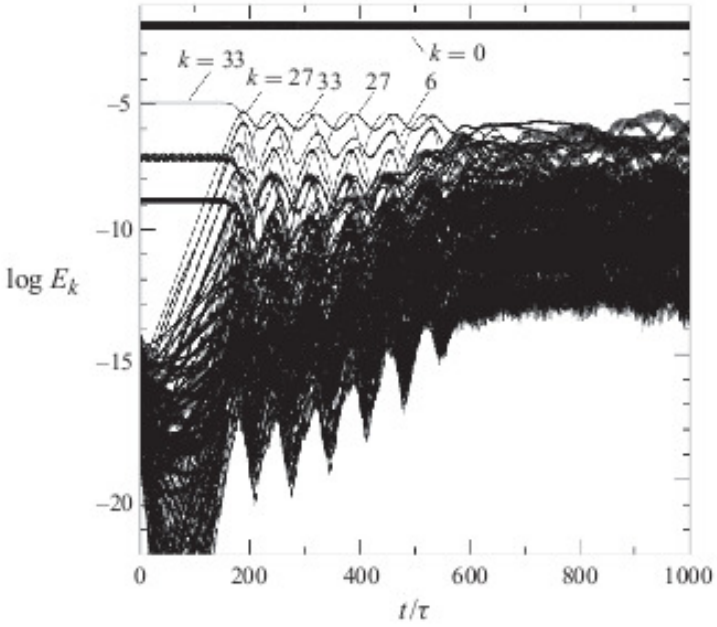

Figure 1.6: Evolution of the Fourier modal energies at $\Psi = 4/3$, $Re = 1200$, starting at $t = 0$ with a $k = 33$ travelling wave solution to which a small amount of Gaussian white noise was added (adapted from Blackburn & Lopez, 2011).

solutions. Supposedly, the utilisation of a cylindrical cavity will get rid of the disadvantages of the annulus because the bifurcating modes are likely to be much smaller. With this setting, the first step ought to be the caracterisation of the base state, the exploration in search of the first instabilities (synchronous modes A and B, and the QP mode) and the obtaining of saturated states. Later on, the interaction and coexistence of solutions should be examined in case of being possible. Our research group, as well as other internation groups, complement all the results from the numerics with bifurcation theory. The comparison with experimental results would be desirable, but as far as we know, there is no one at all conducting this class of experiments. Nevertheless, Dr. Laura Casanellas and Prof. Jordi Ortín at the Non-Linear Physics Laboratory of the Department of ECM, Barcelona University, have been carrying out their investigation with viscoelastic fluids in large aspect ratio cylinders. As a consequence, in addition to the intrinsic interest of these fluids, commencing a new line of research with viscoelastic fluids is worth doing for potential joint collaborations.

1.3 Outline of the thesis

This thesis is structured in the following manner. The mathematical formulation of the problem and the numerical methods are presented in Chapter 2. The numerical schemes are adapted from the previous code described in Mercader *et al.* (2010) and the spectral convergence of the code is corroborated nearly at the end of the chapter. Chapters 3 and 4 are devoted to numerical computations of a Newtonian fluid in a cylindrical cavity whose lateral sidewall oscillates periodically in time. The main results of Chapter 3 have been published in Panades *et al.* (2011) and deal with the characterisation of the basic state and the first hydrodynamic instabilities that the flow experiences. Chapter 4, presented in Panades *et al.* (2013), is a natural continuation of the previous one and focuses the attention on the secondary bifurcations that emerge from the intersection of first two bifurcation curves. Chapter 5 concentrates on some preliminary results stemming from dynamical systems theory and normal form analysis in an attempt to unfold the bifurcations of the former chapter. In fact, these techniques are also employed in the bifurcation analysis of Chapter 3. Chapter 6 represents an introductory work on the viscoelastic flow created by the oscillatory cylindrical cavity. In fact, this problem is far beyond our expectations, thus being a mere stepping stone for future investigations. A general overview of the main results, as well as the future perspectives, are provided in Chapter 7. Finally, some complementary material can be found in the appendices. Appendix A includes all the details about the formulation of the problems in cylindrical coordinates. Appendix B contains the explicit derivations of the normal forms that appear in our problem.

CHAPTER 2
MATHEMATICAL FORMULATION AND NUMERICAL METHODS

In fluid dynamics, the incompressible Navier-Stokes equations govern the dynamics of Newtonian flows. These equations are obtained after assuming a linear relation between the shear rate and the stress tensor in the conservation equation of the momentum, being the viscosity the constant of proportionality between them (Batchelor, 1967). In order to solve efficiently the Navier-Stokes equations, spectral methods have been widely employed (Fornberg, 1998; Boyd, 2000; Trefethen, 2000). Spectral Galerkin and pseudospectral collocation methods are some examples of these techniques. The latter is usually preferred because of its simplicity in the formulation and implementation, and is chosen in the current problem.

The numerical simulation of Newtonian flows in cylindrical cavities has been tackled from different perspectives. In all cases, the main issue lies in fulfilling numerically the divergence-free condition of incompressible fluids. In order to attain this requirement, a first option consists in writing the velocity field in terms of scalar potentials that satisfy the incompressibility condition by construction. A clear advantage of this method is the absence of the pressure in the formulation. Unfortunately, in enclosed geometries such as cylindrical cavities, the result is a system of partial differential equations of higher order with coupled boundary conditions, as can be observed in the linear stability analysis of the Rayleigh-Bénard convection (Marques *et al.*, 1993). In order to decouple the boundary conditions in the convection of a rotating cylinder, a different set of velocity potentials were employed (Goldstein *et al.*, 1998). Few years ago, Boronski & Tuckerman (2007) applied the influence matrix method to dispose of the mentioned coupling and also lower the order of the system of equations in the magnetohydrodynamic scenario.

Another possible approach to satisfy the divergence-free condition is based on projection methods formulated in terms of primitive variables. The main advantage of this technique is the fact that there is only one sequence of decoupled elliptic equations for the velocity and the pressure to be solved (Guermond *et al.*, 2006). These methods have been effective when solving the Navier-Stokes equations (Lopez *et al.*, 2002), convection of binary mixtures (Mercader *et al.*, 2008) and thermal convection problems (Mercader *et al.*, 2010). Our choice is completely based on the latter reference but applied to the purely hydrodynamic case of an enclosed cylinder driven by oscillations of the sidewall. Besides the advantages of this improved projection scheme, which was firstly proposed by Hughes & Randriamampianina (1998), the spatial discretisation of the code also copes with the characteristic problems of the cylindrical geometries. In the radial and vertical

direction Chebyshev-collocation is considered, while in azimuth it is Fourier-Galerkin. Furthermore, the problems concerning to the clustering near the axis are solved by means of considering radial expansions in the diameter. Last but not least, the singularity at the origin is avoided with the help of ensuring that this point is not a collocation point and by considering the proper radial parity of the Fourier components of the variables.

In addition to the purely hydrodynamic flow, the simulation of non-Newtonian flows with these numerical techniques is within the scope of this thesis. In a naive way, it can be stated that non-Newtonian fluids are those that do not satisfy the linear relation expressed in the first paragraph of this chapter. Some examples of non-Newtoninan fluids are biofluids, polymer solutions, emulsions and all kind of mixtures (Larson, 1999). Truth is that these fluids represent a daunting challenge that has been addressed quite recently in comparison with Newtonian flows. To the extent of our knowledge, there are some experiments with non-Newtonian fluids in a cylindrical cavity periodically forced in the axial direction (Torralba *et al.*, 2005, 2007; Casanellas & Ortín, 2012*a*). These experiments have been performed in a cylinder of height-to-radius ratio of twenty with wormlike micellar solutions, one type of viscoelastic fluid. Even though these micellar solutions are highly concentrated, the departing point must be as close as possible to the Newtonian case in order to facilitate the comparison. Therefore, a dilute viscoelastic solution is preferred and the simplest model is the so-called Oldroyd-B model (Morozov & van Saarlos, 2007). The constitutive equations derived from this model consider the polymers as two beads connected by a Hookean spring immersed in a solvent. The main drawback of the Oldroyd-B model is the fact that allows the polymers to be extended infinitely. In order to avoid this shortcoming, finitely extensible non-linear elastic hooks can be supposed, thus resulting in the FENE-P model, or by including a non-linear saturation term, as is the case for the Giesekus constitutive equation (Larson, 1999).

This chapter has the following structure. In Section §2.1 the governing equations, numerical scheme and symmetries of the Newtonian flow are detailed. Section §2.2 is analogous to the former but considering viscoelastic fluids instead. In Sections §2.3 and §2.4 some features of the spectral convergence and the linear stability analysis are described. This chapter concludes with Section §2.5 that discusses and synthesises the main characteristics of the methods.

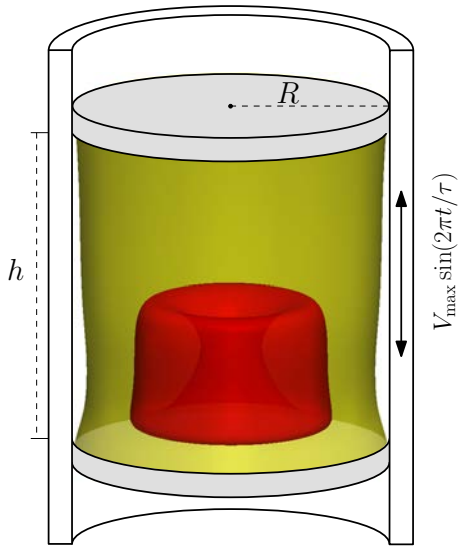

Figure 2.1: Schematic of the apparatus. The base state is displayed, showing the roller (isosurfaces of axial velocity) formed due to the motion of the sidewall; it is the analogous of the roller in figure 1.4 for the periodically forced cavity flow.

2.1 Newtonian fluid

2.1.1 Governing equations

Consider a Newtonian fluid of dynamic viscosity η and density ρ, thus kinematic viscosity $\nu = \eta/\rho$, confined in a finite cylinder of radius R and height h, whose sidewall oscillates harmonically in the axial direction, with period T and maximum axial velocity $V_{\max}$, while the top and bottom lids remain at rest, as shown schematically in Figure 2.1. The system is non-dimensionalised taking R as the length scale, and the viscous time $\tau_\nu = R^2/\nu$ as the time scale, so the velocity and the pressure scale with ν/R and $\rho\nu^2/R^2$. In the simulations the radius and the viscous time are the units of lenght and time, that is to say $R = 1$ and $\tau_\nu = 1$. In this problem, there are three non-dimensional parameters:

$$\text{Aspect ratio} \qquad \Gamma = h/R, \tag{2.1}$$

$$\text{Reynolds number} \qquad Re = V_{\max}R/\nu, \tag{2.2}$$

$$\text{Stokes number} \qquad St = R^2/\nu T. \tag{2.3}$$

The aspect ratio defines the geometry of the problem, while Re and St are non-dimensional measures of the amplitude and frequency of the forcing; the inverse of the Stokes number is precisely the non-dimensional period of the oscillations, $\tau = 1/St$. In this thesis, the aspect ratio is fixed at $\Gamma = 2$. The non-dimensional Navier-Stokes equations governing

the flow are

$$\Big(\frac{\partial}{\partial t} + \mathbf{u}\cdot\nabla\Big)\mathbf{u} = -\nabla p + \nabla^2\mathbf{u}, \tag{2.4a}$$

$$\nabla\cdot\mathbf{u} = 0, \tag{2.4b}$$

where $\mathbf{u} = (u, v, w)$ is the velocity field in cylindrical coordinates $(r, \theta, z) \in [0, 1] \times [0, 2\pi] \times [-\Gamma/2, \Gamma/2]$, and p is the kinematic pressure. The vorticity associated with the velocity field is $\nabla \times \mathbf{u} = (\xi, \eta, \zeta)$. No-slip velocity boundary conditions are used on all walls. Thus, the velocity is zero on stationary top and bottom endwalls, and the z-component of velocity at the sidewall oscillates periodically in time:

$$\mathbf{u}(r, \theta, \pm\Gamma/2, t) = (0, 0, 0), \tag{2.5a}$$

$$\mathbf{u}(1, \theta, z, t) = \big(0, 0, Re\sin(2\pi St\, t)\big). \tag{2.5b}$$

Therefore, the amplitude of the vertical oscillation of the cylinder wall, Δz, in terms of the non-dimensional parameters of the problem is given by $\Delta z = Re/(2\pi St)$, where its non-dimensionalisation has been obtained using the radius R.

Since the flow is incompressible of constant density, the oscillating sidewall problem is identical to having a stationary sidewall with the top and bottom endwalls oscillating together in the axial direction. These idealised boundary conditions are discontinuous at the junctions where the stationary lids meet the oscillating sidewall. In a physical experiment there are small but finite gaps at these junctions where the axial velocity adjusts rapidly to zero. For a proper use of spectral techniques, a regularisation of this discontinuity is implemented of the form

$$w(1, \theta, z, t) = Re\sin(2\pi St\, t)\left[1 - \exp\left(-\frac{\Gamma/2 - z}{\epsilon}\right)\right]\left[1 - \exp\left(-\frac{\Gamma/2 + z}{\epsilon}\right)\right], \tag{2.6}$$

where ϵ is a small parameter that mimics the small physical gaps ($\epsilon = 6 \times 10^{-3}$ has been used as a fixed parameter). The use of $\epsilon \neq 0$ regularises the otherwise discontinuous boundary conditions; see Lopez & Shen (1998) for further details on the use of this technique in spectral codes.

2.1.2 Numerical scheme

The spectral collocation solver used here is based on the scheme described in Mercader *et al.* (2010). This spectral solver has been tested and used in a wide variety of flows in enclosed cylinders (Marques *et al.*, 2007; Lopez *et al.*, 2007, 2009; Lopez & Marques,

2009). A second-order time-splitting method based on the work of Hughes & Randriamampianina (1998) is utilised. The spatial discretisation considers Galerkin-Fourier expansions in the azimuthal periodic direction and Chebyshev-collocation in the finite coordinates.

Temporal discretisation

Concerning the time discretisation, the governing equations have been solved using a second-order time-spliting method based on a combination of Adams-Bashforth and backward differentiation schemes (Karniadakis *et al.*, 1991; Ascher *et al.*, 1995; Hughes & Randriamampianina, 1998). This numerical scheme is semi-implicit and has been chosen because of its good stability properties. The Navier-Stokes equations (2.4) are written as:

$$\nabla \cdot \mathbf{u}^{n+1} = 0, \tag{2.7a}$$

$$\frac{3\mathbf{u}^{n+1} - 4\mathbf{u}^{n} + \mathbf{u}^{n-1}}{2\Delta t} = -\nabla p^{n+1} - 2\mathbf{N}\left(\mathbf{u}^{n}\right) + \mathbf{N}\left(\mathbf{u}^{n-1}\right) + \nabla^2 \mathbf{u}^{n+1}, \tag{2.7b}$$

where $\mathbf{N}(\mathbf{u}) = \mathbf{u} \cdot \nabla \mathbf{u}$ is the non-linear term of the velocity, Δt the time step, and n the iteration. Time steps of $\Delta t = 10^{-5}$ have been required to ensure numerical stability and accuracy of the temporal scheme.

The projection scheme is adopted from Hughes & Randriamampianina (1998) and is divided in three substeps. Following the prescriptions of Karniadakis *et al.* (1991), the first fraction step consists in computing a predictor for the pressure, $\bar{p}^{n+1}$, obtained from the Navier-Stokes and continuity equations:

$$\nabla^2 \bar{p}^{n+1} = \nabla \cdot \left[-2\mathbf{N}\left(\mathbf{u}^{n}\right) + \mathbf{N}\left(\mathbf{u}^{n-1}\right)\right], \tag{2.8}$$

with the consistent Neumann boundary condition:

$$\frac{\partial \bar{p}^{n+1}}{\partial n} = \mathbf{n} \cdot \left[2\mathbf{L}(\mathbf{u}^{n}) - \mathbf{L}(\mathbf{u}^{n-1}) - 2\mathbf{N}(\mathbf{u}^{n}) + \mathbf{N}(\mathbf{u}^{n-1}) - \frac{3\mathbf{u}^{n+1} - 4\mathbf{u}^{n} + \mathbf{u}^{n-1}}{2\Delta t}\right], \tag{2.9}$$

where the term $\mathbf{u}^{n+1}$ are the known boundary conditions for the velocity given by (2.5), and $\mathbf{L}(\mathbf{u}) = \nabla^2 \mathbf{u} = \nabla(\nabla \cdot \mathbf{u}) - \nabla \times (\nabla \times \mathbf{u}) = -\nabla \times (\nabla \times \mathbf{u})$, corresponds to the diffusion term, which has been decomposed in solenoidal and irrotational operators. Afterwards, the momentum equation including the preliminary pressure, for a predictor velocity field, $\mathbf{u}^{*}$, is solved:

$$\left(\nabla^2 - \frac{3}{2\Delta t}\right)\mathbf{u}^{*} = \nabla \bar{p}^{n+1} + 2\mathbf{N}(\mathbf{u}^{n}) - \mathbf{N}(\mathbf{u}^{n-1}) - \frac{4\mathbf{u}^{n} - \mathbf{u}^{n-1}}{2\Delta t}, \tag{2.10}$$

employing the actual Dirichlet boundary conditions for the velocity (2.5). Since the linear viscous term in cylindrical coordinates couples the velocity components, the utilisation of the linear combinations (A.22) becomes necessary, hence introducing u_α and u_β. After computing these fictitious velocities, the physical components u and v are recovered using the transformation described by (A.23). In the final stage, the correction step is based on the evaluation of:

$$\frac{3(\mathbf{u}^{n+1} - \mathbf{u}^*)}{2\Delta t} = -\nabla(p^{n+1} - \bar{p}^{n+1}), \tag{2.11a}$$

$$\nabla \cdot \mathbf{u}^{n+1} = 0. \tag{2.11b}$$

Considering $\phi = 2(p^{n+1} - \bar{p}^{n+1})\Delta t/3$, the system poses a Poisson equation for this variable:

$$\Delta\phi = \nabla \cdot \mathbf{u}^*, \tag{2.12}$$

with the consistent Neumann boundary conditions:

$$\frac{\partial\phi}{\partial n} = 0, \tag{2.13}$$

and the update of the pressure and the velocity is immediate:

$$p^{n+1} = \bar{p}^{n+1} + \frac{3\phi}{2\Delta t}, \tag{2.14a}$$

$$\mathbf{u}^{n+1} = \mathbf{u}^* - \nabla\phi. \tag{2.14b}$$

Spatial discretisation

The spatial discretisation is via a Galerkin-Fourier expansion in θ and a Chebyshev collocation in $x = 2r$ and z, of the form

$$(u, w, p)(r, \theta, z) = \sum_{l=0}^{n_r} \sum_{n=0}^{n_z} \sum_{m=-n_\theta/2}^{n_\theta/2-1} a_{lnm} T_l(x) T_n(z) e^{\mathrm{i}m\theta} = \sum_{m=-n_\theta/2}^{n_\theta/2-1} F_m(r, z) e^{\mathrm{i}m\theta}, \tag{2.15}$$

for the radial velocity u, the axial velocity w and the pressure p, where T_l and T_n are Chebyshev polynomials of degree less or equal than n_r and n_z, respectively. For Newtonian flows, the results presented along this thesis have been computed with $n_r = 48$, $n_z = 96$ and $n_\theta = 20$, and this resolution resolves all the spatial scales in the solutions presented. The Fourier components $F_m(r, z)$ are separated in their real and imaginary parts, thus fulfilling:

$$F_0(r, z) = f_0(r, z), \tag{2.16a}$$

$$F_{-n_\theta/2}(r,z) = f_{n_\theta-1}(r,z), \tag{2.16b}$$

$$F_m(r,z) = f_{2m-1}(r,z) + \mathrm{i} f_{2m}(r,z), \text{ for } m = 1,\ldots,n_\theta/2-1, \tag{2.16c}$$

$$F_{-m}(r,z) = \overline{F}_m(r,z), \tag{2.16d}$$

where the overbar means complex conjugate and f is a real-valued function. Equation (2.16c) shows the separation in real (subscript $2m-1$) and imaginary (subscript $2m$) parts, hence providing a total of n_θ independent real functions, in case of including the axisymmetric component too.

The azimuthal velocity v has a slightly different expansion in Fourier

$$v(r,\theta,z) = \mathrm{i} \sum_{m=-n_\theta/2}^{n_\theta/2-1} F_m(r,z) e^{\mathrm{i}m\theta}, \tag{2.17}$$

and as a consequence possesses another features:

$$F_0(r,z) = \mathrm{i} f_0(r,z), \tag{2.18a}$$

$$F_{-n_\theta/2}(r,z) = \mathrm{i} f_{n_\theta-1}(r,z), \tag{2.18b}$$

$$F_m(r,z) = \mathrm{i} f_{2m-1}(r,z) - f_{2m}(r,z), \text{ for } m = 1,\ldots,n_\theta/2-1, \tag{2.18c}$$

$$F_{-m}(r,z) = -\overline{F}_m(r,z). \tag{2.18d}$$

Because of the different expansions in real (2.15) or imaginary (2.17) series, an equation for the m Fourier mode splits into a purely real and another imaginary equation with functions f_{2m-1} and f_{2m}, respectively. This choice clearly facilitates the implementation and solution of the equations.

The change to cylindrical variables generates an apparent singularity at the axis $r = 0$ and the Fourier components have to take into account this issue. Therefore, some regularity conditions should be considered at the origin for the Fourier coefficients (Lopez *et al.*, 2002). Different options are decribed in Boyd (2000), including our choice, the unshifted Chebyshev polynomials of appropriate parity. Other authors have considered more restrictive conditions of the radial Chebyshev interpolants in order the solution to satisfy analyticity conditions in a neighbourhood of the origin (Priymak & Miyazaki, 1998). By means of forcing the Fourier components to have the correct parity, the problem becomes well-posed. Furthermore, this weak formulation has to be complemented with never chosing the origin as a collocation point and avoiding clustering near this point. In cylindrical coordinates, any scalar function fulfills $f(r,\theta+\pi,z) = f(-r,\theta,z)$ because $(r,\theta+\pi,z)$ is equivalent to $(-r,\theta,z)$. Unlike scalar functions, polar magnitudes

possess the antisymmetric property, thus satisfying $f(r,\theta+\pi,z)\hat{r} = -f(-r,\theta,z)\hat{r}$ and $f(r,\theta+\pi,z)\hat{\theta} = -f(-r,\theta,z)\hat{\theta}$. Consequently, $F_m(r,z)$ of w and p, must have parity m, whilst those of u and v, have to possess the same parity as $m+1$ (Lopez *et al.*, 2002; Mercader *et al.*, 2010). Even though the pole conditions are not imposed in the code explicitly, they are satisfied in a natural way because of the considerations made with the parity of the Fourier coefficients (Mercader *et al.*, 1991, 2010).

As it has been stated at the beginning of this subsection, the radial Chebyshev expansion is performed in $x = 2r \in [-1,1]$, so the collocation points are distributed according to:

$$r_l = \cos\left(\frac{\pi l}{2n_r+1}\right), \text{ for } l = 0,\ldots,n_r, \tag{2.19}$$

while in the axial direction, they follow the usual distribution:

$$z_n = \frac{\Gamma}{2}\cos\left(\frac{\pi n}{n_z}\right), \text{ for } n = 0,\ldots,n_z; \tag{2.20}$$

see Fornberg (1998) or Trefethen (2000). Thanks to this method, the coordinate $r = 0$ is never a collocation point and the problem with the origin is solved. Moreover, the collocation points are clustered near the lids and the sidewalls, where the dynamics are prone to be more complex.

Since both spectral differentiation matrices for $x = 2r$ and z are equivalent, a generic set of collocation points q_i with $i = 0,\ldots,n_q$, is introduced to avoid unnecessary repetitions. The first-order differentiation matrix is given by

$$\mathcal{D}^{(1)}_{ij} = \begin{cases} (-1)^{i+j}\dfrac{c_i}{c_j(q_i-q_j)}, & i \neq j, \\ -\dfrac{q_j}{2(1-q_j^2)}, & 1 \leq i = j \leq n_q - 1, \\ \dfrac{2n_q^2+1}{6}, & i = j = 0, \\ -\dfrac{2n_q^2+1}{6}, & i = j = n_q, \end{cases} \tag{2.21}$$

while the second-order differentiation matrix is

$$\mathcal{D}^{(2)}_{ij} = \begin{cases} (-1)^{i+j}\,\dfrac{(q_i^2+q_iq_j-2)}{c_j(1-q_i^2)(q_i-q_j)}, & i\neq j,\ 1\leq i\leq n_q-1,\ 0\leq j\leq n_q, \\ -\dfrac{(n_q^2-1)(1-q_i^2)+3}{3(1-q_i^2)^2}, & 1\leq i=j\leq n_q-1, \\ (-1)^{j}\,\dfrac{2[(2n_q^2+1)(1-q_j)-6]}{3c_j(1-q_j)^2}, & i=0,\ 1\leq j\leq n_q, \\ (-1)^{n_q+j}\,\dfrac{2[(2n_q^2+1)(1+q_j)-6]}{3c_j(1+q_j)^2}, & i=n_q,\ 0\leq j\leq n_q-1, \\ \dfrac{n_q^4-1}{15}, & i=j=0,n_q, \end{cases} \tag{2.22}$$

where $c_i = 1$ for $1 \leq i \leq n_q - 1$, and $c_0 = c_{n_q} = 2$ (Zhao & Yedlin, 1994; Boyd, 2000). Instead of employing the differentiation matrices for x, the radial derivatives are computed via two new matrices that take into consideration the parity of the functions to be differentiated

$$\mathcal{D}^{(k)\,,\,\text{even}}_{ij} = \mathcal{D}^{(k)}_{i\,j} + \mathcal{D}^{(k)}_{i\,n_x-j}, \tag{2.23a}$$

$$\mathcal{D}^{(k)\,,\,\text{odd}}_{ij} = \mathcal{D}^{(k)}_{i\,j} - \mathcal{D}^{(k)}_{i\,n_x-j}, \tag{2.23b}$$

with $i, j = 0, \ldots, n_r$, and $n_x = 2n_r + 1$. Thus, the matrix with the even superscript must be applied to odd Fourier coefficients of u and v, and even Fourier components of w and p. The complementary is used for the odd superscript: even components for u and v, and odd coefficients for w and p.

Due to the time splitting described in the former subsection, several Helmholtz and Poisson equations for the different Fourier modes are posed and have to be solved. The differential operators of the Poisson and Helmholtz equations for w, p and ϕ, expressed by

$$\left(\partial_r^2 + \frac{1}{r}\partial_r - \frac{m^2}{r^2} + \partial_z^2 + a\right) f = h, \tag{2.24}$$

and the decoupling combinations u_α and u_β for u and v

$$\left(\partial_r^2 + \frac{1}{r}\partial_r - \frac{(m\pm 1)^2}{r^2} + \partial_z^2 + a\right) f = h, \tag{2.25}$$

are diagonalised in the radial and axial coordinates only once in a preprocessing stage, following Zhao & Yedlin (1994).

2.1.3 Symmetries

The governing equations and boundary conditions are invariant to the following spatial symmetries:

$$K_\beta(u,v,w)(r,\theta,z,t) = (u,-v,w)(r,2\beta-\theta,z,t), \tag{2.26a}$$

$$R_\alpha(u,v,w)(r,\theta,z,t) = (u,v,w)(r,\theta+\alpha,z,t), \tag{2.26b}$$

for any angle α and β. K_β represents reflections about the meridional plane $\theta = \beta$, whilst R_α signifies rotations about the cylinder axis. K_β and R_α generate the groups Z_2 and $SO(2)$, but the two operators do not commute ($K_\beta R_\alpha = R_{-\alpha}K_\beta$), so the symmetry group generated by K_β and R_α is $O(2)$ and acts in the periodic azimuthal θ-direction. The horizontal reflection on the mid-plane $z = 0$ acts on the velocity field as:

$$K_z(u,v,w)(r,\theta,z,t) = (u,v,-w)(r,\theta,-z,t). \tag{2.27}$$

Due to the harmonic oscillation of the sidewall, the boundary condition (2.46b) is not K_z invariant. The system is invariant to the spatio-temporal symmetry consisting of a reflection about the mid-plane $z = 0$ together with a half-period evolution in time:

$$H(u,v,w)(r,\theta,z,t) = (u,v,-w)(r,\theta,-z,t+\tau/2). \tag{2.28}$$

The transformation H generates a spatio-temporal Z_2^{ST} symmetry group that commutes with $O(2)$ and its square, H^2, is the identity. Hence, the complete symmetry group of the problem is $O(2)\times Z_2^{ST}$. The action of the spatial symmetry K_β and the spatio-temporal symmetry H on the vorticity is different to the action on the velocity (while the action of the rotations R_α is the same on the velocity and vorticity fields), and are given by:

$$K_\beta(\xi,\eta,\zeta)(r,\theta,z,t) = (-\xi,\eta,-\zeta)(r,2\beta-\theta,z,t), \tag{2.29a}$$

$$H(\xi,\eta,\zeta)(r,\theta,z,t) = (-\xi,-\eta,\zeta)(r,\theta,-z,t+\tau/2). \tag{2.29b}$$

Therefore, the individual symmetries (and the generated groups) are exactly the same as for the periodically driven annular cavity (Blackburn & Lopez, 2011) and analogous to the periodically driven rectangular cavity flows (Blackburn & Lopez, 2003*b*; Vogel *et al.*, 2003) and the two-dimensional time-periodic wake of symmetrical bluff bodies; such as cylinders (Williamson, 1996; Barkley *et al.*, 2000; Blackburn & Lopez, 2003*a*; Blackburn *et al.*, 2005), rings (Leweke & Provansal, 1995) or flat plates (Lasheras & Meiburg, 1990). As occurrs in all these systems, the solutions that bifurcate from the basic state, break some of these symmetries. Hence, it would be convenient to have quantitative measures of the symmetries to know whether the emerging solutions break or preserve them.

In the symmetry $O(2) \times Z_2^{ST}$ corresponding to the problem considered, the spatial part of the spatio-temporal symmetry commutes with the purely spatial symmetries, which simplifies the analysis. Nevertheless, it should be noted that in other similarly periodically forced hydrodynamic systems, the spatial parts of the spatio-temporal symmetry do not commute, and care needs to be exercised; see Lopez & Marques (2000); Marques & Lopez (2000); Avila *et al.* (2007, 2008), and references therein.

R_α symmetry

Because of the basic flow is supposed to be axisymmetric, the kinetic energy associated with each Fourier mode different from zero is considered of great relevance. Indeed, a non-zero value of this magnitude means that the azimuthal rotation symmetries R_α are broken, and the basic flow has bifurcated. Then, this modal kinetic energy is:

$$E_m = \frac{2}{\Gamma} \int_{\mathcal{D}} \mathbf{u}_m \cdot \overline{\mathbf{u}}_m \, r dr dz, \tag{2.30}$$

where the integration domain $\mathcal{D}$ is $(r, z) \in [0, 1] \times [-\Gamma/2, \Gamma/2]$ and the overbar applies the complex conjugate on the velocity field. As the basic flow is axisymmetric, the radial and axial vorticity components give a good measure of the three-dimensional nature of the bifurcated state, as well as the azimuthal velocity. If it is necessary, note that this symmetry can be artificially imposed by means of setting all the non-axisymmetric Fourier components of the velocity equal to zero.

K_β symmetry

In some cases, it is important to impose the preservation of the K_β symmetry. The action of this symmetry on the velocity field is ruled by equation (2.26a). Considering the different expansions of the velocities given by equations (2.15) and (2.17), it is easy to verify that the coefficients have to satisfy these conditions:

$$f_0 = f_{n_\theta - 1} = 0, \text{ for } v, \tag{2.31a}$$

$$f_{2m} = 0, \text{ for } u, v \text{ and } w, \tag{2.31b}$$

where $m = 1, \ldots, n_\theta/2 - 1$. This method has been used effectively in similar problems (Blackburn & Lopez, 2003*b*, 2011). The solutions satisfying the previous equations are invariant under reflections about the $\beta = \theta = 0$ diametral plane.

In other cases, when K_β has been broken, the implementation of a symmetry check for the reflection symmetry is necessary. Let us assume a variable $g(r,\theta,z,t)$ such that:

$$K_\beta g(r,\theta,z,t) = g(r,2\beta-\theta,z,t), \tag{2.32}$$

and expands in Fourier according to (2.15), with Fourier components G_m, for example the axial velocity. Since g is real, $G_{-m} = \overline{G_m}$. Considering that g is K_β-invariant:

$$K_\beta g(r,\theta,z,t) = g(r,\theta,z,t), \tag{2.33}$$

and the Fourier components satisfy

$$e^{2\mathrm{i}m\beta}G_m = G_{-m} = \overline{G_m} \Rightarrow e^{\mathrm{i}m\beta}G_m = \overline{e^{\mathrm{i}m\beta}G_m} \Rightarrow \arg G_m = -m\beta, \tag{2.34}$$

where β can be time-dependent, but it is independent of (r,z). In order to define a symmetry parameter, the phases of the azimuthal Fourier components G_m must be examined. Introducing $G_m = |G_m|e^{\mathrm{i}\phi_m}$, the mean phase and the corresponding standard deviation can be easily computed:

$$\beta_m(t) = \frac{2}{\Gamma}\int_{\mathcal{D}} \phi_m(r,z,t)\, r dr dz, \qquad \sigma^2_{\beta_m}(t) = \frac{2}{\Gamma}\int_{\mathcal{D}} (\phi_m(r,z,t)-\beta_m)^2 r dr dz, \tag{2.35}$$

where $\mathcal{D}$ is $(r,z) \in [0,1]\times[-\Gamma/2,\Gamma/2]$ again. The standard deviation σ_{β_m} is a good measure of the reflection symmetry of the different azimuthal Fourier modes. For a global measure of this asymmetry, the correlation of the angles of the Fourier modes respect to the first one, has to be checked, $\beta_m = m\beta_1$. Therefore, the symmetry parameter S_{K_β} is defined as

$$S^2_{K_\beta} = \sum_{m=1}^{n_\theta/2-1} W_m\big(\sin^2(\beta_m - m\beta_1) + \sigma^2_{\beta_m}\big), \qquad W_m = \|G_m\|_\infty / \sum_{k=1}^{n_\theta/2-1} \|G_k\|_\infty\ , \tag{2.36}$$

which is always positive, and zero precisely when the symmetry line of mode m coincides with the symmetry line of mode one. Each mode has been weighted according to its contribution to the full solution using the maximum norm $\|G_k\|_\infty$ in the domain $\mathcal{D}$.

H symmetry

Concerning to the spatio-temporal symmetry, it remains to give a good measure of H. One option is to observe the flow half-period apart in symmetric planes with respect to $z=0$. A more rigurous estimation might be:

$$S_H = ||w(r,\theta,z,t) + w(r,\theta,-z,t+\tau/2)||_2, \tag{2.37}$$

that is zero for an H-symmetric solution, according to (2.28). In particular, $S_H = 0$ means that w is time-periodic and can be expanded in Fourier:

$$w(r,\theta,z,t) = \sum_j w_j(r,\theta,z) e^{2\pi \mathrm{i} j t/\tau}. \tag{2.38}$$

At the mid-plane $z = 0$ and considering (2.28), it is obtained that

$$w(r,\theta,0,t) = -w(r,\theta,0,t+\tau/2). \tag{2.39}$$

This condition turns into

$$w_j(r,\theta,0) = (-1)^{j+1} w_j(r,\theta,0), \tag{2.40}$$

which means that the even temporal Fourier components of the axial velocity on the mid-plane are zero, for an H-symmetric solution. As a consequence, the magnitude of the even temporal Fourier components is a suitable measure of the H-symmetry breaking, a result useful in the analysis of the solutions.

2.2 Viscoelastic fluid

2.2.1 Governing equations

Consider a viscoelastic fluid with density ρ under the same conditions as the Newtonian flow of the previous section. The total kinematic (dynamic) viscosity of the solution ν (η) is the sum of the solvent ν_s (η_s) and the polymeric contribution ν_p (η_p), thus $\nu = \nu_s + \nu_p$ ($\eta = \eta_s + \eta_p$). Moreover, these polymers introduce an additional characteristic time: the average relaxation time that the polymers need to return to equilibrium after being perturbed, λ. The length, time, velocity, pressure and polymeric stress are scaled using R, $R/V_{\max}$, $\rho V_{\max}^2$ and $\eta_p V_{\max}/R$, respectively. Besides the three dimensionless numbers appearing in (2.1)-(2.3), there are two additional numbers to be considered here:

$$\text{Viscosity ratio} \qquad \beta = \nu_s/\nu, \tag{2.41}$$

$$\text{Weissenberg number} \qquad We = \lambda V_{\max}/R. \tag{2.42}$$

The viscosity ratio provides a deviation of the viscoelastic fluid respect to the Newtonian one. For instance, in the case of a solvent with a small amount of polymers, β is close to one, because $\nu_s > \nu_p$ but of the same order. Nevertheless, in a highly concentrated solution, $\nu_p \gg \nu_s$, so the viscosity ratio tends to zero. The Weissenberg number is the

ratio of the relaxation time of the polymers and the shear rate produced by the oscillatory sidewall. The dimensionless momentum equations for an incompressible viscoelastic fluid are

$$\nabla \cdot \mathbf{u} = 0, \tag{2.43a}$$

$$\frac{\partial \mathbf{u}}{\partial t} + \mathbf{u} \cdot \nabla \mathbf{u} = -\nabla p + \frac{\beta}{Re} \nabla^2 \mathbf{u} + \frac{(1-\beta)}{Re} \nabla \cdot \mathbb{T}, \tag{2.43b}$$

where $\mathbf{u} = (u_r, u_\theta, u_z)$ is the velocity field in cylindrical coordinates $(r, \theta, z) \in [0, 1] \times [0, 2\pi] \times [-\Gamma/2, \Gamma/2]$, p is the hydrodynamic pressure, and $\mathbb{T}$ represents the polymeric stress.

The time evolution of the polymeric stress is provided by an additional constitutive equation that depends on the election of the viscoelastic model. The simplest model of viscoelastic fluid considers the polymers as two beads connected by a linear Hookean spring, experiencing hydrodynamic drag and stochastic Browninan forces, the so-called Oldroyd-B model. This model is able to capture the main features of viscoelastic flows, but allows the polymers to be infinitely extended (Morozov & van Saarlos, 2007). A more sophisticated approach that solves this problem is the FENE-P model. Its constitutive equation represents an extension of the Oldroyd-B equation and makes the springs non-linearly elastic with a finite maximum extension (Larson, 1999). Since this field is novel for us, we will keep ourselves in the Oldroyd-B frame for the sake of simplicity. On the basis of this model, the polymer stress tensor is given in terms of the so-called conformation tensor $\mathbb{C}$ via

$$\mathbb{T} = \frac{\mathbb{C} - \mathbb{I}}{We}, \tag{2.44}$$

where $\mathbb{I}$ is the identity. The conformation tensor is proportional to the ensemble-averaged second moment of the polymer chain end-to-end distance. In other words, this tensor is related with the macroscopic behaviour of the polymer chains and its trace provides the average square polymer elongation. The conformation tensor is symmetric, positive-definite and, at rest, $\mathbb{C} = \mathbb{I}$. From the first two properties, it can be infered that the determinant of this tensor must be always positive. Indeed, measuring this determinant is essential in order to monitorise whether the simulations are running correctly. The components of $\mathbb{C}$ are $\{C_{rr}, C_{r\theta}, C_{rz}, C_{\theta\theta}, C_{\theta z}, C_{zz}\}$ and its evolution equation is

$$\frac{\partial \mathbb{C}}{\partial t} + \mathbf{u} \cdot \nabla \mathbb{C} - \mathbb{C} \cdot \nabla \mathbf{u} - (\nabla \mathbf{u})^\dagger \cdot \mathbb{C} = -\frac{\mathbb{C} - \mathbb{I}}{We} + \left[\kappa \nabla^2 \mathbb{C}\right], \tag{2.45}$$

where the dagger means transposition. In addition, the third and fourth terms make the time derivative of $\mathbb{C}$ independent of the frame of reference; a detailed discussion about this matter can be found in Bird *et al.* (1987). The term in brackets introduces an

artificial diffusion for $\mathbb{C}$ and has been included in order to gain stability when integrating the tensor (Sureshkumar & Beris, 1995). The coefficient of diffusion κ must be chosen as low as possible in order to not affect appreciably the dynamics of the flow, hence $\kappa Re \ll 1$ and $\kappa We \ll 1$ (Thomas *et al.*, 2006, 2009).

Conceptually, the velocity boundary conditions described in the previous section by (2.5) are correct, but now they have to be changed because of the different non-dimensionalisation:

$$\mathbf{u}(r, \theta, \pm\Gamma/2, t) = (0, 0, 0), \tag{2.46a}$$

$$\mathbf{u}(1, \theta, z, t) = \big(0, 0, \sin(2\pi St\, t)\big). \tag{2.46b}$$

As a matter of fact, when the artificial diffusive term is included in the constitutive equation, some boundary conditions for $\mathbb{C}$ are necessary. This question is addressed extensively in the forthcoming section. The inclusion of the diffusive term represents an artifact, as well as the election of the boundary conditions. The most usual procedure is the integration without the diffusive term and then these results are employed as Dirichlet boundary conditions (Sureshkumar & Beris, 1995; Thomas *et al.*, 2006). In an attempt to avoid strong gradients near the wall that are difficult to integrate, another choice that might favour numerical stability are Neumann boundary conditions on all tensor components. This second option possesses also the advantage that the boundary conditions are continuous in the whole domain.

2.2.2 Numerical scheme

The momentum equations for an incompressible viscoelastic fluid (2.43) can be interpreted as the incompressible Navier-Stokes equations (2.4) with an additional forcing term that comes from the polymeric stresses. Hence, the same second-order time-splitting method of Mercader *et al.* (2010) is used for the time evolution of the velocity field. However, the time integration of the constitutive equations is much more difficult because of its highly hyperbolic nature. For this reason, different temporal schemes are used in an attempt to avoid numerical instabilities and subsequent blow-ups. The same spatial discretisation of the former section is used here: Galerkin-Fourier expansions in the periodic azimuthal coordinate and Chebyshev-collocation in the axial and radial directions. Nevertheless, the considerations about the Fourier expansions have to be extended to the components of the conformation tensor.

Temporal discretisation

The momentum equations have been solved using a second-order time-spliting method based on a combination of Adams-Bashforth and backward differentiation schemes (Mercader *et al.*, 2010), similarly to problems of convection:

$$\nabla \cdot \mathbf{u}^{n+1} = 0 \tag{2.47a}$$

$$\begin{aligned}\frac{3\mathbf{u}^{n+1} - 4\mathbf{u}^{n} + \mathbf{u}^{n-1}}{2\Delta t} = &- \nabla p^{n+1} - 2\mathbf{N}\left(\mathbf{u}^{n}\right) + \mathbf{N}\left(\mathbf{u}^{n-1}\right) + \frac{(1-\beta)}{Re}\nabla \cdot \mathbb{T}^{n+1} + \\ &+ \frac{\beta}{Re}\nabla^2 \mathbf{u}^{n+1},\end{aligned} \tag{2.47b}$$

where $\mathbf{N}(\mathbf{u}) = \mathbf{u} \cdot \nabla \mathbf{u}$ is the usual advective term of the velocity. The procedure is analogous to the one explained for a Newtonian flow. After updating the conformation tensor $\mathbb{C}^{n+1}$, which is detailed in the next paragraphs, the polymer stress is computed:

$$\mathbb{T}^{n+1} = \frac{\mathbb{C}^{n+1} - \mathbb{I}}{We}. \tag{2.48}$$

The updated polymer stress is introduced when the predictor for the pressure is solved:

$$\nabla^2 \bar{p}^{n+1} = \nabla \cdot \left[-2\mathbf{N}\left(\mathbf{u}^{n}\right) + \mathbf{N}\left(\mathbf{u}^{n-1}\right) + \frac{(1-\beta)}{Re}\nabla \cdot \mathbb{T}^{n+1} \right], \tag{2.49}$$

with the analogous Neumann boundary condition:

$$\begin{aligned}\frac{\partial \bar{p}^{n+1}}{\partial n} = \mathbf{n} \cdot \Bigg[&2\mathbf{L}(\mathbf{u}^{n}) - \mathbf{L}(\mathbf{u}^{n-1}) - 2\mathbf{N}(\mathbf{u}^{n}) + \mathbf{N}(\mathbf{u}^{n-1}) + \frac{(1-\beta)}{Re}\nabla \cdot \mathbb{T}^{n+1} - \\ &- \frac{3\mathbf{u}^{n+1} + -4\mathbf{u}^{n} + \mathbf{u}^{n-1}}{2\Delta t} \Bigg],\end{aligned} \tag{2.50}$$

where $\mathbf{u}^{n+1}$ are the actual boundary conditions for the velocity, and $\mathbf{L}(\mathbf{u}) = -\nabla \times (\nabla \times \mathbf{u})$. By including the preliminary pressure, a predictor velocity, $\mathbf{u}^*$ is achieved:

$$\begin{aligned}\left(\nabla^2 - \frac{3Re}{2\beta\Delta t}\right)\mathbf{u}^* = \frac{Re}{\beta}\Bigg[&\nabla \bar{p}^{n+1} + 2\mathbf{N}(\mathbf{u}^{n}) - \mathbf{N}(\mathbf{u}^{n-1}) - \frac{(1-\beta)}{Re}\nabla \cdot \mathbb{T}^{n+1} - \\ &- \frac{4\mathbf{u}^{n} - \mathbf{u}^{n-1}}{2\Delta t} \Bigg],\end{aligned} \tag{2.51}$$

employing the real Dirichlet boundary conditions for the velocity. Due to the coupling introduced by the linear viscous term, the combinations (A.22) and (A.23) are necessary again. In the final stage, the corrector step is exactly the same as in the former section. Therefore, equations from (2.11) to (2.14) describe the corrector process perfectly.

Coming back to the first fraction step, the update of the conformation tensor has to be obtained firstly. The Oldroyd-B constitutive equations is discretised similarly to the momentum equations:

$$\frac{3\mathbb{C}^{n+1}-4\mathbb{C}^{n}+\mathbb{C}^{n-1}}{2\Delta t}=-2\mathbb{N}\left(\mathbf{u}^{n},\mathbb{C}^{n}\right)+\mathbb{N}\left(\mathbf{u}^{n-1},\mathbb{C}^{n-1}\right)-\frac{\mathbb{C}^{n+1}-\mathbb{I}}{We}+ \\ +\left[\kappa\nabla^{2}\mathbb{C}^{n+1}\right], \tag{2.52}$$

where $\mathbb{N}(\mathbf{u},\mathbb{C})=\mathbf{u}\cdot\nabla\mathbb{C}-\mathbb{C}\cdot\nabla\mathbf{u}-(\nabla\mathbf{u})^{\dagger}\cdot\mathbb{C}$ is the non-linear term of the Oldroyd-B equation.

The simplest option is the purely explicit update of the conformation tensor, which yields:

$$\mathbb{C}^{n+1}=\frac{1}{\left(\frac{3}{2\Delta t}+\frac{1}{We}\right)}\left[-2\mathbb{N}(\mathbf{u}^{n},\mathbb{C}^{n})+\mathbb{N}(\mathbf{u}^{n-1},\mathbb{C}^{n-1})+\frac{\mathbb{I}}{We}+\frac{4\mathbb{C}^{n}-\mathbb{C}^{n-1}}{2\Delta t}\right]. \tag{2.53}$$

Equation (2.53) is referred as CO (Classical Oldroyd) temporal scheme.

An alternative that has been a common practice in the last years (Sureshkumar & Beris, 1995; Thomas *et al.*, 2006) consists in considering equation (2.53) as an intermediate update at time $n+1/2$

$$\mathbb{C}^{n+1/2}=\frac{1}{\left(\frac{3}{2\Delta t}+\frac{1}{We}\right)}\left[-2\mathbb{N}(\mathbf{u}^{n},\mathbb{C}^{n})+\mathbb{N}(\mathbf{u}^{n-1},\mathbb{C}^{n-1})+\frac{\mathbb{I}}{We}+\frac{4\mathbb{C}^{n}-\mathbb{C}^{n-1}}{2\Delta t}\right], \tag{2.54}$$

and this is followed by solving implicitly the equation with the inclusion of the diffusive term:

$$\left(\nabla^{2}-\frac{2}{\kappa\Delta t}\right)\mathbb{C}^{n+1}=-\nabla^{2}\mathbb{C}^{n}-\frac{2}{\kappa\Delta t}\mathbb{C}^{n+1/2}. \tag{2.55}$$

As it happens with the linear viscous term of the velocity, the laplacian of the conformation tensor in cylindrical coordinates couples different components and the linear combinations described by (A.24) are required. After solving the decoupled equations, the physical components are recovered employing (A.25). Some boundary conditions are necessary for the tensor. The most usual choice considered in the literature are $\mathbb{C}^{n+1}=\mathbb{C}^{n+1/2}$ on the sidewalls. However, there is no such thing as a regularity condition analogous to (2.6) for the conformation tensor reported in the literature, because the problem of a viscoelastic fluid in a cylindrical cavity has not been tackled including the artificial diffusion. As a consequence, no regularity conditions are applied to this artificial Dirichlet boundary conditions. Another option that is analysed in the present work are Neumann boundary conditions equal to zero for all the tensor components, thus making the boundary conditions continuous and regular, plus strong gradients are

avoided near the cylinder boundaries. Therefore, depending on the boundary conditions, there are two additional temporal schemes: DOD (Diffusive Oldroyd Dirichlet) and DON (Diffusive Oldroyd Neumann)).

The last option does not consider the stress diffusion as an artifact, so it is included straightforwardly from the beginning, such as is done in Chokshi & Kumaran (2009). In this case, (2.52) can be integrated implicitly as it is done in Mercader *et al.* (2010) for the heat equation:

$$\left(\nabla^2 - \frac{1}{\kappa}\left(\frac{1}{We} + \frac{3}{2\Delta t}\right)\right)\mathbb{C}^{n+1} = \frac{1}{\kappa}\left[2\mathbb{N}(\mathbf{u}^n, \mathbb{C}^n) - \mathbb{N}(\mathbf{u}^{n-1}, \mathbb{C}^{n-1}) - \frac{\mathbb{I}}{We} - \right. \\ \left. - \frac{4\mathbb{C}^n - \mathbb{C}^{n-1}}{2\Delta t}\right]. \tag{2.56}$$

As in the previous paragraph, the same Dirichlet and Neumann boundary conditions are taken into account. Thus, the following acronyms serve to synthesise the schemes: PDOD (Purely Diffusive Oldroyd Dirichlet) and PDON (Purely Diffusive Oldroyd Neumann).

All the differential operators posed by the Poisson and Helmholtz equations along this subsection of viscoelastic fluids, are diagonalised just once applying the method described in Zhao & Yedlin (1994), as occurred with Newtonian flows. Time steps of $\Delta t = 10^{-2} - 10^{-4}$ have been employed to study the numerical stability and accuracy of the different schemes.

Spatial discretisation

The spatial discretisation is analogous to the Newtonian case: Fourier in the periodic θ direction and Chebyshev in the finite directions r and z. In the same direction as before, some magnitudes expand in real series, following:

$$(u_r, u_z, p, C_{rr}, C_{rz}, C_{\theta\theta}, C_{zz})(r, \theta, z) = \sum_{m=-n_\theta/2}^{n_\theta/2-1} F_m(r, z)e^{\mathrm{i}m\theta}, \tag{2.57}$$

whilst others in imaginary series:

$$(u_\theta, C_{r\theta}, C_{\theta z})(r, \theta, z) = \mathrm{i}\sum_{m=-n_\theta/2}^{n_\theta/2-1} F_m(r, z)e^{\mathrm{i}m\theta}, \tag{2.58}$$

thus possessing the same properties given by (2.16) and (2.18), respectively. Since viscoelastic fluids tend to be more complex, a higher resolution is desirable, so $n_r = 96$, $n_z = 192$ and $n_\theta = 20$ are considered when dealing with them.

Once again, some regularity conditions have to be considered at the origin. As has been mentioned, by means of forcing the correct parity of the Fourier expansions, these regularity conditions become imposed implicitly for the velocity field. The same goes for the tensor components and after applying the same reasoning as Lopez *et al.* (2002), it is found that the m-Fourier coefficients of $C_{rr}, C_{r\theta}, C_{\theta\theta}$ and C_{zz} posess parity m, meanwhile for C_{rz} and $C_{\theta z}$ the parity is $m+1$.

The collocation points in the radial and axial directions are distributed according to (2.19) and (2.20), so $r = 0$ is not a collocation point and the points tend to be clustered near the lids and walls of the cylinder. The usual differentiation matrices are also used and the radial derivatives (2.23) take into account the analogous prescriptions on the parity of the Fourier components: the superscript even (odd) has to be employed on odd (even) Fourier components of u_r, u_θ, C_{rz} and $C_{\theta z}$, and even (odd) coefficients of $u_z, C_{rr}, C_{r\theta}, C_{\theta\theta}$ and C_{zz}.

2.2.3 Modal elastic energy

Concerning to the symmetries, the velocity field of the viscoelastic flow posesses the same spatial and spatio-temporal symmetries. In that section, the kinetic energy of the Fourier components has been introduced. Besides measuring the break of the azimuthal rotation symmetries, the modal kinetic energy is very useful to measure whether the flow has reached a steady state. This magnitude is also useful for a viscoelastic flow, but another global magnitude capable of taking into account the time scale of the polymers is desirable. In this sense, the modal elastic potential energy is defined in Balci *et al.* (2011) as:

$$U_m = \frac{2}{\Gamma} \int_{\mathcal{D}} \text{trace}\left(\mathbb{T}_m\right)\, r dr dz, \tag{2.59}$$

where the integration is over the whole cylinder, thus $\mathcal{D}$ is $(r, z) \in [0, 1] \times [-\Gamma/2, \Gamma/2]$. Indeed, since polymer dynamics tend to be slower than the flow establishment, when the elastic energy of the axisymmetric mode reaches a steady state, means that the whole polymer solution is steady.

2.3 Spectral convergence

All the imaginable numerical tests for this code have been performed in Mercader *et al.* (2010) and this section is devoted to check the spectral accuracy of one of the most

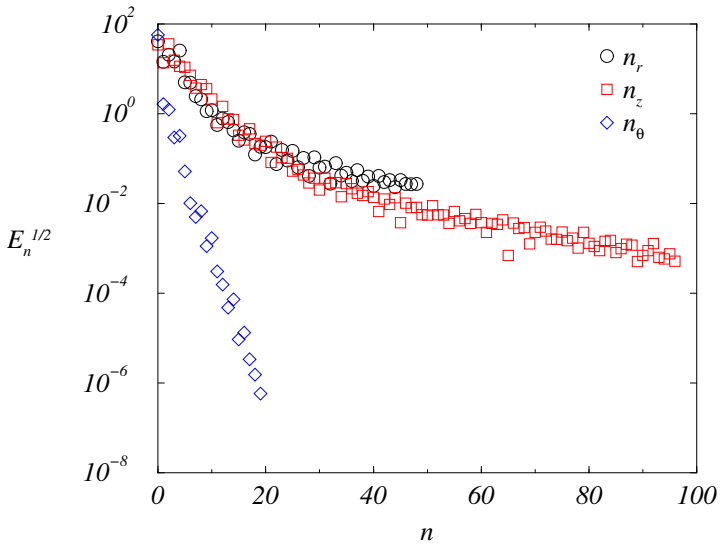

Figure 2.2: Chebyshev amplitudes of the square root of the kinetic energy for the radial coefficients n_r (circumferences) and axial coefficients n_z (squares), and Fourier modes of the square root of the kinetic energy n_θ (diamonds), computed at $(St, Re) = (15.5, 395)$.

complex solutions included in the present thesis. This solution is a special type of travelling waves, which posess $m = 1$ and exist for $(St, Re) = (15.5, 395)$, and are commented exhaustively in Chapter 4. Figure 2.2 shows the Chebyshev amplitudes of the square root of the kinetic energy for the radial coefficients n_r (circumferences) and axial coefficients n_z (squares), and Fourier modes of the square root of the kinetic energy n_θ (diamonds). This figure clearly illustrates the existance of the exponential decay typical from spectral methods for the Fourier coefficients, as well as for the remaining two coefficients at small values of n. Nonetheless, the convergence in these directions seems to become algebraic, rather than spectral. This issue might be caused by the complexity of the solution and is not dramatic at all because its accuracy is still enough: the ratio between the leading coefficients and the ones in the tail, q, is $q_r \approx 1500$ and $q_z \approx 45396$ for the radial and axial coefficients, respectively. For viscoelastic flows, the spectral convergence is crucial to know whether the simulations are going in the right direction and some examples are discussed in Chapter 6.

2.4 Linear stability analysis

The linear stability of the basic state to general three-dimensional perturbations is determined using global linear stability analysis via time evolution of the Navier-Stokes

equations (Lopez, Marques, Rubio & Avila, 2009; Do, Lopez & Marques, 2010). First, a periodic axisymmetric basic state is computed at some point in the parameter space. By means of introducing small random perturbations of amplitude δ into all azimuthal Fourier modes, the stability of the basic flow is determined. For sufficiently small perturbations, the non-linear couplings between Fourier modes are neglectable (below round-off numerical noise) and the growth rates (real parts of the eigenvalues) and structure of the eigenfunctions corresponding to the fastest growing perturbation at each Fourier mode emerge from time evolution. This is tantamount to a matrix-free generalised power method in which the actions of the Jacobian matrices for the perturbations are given by time integration of the Navier-Stokes equations with the aforementioned initial conditions. This direct numerical technique is very efficient as the exponential growth or decay of the perturbations is established in a relatively short amount of time, and there is no need to evolve the disturbances until the non-linear saturation. This technique has been used on a wide variety of fluid dynamics problems where the state whose stability is under analysis is non-trivial (see Lopez & Marques, 2009; Lopez *et al.*, 2009; Rubio *et al.*, 2010, for examples and some further details).

2.5 Discussion

A spectral-projection method formulated in terms of primitive variables is adopted to solve the incompressible Navier-Stokes equations in a cylindrical cavity periodically forced in the axial direction. The numerical formulation includes a second-order semi-implicit scheme for the time integration and a pseudospectral approach for the spatial coordinates: Chebyshev-collocation in the finite axial and radial directions and Fourier-Galerkin in the periodic azimuthal direction. The singularity at $r = 0$ is solved by avoiding clustering around the pole and not considering this point a collocation point. In addition, some regularity conditions are implicitly implemented via the proper parity of the Fourier coefficients. This code is efficient and accurate when dealing with any incompressible flows in cylindrical enclosures and, in the current hydrodynamic scneario, clearly provides spectral convergence.

The same formulation for the momentum equation of the different viscoelastic models is assumed. Because of the numerical difficulties arising when updating the polymer contribution, several numerical approaches are taken into account to obtain good results. Concerning the spatial considerations, analogous parity conditions are employed in the viscoelastic case. The efficiency of these codes has yet to be tested, as well as the spectral

covergence as a function of the different parameters. In fact, these polymers introduce an additional time scale related with their relaxation towards equilibrium. In order to account for the possible effects of the different time scales, the elastic energy has to be studied alongside the kinetic energy. Another consideration that has to be kept in mind is the fact that the determinant of the conformation tensor must be positive no matter what.

Because of the symmetries of the problem, the velocity field of the basic flow has to be axisymmetric and time-periodic with the forcing. This basic state is obtained by temporal evolution in all cases. By means of perturbing all the Fourier modes of this state, the stability of the basic flow is analysed. Furthermore, after waiting enough time, eventually a bifurcated state is obtained or the recovery of the basic state achieved.

CHAPTER 3

TRANSITIONS TO THREE-DIMENSIONAL FLOWS FOR NEWTONIAN FLUIDS

The von Kármán vortex street is a classic problem in fluid dynamics (Guyon, Hulin, Petit & Mitescu, 2001). This case and other bluff-body wakes are invariant in the spanwise direction to both translations ($SO(2)$ symmetry group) and reflections (Z_2 symmetry group), the combination generating the $O(2)$ symmetry group. In addition to $O(2)$, these two-dimensional flows possess a spatio-temporal symmetry of Z_2 type, as is the case for the wake of a circular cylinder in the streamwise direction (Barkley, Tuckerman & Golubitsky, 2000; Blackburn & Lopez, 2003*a*; Blackburn, Marques & Lopez, 2005). As a consequence, the complete symmetry group of these flows is $O(2) \times Z_2^{ST}$.

The transition from two-dimensional to three-dimensional flows in wake flows have been extensively studied. The types of symmetry-breaking bifurcations are completely determined by the symmetry group of the system, and not by the particulars of the physical mechanisms responsible for the bifurcation, and have been analysed in detail in Marques *et al.* (2004). The equivariant branching lemma (see, for example Golubitsky *et al.*, 1988; Chossat & Lauterbach, 2000) formalises the notion that the symmetries of the system govern the types of possible bifurcations that may occur, as well as the symmetry properties of the bifurcating solutions themselves. The main results obtained for systems with $O(2) \times Z_2^{ST}$ spatio-temporal symmetry determine that there are two types of bifurcations, one synchronous and the other resulting in quasiperiodic flows. Both types come in two different flavors, depending on the symmetries of the bifurcated solutions. There are two synchronous modes, A and B, that break or preserve the space-time symmetry Z_2^{ST}, respectively. The quasiperiodic solutions have the form of modulated travelling waves or modulated standing waves in the spanwise direction; they differ in their symmetry properties: the travelling waves preserve a space-time symmetry, while the standing wave preserves a purely spatial reflection symmetry.

The analysis of symmetric bluff-body wakes (see a summary in Blackburn *et al.*, 2005), starting with circular cylinders, and followed by other symmetric bodies, the square cylinder and a flat plate, have been successful in observing the two kinds of synchronous modes. Unfortunately, the quasiperiodic modes do not manifest themselves as primary bifurcations, and can only be observed or computed as secondary or higher bifurcations, in the form of mixed modes. The presence of a single control parameter leaves little room for manoeuvre to find the quasiperiodic modes as primary bifurcations. A reasonable option is the study of similar systems with more governing parameters, such

as axisymmetric bluff-body wakes in the flow past a ring (Leweke & Provansal, 1995; Sheard *et al.*, 2004) or the wakes produced in a square cylinder that has been rotated a certain angle (Blackburn & Sheard, 2010). Unluckily, the spatio-temporal symmetry is not satisfied strictly and this asymmetry produce some subharmonic modes that are not present in the exact symmetry case.

In order to better understand this transition, other fluid problems with the same symmetry group and more than one parameter have been studied. Flows driven by a periodic motion of one of the container walls resulted in systems with the same symmetry group. Such systems include the periodically driven rectangular cavity of infinite spanwise (Lopez & Hirsa, 2001; Vogel *et al.*, 2003; Blackburn & Lopez, 2003*b*; Leung *et al.*, 2005) and the driven annular cavity (Blackburn & Lopez, 2011). In the rectangular cavity, the $O(2)$ invariance is only an idealisation of the corresponding experimental flow due to the finite extent of the spanwise direction. Therefore, in the experiments, instead of finding the travelling waves predicted by the theory, spanwise endwalls effects resulted in quasiperiodic states that are neither spanwise symmetric nor spanwise travelling (Leung *et al.*, 2005). Cylindrical geometries are very useful in the sense that the azimuthal direction is physically periodic and have the $O(2)$ symmetry group exactly fulfilled. In the annular driven geometry with large radius ratios, the quasiperiodic modes possess very large azimuthal wave number and have not been found as non-linearly saturated pure modes, but instead they are mixed with contributions from the synchronous A mode, thus producing complicated solutions, as is observed in Blackburn & Lopez (2011).

The system under consideration, a finite circular cylinder with an axially oscillating sidewall, solves all the mentioned problems and makes it worth studying. This chapter is structured as follows. In Section §3.1 the base state of the system is computed, and its changes when parameters are varied. Section §3.2 is devoted to the linear stability analysis of the basic flow, and compared with similar flows. In Section §3.3 the three-dimensional structure and symmetries of the different unstable modes found are analysed in detail. Finally, the main results are summarised and gathered in Section §3.4. The main findings of this chapter can be found in Panades *et al.* (2011).

3.1 Basic states

The basic flow, having all the symmetries of the problem, is always axisymmetric and time-periodic, synchronous with the forcing. The axial oscillations of the cylinder side-

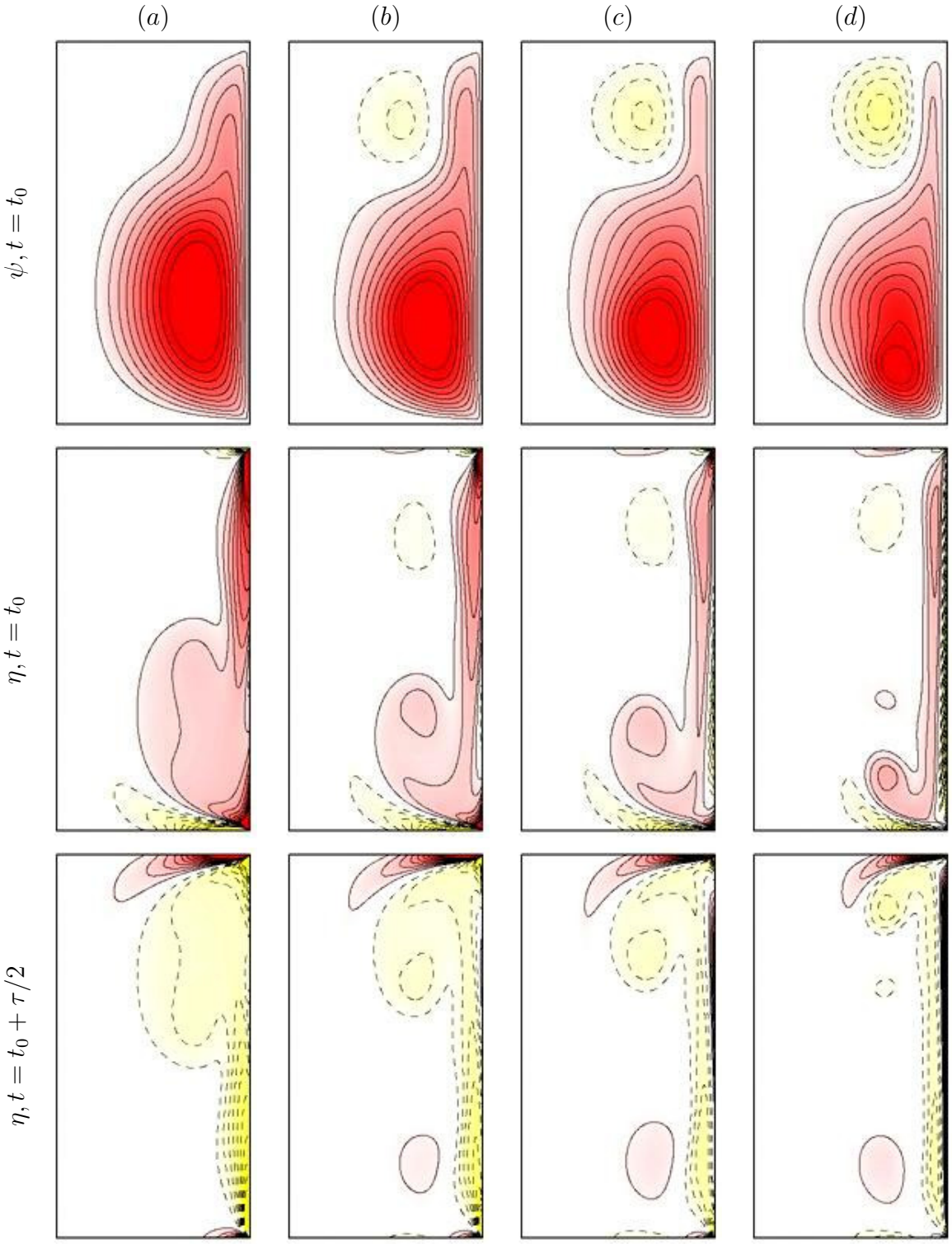

Figure 3.1: Contours of streamfunction, ψ, and azimuthal vorticity, η, of the basic state at four parameter values, for amplitudes Re very close to, and above, the corresponding critical values: (a) $(St, Re) = (10, 340)$, (b) $(St, Re) = (32, 525)$, (c) $(St, Re) = (50, 615)$ and (d) $(St, Re) = (100, 700)$. Solid (dashed) contours are positive (negative); light/dark (yellow/red) colours correspond to negative/positive values. For each St, t_0 has been selected where the oblique jet at the bottom corner is most intense.

wall produce periodic Stokes-type boundary layers on the oscillating wall. These layers separate from the sidewall and move towards the cylinder axis after colliding with the endwalls to form rollers. The term roller refers to large-scale rotating flow structures with primarily azimuthal vorticity, η. These rollers are formed every half-period alternatively on each endwall. Since the basic flow is axisymmetric, a streamfunction (ψ, such that $u = -1/r\,\partial\psi/\partial z$ and $w = 1/r\,\partial\psi/\partial r$) is defined and instantaneous contours of this magnitude are shown in the first row of Figure 3.1 for four increasing values of the forcing frequency St, and for amplitudes Re, very close to, and above, the critical value at which the basic flow becomes unstable. These unstable basic states are computed in the axisymmetric subspace. In all cases the figures represent meridional planes $(r, z) \in [0, 1] \times [-\Gamma/2, \Gamma/2]$.

The magnitude and size of the rollers change substantially with St. For small forcing frequencies, there is enough time for these rollers to dissipate during part of the forcing period, and so in Figure 3.1(a) a single roller fills the whole domain during almost all the period, whereas for large frequencies the rollers persist at both ends throughout the whole forcing cycle, as can be observed in Figures 3.1(b)-(d). The Stokes number determines the size of the rollers and their dissipation, and the Reynolds number measures the strength of their collision with the lids and the recirculation of the fluid. The characteristics of the rollers are similar to the ones described in previous works for the planar case (Blackburn & Lopez, 2003b) and for an annular cavity (Blackburn & Lopez, 2011), but in the present analysis the curvature effects are much more important, and the flow geometry is altered relavantly near the cylinder axis.

Instantaneous contours of the azimuthal vorticity are shown in the second and the third rows of Figure 3.1. These contours are well suited to describe the boundary layers that form at the sidewall and endwalls, and verify the spatio-temporal symmetry H. The sidewall boundary layer is a Stokes-type boundary layer whose thickness is proportional to $St^{-1/2}$ (Batchelor, 1967; Schlichting & Kestin, 1979; Marques & Lopez, 1997), so the boundary layer becomes thinner for larger values of the forcing frequency St, and also becomes finer as the amplitude of the forcing Re is increased. The sidewall boundary layer, dragged by the cylinder sidewall motion, separates upon colliding with the endwalls, and from the corners where the sidewall and endwalls meet, the boundary layer enters the bulk of the fluid, forming axisymmetric oblique jets that result in the formation of the rollers. This process is analogous to the formation of a vortex roller near the junction of an impulsively started plate and a stationary plate, where there is a jump in the velocity (Allen & Lopez, 2007). The jets are clearly seen in the azimuthal vorticity contours: the jet centerline coincides with the azimuthal vorticity zero contour,

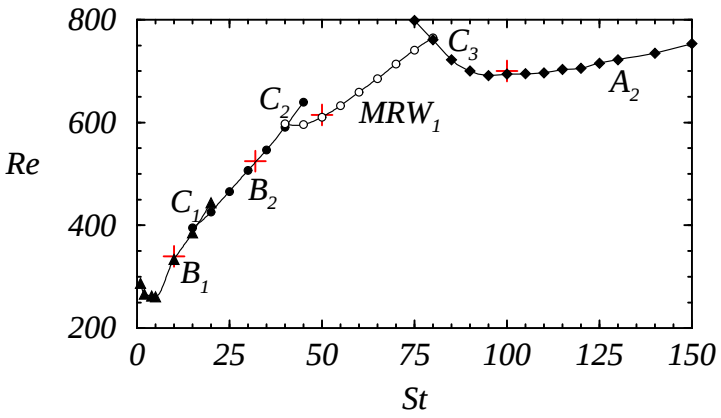

Figure 3.2: Critical Reynolds number, Re_c, as a function of the Stokes number, St, for the transition from the basic state to the different three-dimensional states: B_1, B_2, MRW_1 and A_2. The crosses correspond to the four basic states depicted in Figure 3.1.

and on each side it is surrounded by regions with intense azimuthal vorticity of opposite signs. Oscillating boundary layers also form on the endwalls with azimuthal vorticity of opposite sign to that of the rollers, as a result of the jet dynamics just described, and because the endwalls are at rest. Regarding the spatio-temporal symmetry, these states clearly preserve H because the azimuthal vorticity is reflected respect to the $z = 0$ plane after advancing a half-period.

3.2 Stability of the basic flow

By increasing the amplitude of the forcing Re beyond a critical value $Re_c(St)$, the basic state undergoes a symmetry-breaking bifurcation yielding a new three-dimensional state. Depending on St, the basic state may undergo either synchronous or Neimark-Sacker bifurcations. The stability of the basic flow has been comprehensively explored for $St \in [1, 150]$, revealing two synchronous modes (A and B) that bifurcate from the axisymmetric state by breaking the symmetries differently in each case. There is also a novel quasiperiodic mode that manifests as modulated rotating waves MRW. Subscripts for each of these states are used here to indicate their azimuthal wave number m.

The bifurcation curves for the different modes in (St, Re)-space are shown in Figure 3.2 and are obtained using the method described in Section §2.4. At low St, mode B is the first to become critical with increasing Re, while at high St mode A is the first. At intermediate values $St \in [40.573, 79.643]$, the quasiperiodic mode bifurcates first, in the form of modulated rotating waves MRW. The synchronous mode A al-

ways has an azimuthal wave number $m = 2$ (A_2), the quasiperiodic mode has $m = 1$ (MRW_1), and the synchronous mode B may have either $m = 1$ or $m = 2$ depending on St. The bifurcations to the four different states (B_1, B_2, MRW_1 and A_2) when varying the forcing frequency St are separated by three codimension-two or bicritical bifurcation points, C_i with $i = 1, 2, 3$, at which two of the states bifurcate simultaneously, and their locations in the (St, Re)-space are $C_1 = (15.636, 394.57)$, $C_2 = (40.573, 596.12)$ and $C_3 = (79.643, 764.51)$. The four base states shown in Figure 3.1 correspond to the four distinct bifurcated states in Figure 3.2 marked with crosses. The synchronous modes for small St have azimuthal wave number $m = 1$ (B_1) and a single roller fills the domain most of the time, whereas they have azimuthal wave number $m = 2$ (B_2 and A_2) for larger $St > 15$ and two rollers persist throughout the whole forcing cycle. However, the quasiperiodic MRW_1 has azimuthal wave number $m = 1$ although it is dominant in a St region where the two rollers persist.

A very similar scenario occurred in the periodically driven rectangular cavity problem, as illustrated in Figure 1.5, showing the critical Re number as a function of St in the cavity flow (adapted from Blackburn & Lopez, 2003*b*; Leung *et al.*, 2005). Figures 3.2 and 1.5 are strikingly similar, and they only differ in their scaling. The critical Re and St for the rectangular cavity are about a factor of two larger than for the cylinder case, so that the marginal curve in the cavity flow occurs at higher Re number, and the different modes are shifted to higher St. The qualitative shape of the marginal curves are very similar in both cases, and the shift in (St, Re) reflects the different geometries of the two problems. An important difference between the two problems is that in the driven rectangular cavity the wave number of the bifurcated solution varies continuously, while in the cylinder problem it is discrete (and in fact of very small wave number, either $m = 1$ or $m = 2$). However, the qualitative trend is the same in both problems. In the driven rectangular cavity, the wave number of mode B increases with St, while for QP and A their wave numbers are almost independent of St (Leung *et al.*, 2005). In the cylinder problem, the azimuthal wave number of mode B also increases with St (varying from $m = 1$ to $m = 2$), while for MRW and A their azimuthal wave numbers do not change with St ($m = 1$ for MRW and $m = 2$ for A).

A detailed comparison with the annular cavity problem (Blackburn & Lopez, 2011) is not possible for a number of reasons. That study focused on the modulated rotating waves at a single value of $St = 100$, and at that value of St the MRW were found to be unstable. The non-linear flows were complicated, showing mixed characteristics between the synchronous and quasiperiodic modes. Nevertheless, the different modes obtained in the present cylinder problem were also present in the annular cavity problem. The radius

ratio used in the annular study was close to one, so that both inner and outer radii were much larger than the annular gap. That choice of the radius ratio was made to compare with the rectangular cavity flow problem, which corresponds to the radius-ratio-going-to-one limit. As a result, the azimuthal wave numbers of the bifurcating states were very large (between $m = 30$ and $m = 35$ for the dominant modes in the parameter regime considered). In contrast, in the cylinder problem which corresponds to radius ratio equal to zero, the azimuthal wave numbers are very small ($m = 1$ and $m = 2$). Furthermore, even though the two problems have the same symmetry group, the flow domain in the cylinder is singly-connected whereas in the annulus it is doubly-connected.

3.3 Three-dimensional structure and symmetries of the unstable modes

After perturbing the axisymmetric basic flow with $Re > Re_c(St)$, a new three-dimensional periodic or quasiperiodic state is obtained, once the saturation is reached. This bifurcated state depends strongly on the mode that drives the instability, and on the precise values of (St, Re). When describing these bifurcated flows, the term braid, which is widely used in similar flows, is employed to denote smaller-scale meridional structures with vorticity components ξ and ζ. Braids are typically generated through the amplification of spanwise-orthogonal perturbations of the rollers in rectangular cavities, and in cylindrical and annular geometries the amplification of meridional perturbations of the rollers gives rise to these kind of structures.

In the following subsections the symmetries and features of the different bifurcated solutions are described and illustrated with results computed at given values of St. Modes B_1, B_2 and A_2 are computed at $St = 10$, 32, 100, respectively, whilst mode MRW_1 at $St = 50$, and their corresponding base states have already been illustrated in Figure 3.1. All the solutions have been computed at Re slightly above Re_c.

3.3.1 Synchronous modes

Three-dimensional synchronous states result when a pair of purely real eigenvalues (multiplicity two due to the $O(2)$ symmetry) cross the unit circle at $+1$ in the complex plane. When a synchronous axisymmetric flow is perturbed, the energies of the Fourier modes may grow or decay depending on the case, but regardless their evolution is clearly

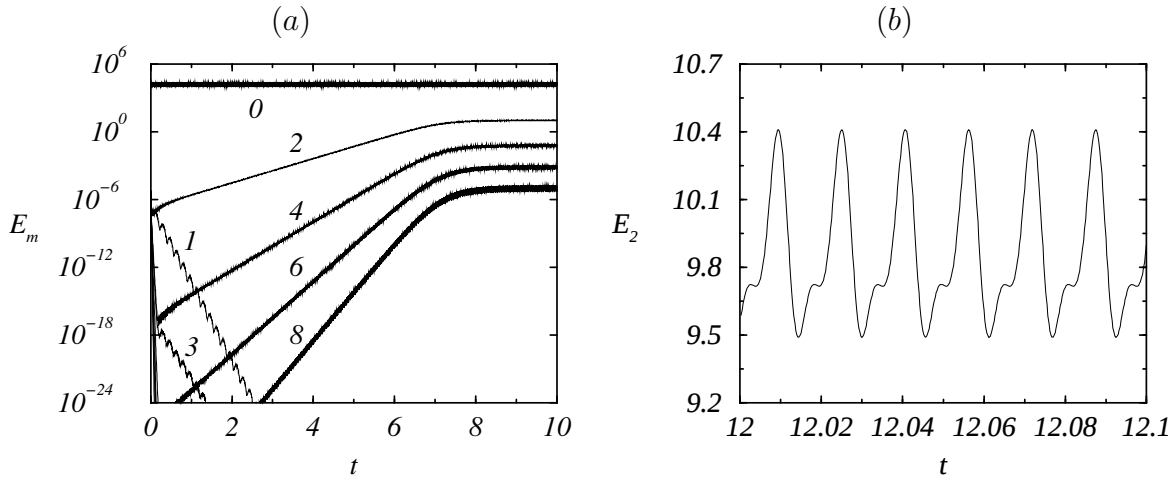

Figure 3.3: (a) Time series of the energies of the leading Fourier modes, with azimuthal wave numbers m as indicated, for the B_2 state at $(St, Re) = (32, 525)$; and (b) a close-up of $E_2(t)$ after saturation.

modulated by the sidewall frequency. When the basic flow is unstable to synchronous modes, the Fourier spectra begin to grow and after some time reach an asymptotic state where the modes are saturated but oscillate with the driving frequency of the sidewall about a mean value. Such an evolution can be seen in Figure 3.3, where the energies, E_m, of the leading Fourier modes are shown as a function of time for the B_2 state at $(St, Re) = (32, 525)$; the inset displays the oscillations in the energy, synchronous with the forcing ($\tau = 1/St = 1/32 = 0.03125$), but with the period halved because the energy is a sum of squares of the velocities. Since in this case the first mode is linearly stable and quasiperiodic, the odd modes decay exponentially in a process that involves two frequencies.

The three-dimensional structures of modes A and B are visualised in Figure 3.4 with the aid of perspective views of instantaneous isosurfaces of the radial vorticity (dark/light or red/yellow are positive/negative values), which show the braid structures, and azimuthal vorticity (translucent), exhibiting the rollers. Note that the only component of vorticity of the axisymmetric base state that is non-zero is the azimuthal component, and that the braids are comprised of radial and axial components of vorticity and are a direct result of breaking axisymmetry. In general terms, braids are located near the lids and away from the sidewall, and they are born on the oblique jets alternatively emerging from the top and bottom corners. Nevertheless, there are some subtle variations. For A_2, braids suffer slight changes in shape and their behavior is quite regular as is that of the rollers. Notice that the shape of each roller is essentially the same as those of the

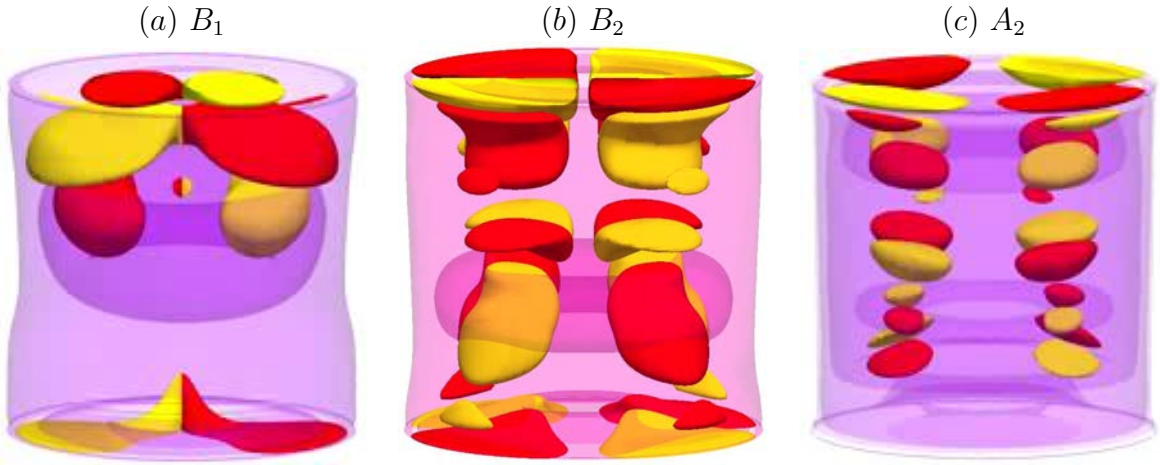

Figure 3.4: Isosurfaces of radial vorticity ξ (solid) and azimuthal vorticity η (translucent) for the synchronous states (*a*) B_1 at $(St, Re) = (10, 340)$ with $\xi = \pm 50$ and $\eta = \pm 500$, (*b*) B_2 at $(St, Re) = (32, 525)$ with $\xi = \pm 40$ and $\eta = \pm 1000$, and (*c*) A_2 at $(St, Re) = (100, 700)$ with $\xi = \pm 150$ and $\eta = \pm 800$. Dark/light (red/yellow) isosurfaces indicate positive/negative values of ξ. This colour convention for the isosurfaces is used along this chapter.

basic states. For B_1 and B_2, braids change abruptly during a forcing cycle, as do the rollers in this regime, and their dynamics (creation, merging and destruction) are much more complex. In addition, the azimuthal vorticity of the B modes is very different from that of the corresponding basic state.

As the bifurcated solutions are no longer axisymmetric, the $O(2)$ symmetry has been broken. Of the continuous family of rotations R_α, there only remains the discrete symmetry $R_{2\pi/m}$, a rotation of angle $2\pi/m$ around the axis, and its powers. The azimuthal wave number of the bifurcated solution is m. The continuous family of reflection symmetries about meridional planes, K_β, is also reduced to a collection of m reflection planes at angles π/m apart, as was shown in Marques *et al.* (2004). These spatial symmetries are clearly evident in Figures 3.5 and 3.6. The planes of reflection symmetry correspond to the diameters with zero axial vorticity. Note that when the symmetry is preserved, the axial vorticity changes sign according to (2.29a). The rotation and meridional reflection symmetries just described generate the so-called D_m symmetry group (or dihedral group) with $2m$ elements, consisting of m rotations and m meridional reflections. When $m = 1$, this group contains only the identity and one meridional reflection, and is isomorphic to Z_2.

Now, let us examine what happens with the spatio-temporal symmetry H. Figure 3.5 exhibits contours of the axial vorticity of the critical eigenvectors for the B_1, B_2 and A_2

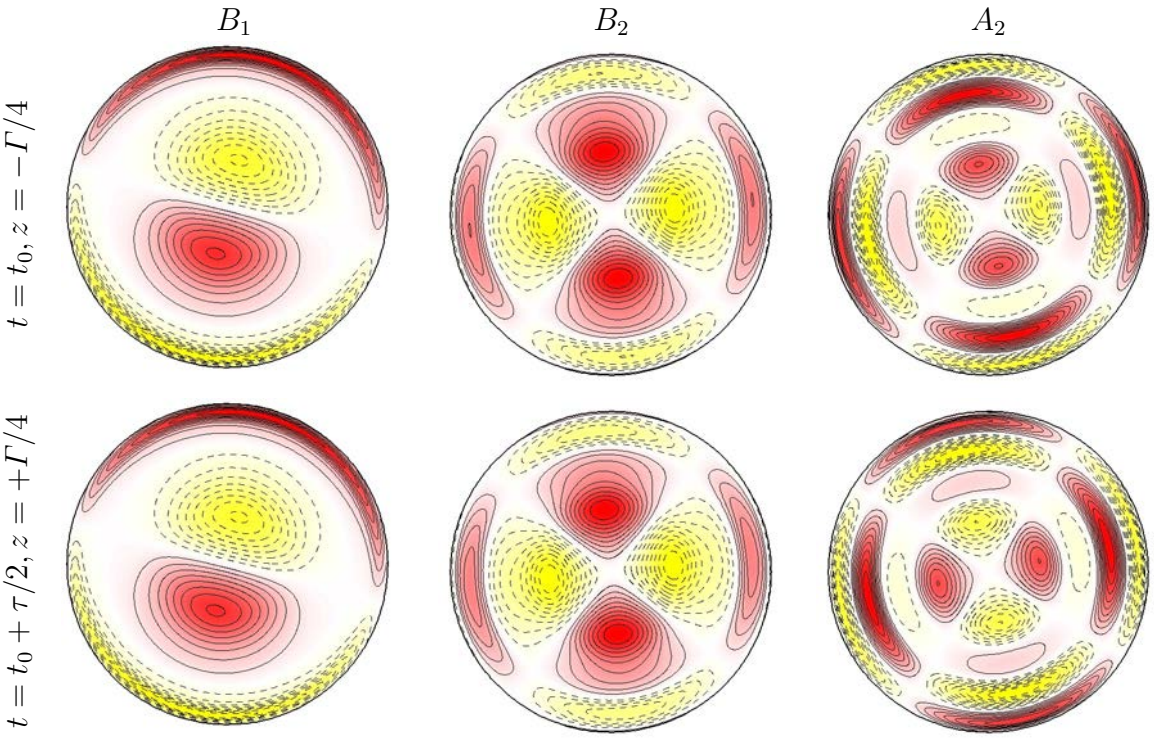

Figure 3.5: Axial vorticity contours of the eigenfunctions at the bifurcation to states B_1, B_2 and A_2 shown in Figure 3.4, in the z-sections and times indicated; t_0 is a convenient time. Solid (dashed) contours are positive (negative); light/dark (yellow/red) colours correspond to negative/positive values. This contour/colour convention is used in all subsequent cross-sections.

bifurcations in a horizontal section $z = -\Gamma/4$ for a given time, and in the reflection-symmetric section $z = +\Gamma/4$ after advancing half the forcing period. The figure shows that the bifurcations to B_1 and B_2 are H-symmetric, i.e. the values of the axial vorticity ζ of the eigenfunctions, at a given time t_0 and at $z = -\Gamma/4$, are the same as the values of ζ advancing time by half the forcing period, $t_0 + \tau/2$, on the reflection-symmetric plane $z = +\Gamma/4$. The eigenfunction of the A_2 bifurcation is not H-symmetric, but changes sign, so the H symmetry is broken in this bifurcation. However, H combined with the rotation $R_{\pi/m}$, with $m = 2$ (half the angle of the rotational symmetry of the state), results in a new space-time symmetry of the A_2 eigenfunction. This is precisely the expected behavior from bifurcation theory (Marques *et al.*, 2004): there are only two options for three-dimensional synchronous eigenfunctions under the action of the space-time symmetry H, either multiplication by $+1$ or -1. The behavior of all the

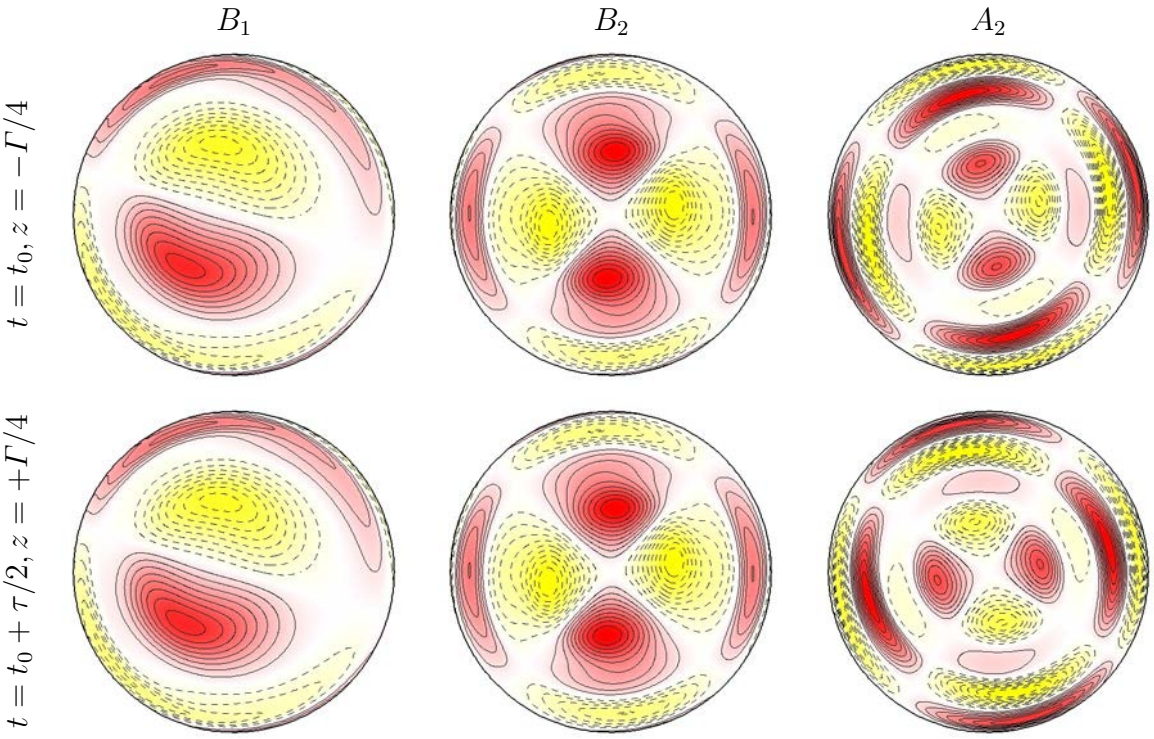

Figure 3.6: Axial vorticity contours of the non-linear saturated states corresponding to B_1, B_2 and A_2 shown in Figure 3.4, in the z-sections and times indicated; t_0 is a convenient time. Contour/colour convention as in Figure 3.5.

velocity and vorticity components is given by

$$H \text{ preserved:} \quad \begin{cases} (u,v,w)(r,\theta,z,t) = (u,v,-w)(r,\theta,-z,t+\tau/2), \\ (\xi,\eta,\zeta)(r,\theta,z,t) = (-\xi,-\eta,\zeta)(r,\theta,-z,t+\tau/2), \end{cases} \tag{3.1}$$

$$H \text{ broken:} \quad \begin{cases} (u,v,w)_{\mathrm{e}}(r,\theta,z,t) = (-u,-v,w)_{\mathrm{e}}(r,\theta,-z,t+\tau/2), \\ (\xi,\eta,\zeta)_{\mathrm{e}}(r,\theta,z,t) = (\xi,\eta,-\zeta)_{\mathrm{e}}(r,\theta,-z,t+\tau/2), \end{cases} \tag{3.2}$$

$$R_{\pi/m}H \text{ preserved:} \quad \begin{cases} (u,v,w)(r,\theta,z,t) = (u,v,-w)(r,\theta+\pi/m,-z,t+\tau/2), \\ (\xi,\eta,\zeta)(r,\theta,z,t) = (-\xi,-\eta,\zeta)(r,\theta+\pi/m,-z,t+\tau/2), \end{cases} \tag{3.3}$$

The space-time symmetries of the eigenfunctions are inherited by the non-linear saturated states (as long as no additional bifurcations take place in the saturation process). However, the multiplication by -1, whose action is described by (3.2), is a property only of the eigenfunction and not of the resulting saturated non-linear state. The reason is that the eigenfunctions are pure Fourier modes in the azimuthal direction, and when they develop into fully non-linear three-dimensional bifurcated solutions, Fourier harmonics appear, and the even harmonics (including the zero mode) are multiplied by $(-1)^2 = +1$ under the action of H, so the full non-linear solution does not have the

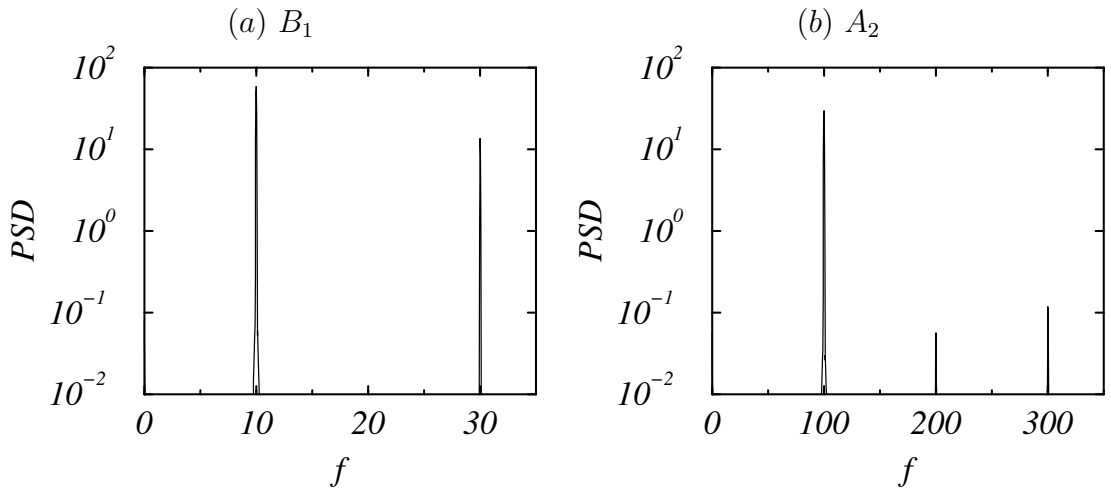

Figure 3.7: FFT of the time series of the near-wall axial velocity at mid-height $(r, \theta, z)_P = (0.9, 0, 0)$ for the (a) B_1 at $(St, Re) = (10, 340)$, and (b) A_2 at $(St, Re) = (100, 700)$.

multiplication by -1 property, (3.2), that the eigenfunction possesses. Figure 3.6 shows the same information as in Figure 3.5, but for the full non-linear bifurcated solutions, illustrating the symmetry properties of the saturated states. The non-linear states are not invariant to the action (3.2), in contrast with the eigenfunctions, hence the use of the subscript e refers to the eigenfunction. The preserved symmetries, H (3.1) and $R_{\pi/m}H$ (3.3), clearly persist in the non-linear states.

In order to check more rigorously the spatial symmetries of mode B_1, the asymmetry parameter, S_{K_β}, is employed, thus yielding $S_{K_\beta}(B_1) = 0.0154$. The measurement of S_{K_β} for the bifurcated states with even Fourier modes (B_2 and A_2) is not possible due to the absence of the first Fourier mode. A more rigurous estimation of the spatio-temporal H symmetry breaking based on Fourier analysis is explained in Section §2.1.3. Figure 3.7 displays the power spectral density (PSD) after computing the Fast Fourier Transform (FFT) of the near-wall axial velocity at mid-height $(r, \theta, z)_P = (0.9, 0, 0)$ for the two types of synchronous modes. The B modes, represented by a B_1 solution computed at $(St, Re) = (10, 340)$ in Figure 3.7(a), only possess one frequency and its linear odd combinations; meanwhile, the A_2 mode calculated at $(St, Re) = (100, 700)$ has a sole frequency and the even and odd harmonics. Therefore, both modes are synchronous and the A modes do not preserve H, whilst B modes do.

Synchronous modes A and B with azimuthal wave number m have the same spatial symmetry group, the dihedral group D_m, and they also have one spatio-temporal symmetry: H for the B modes, and $R_{\pi/m}H$ for the A modes. However, the complete

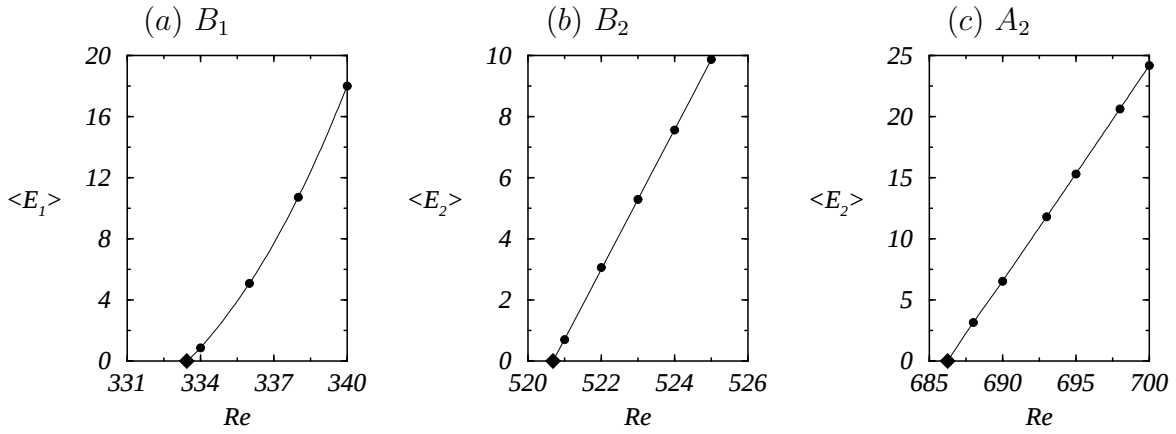

Figure 3.8: Time average of the energy of the dominant mode for the synchronous solutions as a function of Re, (a) B_1 solutions at $St = 10$, (b) B_2 solutions at $St = 32$, and (c) A_2 solutions at $St = 100$. The diamond corresponds to the critical Re obtained by linear stability analysis and the solid disks correspond to computed non-linear solutions.

symmetry groups of the bifurcated states are different: as H commutes with $O(2)$ it also commutes with the subgroup D_m, and the complete symmetry group for the B modes is the direct product $D_m \times Z_2^{ST}$. Nevertheless, $R_{\pi/m}H$ does not commute with D_m, because rotations and meridional reflections do not commute ($K_\beta R_\alpha = R_{-\alpha}K_\beta$). So, for the A modes the complete symmetry group is the semidirect product $D_m \rtimes Z_2^{ST}$. This is an example of a complete symmetry group where the spatial and spatio-temporal symmetries do not commute, a possibility discussed in Marques *et al.* (2004), and also from a more theoretical point of view in Lamb (1996); Lamb & Melbourne (1999).

The three bifurcations to B_1, B_2 and A_2 are supercritical, as shown in Figure 3.8, where the time-averaged energy of the dominant mode $\langle E_m \rangle$ is plotted as a function of the Reynolds number. The plot in Figure 3.8(a) is not linear, but this is not surprising as the path of increasing Re in the (St, Re)-parameter space is not normal to the bifurcation curve (see Figure 3.2). There is no hysteresis and the behavior of $\langle E_m \rangle$ is linear as Re approaches the critical value (⧫). The normal form for the amplitude of the bifurcated synchronous solutions in the supercritical case is given by $\dot{A} = A(\mu - c|A|^2)$. When saturation is reached, $\dot{A} = 0$ and $Re - Re_c = \mu = c|A|^2 = d\langle E_m \rangle$, the observed linear behavior close to the bifurcation point in all cases.

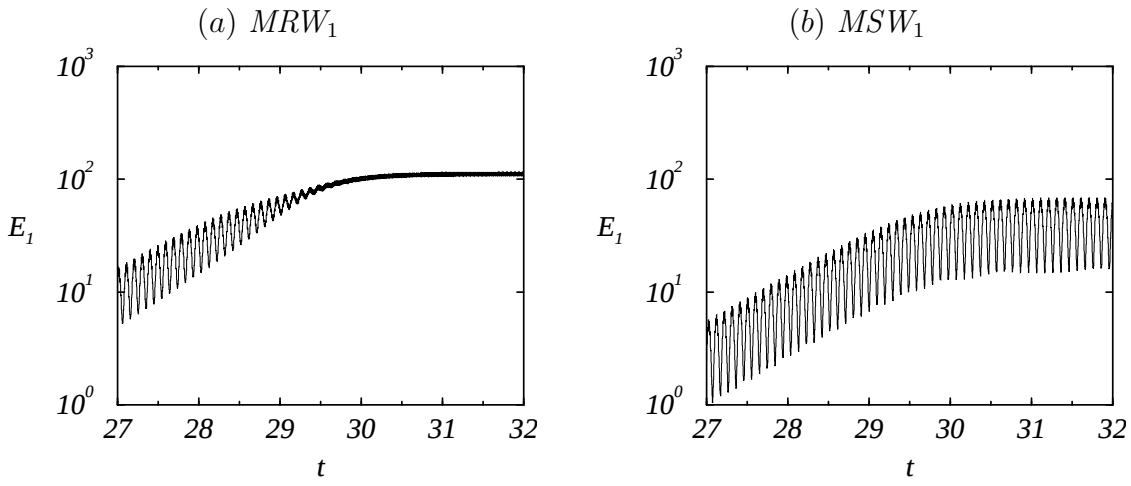

Figure 3.9: Time series of the energy of the first Fourier mode, for (a) MRW_1 and (b) MSW_1, at $(St, Re) = (50, 615)$ near the saturation.

3.3.2 Quasiperiodic mode

The onset of the quasiperiodic states occurs when two complex-conjugate pairs of eigenvalues cross the unit circle, thus introducing a second frequency f_2 related to the phase of the complex-conjugate pairs. The second frequency f_2 can manifest itself in two ways, depending on whether the bifurcation breaks K_β or R_α of the $O(2)$ symmetry of the basic state. In the linear stability analysis only appears the reference to mode MRW_1, but this term encompasses modulated θ-travelling wave (MRW) and modulated standing wave (MSW) states. Due to the $O(2)$ symmetry of the governing equations, there are two pairs of complex conjugate eigenvalues that bifurcate simultaneously, and correspond to modulated θ-travelling waves, which can travel in the positive or negative θ-direction; after a period of the forcing, the flow pattern repeats itself, but rotated a certain angle, $\pm\theta_0$, related to the second frequency by $\theta_0 = 2\pi f_2/St$, where St is the forcing frequency. K_β transforms each one of the MRW into the other, therefore the K_β-symmetry is broken; the $SO(2)$ rotational symmetry is also broken, because the solution has azimuthal wave number $m = 1$; however, as they are modulated travelling waves, there is a preserved space-time symmetry, consisting of advancing one forcing period in time combined with the rotation $R_{\pm\theta_0}$. Besides the two MRW solutions, there is also a third non-linear solution corresponding to a symmetric combination of the two MRW states; these states, called modulated standing waves MSW, are K_β-symmetric, but the $SO(2)$ rotational symmetry is broken too. For these solutions, there is no such thing as the emergence of a new spatio-temporal symmetry.

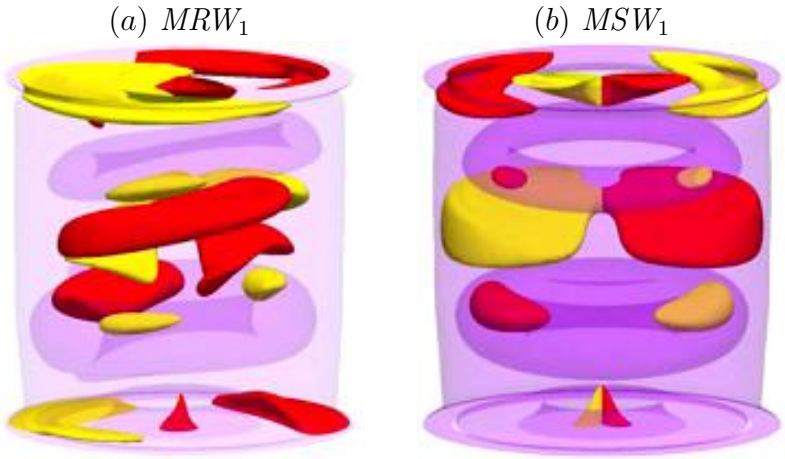

Figure 3.10: Isosurfaces of radial vorticity ξ (solid) and azimuthal vorticity η (translucent) for (a) MRW_1 with $\xi = \pm 180$, and (b) MSW_1 with $\xi = \pm 120$, both with $\eta = \pm 1000$ and computed at $(St, Re) = (50, 615)$. Contour convention as in Figure 3.4.

Only one of the two families of solutions, *MRW* and *MSW*, is stable (Crawford & Knobloch, 1991; Marques, Lopez & Blackburn, 2004). In the present problem, as in the case for the driven annular cavity (Blackburn & Lopez, 2003*b*) and for the driven annular cavity (Leung *et al.*, 2005), the stable solutions are *MRW*; their sense of travel depends on the initial condition for the sign of the azimuthal velocity perturbation. In order to obtain *MSW*, it is necessary to enforce the K_β symmetry, restricting the computations to the appropriate Fourier subspace, as is explained in Section §2.1.3. When an axisymmetric flow unstable to MRW_1 mode is perturbed, the energies of all Fourier modes begin to grow with the driving frequency and this is additionally modulated by the quasiperiodic frequency, which is the same for both states and the value is $f_2 \approx 10.31$, as exhibited in Figure 3.9. However, when *MSW* reaches a saturated state, the energies of the Fourier modes retain both characteristic times and now $f_2 \approx 10.07$, shown in Figure 3.9(b); whilst the quasiperiodic frequency for *MRW*, being related to the azimuthal precession of the pattern, does not manifest in the energy of the Fourier modes, Figure 3.9(a).

The three-dimensional structures of these quasiperiodic flows are visualised in Figure 3.10 by means of perspective views of instantaneous isosurfaces of the radial vorticity and azimuthal vorticity, as it is done in for the synchronous modes in Figure 3.4. Braids are concentrated on the cylinder endwalls away from the sidewall and suffer large variations in all cases. As for the synchronous modes, the braids seem to be born along the oblique jets emerging from the corners and propagate into the interior, interacting in a complex way with the braids coming from the other endwall. For *MSW*, the braids possess very regular shapes and look quite similar to those of the synchronous states,

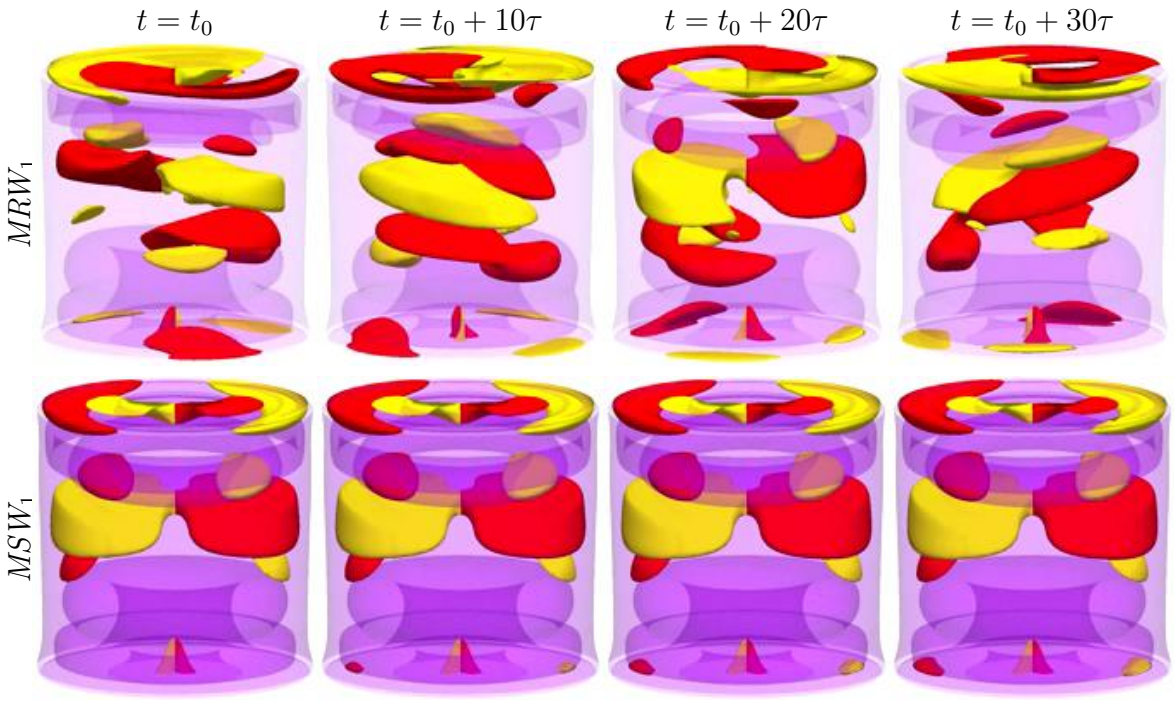

Figure 3.11: Same solutions and isosurface levels as in Figure 3.10, but strobed every 10 forcing periods; t_0 is a convenient time.

and the rollers are virtually not distorted. Contrarily, for *MRW*, the braids have a helical structure and the rollers do not resemble the corresponding base flow rollers at all. In fact, the rollers in *MRW* are tilted with respect to the horizontal rollers in the base state.

Figure 3.11 displays the same contours as in Figure 3.10, all at the same phase at integer multiples of the forcing period apart. For *MRW*, the strobed structures do not change in a frame of reference that rotates in the azimuthal direction an angle θ_0 each forcing period, justifying the name of modulated rotating wave. For the *MRW* shown in Figures 3.10 and 3.11 at $(St, Re) = (50, 615)$, this value is $\theta_0 \approx 28.77°$. This results in a precession frequency $f_2 = 3.996$. For *MSW*, the strobed structures vary substantially in one period, as can be seen in the sequence represented in the second row of Figure 3.11. In general, the ratio between the quasiperiodic and sidewall periods are not commensurate, and the flow structure never repeats itself. However, the flow structure of *MSW* remains almost unchanged after ten forcing periods, as can be observed in Figure 3.11; the only noticeable difference is the formation of braids very close to the bottom lid. This is because the ratio of quasiperiodic to forcing frequencies is very close to 1/10 for the parameter values $(St, Re) = (50, 615)$ of *MSW*, thus $f_2 \approx 5$; this question is explored in more detail at the end of the present section.

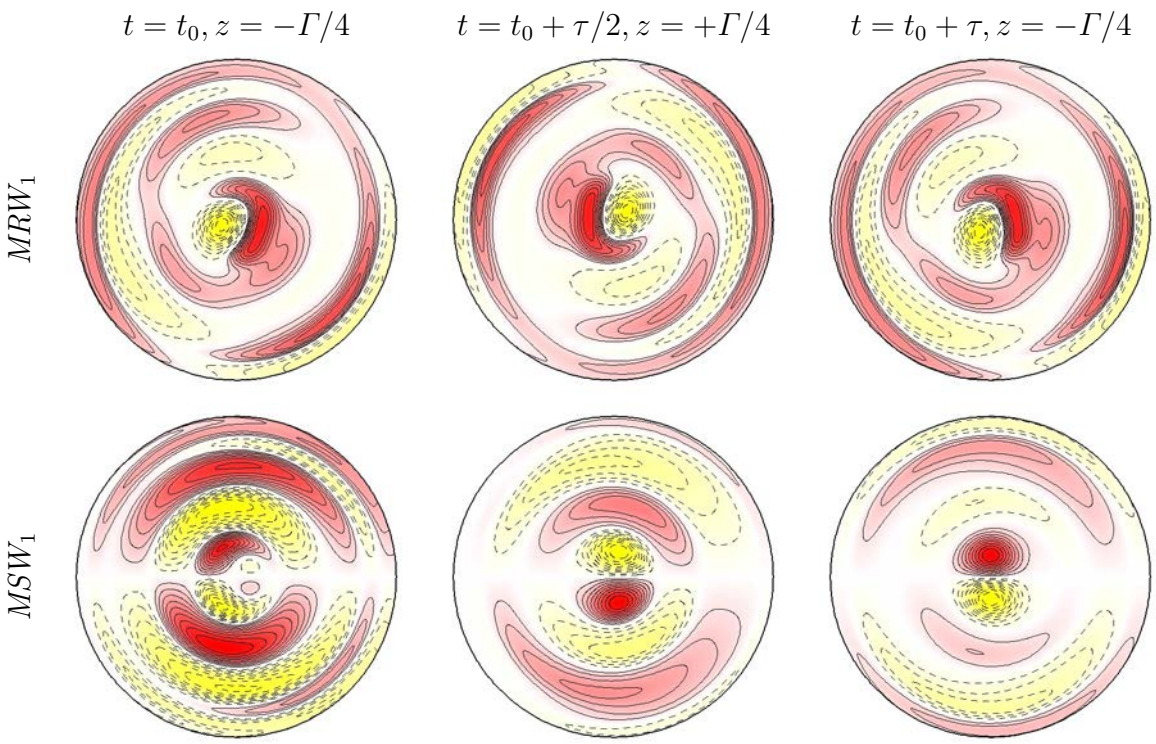

Figure 3.12: Axial vorticity contours of the non-linear saturated states corresponding to MRW_1 and MSW_1 shown in Figure 3.4; t_0 is at the beginning of the forcing period. Contour/colour convention as in Figure 3.5.

In order to check the symmetries, Figure 3.12 exhibits contours of the axial vorticity for the MRW_1 and MSW_1 in z-sections $z = \pm\Gamma/4$ at the beginning of the forcing period, and after advancing half-period and a whole period. Concerning to the spatial symmetries, the MSW_1 solutions possess the dihedral group D_1, as well as the synchronous B_1 modes do, while there is no trace of the initial spatio-temporal H symmetry. Contrarily, the MRW_1 solutions do not have any of the initial symmetries of the basic flow, and are invariant under the transformation of advancing one forcing period combined with rotating an angle θ_0. The asymmetry parameter, S_{K_β}, is perfect to corroborate rigorously the spatial symmetry breaking in the current cases: $S_{K_\beta}(MSW_1) = 0$ and $S_{K_\beta}(MRW_1) = 0.774$.

In contrast to the synchronous bifurcations, which are supercritical, the quasiperiodic bifurcation is subcritical, for both *MRW* and *MSW*. Figure 3.13 shows the time average of the energy of the $m = 1$ dominant mode for the quasiperiodic solutions, $\langle E_1 \rangle$, as a function of Re. Obviously, this magnitude is averaged over the two characteristic times for the *MSW*. The *MRW* solutions show a well-defined hysteretic region; for *MSW*, the hysteretic region is very costly to compute as there are extremely long transients. The

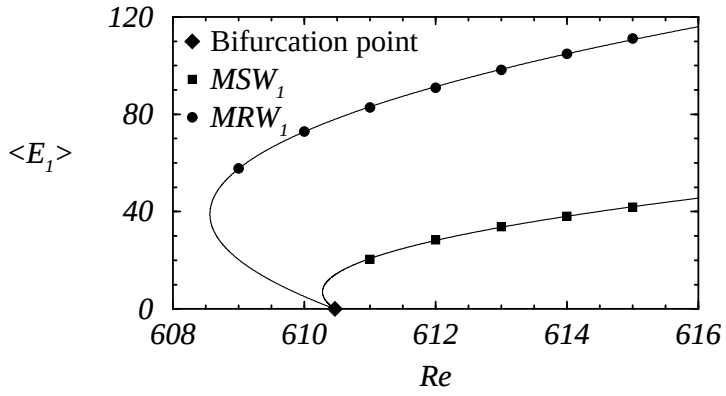

Figure 3.13: Time average of the energy of the $m = 1$ dominant mode for the quasiperiodic solutions as a function of Re, for $St = 50$. The diamond corresponds to the critical Re obtained by linear stability analysis. Symbols correspond to computed saturated solutions, and the curves are best fits to the parabolic profiles predicted by normal form theory.

energies do not behave linearly on the branch close to the critical Reynolds number, $Re_{\rm c} = 610.47$ for $St = 50$. The computed energy amplitudes can be fitted utilising the normal form theory. According to Marques *et al.* (2004), the amplitudes of the bifurcated solutions vary as

$$Re - Re_{\rm c} = \mu = a|A|^4 - b|A|^2 = a\langle E_1\rangle^2 - b\langle E_1\rangle, \tag{3.4}$$

where a quartic term has been included due to the subcritical nature of the bifurcation. The fitting parameters a and b can be expressed in terms of the energy and Re at the saddle-node point:

$$\frac{Re - Re_{\rm c}}{Re_{\rm c} - Re_{SN}} = \frac{\langle E_1\rangle}{\langle E_1\rangle_{SN}}\left(\frac{\langle E_1\rangle}{\langle E_1\rangle_{SN}} - 2\right). \tag{3.5}$$

The solid lines in Figure 3.13 are the best fits of this expression to the computed values. The agreement is very reasonable and provides good estimates of the Reynolds numbers of the saddle-node bifurcations. The estimates are $Re_{SN} \approx 608.57$ for *MRW* and $Re_{SN} \approx 610.28$ for *MSW*.

The frequencies of the quasiperiodic states can be computed via FFT of the time series of a convenient variable; for this purpose, the value of the axial velocity at a point P close to the sidewall at the cylinder mid-plane, $(r, \theta, z)_P = (0.9, 0, 0)$ has been chosen again. Figure 3.14(a) displays the PSD for *MRW* at $(St, Re) = (50, 615)$. The spectrum is clearly quasiperiodic, thus having two well-defined frequencies, $St = 50$ and $f_2 = 3.996$, and their linear odd combinations. The ratio of the frequencies is close to resonance, $f_2/St = 0.0799 \approx 2/25$, and so a small frequency corresponding to

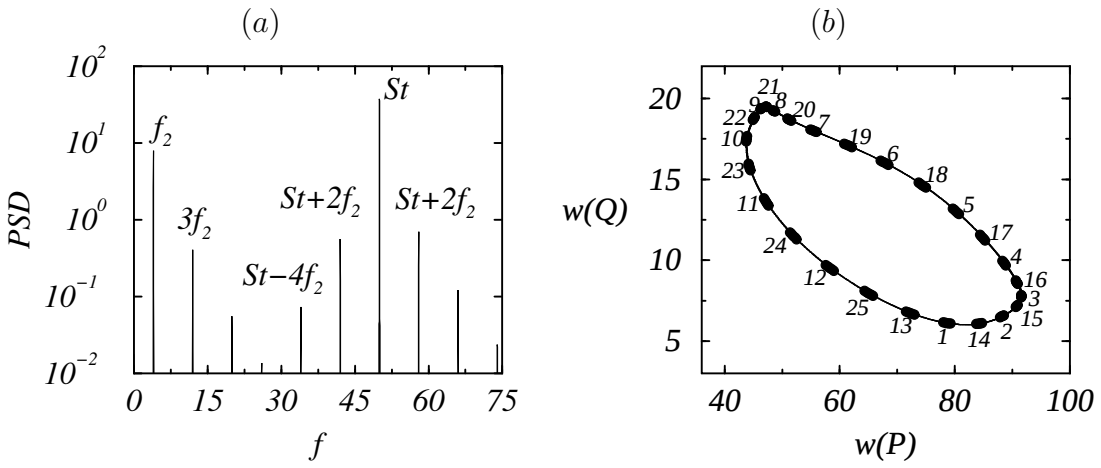

Figure 3.14: (a) FFT of the time series of the near-wall axial velocity at mid-height $(r, \theta, z)_P = (0.9, 0, 0)$, and (b) a Poincaré section strobing every τ for *MRW* at $(St, Re) = (50, 615)$. Symbols • and numbers in (b) correspond to successive iterates, showing that the frequency ratio is close to rational: $f_2/St \approx 2/25$.

$2St - 25f_2 \approx 0.1$ is also present. The FFT supplies f_2 up to a multiple of the forcing frequency; its precise value must be obtained by other methods. In order to analyse in detail how close to resonance the Neimark-Sacker bifurcation is and also to confirm the value of the second frequency, Poincaré sections of the quasiperiodic states by strobing the *MRW* solution every period τ have been computed. The Poincaré section is shown in Figure 3.14(b), where the infinite-dimensional phase space has been projected into the plane corresponding to the values of the axial velocity w at two different locations P and Q in the cylindrical domain. The point P is the same used for computing the FFT, at $(r, \theta, z)_P = (0.9, 0, 0)$, and Q is close to the top endwall at $(r, \theta, z)_Q = (0.9, 0, 0.95)$. The closed curve is the section of the two-torus where the solution lives, and the symbols • correspond to successive iterates that are numbered in the figure. The iterates undergo two turns on the section before almost coinciding with the initial point after 25 iterates, so the rotation number (ratio of the frequencies f_2/St) is approximately 2/25. This justifies the selection of $f_2 = 3.996$ from the FFT. In this Poincaré section, there are 25 clusters of 5 points, so a total of 125 iterates. For this kind of solutions the second frequency can also be estimated by measuring the angle θ_0 rotated by the flow pattern after one forcing period τ, for instance in the first row of Figure 3.12, and the result is in full agreement with the Poincaré section method.

Figure 3.15(a) depicts the PSD for *MSW* at $(St, Re) = (50, 615)$. The second frequency is $f_2 = 5.035$, quite different and greater than the frequency of *MRW*. In this case, another resonance is present and more discernible. From the Poincaré section in

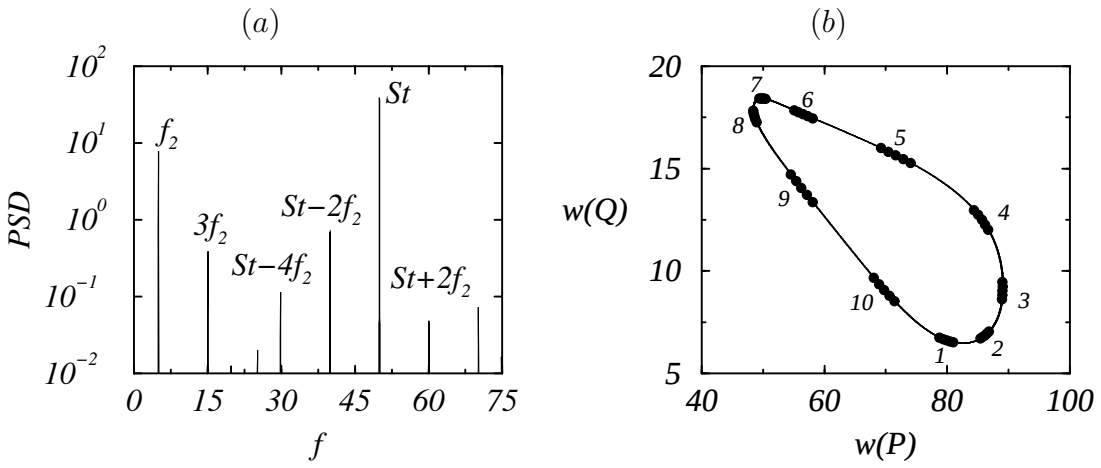

Figure 3.15: (a) FFT of the time series of the near-wall axial velocity at mid-height $(r, \theta, z)_P = (0.9, 0, 0)$, and (b) a Poincaré section strobing every τ for MSW at $(St, Re) = (50, 615)$. Symbols $\bullet$ and numbers in (b) correspond to successive iterates, showing that the frequency ratio is close to rational: $f_2/St \approx 1/10$.

Figure 3.15(b), the tenth iterate, after 10τ, almost coincides with the initial point. As a consequence, the rotation number (frequency ratio) is $f_2/St = 0.1007 \approx 1/10$, and a very small frequency appears, $10f_2 - St \approx 0.353$. This quasiperiodic frequency measured in the energy, Figure 3.9(b), is doubled because this magnitude goes as the square of the velocity.

Since these solutions are quasiperiodic and synchronous with the forcing, they cannot be H-symmetric. Nevertheless, there are no even linear combinations in the spectra, thus indicating that the solutions are almost H-symmetric. The reason is the fact that in both scenarios the frequencies are almost in resonance, so the solution is periodic and fulfills exactly the spatio-temporal symmetry with period $\tau_2 = 1/f_2$.

As a matter of fact, the frequencies associated with MRW and MSW for $(St, Re) = (50, 615)$ are rather different, and this is the reason behind exploring f_2 as a function of Re, for fixed $St = 50$; the results are shown in Figure 3.16. The critical frequency at the bifurcation point, $f_{2,\mathrm{c}} = 5.1572$, and the value of f_2 for the most dangerous eigenfunction as a function of Re, are also plotted. The quasiperiodic frequency for the eigenfunctions is computed directly from the FFT of the axial velocity, or in the time series of the energy, such as Figure 3.9, and halving the obtained value. The second frequency for the eigenfunction is almost constant, as is that for MSW with f_2 slightly smaller than the critical frequency $f_{2,\mathrm{c}}$. In contrast, the second frequency of MRW is substantially smaller than the critical value, and it decreases with Re, the amplitude of the forcing.

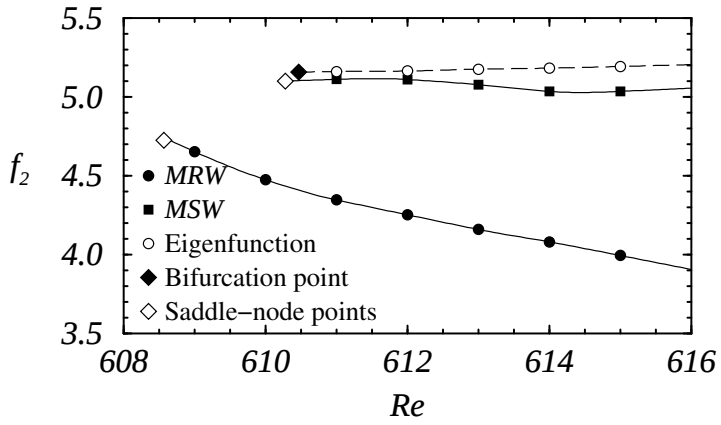

Figure 3.16: Computed frequencies f_2 of the quasiperiodic states *MRW* and *MSW* as a function of Re. Also included are the frequencies of the most unstable eigenfunction, the critical value ⧫, and the saddle-node points ◊.

This fact is probably related to the fact that the energy of the *MRW* is much larger than the energy of *MSW*, and also to the larger subcriticality of the modulated rotating waves, as exhibited in Figure 3.13.

From Figure 3.16, it is observable that f_2 for *MRW* and for *MSW* at $(St, Re) = (50, 615)$ is very close to 4 and 5, respectively. As the forcing frequency is $St = 50$, the ratio f_2/St is very close to a rational number (2/25 and 1/10, respectively), as already noted from measuring the frequencies via FFT and Poincaré sections. Of course, along the curves $f_2(Re)$, other resonances can be located, but they all have large denominators, so no new dynamics associated with these resonances is expected in this region (Kuznetsov, 2004).

3.4 Conclusions

Several fluid systems with complete symmetry group $O(2) \times Z_2^{ST}$ have been explored in recent years. Flows with this symmetry group only have three possibilities for the transition from the basic state to three-dimensional flows: synchronous modes preserving or breaking the space-time symmetry H or quasiperiodic modes, that come in two flavors, either modulated travelling waves or modulated standing waves. Such systems include symmetric bluff-body wakes produced by circular and square cylinders, rings and flat plates, and flows driven by the periodic motion of one of the container walls, for example the rectangular driven cavity and a driven annular cavity. The periodically driven flows

are preferred because all the bifurctated states can manifest as primary bifurcations. Unfortunately, the mentioned periodically driven systems have some drawbacks and the cylindrical driven cavity with moderate aspect ratio has been analysed because is has two advantages over them. First, the $O(2)$ symmetry is exactly fulfilled by the cylindrical geometry (periodicity in the azimuthal direction), eliminating the spanwise endwall effects of the rectangular cavity. And second, the bifurcated states have small azimuthal wave numbers (typically $m = 1$ or 2), so the competition between different modes is greatly reduced.

As a starting point of the analysis, the periodic synchronous base states have been computed for different forcing amplitudes, Re, and forcing frequencies, St. These are non-trivial states, with axisymmetric rollers forming alternatively close to each of the endwalls due to the periodic oscillation of the cylinder sidewall. This oscillation produces axisymmetric jets of azimuthal vorticity, emerging from the corners, moving into the interior, and forming the rollers.

The linear stability analysis of the base state has resulted in the computation of the marginal stability curve. Synchronous bifurcations that preserve the symmetry H are found for small forcing frequencies St, while for larger St values the ones breaking H are the most unstable. In between, for intermediate St values, there is a transition to quasiperiodic solutions. The form of the instabilities is the same for all cases, in that the formation of braids that are small-scale meridional perturbations of the rollers. The size and persistence of these braids depend strongly on St. These results are in good agreement with previous results in flows with the same symmetries, and the marginal curve bears a great resemblance to the one corresponding to the driven rectangular cavity problem. Moreover, three codimension-two points have been successfully identified and represent a stepping stone towards future studies.

In addition, the non-linear saturated states have been computed and analysed in detail. In all cases, sufficiently close to the bifurcation curve, these are pure modes. The quasiperiodic stable solutions in the present problem are modulated rotating waves, and by restricting the computations to the appropriate subspace, the unstable modulated standing waves have been found. As a result of these non-linear simulations, it is established that the bifurcations to synchronous states are supercritical, whilst the bifurcations to quasiperiodic states are subcritical. A careful analysis of the quasiperiodic frequency f_2 of the modulated standing waves has shown that f_2 is almost constant and very close to the frequency that emerges from the linear stability analysis, whereas the modulated rotating waves exhibit a smaller frequency that varies significantly with St.

CHAPTER 4

COMPETITION OF SYNCHRONOUS MODES IN NEWTONIAN FLOWS

The transition from two-dimensional to three-dimensional flows is of fundamental interest in fluid dynamics. Planar two-dimensional flows like the von Kármán vortex street, or axisymmetric flows with zero azimuthal velocity are examples of such two-dimensional flows. The time-periodic Kármán vortex street and other bluff-body wakes are invariant in the spanwise direction to both translations and reflections, thus generating the $O(2)$ symmetry group. Furthermore, these flows have an additional spacetime symmetry: a reflection about the wake centre line followed by a half-period temporal evolution. In several wake flows, two distinct synchronous modes that break into the spanwise direction (with real Floquet exponent) have been observed experimentally (Williamson, 1988; Meiburg & Lasheras, 1988; Williamson, 1996; Julien *et al.*, 2003), computed as direct instabilities from the flow (Meiburg & Lasheras, 1988; Barkley & Henderson, 1996; Robichaux *et al.*, 1999; Blackburn *et al.*, 2005; Blackburn & Lopez, 2011), and studied theoretically (Lasheras & Meiburg, 1990; Barkley *et al.*, 2000; Marques *et al.*, 2004). These modes are associated with breaking or preserving the spatio-temporal symmetry. Unfortunately, wake flows can only be studied in terms of a single control parameter, therefore only one of both synchronous modes can be observed at onset, the other one appearing at secondary bifurcations in the form of mixed modes or complex time-dependent flows. Additionally, there are instabilities of the basic periodic flow with complex Floquet multipliers, resulting in quasiperiodic flows, which may also appear in secondary instabilities. As a consequence, analysing the ineraction of the three-dimensional modes in this kind of secondary bifurcations is far from simple.

In order to better understand the three-dimensional bifurcated modes, other fluid problems with the same symmetry group (spatial $O(2)$ symmetry and spatio-temporal Z_2 symmetry) have been studied. One of these problems is the flow in a rectangular cavity driven by the periodic oscillation of one wall (Vogel *et al.*, 2003; Blackburn & Lopez, 2003*a*,*b*; Marques *et al.*, 2004; Leung *et al.*, 2005). In this case, both synchronous and quasiperiodic modes have been obtained and analysed experimentally and numerically as the primary bifurcation for different control parameters. However, as in many wake scenarios, the spanwise direction is not really periodic, but of infinite extent. By expanding in Fourier series, this flow is made periodic, but the wave number varies continuously, resulting in a continuum of bifurcating modes that interact in a complex manner.

A periodically driven annular cavity solves this issue and has been considered in Blackburn & Lopez (2011). This case is a continuous deformation of the planar driven cavity flow in the sense that the infinite spanwise direction becomes a periodic angular direction with a discrete set of azimuthal wave numbers. The curvature of the annulus in conjunction with the Reynolds number, determines the first mode to become unstable. It is found that even very near the onset of three-dimensional instabilities, the dynamics are dominated by a variety of mixed modes with complicated spatio-temporal structures. Even though the latter problem has the correct symmetries and it is possible to select which one of the three-dimensional modes becomes unstable first, the complexities of the dynamics and the mode interactions right from the onset do not allow a detailed analysis of the bifurcated modes and their interactions. This phenomenon is attributed to the fact that the azimuthal wave numbers of the bifurcated solutions are large, so there are many modes bifurcating in a very narrow parameter range, rendering impossible to follow the cascade of secondary bifurcations taking place.

The system under consideration, a fluid confined in a finite cylinder driven by axial oscillations of the sidewall, possesses all the mentioned symmetries and the azimuthal wave numbers of the bifurcated solutions are much smaller in comparison with the annulus scenario. The linear stability analysis of this flow (Panades *et al.*, 2011) revealed that by an appropriate selection of the forcing frequency both the synchronous and the quasiperiodic modes could be obtained, and three codimension-two points where two of these different modes bifurcate simultaneously were found. These codimension-two points act as organising centers of the dynamics, and detailed analysis of the bifurcations and mode interactions around the first bicritical point is presented here. In this case, two synchronous modes that preserve the spatio-temporal symmetry and possess azimuthal wave numbers $m = 1$ and 2 compete vastly, thus producing very rich dynamics and a wide variety of novel states.

The structure of this chapter is the following. Section §4.1 is referred to the states that are obtained close to the bicritical point, meanwhile Section §4.2 deals with the solutions unraveled far away from it. The bestiary of bifurcations occurring around the codimension-two point are discussed in Section §4.3. Finally, the main findings are summarised and commented in Section §4.4. The main results of this chapter have been published in Panades *et al.* (2013).

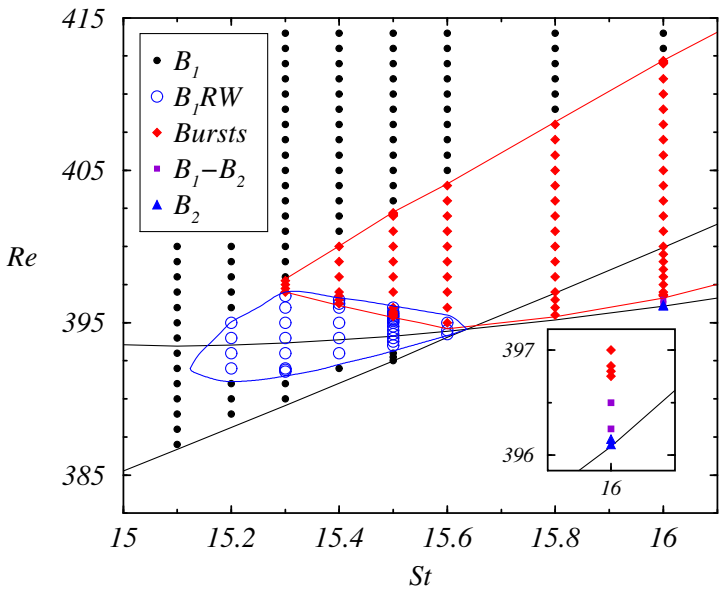

Figure 4.1: Families of bifurcated states near the bicritical point C_1. The bifurcation curves from the base state are indicated as black solid lines.

4.1 Dynamics close to the codimension-two point

The intersection of two linear stability curves determines a codimension-two or bicritical point. As it has been discussed in Section §3.2, Figure 3.2 exhibits three points of this kind (crosses) because of the B_1-B_2, B_2-MRW_1 and MRW_1-A_2 intersections. The present chapter is focused on the analysis of the first codimension-two point, C_1, where the synchronous modes B_1 and B_2 bifurcate simultaneously and is located at $(St_c, Re_c) = (15.636, 394.57)$. As a reminder, these synchronous states only possess the frequency associated with the forcing and, since they are no longer axisymmetric, the symmetry $O(2)$ has been broken. Nevertheless, there still remain the discrete symmetry $R_{2\pi/m}$ (a rotation of angle $2\pi/m$ around the axis) and its powers, and a collection of m reflection planes at angles π/m apart. The rotation and meridional reflection symmetries just described generate the D_m symmetry group with $2m$ elements, consisting of m rotations (including the identity) and m meridional reflections. Furthermore, these B modes are invariant under the symmetry H. Hence, the complete symmetry group of the bifurcated mode B_m is $D_m \rtimes Z_2^{ST}$.

Comprehensive numerical explorations of the two-dimensional parameter space around this bicritical point C_1 have been performed, looking at the subsequent bifurcations of the B_1 and B_2 states, their interactions and multiplicity, and transitions between them. A summary of these results is detailed in Figure 4.1, that shows the critical Reynolds

number, Re_c, as a function of the Stokes number, St, near C_1. The solid black curves of this figure are the same bifurcation curves appearing in Figure 3.2, but without symbols, which are used for the bifurcated states. For instance, on the left side of C_1, B_1 modes (black circles) bifurcate first, while on the other side B_2 modes (blue solid triangles) do. In addition to these known solutions, other states that might stem from C_1 are achieved. These novel states are the rotating waves B_1RW (blue circumferences) that bifurcate from B_1, the B_1-B_2 mixed modes (violet solid squares) that emerge from B_2, and the bursting solutions (red solid diamonds) covering a large region in parameter space. In the following sections all of these states are discussed in detail. Some additional curves are sketched to delimit their regions of existence. The inset in Figure 4.1 displays a zoom near the linear stability curve at $St = 16$ in order to be capable of observing the different states that appear very close to the B_2 bifurcation curve. Similar cascades of bifurcations resulting in flows with complex dynamics have been reported in an annulus of radius ratio close to one also driven by axial oscillations of the sidewall (Blackburn & Lopez, 2011). In this problem, the azimuthal wave numbers of the bifurcated solutions are at least one order of magnitude larger than in our problem, so there is a strong competition between the bifurcating modes. Consequently, the system suffers a rapid succession of bifurcations in a very narrow parameter range and cannot be resolved numerically. In our scenario, this succession of bifurcations is discernible because of the relatively small wave numbers, as is exhibited in the inset of Figure 4.1.

4.1.1 Below the bicritical point

As can be observed in Figure 4.1, for Stokes number values below C_1, $St < St_c = 15.636$, the bifurcated mode B_1 exists for a wide range of Reynolds numbers. However, on the vicinity of the codimension-two point, this mode becomes unstable in a small Re region before becoming stable again. Recalling the main features of B_1, this mode preserves the H symmetry and, with regard to the spatial symmetries, $O(2)$ reduces to D_1, generated by the reflection symmetry about a sole meridional plane, and no rotational symmetry remains. Therefore, the symmetry group of B_1 is $D_1 \rtimes Z_2^{ST}$.

B_1RW solution

Starting with a pure B_1 state and increasing Re for frequencies within the range $15.1 < St < St_c = 15.636$, the mode B_1 undergoes a bifurcation, becoming a modulated rotating wave B_1RW (blue circumferences in Figure 4.1). Figure 4.2(a) depicts the time series of

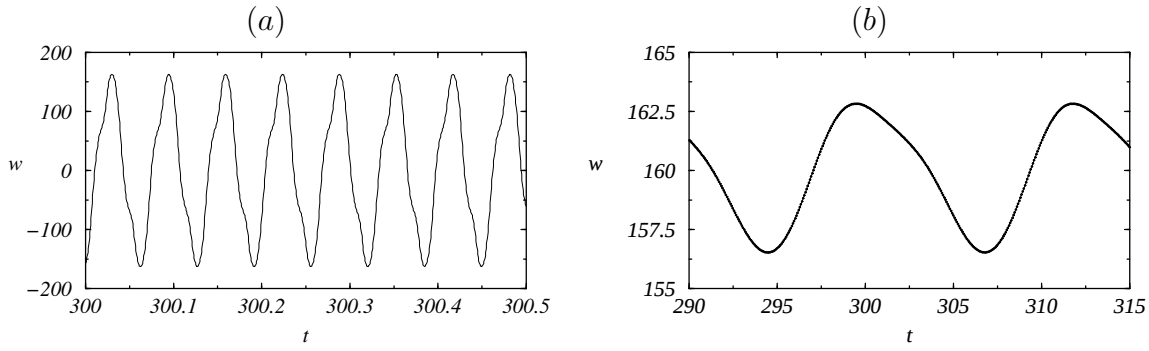

Figure 4.2: Rotating wave solution B_1RW for $(St, Re) = (15.5, 395)$. Time series of the near-wall axial velocity at mid-height $(r, \theta, z) = (0.9, 0, 0)$. (a) shows about eight forcing periods. (b) plots the maximum values in (a), that displays the slow variation of the axial veocity due to the slow precession rate of the rotating wave, in a much larger time scale.

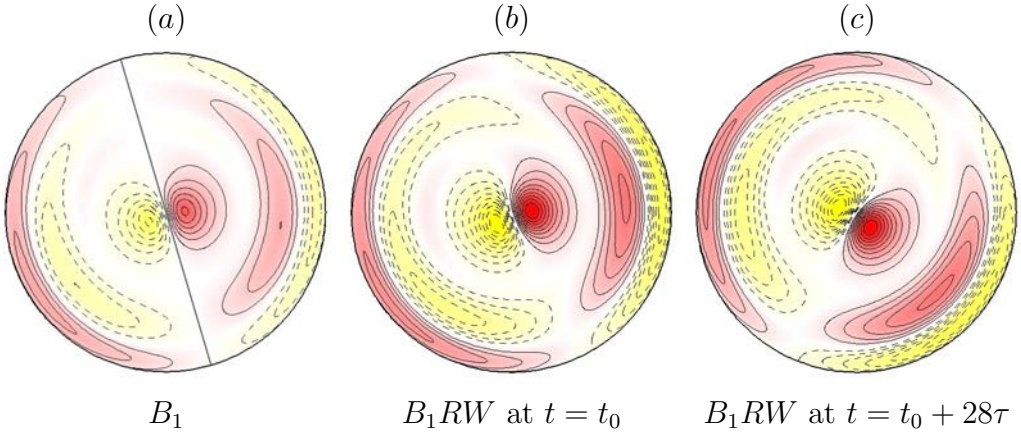

Figure 4.3: (a) Pure B_1 mode at $(St, Re) = (15.5, 393)$. The straight line is the K_β reflection symmetry axis. (b) and (c) Rotating wave solution B_1RW for $(St, Re) = (15.5, 395)$. All snapshots are taken at the beginning of a forcing period; (b) and (c) are taken 28 forcing periods apart. Plots show axial vorticity contours at the horizontal section $z = -\Gamma/4$. Solid (dashed) contours are positive (negative); light/dark (yellow/red) colours correspond to negative/positive values. This contour/colour convention is used in all subsequent cross-sections.

the axial velocity of one of these B_1RW states in a fixed point near the sidewall at mid-height $(r, \theta, z) = (0.9, 0, 0)$, that looks periodic and very similar to the corresponding time series for B_1. However, by looking at the maximum values of this time series over a long time interval, a slow variation with a large period is clearly observable in Figure 4.2(b); for the depicted solution at $(St, Re) = (15.5, 395)$, its value is $\tau_2 \approx 12.321 \approx 190.98\tau$, two orders of magnitude larger than the forcing period τ.

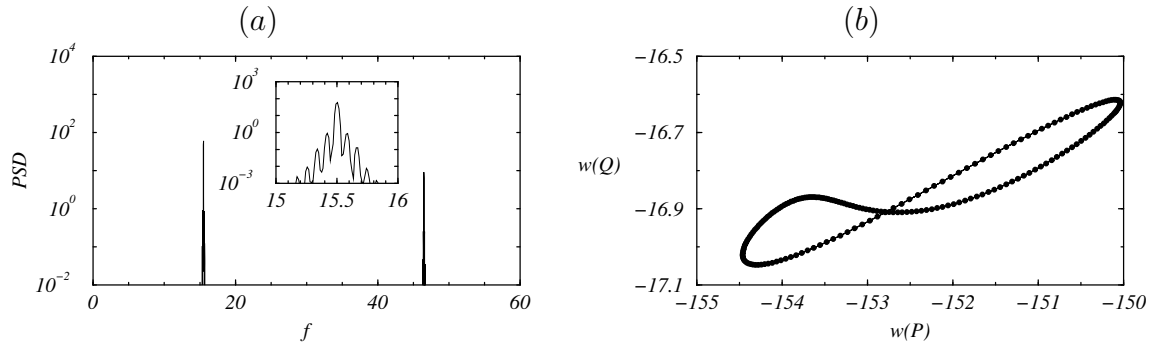

Figure 4.4: (a) FFT of the time series in Figure 4.2(b). (b) Poincaré section (bullets) using two axial velocities measured near the wall: $(r,\theta,z)_P = (0.9, 0, 0)$ and $(r,\theta,z)_Q = (0.9, 0, 0.95)$.

Panels (a) and (b) of Figure 4.3 compare the common mode B_1 with the B_1RW, and by looking at the latter after 28 forcing periods in Figure 4.3(c), its rotating nature becomes evident; the solution has rotated about 53°, in full agreement with the measured precession frequency $f_2 = 1/\tau_2 \approx 0.0812$. In fact, this state is a modulated rotating wave, because the flow structure changes during the forcing period; nevertheless, if the flow is strobed with the forcing frequency, the structure looks the same but rotated a certain angle, as shown in Figures 4.3(b) and (c). This behaviour is completely equivalent to the MRW_1 solutions appearing at higher St that have been analysed in Chapter 3.

As a matter of fact, B_1RW is a quasiperiodic solution with two well-defined frequencies, the forcing frequency $St = 15.5$ and a much smaller frequency related with the rotation, $f_2 = 0.0812$. Figure 4.4(a) exhibits the power spectral density (PSD) after computing the Fast Fourier Transform (FFT) of Figure 4.2(b), showing a single frequency St and its first harmonic; the very small second frequency f_2 is made apparent at the inset showing $St \pm j f_2$ for $j = 1, 2$ and 3, in the form of additional peaks very close to the $St = 15.5$ peak. The frequency of rotation is corroborated using the Poincaré sections in the same way as in the previous chapter. Figure 4.4(b) represents a Poincaré section of the B_1RW state, consisting in sampling the values of the axial velocities at two different points P and Q with the forcing frequency. The bullets represent consecutive points of the reduced space and after 191 iterates, consistent with $f_2/St = 0.00524 \approx 1/191$, the full cycle is covered.

In relation to the symmetries of the B_1RW solutions, it is obvious from Figures 4.3(b) and (c) that the reflection symmetry K_β has been broken, so no purely spatial symmetry remains. This can be verified by computing the symmetry parameter of this B_1RW solution, that gives $S_{K_\beta}(B_1RW) = 0.478$, to be compared with the value corresponding

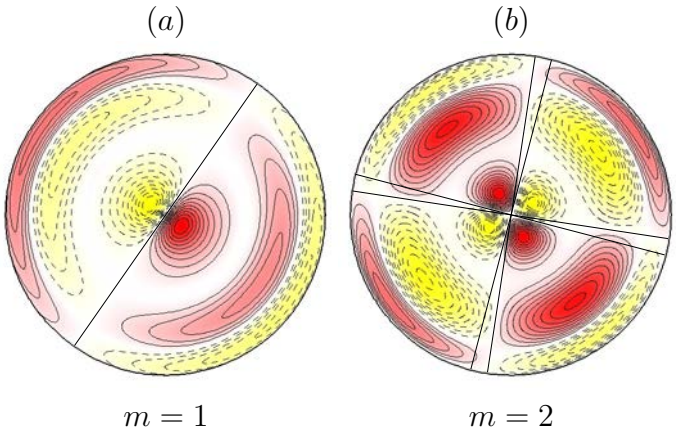

Figure 4.5: Axial vorticity contours of the rotating wave solution B_1RW in Figure 4.3(c). The plots show the contributions of the first ($m = 1$) and second ($m = 2$) Fourier modes. Straight lines are reflection K_β symmetry axes. Contour/colour convention as in Figure 4.3.

to the symmetric solution B_1 in Figure 4.3(a), $S_{K_\beta}(B_1) = 8.29 \times 10^{-10}$. Furthermore, S_{K_β} for B_1RW and MRW_1 has the same order of magnitude, thus indicating that both solutions have broken K_β. This parameter is an appropriate measure of the symmetry breaking, and it is plotted in Figure 4.23(a) in order to be contrasted with the other solutions. Figure 4.5 displays the contributions of the first (a) and second (b) azimuthal Fourier components to the B_1RW solution of Figure 4.3(c), and helps to understand the reason behind the breaking of K_β. First of all, the angle β_2 for the azimuthal Fourier component $m = 2$ is not the same in different points of the domain: Figure 4.5(b) shows that close to the sidewall and in the bulk the flow possesses different symmetry axis (straight lines in the figure), and they differ in about 6°. Secondly, in both modes the β angles of the K_β symmetry do not satisfy the relation $\beta_2 = 2\beta_1$: from the figure, $\beta_1 \approx 55°$ and $\beta_2 \approx 168°$ (the averaged value). Therefore, in the expression of the symmetry parameter (2.36), both terms $\sin^2(\beta_2 - 2\beta_1)$ and $\sigma^2_{\beta_2}$ are different from zero and have a noteworthy contribution.

As has been discussed in Section §2.1.3, K_β can be numerically imposed. Applying this method to B_1RW, the result is that depending on the parameters pure synchronous B_1 and B_2 modes are recovered. For instance, a solution of this kind at $(St, Re) = (15.5, 393.5)$, which is below the marginal curve of B_2, turns into a B_1 mode, whilst another one at $(St, Re) = (15.5, 395)$, above that curve, becomes a B_2 solution.

About the spatio-temporal symmetry H, since the solution is quasiperiodic and synchronous with the forcing, it cannot be considered H-symmetric. However, the Fourier

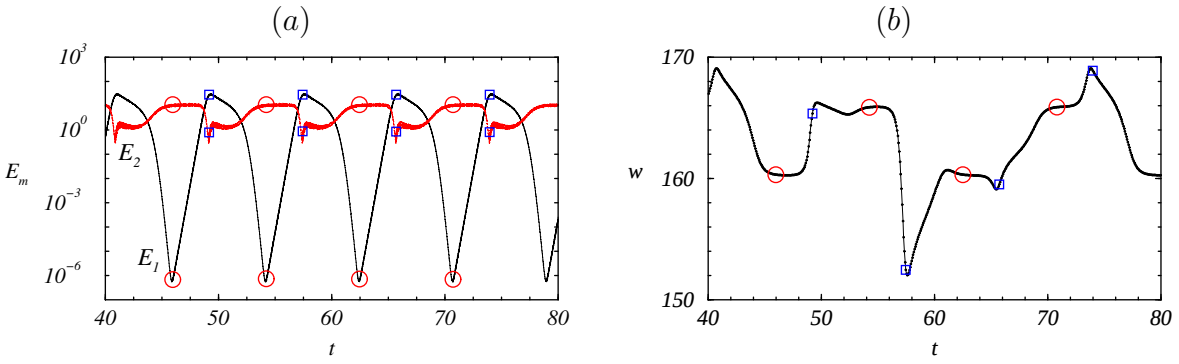

Figure 4.6: Bursting solution at $(St, Re) = (15.5, 400)$. Time series of (a) the energy of the Fourier modes E_1 and E_2, and (b) maximum values of the near-wall axial velocity at mid-height $(r, \theta, z) = (0.9, 0, 0)$; same plot as in Figure 4.2(b).

transform of the axial velocity on the mid-plane shown in Figure 4.4(a) has zero (or very small) even temporal Fourier components, as occurs for a B_1 synchronous mode in Figure 3.7(a), indicating that the solution is almost H-symmetric. There are two reasons for this approximate symmetry. The first one is that the amplitude of the modulation due to the second frequency is very small; comparing Figures 4.2(a) and (b) it is perceived that the modulation amplitude is about 1% of the amplitude of the axial velocity. The second reason is that the two frequencies are almost in resonance, so τ_2 is very close to an integer multiple of τ: $\tau_2 = 190.98\tau \approx 191\tau$. When the ratio is integer, the solution is periodic and exactly satisfies the H symmetry (with period τ_2).

Bursting solution

For forcing frequencies close to the codimension-two point C_1, $15.3 \leq St < St_c = 15.636$, the stable B_1 mode existing at large Re does not bifurcate into the rotating wave solution B_1RW when decreasing Re, but undergoes a bifurcation to a more complicated bursting state (red solid diamonds in Figure 4.1). The bursting state and the B_1RW coexist in a narrow hysteretic region observable in Figure 4.1, and become unstable exiting the region, evolving one into the other.

Figure 4.6(a) exhibits the time series of the energies of the first and second azimuthal Fourier components, of the bursting solution at $(St, Re) = (15.5, 400)$. Both modes have comparable energies, and the resulting state alternates between both, showing plateaus where the energy is almost constant followed by rapid excursions, thus the name bursting solution. These solutions are periodic in time, and the period from the energy plot is

$\tau_2 \approx 8.2417 \approx 127.75\tau$. The solution is most of the time very close to a B_2 mode, with excursions to a mode B_1. But the energy, being a global measure, does not capture the details of the flow. Figure 4.6(b) provides the evolution of the maximum values of the axial velocity at $(r, \theta, z) = (0.9, 0, 0)$. Measuring the period using this figure a different result is obtained, $\tau_2 \approx 33.065 \approx 512.51\tau$. This value is four times the one obtained from the energy plot. The reason behind is the fact that the energy does not distinguish between solutions with the same structure, but rotated a certain angle.

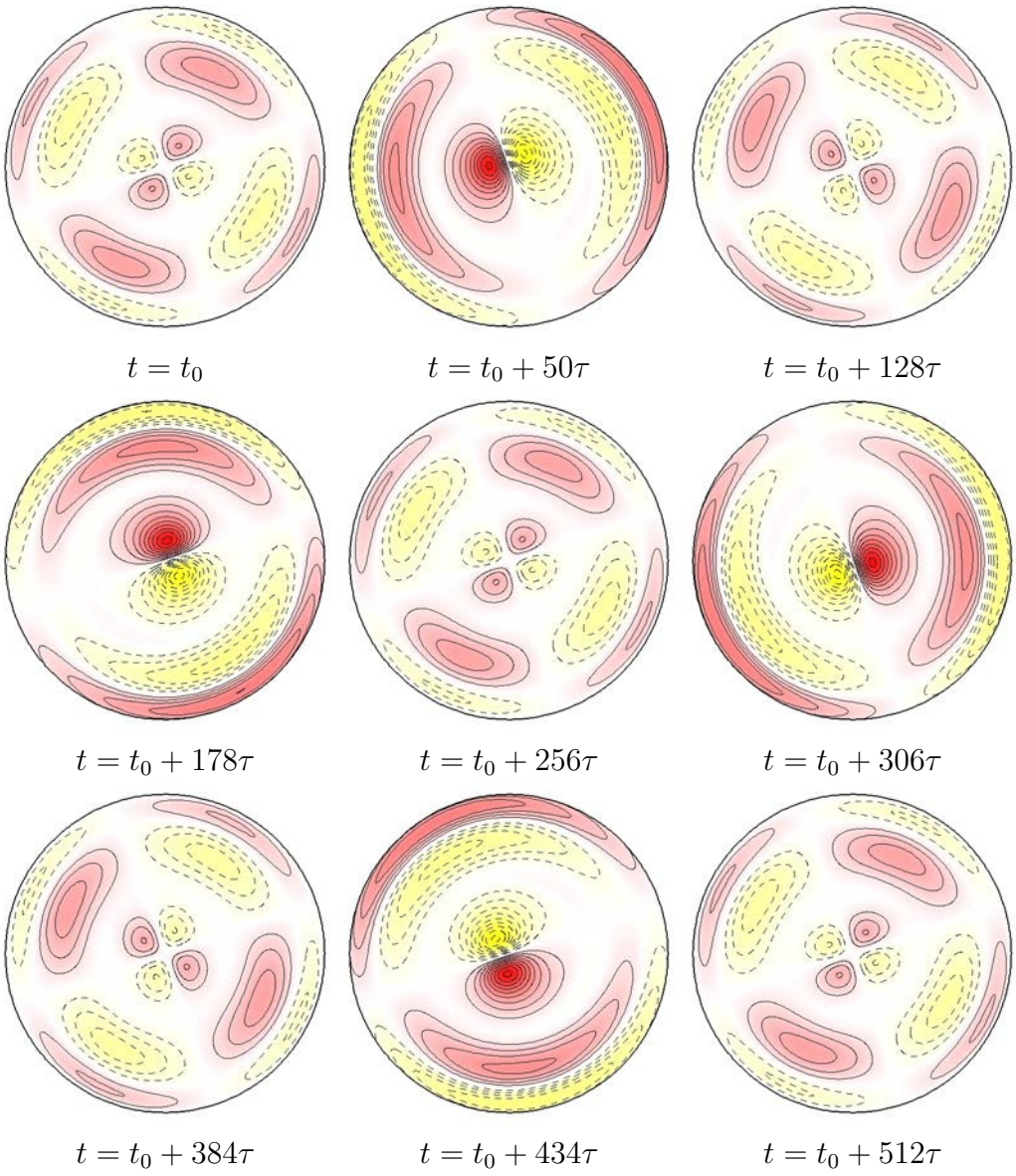

Figure 4.7: Axial vorticity contours at $z = -\Gamma/4$ and different times of the bursts at $(St, Re) = (15.5, 400)$; t_0 is at the beginning of the forcing period and each snapshot corresponds to consecutive minima of E_1 and E_2. Contour/colour convention as in Figure 4.3.

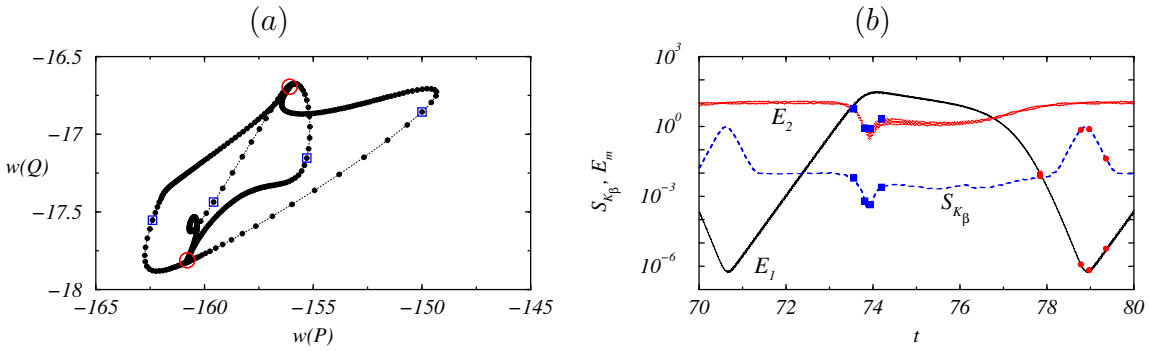

Figure 4.8: Bursting solution at $(St, Re) = (15.5, 400)$. (a) Poincaré section (bullets) using two axial velocities measured near the wall. The minima of E_1 (circumferences) and E_2 (open squares) indicated in Figure 4.6 and 4.7 are also plotted. (b) Time evolution of the K_β asymmetry parameter, S_{K_β}; symbols refer to Figure 4.9.

In Figure 4.7, contours of axial vorticity at $z = -\Gamma/4$ corresponding to consecutive minima of E_1 and E_2 in Figure 4.6(a) are depicted; t_0 is taken at the beginning of the forcing period. The solutions are almost identical to the pure synchronous modes B_1 (at the minimum of the $m = 2$ mode, blue open squares in the figures) and B_2 (at the minimum of the $m = 1$ mode, red circumferences in the figures). But the solutions at two consecutive minima of the $m = 2$ mode (almost pure B_1 modes) are rotated $\pi/2$; therefore, the initial state is recovered after four alternations of the synchronous modes, almost 512 forcing periods, and the discrepancy between the measures of τ_2 in the previous paragraph gets explained.

As it happens with the rotating waves, the bursting solution is also quasiperiodic and there are two well-defined frequencies, the forcing frequency, $St = 15.5$, and a very small frequency associated with the bursts, $f_2 = 0.0302$. Figure 4.19(b) displays the PSD related with the velocity in Figure 4.6(b), showing the forcing frequency and its first harmonic. The presence of a second frequency is evident. Unfortunately, since this frequency is so small, a large temporal series would be necessary to measure f_2 precisely and this is not the case. Once again, the Poincaré section of the bursting solution, which is displayed in Figure 4.8(a), provides a good measure of the second frequency. This Poincaré section is quite convoluted, and the slow down where the solution is close to a pure B_2 mode and the fast excursion approaching a pure B_1 mode are captured. The bullets represent 513 consecutive points in the reduced space and corroborate that the mentioned f_2 is correct, because $St/f_2 = 512.51$, and a whole lap around the cycle is done. The blue open squares and red circumferences correspond to the minima of the first and second Fourier mode displayed in Figure 4.7. Moreover, there seem to be

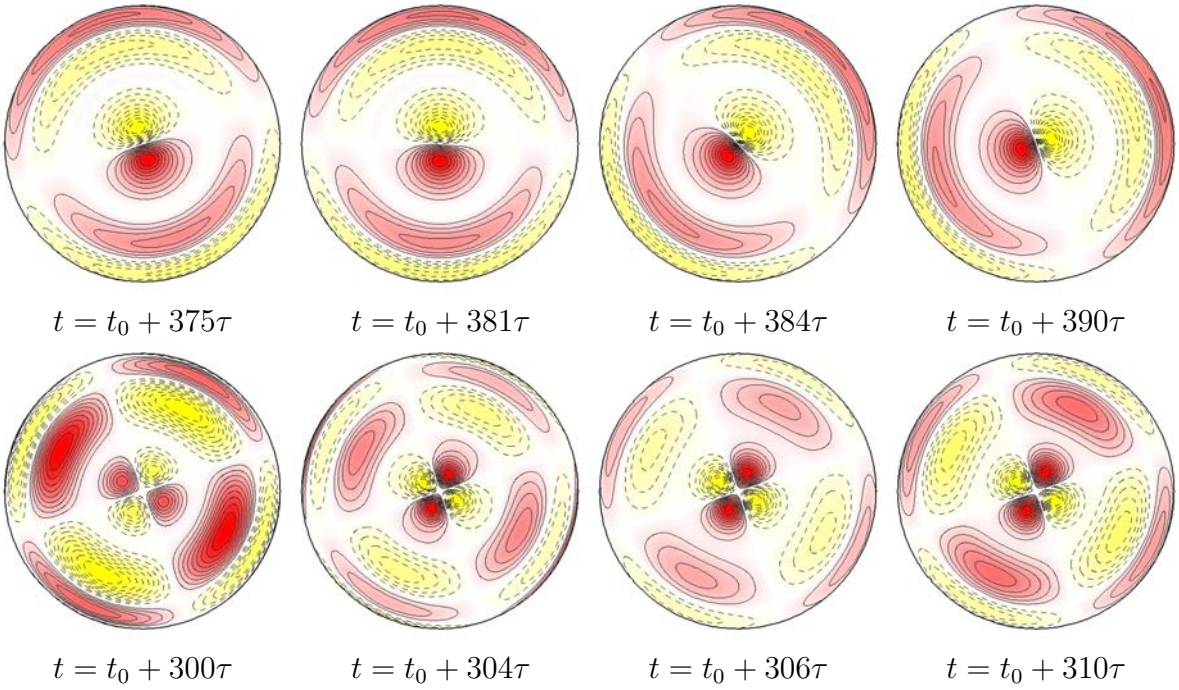

Figure 4.9: Axial vorticity contours at $z = -\Gamma/4$ and different times of the bursts at $(St, Re) = (15.5, 400)$; t_0 is at the beginning of the forcing period. The first row represents the first Fourier mode contribution near its minimum, while the second one the analogous for the second mode. The snapshots shown correspond to symbols in Figure 4.8(b). Contour/colour convention as in Figure 4.3.

two accumulation points, which are the two possibilities for the B_2 modes depicted in Figure 4.7. Apparently, there are two ways of entering and another two of escaping each one of these accumulation points (pure B_2 modes).

This solution seems to preserve the spatial symmetries of the pure modes, because most of the time is close to a pure synchronous mode, but it is not the case. Figure 4.8(b) exhibits the evolution of S_{K_β} along a burst: this parameter is most of the time constant, except for a remarkable peak and valley that coincide with the minima of the energies, which are also plotted in the figure. Therefore the reflection symmetry is broken mainly when the energy of the $m = 1$ mode is minimum. Figure 4.9 helps to understand how this symmetry breaking process takes place. The first row shows a time sequence of the first Fourier mode near the peak of S_{K_β} (minimum of the first mode, red circles in the figure), while the second one exhibits the behaviour of the second mode at the valley (minimum of the second mode, blue solid squares in the figure). At the peak, the first mode becomes almost negligible (the amplitude decreases three orders of magnitude, and the energy seven), while precessing in a fashion similar to the B_1RW of the former

subsection; the total rotation of the first Fourier mode is exactly $\pi/2$. When this mode is rotating, the reflection planes between the first and the second Fourier mode become uncorrelated, thus enhancing S_{K_β}. The second mode does not rotate continuously at any stage, and what happens is that it changes sign when it is close to the minimum of the second mode; the change of sign is not uniform, but begins near the axis and propagates towards the sidewall. Therefore, the valley in S_{K_β} is created when the second mode becomes minimum. The maximum of S_{K_β} is a good measure of the symmetry breaking for this solution, and it is plotted in Figure 4.23 for comparison with other solutions. In case of restricting the computations to the subspace that preserves the K_β symmetry, the synchronous B_2 modes are recovered.

Regarding to the spatio-temporal H symmetry, mention that it is not preserved because of the second frequency associated with the bursts, that makes it a quasiperiodic solution. Curiously, but for the same reasons as the rotating wave solution B_1RW, the even temporal Fourier components of the axial velocity on the mid-plane are very close to zero, indicating that the solution is almost H-symmetric, shown in 4.19(b).

4.1.2 Above the bicritical point

For $St > St_c$, at the right side of C_1 in Figure 4.1, the bifurcated mode B_2 exists in a very narrow region very close to the linear stability curve, as presented in the inset of Figure 4.1. This synchronous mode becomes rapidly unstable when increasing Re, and a synchronous mixed mode emerges subsequently. This mixed mode solution persists a little longer, but rapidly becomes unstable and reverts to the bursting solution already mentioned in the previous section. By further increasing Re, the pure B_1 mode is achieved.

The synchronous B_2 mode (blue solid triangles in Figure 4.1) has been exhaustively analysed in Chapter 3. Summing-up, this solution is synchronous and possesses the symmetry group $D_2 \rtimes Z_2^{ST}$. The spatial symmetries D_2, which are illustrated in Figure 4.10(a), depicting axial vorticity contours of B_2 at $(St, Re) = (16, 396.25)$, are generated by two orthogonal reflection planes, whose product is a half-turn (a rotation of π around the cylinder axis). This pure B_2 mode is also H-symmetric. Since it is a pure B_2 mode, only even azimuthal Fourier components are present in this solution.

Synchronous B_1-B_2 mixed mode solutions (violet solid squares in Figure 4.1) emerge rapidly from the B_2 solutions. Starting from B_2 and augmenting Re, the first azimuthal

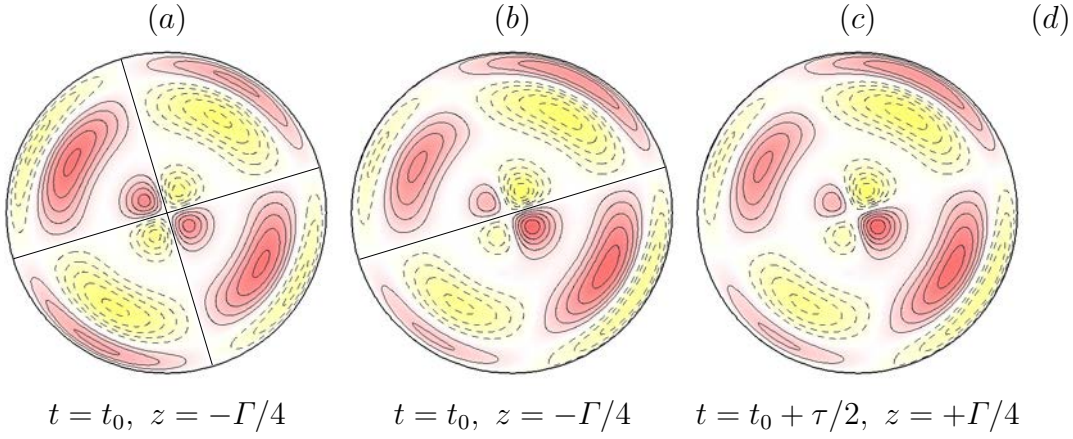

Figure 4.10: (a) Axial vorticity contours of the B_2 pure mode at $(St, Re) = (16, 396.15)$. (b) and (c) Axial vorticity contours of the B_1-B_2 mixed mode at $(St, Re) = (16, 396.25)$, in the z-sections and times indicated; t_0 is at the beginning of the forcing period. The straight lines are the K_β reflection symmetry axes. Contour/colour convention as in Figure 4.3.

Fourier mode becomes unstable, and after an oscillatory transient, a B_1-B_2 mixed mode state is obtained, that is synchronous with the forcing. A steady bifurcation occurs here and in the process the D_2 symmetry is lost. Figure 4.10(b) displays contours of axial vorticity for the mixed mode B_1-B_2. This solution has the same spatial symmetries as the pure B_1 mode: D_1, consisting of a single reflection symmetry K_β. As can be observed in the figure, the even azimuthal modes are still dominant, but the presence of the modus one modifies the symmetries of the mixed solution. Panel (c) of Figure 4.10 exhibits the invariance of this mixed mode solution under the spacetime symmetry H. This feature is also confirmed by scrutinising the PSD of the axial velocity on the mid-plane, and checking the absence of the even temporal Fourier components. Obviously, since this solution is K_β-symmetric, the same state is recovered when the computations impose this symmetry artificially.

To sum up, the main difference between the dynamics below and above the bicritical point is the rapid sequence of bifurcations taking place above C_1, resulting almost immediately in bursting states that are quasiperiodic and possess very rich dynamics. In contrast, below C_1 the pure mode B_1 exists and is stable in a very large parameter domain, except in a region close to the codimension-two point, where two kinds of quasiperiodic solutions (modulated rotating waves and bursting solutions) come into sight.

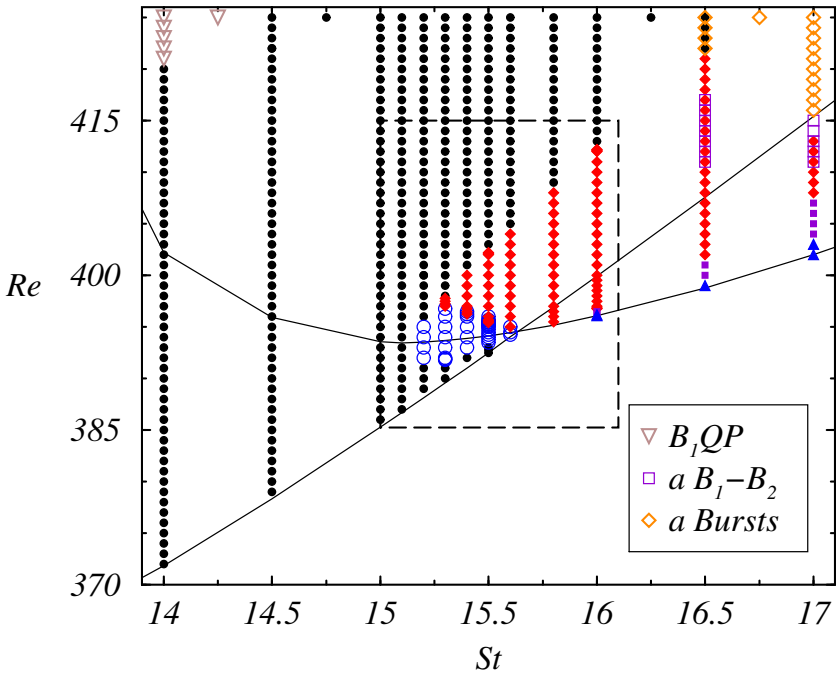

Figure 4.11: Families of bifurcated states around the bicritical point C_1. The bifurcation curves from the base state are indicated as black solid lines. The dashed rectangle corresponds to Figure 4.1. The new bifurcated states away from the bicritical point C_1 are indicated in the figure legend.

4.2 Dynamics away from the codimension-two point

In the previous section, the dynamics and bifurcations close to the codimension-two point C_1 have been analysed. In the present section, the analysis to secondary bifurcations is extended in a larger region of parameter space, where a wealth of additional bifurcations is found. These new results are summarised in Figure 4.11, where the different symbols correspond to numerically computed states. The previous bifurcations of Figure 4.1 correspond to the region close to C_1 indicated by a dashed rectangle in Figure 4.11. As in Figure 4.1, the black solid curves correspond to the bifurcation curves of the basic state that meet at C_1, and the states sketched in the previous section have been included. In addition to the mentioned states, some novel states emerge away from C_1. For instance, for Stokes numbers below St_c, the synchronous B_1 modes become quasiperiodic (brown open down triangles), while for $St > St_c$, new families of mixed modes (violet open squares) and bursting solutions (orange open diamonds), different from the ones previously obtained, enter the stage. Furthermore, at sufficiently high Re, chaotic solutions develop from the B_1QP, as well as, from the asymmetric bursts (not shown in Figure 4.11). This cascade of bifurcations towards chaotic states complements

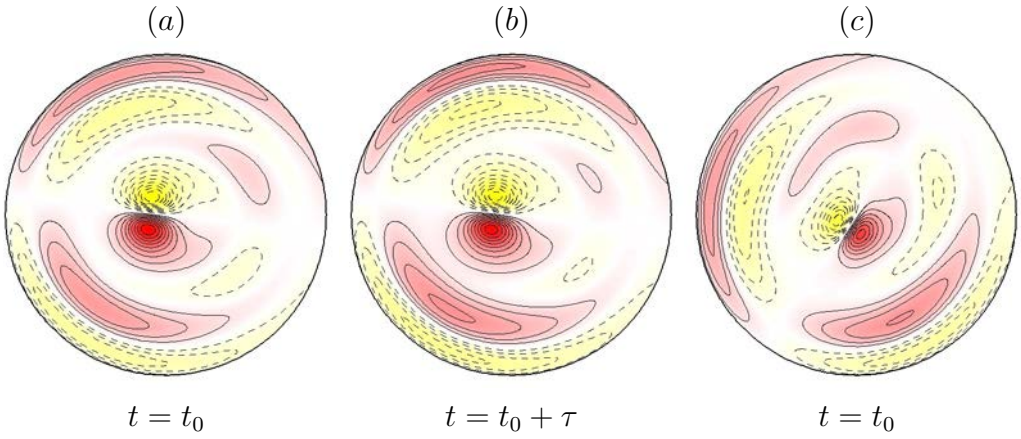

Figure 4.12: Axial vorticity contours at $z = -\Gamma/4$ and different times; t_0 is at the beginning of the forcing period. (a) and (b) Quasiperiodic solution B_1QP at $(St, Re) = (14, 425)$. (c) B_1 chaotic solution for $(St, Re) = (14, 500)$. Contour/colour convention as in Figure 4.3.

the picture sketched in the previous section and helps to better understand the process described in Blackburn & Lopez (2011).

4.2.1 Small St numbers

The pure mode B_1 is very robust for small Stokes numbers St. By increasing enough the Reynolds number, B_1 undergoes a sequence of bifurcations strongly resembling the Ruelle-Takens-Newhouse route to chaos. The periodic solution B_1 bifurcates first to a quasiperiodic solution with two frequencies, and by further increasing Re the torus is destroyed and a chaotic state appears. The quasiperiodic solution, B_1QP (brown open down triangles in Figure 4.11), is a B_1 mode pulsating with an additional characteristic frequency; this is clearly observed in Figure 4.12(a) and (b), showing two axial vorticity contours at the beginning of the forcing period. They strongly resemble the pure mode B_1 in Figure 4.3(a), but the intensity of the flow increases and decreases with the second frequency. By further increasing the Reynolds number, other frequencies become apparent, and eventually the B_1QP solutions acquire a chaotic pattern. A snapshot of these chaotic solutions is shown in Figure 4.12(c). The main difference with B_1QP is that the reflectional symmetry K_β is clearly broken in the chaotic solution. This can be verified by computing the symmetry parameter of these two solutions: $S_{K_\beta}(B_1QP) = (a)0.0234, (b)0.0132$ and $S_{K_\beta}(\text{chaotic}) = 0.362$. The asymmetry parameter for the quasiperiodic solution has the same order of magnitude as the B_1 mode

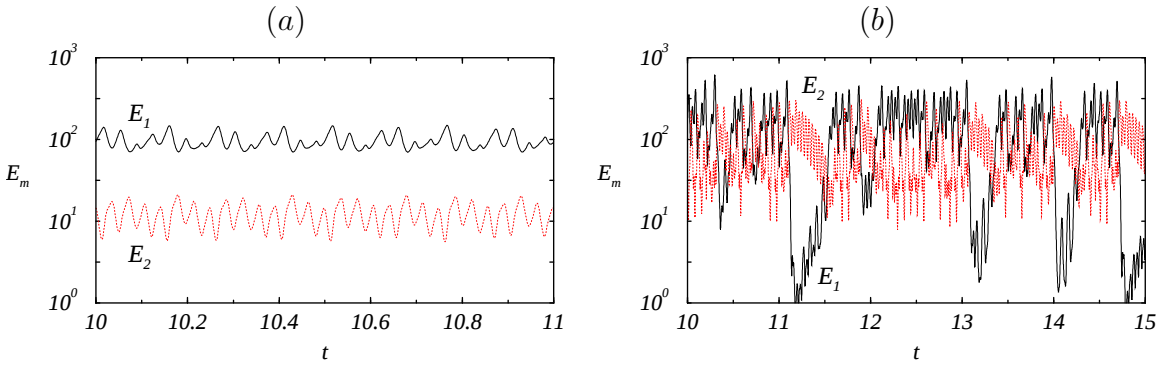

Figure 4.13: Time series of energy of the Fourier mode E_1 and E_2 for (a) the B_1QP at $(St, Re) = (14, 425)$, and for (b) the B_1 chaotic solution at $(St, Re) = (14, 500)$.

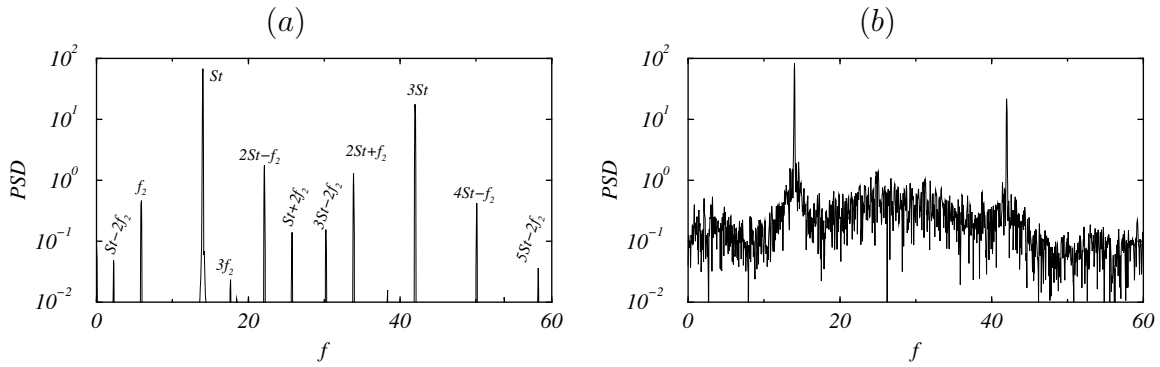

Figure 4.14: FFT of the time series of the near-wall axial velocity at mid-height $(r, \theta, z) = (0.9, 0, 0)$, for the (a) B_1QP at $(St, Re) = (14, 425)$ and (b) B_1 chaotic solution at $(St, Re) = (14, 500)$.

analysed in Section §3.3.1. The symmetry parameter of the chaotic state is one order of magnitude larger, so the symmetry breaking can be visually observed. By means of imposing the K_β symmetry artificially, the same states are recovered with the difference that both solutions preserve K_β respect to $\beta = 0$ and $S_{K_\beta}(B_1QP) = S_{K_\beta}(\text{chaotic}) = 0$. With regard to the spatio-temporal symmetry, as both states have more than one frequency and are not periodic, the H symmetry is broken.

The chaotic character of the state at $(St, Re) = (14, 500)$ cannot be discerned in the snapshot shown in Figure 4.12(c), but it is evident by comparing the time series of the energies of the first and second Fourier modes shown in Figure 4.13(a) for the B_1QP and (b) for the chaotic state. The chaotic state is much more complex with a strong competition between both modes, and shows random time intervals where the azimuthal mode $m = 2$ is dominant. The solution alternates between pure modes, mixed

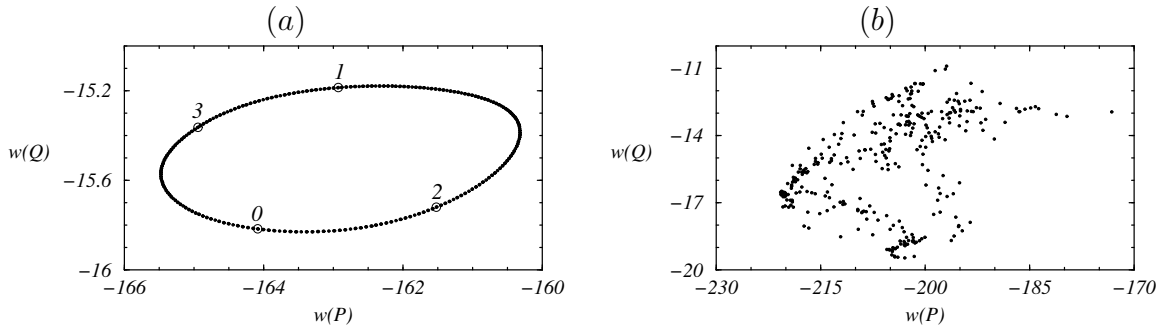

Figure 4.15: Poincaré sections (bullets) using two axial velocities measured at $(r, \theta, z)_P = (0.9, 0, 0)$ and $(r, \theta, z)_Q = (0.9, 0, 0)$, for the (a) B_1QP at $(St, Re) = (14, 425)$ and (b) B_1 chaotic solution at $(St, Re) = (14, 500)$.

modes or largely distorted modes without a precise pattern. The comparison of the Fourier transforms of the axial velocity on the mid-plane for the two states is shown in Figure 4.14. The PSD of B_1QP is clearly quasiperiodic with two well-defined frequencies and their linear combinations, while the PSD of the chaotic state exhibits a broad band of frequencies, and only a few multiples of the forcing frequency are outstanding. Notice that in both Fourier transforms the even multiples of the forcing frequency are very small, indicating that the spatio-temporal symmetry H is still approximately fulfilled.

Figure 4.15 represents the Poincaré section of two axial velocities measured at $z = 0$ and $z = 0.95$ near the sidewall after performing a sampling of points every forcing period (bullets). The Poincaré section for the B_1QP displayed in Figure 4.15(a) produces a perfect cycle, so this solution lives in a two-torus. The big circumferences represent four consecutive points in the reduced space, and it is observed that the second iteration approaches the initial point and the third one surpasses it, in excellent agreement with the second frequency $f_2 = 5.89$ measured from the Fourier transform in Figure 4.14(a), that provides $St/f_2 = 2.38$, indicating that going around the circle takes more than two iterates. Figure 4.15(b) represents the Poincaré section of the chaotic state at $(St, Re) = (14, 500)$. The result cannot be considered a limit cycle in any case. The two-torus has been destroyed, and the points observed might be considered the Poincaré section of a chaotic attractor. Curiously, the B_1QP solution shares a strong similarity with the MSW_1 of the previous chapter.

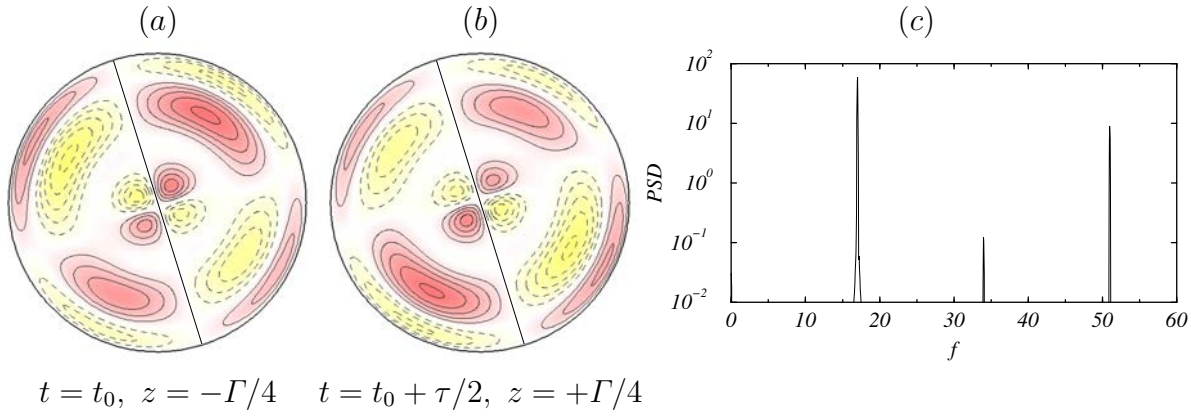

Figure 4.16: Asymmetric B_1-B_2 mixed mode at $(St, Re) = (17, 414)$. (a) and (b) Axial vorticity contours in the z-sections and times indicated; t_0 is at the beginning of the forcing period. Straight lines are K_β reflection symmetry axes. Contour/colour convention as in Figure 4.3. (c) FFT of the time series of the axial velocity at mid-plane near the wall $(r, \theta, z) = (0.9, 0, 0)$.

4.2.2 Large St numbers

Observing Figure 4.11, for higher St than the bicritical value, two new branches of solutions turn up. These two new solutions are called asymmetric mixed modes and asymmetric bursts. The asymmetric mixed modes are very similar in some aspects to the former mixed modes, but do not preserve the spatio-temporal symmetry H, thus the *asymmetric* adjective. Since the asymmetric bursts bifurcate from the asymmetric mixed modes, they are called asymmetric too. By further increasing Re above the range of Figure 4.11, irregular or chaotic bursting solutions are obtained.

B_1-B_2 asymmetric mixed mode solution

The mentioned asymmetric B_1-B_2 mixed modes solutions (violet open squares in Figure 4.11) are obtained far away from C_1 and its branch coexists in the parameter space with the bursts. By increasing Re at $St = 17$, the symmetric bursts of the former section become unstable, and after a transient the new asymmetric mixed mode is achieved. When continued to smaller Re, this new branch of solutions coexists with the burst branch and there is a noticeable hysteresis region, as can be seen in Figure 4.11. This asymmetric mixed mode has a single characteristic time, the forcing period, hence this solution is synchronous, like the B_1-B_2 H-symmetric mixed modes discussed in Section 4.1.2.

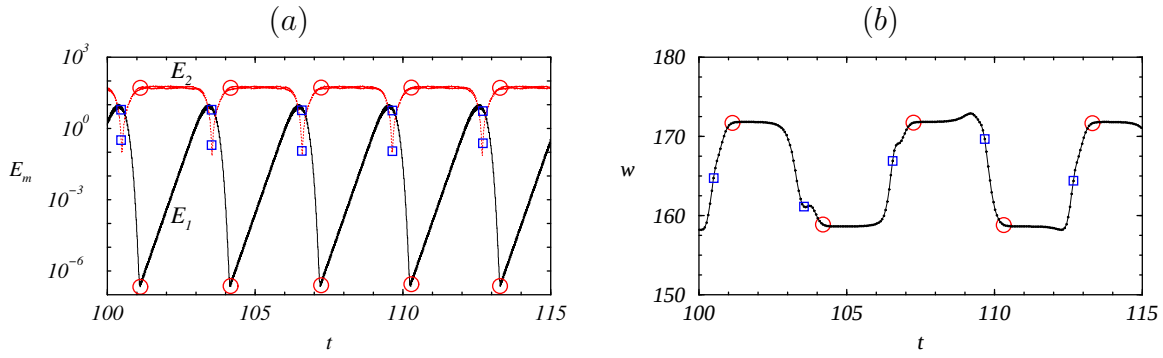

Figure 4.17: Asymmetric bursting solution at $(St, Re) = (17, 425)$. Time series of (a) the energy of the Fourier modes E_1 and E_2, and (b) maximum values of the near-wall axial velocity at mid-height $(r, \theta, z) = (0.9, 0, 0)$.

In Figure 4.16(a) and (b), contours of axial vorticity are depicted separated half-forcing-period, and in symmetric planes with respect to $z = 0$, for the asymmetric mixed mode at $(St, Re) = (17, 414)$. At first sight the solution resembles the pure mode B_2 of Figure 4.10(a). Nevertheless, the difference in strength of the four quadrants in Figure 4.16(a) and (b), breaks the rotational symmetry of π. Therefore this solution preserves exactly the same spatial symmetries as the pure B_1 modes do: of the continuous family of symmetries $O(2)$ of the governing equations, the final state only has one reflection plane of symmetry. In addition, it is observed by inspection of the figures that this solution does not preserve the spatio-temporal H symmetry: the two snapshots, that should be identical if this solution was H-symmetric, are rotated a factor of π. Therefore, as occurred with the A_2 modes in the previous paper, a new spatio-temporal symmetry arises: the H symmetry combined with a rotation of π. Fig. 4.16(c) represents the PSD of the time series of the axial velocity at mid-plane near the wall, and there is clearly a single frequency, the forcing frequency, therefore it is a synchronous state. In contrast with all the previous solutions, the spectrum manifests even and odd harmonics of this sole frequency, which is also a clear indication of the breaking of the spatio-temporal symmetry H, as occurred for the A_2 mode in Figure 3.7(b). As a curiosity, this asymmetric mixed mode does no longer exist when K_β is numerically enforced, and the simulations result in the common B_2 solution.

Asymmetric bursting solution

Starting with the asymmetric B_1-B_2 mixed modes and further increasing Re, these modes become unstable, and evolve towards a branch of asymmetric bursts (orange

open diamonds in Figure 4.11). Both asymmetric solution branches can be continued to smaller St values, and they coexist in a wide parameter region with the symmetric mixed modes and bursts, as it can be seen in Figure 4.11.

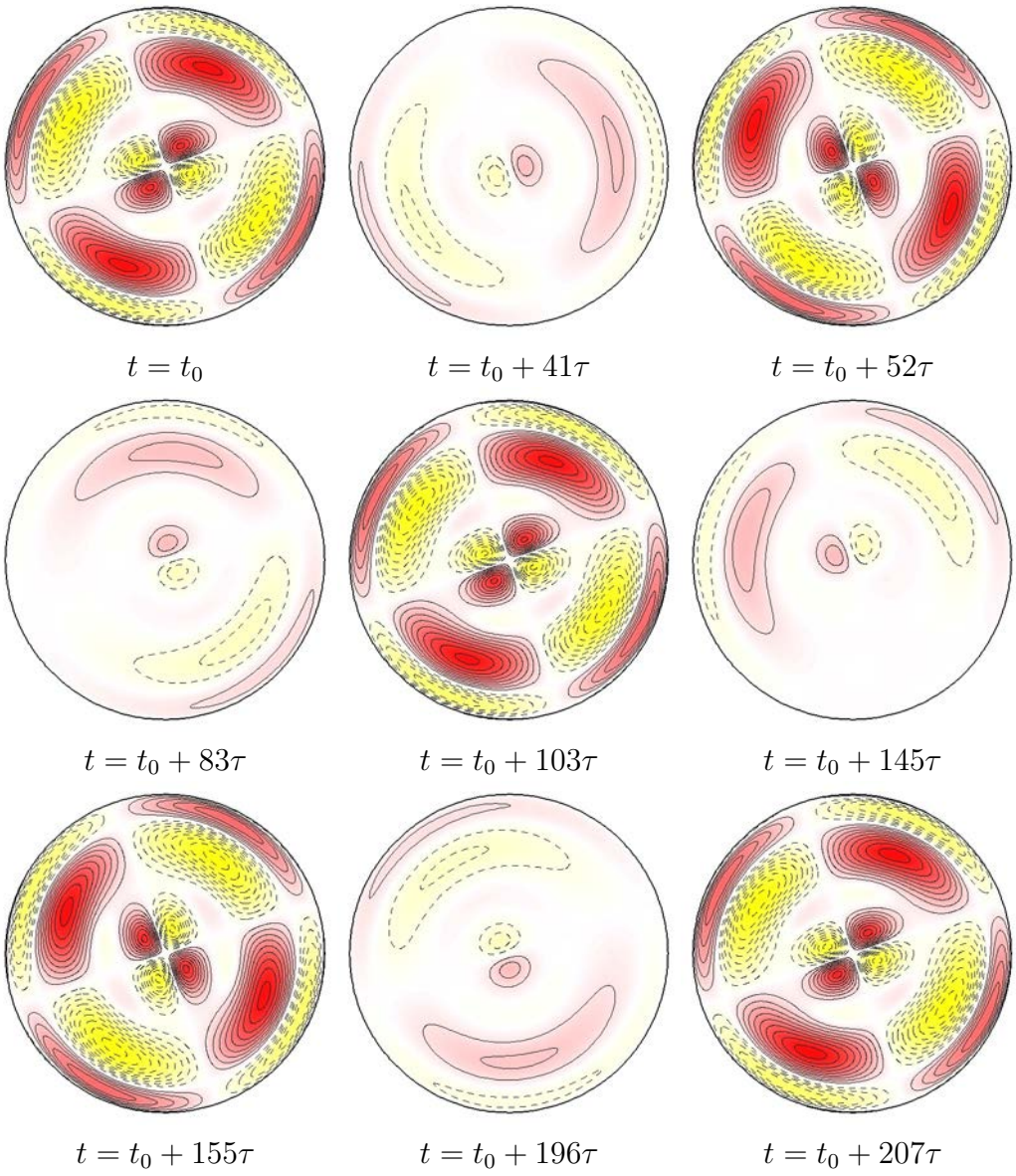

Figure 4.18: Axial vorticity contours at $z = -\Gamma/4$ and different times of the asymmetric bursts at $(St, Re) = (17, 425)$; t_0 is at the beginning of the forcing period and each snapshot corresponds to consecutive minima of E_1 and E_2. Contour/colour convention as in Figure 4.3.

Figure 4.17(a) shows the time series of the energies of the asymmetric bursts at $(St, Re) = (17, 425)$. This time series is very similar to the one corresponding to the symmetric bursts in Figure 4.6(a), but now the energy of the second mode is at least one

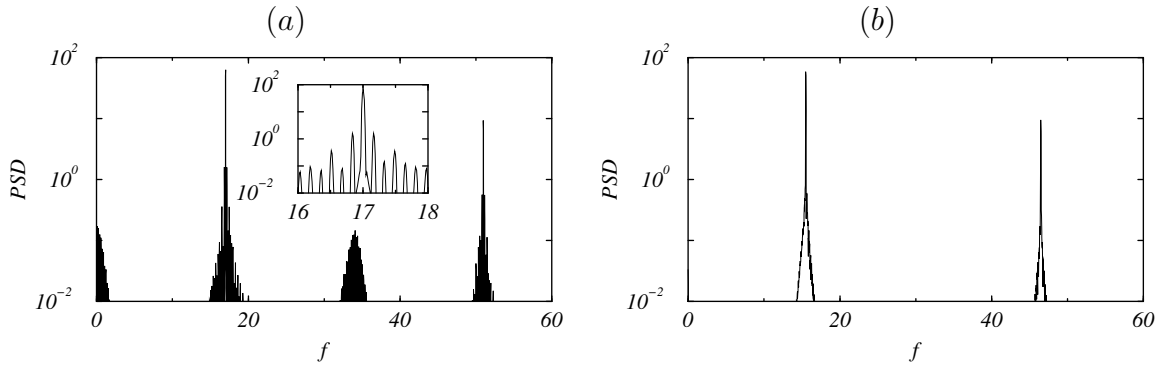

Figure 4.19: FFT of the time series of (a) the asymmetric burst in Figure 4.17(b), and (b) the symmetric burst in Figure 4.6(b).

order of magnitude larger than the first one, except in a very narrow temporal window where it dominates. Figure 4.17(b) displays the evolution of the maximum values of the axial velocity at $z = 0$ near the wall. As for the symmetric bursts, in Figure 4.6(b), the period measured from the axial velocity is four times the value obtained from the energy plot. The reason is the same as in the symmetric bursts: the solutions at two consecutive minima of the $m = 2$ mode (almost pure B_1 modes) are rotated $\pi/2$, so it takes four bursts to recover the initial state. The period measured in Figure 4.17(b) is $\tau_2 \approx 12.212$, very long when compared with the forcing period $\tau = 1/St = 0.0588$: $\tau_2/\tau \approx 207.6$.

As it has been done for the bursts of the previous section, Figure 4.18 shows contours of axial vorticity at $z = -\Gamma/4$ that correspond to the succession of minima of E_1 and E_2 appearing in Figure 4.17(a). The solutions correspond to a modus B_1 (at the minimum of the $m = 2$ mode, blue open squares in the figures) and B_2 (at the minimum of the $m = 1$ mode, red circumferences in the figures). In this case, the solutions at two consecutive minima of the $m = 2$ mode (almost pure B_1 modes) have also rotated $\pi/2$, and the initial state is recovered after four alternations; almost 207 forcing periods, in concordance with the estimation.

Consequently, this asymmetric bursts are quasiperiodic too, with two frequencies, $St = 17$ and $f_2 = 0.0816$. Figure 4.19(a) represents the PSD of the asymmetric bursting time series in Figure 4.17(b). The second frequency is observable in the inset of this PSD with the presence of additional peaks at $St \pm 2jf_2$ for $j = 1, 2, 3, 4, 5$ and 6. Actually, measurements made to the other bursting solutions, corresponding to Figure 4.19(b), may exhibit the same frequency distribution of the inset.

In order to complement the picture of this asymmetric bursts, the bullets in Fig-

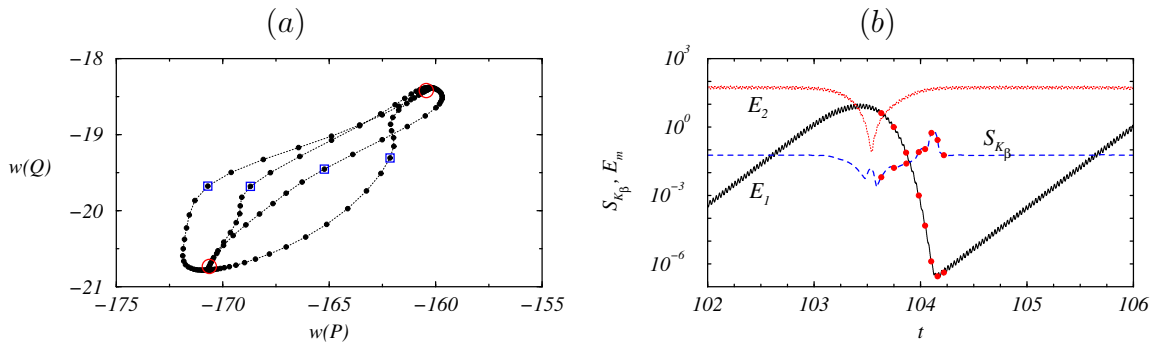

Figure 4.20: Asymmetric bursting solution at $(St, Re) = (17, 425)$. (a) Poincaré section (bullets) using two axial velocities measured near the wall. The minima of E_1 (circumferences) and E_2 (open squares) indicated in Figure 4.17 and 4.18 are also plotted. (b) Time evolution of the K_β asymmetry parameter, S_{K_β}; symbols refer to Figure 4.21.

ure 4.20(a) represent the Poincaré section of the asymmetric bursting solution considered, using two axial velocities measured near the wall at $z = 0$ and $z = 0.95$. This section is analogous to Figure 4.8(a) from the symmetric bursts and possesses the same properties.

In the same direction as in the symmetic bursts, Figure 4.20(b) exhibits the evolution of S_{K_β} along an asymmetric burst: this parameter is most of the time constant, except for a remarkable peak and valley that coincide with the minima of the energies, also plotted in the figure. Therefore the reflection symmetry is broken mainly when the energy of the $m = 1$ mode is minimum, and the plot is similar to Figure 4.8(b) for the symmetric bursts. However, the asymmetric bursts break the K_β reflection symmetry in a different way that the symmetric bursts. Azimuthal mode one preserved reflection symmetry, while mode two slightly broke it in the symmetric bursts. The spike in the evolution of the symmetry parameter S_{K_β} was due to the fact that mode one rotated $\pi/2$ when it was very close to its minimum, but remaining reflection-symmetric while rotating, as it is illustrated in the first row of Figure 4.9. For the asymmetric bursts, the azimuthal mode two behaves in the same way as for the symmetric bursts, but mode one differs enormously. Figure 4.21 shows a time sequence of the first Fourier mode along the rapid decrease and about the minimum value of its energy. The eight snapshots in Figure 4.21 correspond to the eight red circles in Figure 4.20(b). The first five snapshots along the rapid decrease of mode one show that the symmetry line does not change and the mode is reflection-symmetric, although the shape of this mode changes remarkably. The three last snapshots, about the minimum, shows that mode one breaks the reflection symmetry becoming distorted near the axis, where the pattern starts rotating, while the pattern

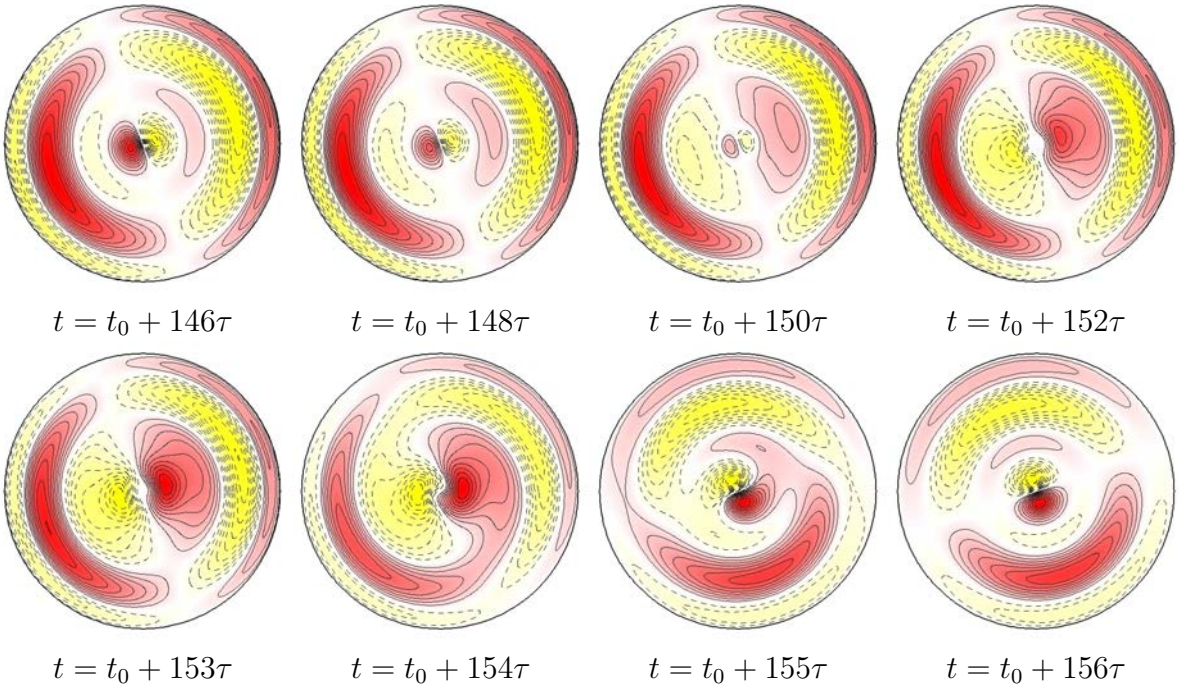

Figure 4.21: Axial vorticity contours at $z = -\Gamma/4$ and different times of the asymmetric bursts at $(St, Re) = (17, 425)$; t_0 is at the beginning of the forcing period. Only the first azimuthal Fourier component is plotted, at the points indicated by red circles in Figure 4.20(b). Contour/colour convention as in Figure 4.3.

close to the sidewall does not move at the beginning of the process (snapshot 6), then rapidly rotating (snapshot 7), until finally the reflection symmetry is restored with mode one having rotated $\pi/2$ with respect to the starting point (snapshot 1). The distorted spiral pattern near the axis resembles the quasiperiodic mode MRW_1 of Figure 3.12 that bifurcates at much larger St values. This resemblance suggests that the influence of the quasiperiodic modes could be the origin of the two families of asymmetric solutions found. By means of imposing the K_β symmetry artificially, this solution cease to exist and the usual synchronous B_2 mode is obtained. This feature, which is common in the two asymmetric families, might indicate that these solution come from a branch that has nothing to do with the B_1 and B_2 curves.

Concerning to the spatio-temporal symmetry of this asymmetric bursting solution, let us turn again to the PSD of Figure 4.19(a). These solutions clearly manifest that are not H-symmetric because of the presence of the even Fourier components. This is not surprising, because the asymmetric bursts seem to bifurcate from the asymmetric mixed modes, that neither are H-symmetric.

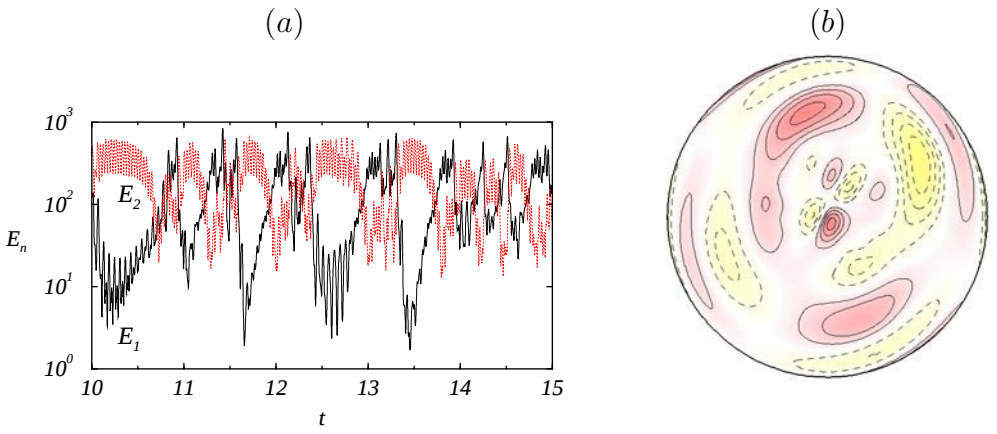

Figure 4.22: Irregular bursts at $(St, Re) = (17, 550)$. (a) Time series of the energy of the Fourier modes E_1 and E_2. (b) Axial vorticity contour at $z = -\Gamma/4$. Contour/colour convention as in Figure 4.3.

Irregular bursting solution

Starting from an asymmetric bursting solution and increasing Re beyond the limits in Figure 4.11, the bursts become chaotic and irregular. Figure 4.22(a) shows the time series of the energies of the first and second azimuthal Fourier modes after saturation for the irregular burst at $(St, Re) = (17, 550)$. In this case, both modes acquire energies of similar order of magnitude, showing irregular bursts from time to time and chaotic temporal behaviour.

In Figure 4.22(b), a contour of axial vorticity is depicted for $z = -\Gamma/4$ at a particular time. This snapshot corresponds to a B_2 mode that is strongly inflenced by a B_1 mode, some kind of irregular mixed mode. A sequence of cross-sections demonstrates the irregular nature of these bursts: the presence of pure modes can be observed sporadically, but most of the time there is a large interaction between the different modes. This solution resembles the solutions in the bursting scenarios, however the visits to the B_1 state are not periodic but random, and between consecutive visits, the B_1 pattern rotates randomly approximately $\pm\pi/2$. Concerning the spatial symmetries, when the solution approaches a pure or a mixed mode the corresponding spatial symmetries are observed, but otherwise the solution is largely distorted without any symmetry. For example, $S_{K_\beta}(\text{irregular}) = 0.545$ in Figure 4.22(b). The Fourier transforms of the axial velocity on the mid-plane for this state is not shown but is very similar to the other chaotic solution, displayed in Figure 4.14(b), and only possesses the odd Fourier components too. Concerning the artificial enforcing of K_β, a symmetric mixed mode with $\langle E_1 \rangle \ll \langle E_2 \rangle$ is achieved.

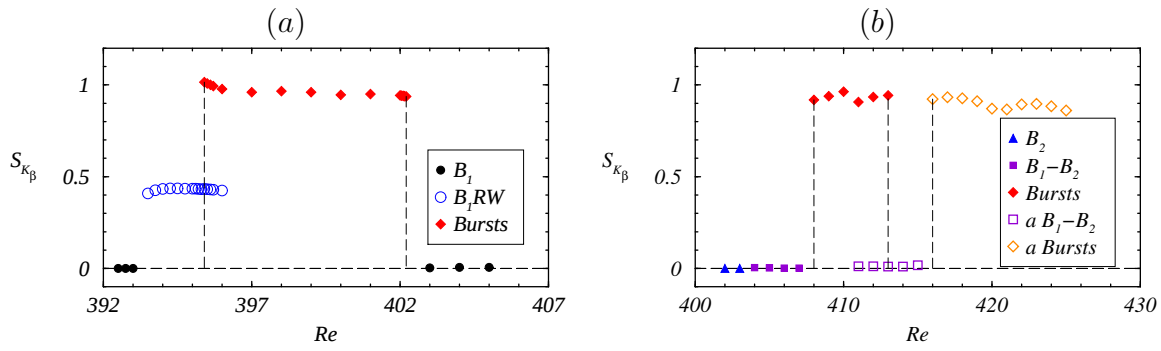

Figure 4.23: K_β asymmetry parameter, S_{K_β}, as a function of the Reynolds number, Re, for (a) $St = 15.5$ and (b) $St = 17$.

4.3 Discussion

The main findings are summarised in Figure 4.11, and in particular in Figure 4.23, showing the variation of the asymmetry parameter S_{K_β} for the different families of solutions along two one-dimensional parameter paths at $St = 15.5$ and $St = 17$, below and above the codimension-two point C_1. Close to this bicritical point, the dynamics is dominated by two families of solutions, with dynamics governed by a very low frequency, in addition to the forcing frequency. They are the modulated rotating waves B_1RW (blue circumferences) and the symmetric bursting solutions (red solid diamonds). The modulated rotating waves B_1RW are present only below C_1, for $St < St_c$. Above the bicritical point C_1, a succession of three bifurcations (Base state $\rightarrow$ B_2 $\rightarrow$ B_1-B_2 $\rightarrow$ Bursts) occurs rapidly, resulting in bursting solutions. These rapid cascades of bifurcations are typical of fluid problems with $O(2) \times Z_2^{ST}$ symmetry, and in the present problem it has been possible to resolve the details of the cascade for the first time. Close to C_1 the bifurcated solutions preserve the spatio-temporal symmetry H exactly for the synchronous solutions and very approximately for the quasiperiodic solutions. However, when increasing St and Re, additional families of mixed and bursting solutions breaking the H symmetry appear. These asymmetric solutions coexist and interact with the symmetric families, and when increasing Re they become chaotic. As a matter of fact, S_{K_β} is very useful to classify the existing solutions but further insight is necessery to understand their origin.

In order to unravel the onset of the B_1RW, let us focus on their small frequencies. Figure 4.24 exhibits the periods of rotation τ_2 for the B_1RW states in the region where these solutions exist. It is observed that the period goes to infinity, so the precession frequency $f_2 = 1/\tau_2$ goes to zero along the bifurcation curve $B_1 \rightarrow B_1RW$. The pure

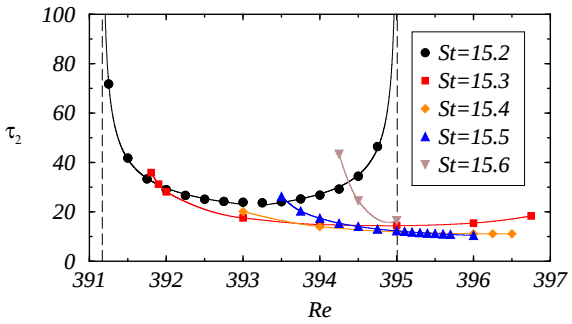

Figure 4.24: Period τ_2 of the B_1RW solutions as a function of Re for different Stokes numbers St as indicated.

mode B_1 does not precess, because it is K_β-reflection invariant, and there is a continuous family of B_1, the group orbit of $SO(2)$ acting on them. What occurs is that in the bifurcation $B_1 \to B_1RW$, the K_β-reflection symmetry is broken, and the bifurcated solutions start to drift along the group orbit, resulting in a (modulated) rotating wave. Although the bifurcated state is quasiperiodic (it has two frequencies, so it lives on a two-torus), the bifurcating eigenvalue is real, and the second frequency comes from the symmetry breaking and the corresponding drift along the group orbit (Crawford & Knobloch, 1991); the bifurcation is a pitchfork breaking K_β, that generates a drift because of the continuous family of B_1 solutions. It has been manifested in Crawford & Knobloch (1991) that the period τ_2 must vary as the inverse of the square root of the distance to the bifurcation point, a result consistent with the periods computed and shown in Figure 4.24. The curves displayed in the figure are splines to guide the eye, except the curves for $St = 15.2$ that correspond to square-root fits. The data adjusts very well, corroborating the mentioned square-root law. The largest period computed corresponds to the curve for $(St, Re) = (15.2, 395)$, that gives $\tau_2 \approx 259$, which in the figure is out of range.

In the same direction, to understand the origin of the small frequency of the bursting solutions and the kind of bifurcations they undergo, the period τ_2 is plotted in Figure 4.25(a) as a function of the Reynolds number Re for different St values. The periods τ_2 become very large when approaching the upper Re bifurcation curve in Figure 4.1, where B_1 bifurcates to the bursting solution. This happens not only for $St < St_c$, below the codimension-two point C_1, but also for $St_c < St \leq 16$. This infinite period bifurcation is called a saddle-node infinite cycle (SNIC) bifurcation, and occurs when a saddle-node bifurcation takes place on an invariant cycle (Kuznetsov, 2004). Previously to the bifurcation, there exists a stable limit cycle. At the bifurcation a saddle-node

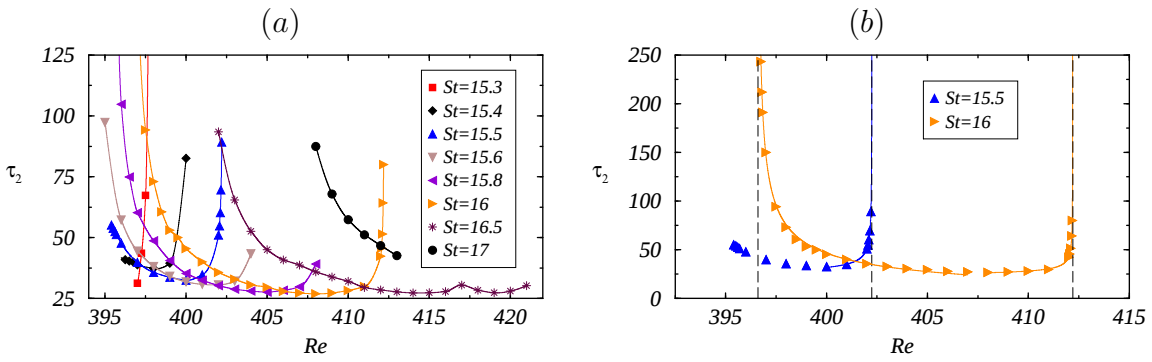

Figure 4.25: (a) Period τ_2 of the bursting solutions. The symbols are computed values, and the solid lines are splines plotted to guide the eye. (b) Square-root fits to some of the SNIC bifurcations in (a). The dashed lines indicate the Re bifurcation value obtained from the fit.

appears on the limit cycle. After the bifurcation, the saddle-node splits into two fixed points, one stable and the other unstable, destroying the limit cycle in the process. In our problem, there is a quasiperiodic solution on a two-torus, the bursting solution, instead of a limit cycle; but the dynamics on a Poincaré section of the torus are the same as the dynamics just described for the SNIC bifurcation. The fixed points that appear on the SNIC bifurcation correspond in our case to the B_1 synchronous solution. This scenario is common in fluid dynamics, and is described in detail for example in Lopez & Marques (2009), in a rotating convection problem. A characteristic signature of a SNIC bifurcation is the law followed by the period when approaching the bifurcation, that also scales as the inverse of the square root of the distance to the bifurcation point (Strogatz, 1994). Indeed, the periods shown in Figure 4.25(a) that connect the bursts with the B_1 mode follow the square-root law, as shown in Figure 4.25(b). The bifurcation of the bursting solutions for low Re values is also an infinite period bifurcation for $St \in [15.8, 17]$, above the bicritical C_1 point, as is clearly seen in Figure 4.25(a). In this scenario, τ_2 also follows the square-root law as shown in Figure 4.25(b), so it is considered a SNIC bifurcation, this time with the sinchronous mixed mode solution B_1-B_2. However, below C_1, there are not stable limit cycles available, and the bifurcation of the bursts takes place at a finite value of the period, and might be considered a saddle-node bifurcation of bursting solutions. When approaching the bicritical point C_1 from below ($St < St_c$), the period at the bifurcation becomes very large ($St = 15.5$ and 15.6), suggesting that it is likely to become infinite at the C_1 point, exactly what happens just on the other side of C_1 ($St > St_c$). The periods for $St = 16.5$ and 17 do not go to infinity in the high Re region because for these large St values other branches of solutions appear and the bursting solutions no longer bifurcate from B_1, as it can be

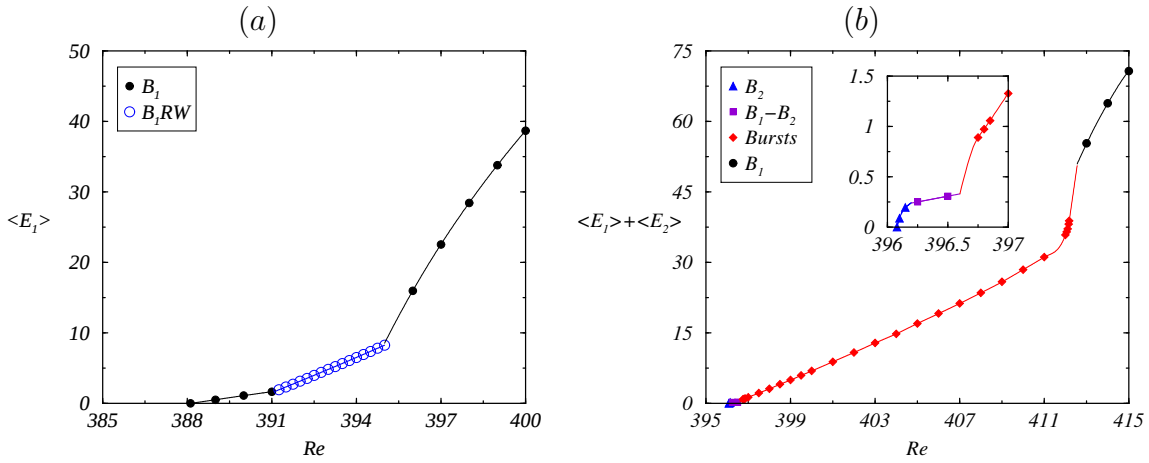

Figure 4.26: Time average of the energy of the dominant modes as a function of Re considering the branches of solutions at different St: (a) first mode $St = 15.2$, and (b) first and second Fourier mode $St = 16$.

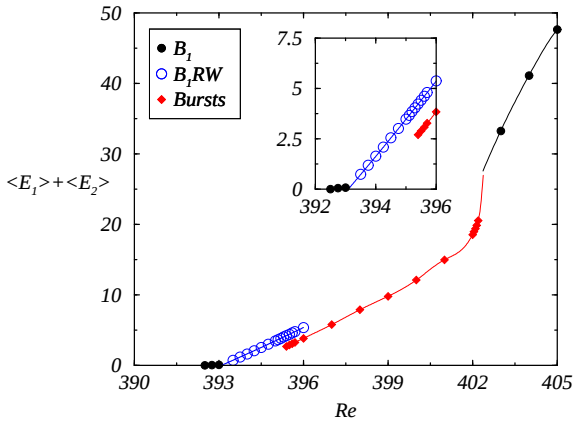

Figure 4.27: Time average of the energy of the first and second modes as a function of Re considering the branches of solutions at $St = 15.5$

observed in Figure 4.11.

Both bifurcations appear in infinite period bifurcations and the critical values can be estimated using square-root fits. As it has been done in the former chapter, an analysis in terms of the energy might be desirable to complement the picture. Figure 4.26 shows the time-averaged energy of the dominant modes $\langle E_m \rangle$ as a function of the Reynolds number for the different families of solutions that appear at (a) $St = 15.2$ and (b) $St = 16$. On the one hand, for $St = 15.2$, the dynamics is clearly ruled by the first Fourier mode. On the other hand, the existance of the mixed modes and the bursts, which possess remarkable contributions of the two first modes, demand the usage of both

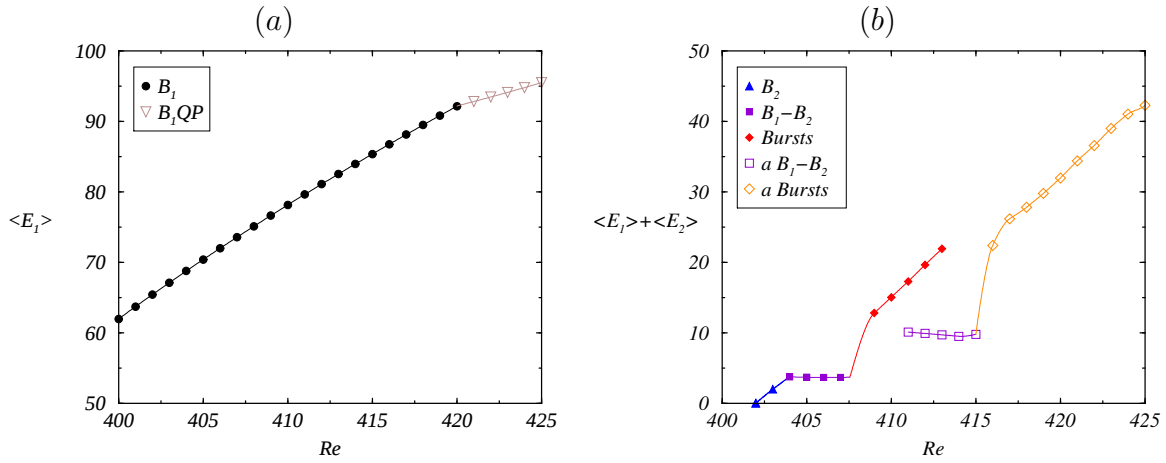

Figure 4.28: Time average of the energy of the dominant modes as a function of Re considering the branches of solutions at different St: (a) first mode $St = 14$, and (b) first and second Fourier mode $St = 17$.

averages. Solutions that involve two frequencies in the energy series have been averaged over the two characteristic times. As a matter of fact, the B_1RW solution clearly bifurcates supercritically from the B_1 mode and the critical values can be estimated as the intersection of linear fits. According to Figure 4.26(b), the bursts are supercritical bifurcations from the mixed modes and the B_1 modes, but the obtaining of critical value is not so effective as is in Figure 4.26(a). The most important conclusion that can be extracted from the inset of Figure 4.26(b), as well as from Figure 4.28(b), is the fact that the mixed modes bifurcate supercritically from the pure B_2 modes and the bifurcating value can be obtained from simple fits. Nevertheless, the interaction between the bursts and the B_1RW is quite obscure. Apparently, from Figure 4.27, the two families seem to be disconnected and create a rather small region of hysteresis, in accordance with Figure 4.23(a).

Before reaching the chaotic regions away from C_1 (B_1 chaotic solution and irregular bursts), the flow suffers several bifurcations. The B_1QP solution emerges from the B_1 mode with the appearance of an additional pulsating frequency. Figure 4.28(a) displays the time average of the first Fourier mode, and the transition between both solutions seems to be supercritical and the critical value well-defined. Recall that beyond the range of this figure, the dynamics of the B_1QP turns more and more complex and eventually becomes chaotic. This resembles the classical Ruelle-Takens-Newhouse route to chaos. By means of increasing the parameter, the flow undergoes a sequence of Hopf bifurcations and each one of them introduces an additional frequency. With the presence of a third period, the flow is prone to become chaotic (Eckmann, 1981). Actually, this

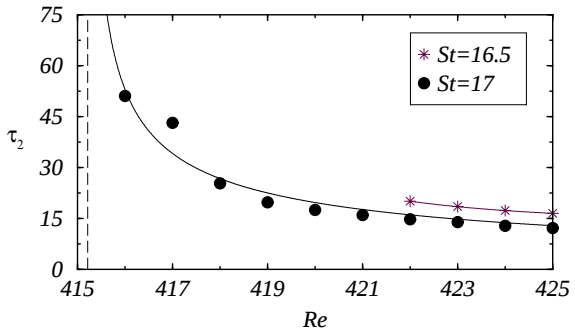

Figure 4.29: Period τ_2 of the B_1RW solutions as a function of Re for different Stokes numbers St as indicated.

is what seems to happen at even higher Re.

Concerning to the families of solutions that do not preserve the spatio-temporal symmetry, Figure 4.28(b) exhibits the apparent disconnection between the asymmetric mixed modes and the symmetric bursts at $St = 17$. There are some strong evidences indicating that the asymmetric branch might come from the A_2 synchronous or MRW_1 quasiperiodic modes, thus explaining the separation with the symmetric branches. Nevertheless, understanding the relation between the asymmetric families should be possible in terms of the secondary frequency too. Figure 4.29 displays τ_2 as a function of Re at the different St where the asymmetric bursts exist. The same square-root fit employed for the symmetric bursts adjusts the data pretty well at $St = 17$ and provides a critical value for a feasable SNIC bifurcation from the asymmetric mixed modes. Note that these asymmetric bursts are quite robust and the irregular bursts only emerge after having increased Re in a great measure. The bifurcation that the asymmetric bursts might undergo to become irregular could be attributed to the Ruelle-Takens-Newhouse scenario again: a Hopf bifurcation introduces another frequency that might induce the flow to become chaotic because it would possess a total of three.

4.4 Conclusions

The three-dimensional dynamics of fluid problems with spatial $O(2)$ symmetry and spatio-temporal Z_2 symmetry has aroused the interest of the fluid dynamics community in recent years, owing to its relevance to wakes and periodically forced flows. Experiments and numerical simulations have been conducted in these flows, looking for the three-dimensional dynamics after breaking the $O(2)$ symmetry Williamson (1996);

Julien *et al.* (2003); Blackburn *et al.* (2005); Leung *et al.* (2005); Blackburn & Lopez (2011). In these different settings, the analysis of the three-dimensional dynamics has faced different drawbacks. In the wake flows, the lack of enough control parameters does not allow the separated analysis of the different instability modes, that can be only observed at secondary bifurcations that become chaotic rapidly when increasing the control parameter. In other flows Leung *et al.* (2005); Blackburn & Lopez (2011) the dynamics are dominated by a variety of mixed modes with complicated spatio-temporal structures, even very near the onset of three-dimensional instabilities. The problem of a Newtonian fluid enclosed in a cylindrical cavity whose sidewall oscillates harmonically in the axial direction, solves the aforementioned problems.

As a consequence, the detailed analysis of the secondary bifurcations appearing in the neighborhood of the first codimension-two point C_1 has been possible for the first time. This bicritical point acts as the organising center of the dynamics at moderate frequency forcing values ($St \leq 17$) and a series of different families of solutions emerge from C_1. Since C_1 is the intersection of the marginal curves of the B_1 and B_2 mode, the appearance of a synchronous B_1-B_2 mixed mode through a synchronous bifurcation seems somehow predictable. Nevertheless, the emergence of two novel quasiperiodic states (B_1RW and bursts) is quite outstanding. The B_1RW solution comes from a pitchfork bifurcation of the B_1 mode that breaks K_β in the process. This solution is a rotating wave, similar to the MRW_1, but completely unrelated with the complex eigenvalues of a Neimark-Sacker bifurcation. The bursts enter the stage by means of a SNIC bifurcation of either the B_1 mode or the B_1-B_2 mixed modes. Solutions with a similar behaviour have been reported in systems with pure $1:2$ modal resonance (Mercader *et al.*, 2002; Nore *et al.*, 2003), but this is the first time in obtaining this kind of states in periodically forced systems.

Some other solutions, which after some reasoning suggest to be disconnected from C_1, have been found. The succesion of bifurcations from B_1 states towards a chaotic solution, passing through the quasiperiodic solution B_1QP, conveys the impression of a Ruelle-Takens-Newhouse route to chaos. All of these solutions seem to preserve the H symmetry, in contrast with the asymmetric B_1-B_2 mixed mode and asymmetric bursts. These states have nothing to do with the linear stability curves of B_1 and B_2 and may have the origin in the A_2 and MRW_1 branches. The asymmetric bursts come from a SNIC bifurcation of the asymmetric mixed modes. By means of increasing Re, these bursts eventually become chaotic.

In contrast with the annulus scenario (Blackburn & Lopez, 2011), a comprehensible transition to a series of chaotic solutions has been possible in a periodically forced cylin-

der. Hopefully the combination with the analysis of the remaining bicritical points, will complement the transition to chaos in wakes and periodically forced systems. Furthermore, the analysis of these complex bicritical points from a theoretical dynamical system perspective yet to addressed, and it would also shed light on the understanding of these complicated processes. All the bifurcations that have been detected are supercritical and there are some hysteresis regions caused by the disconnectedness of unrelated branches of solutions.

CHAPTER 5

NORMAL FORM ANALYSIS OF THE $1:2$ MODE INTERACTION

A normal form is a low-dimensional system with a polynomial expression that is able to describe the dynamics of a full non-linear system in the neighbourhood of a bifurcation. For example, the normal form for a mode B_m bifurcation (described in Appendix B) up to and including third order terms in A and the small bifurcation parameter, is

$$\mathcal{P}: \ A \mapsto A(1+\mu-a|A|^2), \tag{5.1}$$

where $\mu, a \in \mathbb{R}$. A and $\overline{A}$ are the amplitudes of the pair of eigenfunctions associated with the bifurcation, with eigenvalues $+1$. As the base state that bifurcates is a periodic solution, the normal form analysis is made on the Poincaré map $\mathcal{P}$ of the periodic solution, consisting in strobing the solutions with the forcing frequency. In fact, due to the spatio-temporal symmetry $\mathcal{H}$ of the base state (2.28), it is often convenient to analyse the normal form of $\mathcal{H}$, and then obtain the corresponding normal form of the Poincaré map by squaring $\mathcal{H}$: $\mathcal{P} = \mathcal{H}^2$ (Marques *et al.*, 2004). However, in the case of mode B bifurcations, including the codimension-two point analysed in the previous chapter, the space-time symmetry $\mathcal{H}$ acts as the identity on the bifurcating eigenvectors, and in this case there is no particular advantage on considering the normal form of $\mathcal{H}$, which is identical to the normal form of $\mathcal{P}$ (except for a factor two in some of the normal form coefficients). The action of the symmetries on A is

$$R_\alpha A = \mathrm{e}^{\mathrm{i}m\alpha}A, \qquad K_0 A = \overline{A}, \tag{5.2}$$

where the exponent m indicates that the bifurcating eigenfunctions have broken the $SO(2)$ symmetry, but are still invariant under rotations of $\alpha = 2\pi/m$, i.e. they correspond to a mode B_m.

In the codimension-two point studied in the previous chapter, the synchronous modes B_1 and B_2 bifurcate simultaneously. There is a pair of eigenfunctions associated with mode B_1, with eigenvalues $+1$, and amplitudes A and $\overline{A}$, and a pair of eigenfunctions associated with mode B_2, with eigenvalues $+1$, and amplitudes B and $\overline{B}$. The normal form for $\mathcal{P}$ is discussed in detail in Appendix B, and is given by

$$\mathcal{P}: \begin{cases} A \mapsto A(1+\mu+a_1|A|^2+b_1|B|^2)+\overline{A}B, \\ B \mapsto B(1+\nu+a_2|A|^2+b_2|B|^2)+\sigma A^2, \end{cases} \tag{5.3}$$

where the bifurcation parameters μ, ν and the coefficients a_i, b_i are all real. Close to the codimension-two point $\mu = \nu = 0$, the bifurcations corresponding to B_1 and B_2

are non-degenerate and supercritical, so we expect $a_1 < 0$ and $b_2 < 0$. Additional simplifications are possible in the cubic terms, where one of the a_i coefficients can be chosen arbitrarily (see the discussion on the hypernormal normal form in the Appendix B.1.1). The simplification will be postponed until the discussion of the interpolating Ordinary Differential Equation (ODE) in the next sections.

The normal form (5.3) for the Poincaré map could be analysed, but the analysis of an interpolating ODE is much simpler. In addition, this ODE has already been examined in some detail (see for example Porter & Knobloch, 2001, and references therein), while there is no much knowledge regarding the map normal form (5.3).

5.1 Interpolating ODE

Provided a map

$$x \to F(x, \alpha) = Lx + N(x, \alpha), \tag{5.4}$$

where L is a constant matrix and $N(x, \alpha)$ are non-linear terms (at least order two in x, but it can contain linear terms in the parameters α), we seek an ODE of the form

$$\dot{x} = G(x, \alpha) = \Lambda x + Y(x, \alpha), \tag{5.5}$$

such that the flow at $t = 1$ coincides with F up to a given order in (x, α): $\phi^1(x, \alpha) = F(x, \alpha) + O(k)$. The flow $\phi^t(x, \alpha)$ satisfies the equation (5.5) and the initial condition $\phi^0(x, \alpha) = x$. In order to compute $\phi^t(x, \alpha)$ as a power series in (x, α), a method based on Picard iterations, described in Kuznetsov *et al.* (2004); Marques *et al.* (2013), will be used.

Proposition 5.1.1 *The flow of* (5.5) $\phi^t(x, \alpha)$ *satisfies the integral equation*

$$\phi^t(x, \alpha) = e^{t\Lambda}x + \int_0^t e^{(t-\tau)\Lambda} Y\big(\phi^\tau(x, \alpha), \alpha\big) d\tau \tag{5.6}$$

As Y is non-linear, the terms in ϕ^t of order k, ϕ^t_k, are given by (5.6) in terms of lower order terms. Equation (5.6) and $\phi^1(x, \alpha) = F(x, \alpha)$ must be solved simultaneously order by order in powers of x and α. At order one, $\phi^t_1(x, \alpha) = e^{t\Lambda}x$ and $\phi^1_1 = e^{\Lambda}x = F_1 = Lx$. The equation $e^{\Lambda} = L$ is obtained. This equation does not have a solution in general; for example if L is real with some negative eigenvalues, then it does not exist a real Λ satisfying it. One must resort in these cases to more convoluted strategies, like looking for iterates of F (see Kuznetsov, 2004, Chapter 9), or replacing F by MF, with an

appropriate constant matrix (Kuznetsov *et al.*, 2004). In the current problem (5.3), as L is the identity matrix, the solution is $\Lambda = 0$. Then (5.6) reduces to

$$\phi^t(x,\alpha) = x + \int_0^t Y\big(\phi^\tau(x,\alpha),\alpha\big)d\tau. \tag{5.7}$$

The iterative procedure to solve this equation is given by:

Proposition 5.1.2 *The non-linear terms in $Y(x,\alpha)$ and $\phi^t(x,\alpha)$ can be computed iteratively for $k \geq 2$ as:*

$$H_k(x,\alpha,t) = \int_0^t \Big(Y_{(k-1)}\big(\phi^\tau_{(k-1)}(x,\alpha),\alpha\big)\Big)_k d\tau, \tag{5.8}$$

$$Y_k(x,\alpha) = N_k(x,\alpha) - H_k(x,\alpha,1), \tag{5.9}$$

$$\phi^t_k(x,\alpha) = tY_k(x,\alpha) + H_k(x,\alpha,t). \tag{5.10}$$

where the subscript (m) indicates all the terms up to and including order m.

Note that the subscript m is here a multi-index referring to the order of x and α. In our problem (5.3) there are three non-zero terms in N:

$$N_{1,1} = \begin{pmatrix}\mu A\\ \nu B\end{pmatrix}, \qquad N_{2,0} = \begin{pmatrix}\overline{A}B\\ \sigma A^2\end{pmatrix}, \qquad N_{3,0} = \begin{pmatrix}a_1 A|A|^2 + b_1 A|B|^2\\ a_2 B|A|^2 + b_2 B|B|^2\end{pmatrix}, \tag{5.11}$$

where the subscript m,n refers to terms of order $x^m\alpha^n$, being $x = (A,B)$ and $\alpha = (\mu,\nu)$. The lowest order terms in ϕ are trivial:

$$\phi^t_{0,0} = 0, \qquad \phi^t_{1,0} = x, \qquad \phi^t_{0,1} = 0. \tag{5.12}$$

The remaining terms are computed order by order:

$$N_{1,1} = \int_0^1 Y(\phi^t,\alpha)_{1,1}dt = \int_0^1 Y_{1,1}(\phi^t_{1,0},\alpha)dt = Y_{1,1}(x,\alpha) = \begin{pmatrix}\mu A\\ \nu B\end{pmatrix}, \tag{5.13a}$$

$$N_{2,0} = \int_0^1 Y(\phi^t,\alpha)_{2,0}dt = \int_0^1 Y_{2,0}(\phi^t_{1,0},\alpha)dt = Y_{2,0}(x,\alpha) = \begin{pmatrix}\overline{A}B\\ \sigma A^2\end{pmatrix}, \tag{5.13b}$$

$$\phi^t_{2,0} = \int_0^t Y(\phi^t,\alpha)_{2,0}dt = tY_{2,0}(x,\alpha) = \begin{pmatrix}t\overline{A}B\\ t\sigma A^2\end{pmatrix}, \tag{5.13c}$$

$$\begin{aligned} N_{3,0} &= \int_0^1 Y(\phi^t,\alpha)_{3,0}dt = \int_0^1 \Big(Y_{3,0}(x,\alpha) + Y_{2,0}(x+\phi^t_{2,0}(x,\alpha),\alpha)_{3,0}\Big)dt \\ &= Y_{3,0} + \int_0^1 \begin{pmatrix}(\overline{A}+t\overline{A\overline{B}})(B+t\sigma A^2)\\ \sigma(A+t\overline{A}B)^2)\end{pmatrix}dt = Y_{3,0} + \begin{pmatrix}\frac{1}{2}\sigma A|A|^2 + \frac{1}{2}A|B|^2\\ \sigma B|A|^2\end{pmatrix} \\ &\Rightarrow \quad Y_{3,0} = \begin{pmatrix}(a_1 - \frac{1}{2}\sigma)A|A|^2 + (b_1 - \frac{1}{2})A|B|^2\\ (a_2-\sigma)B|A|^2 + b_2 B|B|^2\end{pmatrix}, \end{aligned} \tag{5.13d}$$

and the resulting interpolating ODE is

$$\dot{A} = A\left(\mu + \left(a_1 - \frac{1}{2}\sigma\right)|A|^2 + \left(b_1 - \frac{1}{2}\right)|B|^2\right) + \overline{A}B, \tag{5.14a}$$

$$\dot{B} = B\left(\nu + (a_2 - \sigma)|A|^2 + b_2|B|^2\right) + \sigma A^2. \tag{5.14b}$$

Now the desired simplification of the cubic terms can be performed. By means of choosing $a_2 = \sigma$, the term $B|A|^2$ term in the second equation is canceled out. We have finally obtained the sought ODE approximating the map up to third order:

$$\dot{A} = A(\mu - a|A|^2 - b|B|^2) + \overline{A}B, \tag{5.15a}$$

$$\dot{B} = B(\nu - c|B|^2) + \sigma A^2, \tag{5.15b}$$

where $a = \frac{1}{2}\sigma - a_1$, $b = \frac{1}{2} - b_1$ and $c = -b_2$.

It is convenient to introduce the modules and phases $A = r\mathrm{e}^{\mathrm{i}\phi}$, $B = \rho\mathrm{e}^{\mathrm{i}\psi}$, and the mixed phase $\theta = 2\phi - \psi$. The dynamics of (r, ρ, θ) decouple from the other phases and, in terms of these variables the three-dimensional normal form of the ODE is achieved

$$\dot{r} = r(\mu - ar^2 - b\rho^2) + r\rho\cos\theta, \tag{5.16a}$$

$$\dot{\rho} = \rho(\nu - c\rho^2) + \sigma r^2\cos\theta, \tag{5.16b}$$

$$\dot{\theta} = -(2\rho + \sigma r^2/\rho)\sin\theta. \tag{5.16c}$$

For the individual phases we obtain

$$\dot{\phi} = -\rho\sin\theta, \qquad \dot{\psi} = \frac{\sigma r^2}{\rho}\sin\theta. \tag{5.17}$$

The action of the symmetries on these variables is

$$R_\alpha(r, \rho, \theta, \phi, \psi) = (r, \rho, \theta, \phi + \alpha, \psi + 2\alpha), \quad K_0(r, \rho, \theta, \phi, \psi) = (r, \rho, -\theta, -\phi, -\psi). \tag{5.18}$$

The three-dimensional normal form (5.16) is $SO(2)$ invariant, while the reflection K_0 changes the sign of all phases. The presence of $1/\rho$ in $\dot{\theta}$ results in discontinuities in θ due to the singularity of the polar coordinates at the origin. This can be avoided by introducing two auxiliary Cartesian variables $x = \rho\cos\theta$ and $y = \rho\sin\theta$, resulting in the three-dimensional normal form

$$\dot{r} = r\big(\mu + x - ar^2 - b(x^2 + y^2)\big), \tag{5.19a}$$

$$\dot{x} = x\big(\nu - c(x^2 + y^2)\big) + \sigma r^2 + 2y^2, \tag{5.19b}$$

$$\dot{y} = y\big(\nu - 2x - c(x^2 + y^2)\big). \tag{5.19c}$$

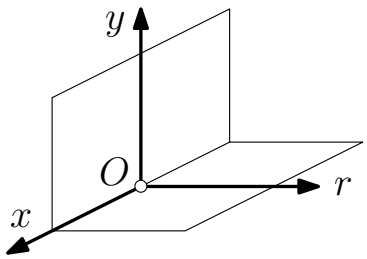

Figure 5.1: Schematic of the phase space of the reduced three-dimensional system (5.19)

The action of the symmetries on (r, x, y) is

$$R_\alpha(r, x, y) = (r, x, y), \qquad K_0(r, x, y) = (r, x, -y), \tag{5.20}$$

and we observe that the solutions with $y = 0$ are reflection symmetric. The evolution of the phases in terms of (r, x, y) is

$$\dot{\phi} = -y, \qquad \dot{\psi} = \frac{\sigma r^2 y}{x^2 + y^2}, \qquad \dot{\theta} = -\Big(2 + \frac{\sigma r^2}{x^2 + y^2}\Big) y. \tag{5.21}$$

The coordinate planes $r = 0$ and $y = 0$, and their intersection the x axis, are all invariant manifolds of the ODE (5.19). Moreover $r \geq 0$, and the symmetry K_0 allow us to study only the case $y \geq 0$: given a solution $(r(t), x(t), y(t))$, $(r(t), x(t), -y(t))$ is also a solution, so the phase portrait for $y \leq 0$ is the reflection image of $y \geq 0$. Therefore it is enough to analyse the ODE (5.19) for $(r, x, y) \in [0, +\infty) \times \mathbb{R} \times [0, +\infty)$, which means that $\theta \in [0, \pi]$. The corresponding phase space is shown in Figure 5.1, that also exhibits the fixed point O at the origin, corresponding to the base state in our problem; (ρ, θ) are the polar coordinates on the invariant plane (x, y).

Although there is not a complete analysis of the different scenarios that can take place in the ODE normal form (5.19), there has been a number of detailed studies focusing on specific scenarios, starting with Dangelmayr (1986) and continuing with a variety of studies focusing in dynamical systems aspects related with heteroclinic dynamics and its applications to specific problems in fluid dynamics (Proctor & Jones, 1988; Armbruster *et al.*, 1988; Echebarría *et al.*, 1997; Porter & Knobloch, 2001; Mercader *et al.*, 2001, 2002; Nore *et al.*, 2003). We will follow the same procedure in the sequel, looking for scenarios that closely resemble the dynamics unravelled in the previous chapter around the codimension-two point B_1-B_2. The starting point is the analysis of the fixed points of (5.19) and their bifurcations, following the references already mentioned, and adapting them to the problem under consideration.

5.2 Fixed points and their stability

Let us start computing the fixed points on the invariant manifolds. The dynamical system restricted to the x axis ($r = y = 0$) is

$$\dot{x} = x(\nu - cx^2), \tag{5.22}$$

which is the normal form of a pitchfork bifurcation. There are three fixed points, $x = 0$ that exist for all ν values, and the pair $x = \pm\sqrt{\nu/c}$, existing for $\nu c \geq 0$. They are fixed points of the four-dimensional ODE (5.15) and also of the original map (5.3), because all the phases are constant (5.21):

$$O: \ (A, B) = (0, 0), \qquad P_\psi: \ (A, B) = (0, \sqrt{\nu/c}\, \mathrm{e}^{\mathrm{i}\psi}). \tag{5.23}$$

The first one, O, is the base state, and P_ψ form a circle of pure B_2 modes in our original fluid problem. This circle of solutions reduces to two solutions in the three-dimensional ODE (5.19),

$$P_+: \ (r, x, y) = (0, \sqrt{\nu/c}, 0), \ \theta = 0, \quad P_-: \ (r, x, y) = (0, -\sqrt{\nu/c}, 0), \ \theta = \pi. \tag{5.24}$$

At $\nu = 0$ the base state O undergoes a pitchfork bifurcation (a pitchfork of revolution of the four-dimensional ODE or map) resulting in the $P_\pm$ new fixed points. The bifurcation line $\nu = 0$ where the mode two solutions are born will be called M_2. As the bifurcation is supercritical in our fluid problem, from now on it will be considered that $c > 0$.

The Jacobian matrix of the ODE (5.19) is

$$J = \begin{pmatrix} \mu + x - 3ar^2 - b(x^2 + y^2) & r(1 - 2bx) & -2bry \\ 2\sigma r & \nu - 3cx^2 - cy^2 & -2cxy + 4y \\ 0 & -2y(1 + cx) & \nu - 2x - cx^2 - 3cy^2 \end{pmatrix}. \tag{5.25}$$

The Jacobian is diagonal at the fixed points O and $P_\pm$, and the diagonal elements are their eigenvalues:

$$J_O = \mathrm{diag}(\mu, \nu, \nu), \qquad J_{P_\pm} = \Big(\mu \pm \sqrt{\frac{\nu}{c}} - \frac{b\nu}{c}, -2\nu, \mp 2\sqrt{\frac{\nu}{c}}\Big). \tag{5.26}$$

The fixed point O is stable for $\mu < 0$ and $\nu < 0$, and unstable in the remaining parameter space. Moreover, O undergoes bifurcations along the straight lines $\mu = 0$ and $\nu = 0$, where some of the eigenvalues go through zero. $P_\pm$ are born from O on the straight line $\nu = 0$, and exist for $\nu > 0$. Very close to the bifurcation line $\nu = 0$, P_- is always unstable, while P_+ is stable for $\mu < 0$ and unstable for $\mu > 0$.

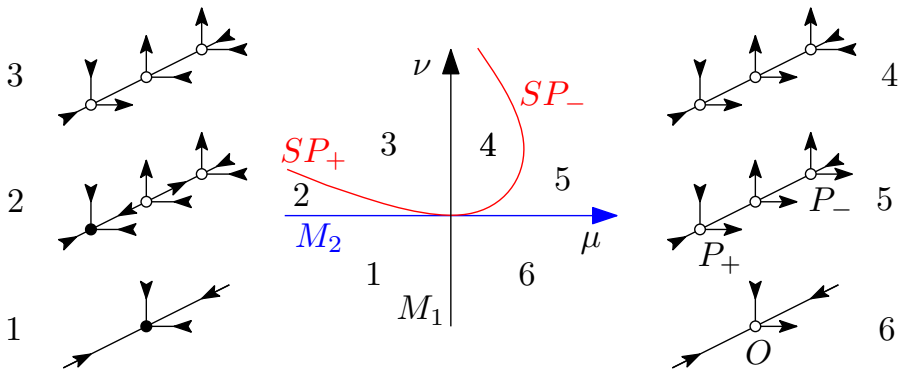

Figure 5.2: Schematic of the bifurcations of the fixed points O and $P_\pm$ on the x axis ($r = y = 0$). There are four bifurcation curves: M_1 where O loses stability to a mode one solution; M_2 where O undergoes a pitchfork bifurcation to a pair of mode two solutions $P_\pm$; and $SP_\pm$ where $P_\pm$ undergo secondary bifurcations.

$P_\pm$ undergo additional bifurcations on the parabola $\mu \pm \sqrt{\nu/c} - b\nu/c$. A convenient parametrisation of the parabola is

$$SP: \ (\mu, \nu) = (bt^2 - t, ct^2), \ t \in \mathbb{R}. \qquad \text{Axis direction: } (b, c). \tag{5.27}$$

$$\text{Vertex: } t_V = \frac{b}{2(b^2 + c^2)}, \quad (\mu, \nu)_V = \frac{b}{4(b^2 + c^2)^2}(-b^2 - 2c^2, bc). \tag{5.28}$$

As $\mu \pm \sqrt{\nu/c} - b\nu/c = \pm|t| - t$, P_+ undergoes a bifurcation when crossing SP for $t > 0$ (SP_+), i.e. for $\mu < 0$ close to the origin, becoming unstable; and P_- undergoes a bifurcation when crossing SP for $t < 0$ (SP_-), i.e. for $\mu > 0$ close to the origin, but continues being unstable. A bifurcation diagram including the bifurcations found until now is shown in Figure 5.2. The SP curve plotted corresponds to the case $b < 0$; for $b > 0$ the curve is obtained by reflection along the vertical axis.

5.2.1 Invariant plane $r = 0$

Let us look for fixed points of (5.19), assuming $r = 0$ and $y > 0$:

$$\left.\begin{array}{c} x\big(\nu - c(x^2 + y^2)\big) + 2y^2 = 0 \\ \nu - 2x - c(x^2 + y^2) = 0 \end{array}\right\} \quad \Rightarrow \quad \nu - c(x^2 + y^2) = 2x, \quad 2x^2 + 2y^2 = 0. \tag{5.29}$$

The only solution is the base state O and there are no additional fixed points on the invariant plane $r = 0$. However, the ODE for the radial coordinate ρ reads (5.16)

$$\dot{\rho} = \rho(\nu - c\rho^2) \tag{5.30}$$

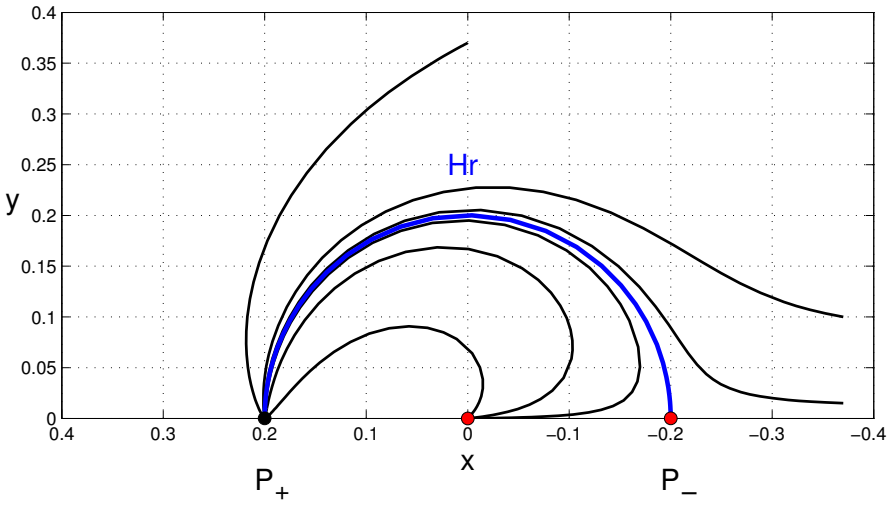

Figure 5.3: Heteroclinic orbit Hr in blue, on the plane (x, y).

which is again the normal form of a pitchfork bifurcation, and results in a stable fixed point $\rho = \sqrt{\nu/c}$ for $\nu > 0$. This fixed point corresponds to an attracting heteroclinic orbit Hr on the (x, y) plane starting from P_- at $t = -\infty$ and ending at P_+ for $t = +\infty$. Figure 5.3 shows the orbit Hr in blue, along with some additional orbits on the (x, y) plane. This orbit exists for all $\nu > 0$ parameter values, and the explicit time dependence is easy to compute:

$$Hr: \ (x(t), y(t)) = \rho\Big(\tanh(2\rho t), \frac{1}{\cosh(2\rho t)}\Big), \qquad \rho = \sqrt{\nu/c}. \tag{5.31}$$

The attracting or repelling character of this orbit outside the invariant plane in the $r = 0$ direction is given by the eigenvalue λ of the $\dot{r}$ equation of (5.19) at the different points of the heteroclinic orbit, parametrised by θ:

$$\mu - \sqrt{\nu/c} - b\nu/c \leq \lambda = \mu + \cos\theta\sqrt{\nu/c} - b\nu/c \leq \mu + \sqrt{\nu/c} - b\nu/c. \tag{5.32}$$

Hr is attracting below SP_+ and repelling below SP_-. Inside the parabola SP, the heteroclinic orbit is attracting close to P_- and repelling close to P_+. Notice that the solutions on the plane $r = 0$ have broken the reflection symmetry K_0, as long as $y \neq 0$. Therefore, the orbit Hr joins two symmetric solutions $P_\pm$ along a path of non-symmetric solutions. The phase dynamics associated with Hr is (5.21) $\dot{\phi} = -y$, $\dot{\psi} = 0$ and $\dot{\theta} = -2y$; in terms of the four-dimensional system (A, B), we have $A = 0$ and $B = \rho e^{i\psi}$ constant, so the whole heteroclinic orbit Hr reduces to a constant B_2 mode. The heteroclinic orbit is an artifact of the singularity of the polar coordinates (ρ, θ). But the heteroclinic orbit Hr becomes significant for solutions with $r \neq 0$ close to Hr, because then the small A

contribution (the mode B_1) undergoes a change of phase of $\pi/2$ (half the phase change of θ that goes from π to 0) when it is close to the heteroclinic orbit Hr. This is the origin of the successive changes in $\pi/2$ along the bursts shown in Figures 4.6 and 4.7. The $\pi/2$ rotation of Fourier mode one (A) while Fourier mode two (B) remains constant can be observed in the first row of Figure 4.9.

5.2.2 Invariant plane $y = 0$

On the invariant plane $y = 0$, and assuming $r > 0$, the fixed points satisfy

$$\left.\begin{array}{r} \mu + x - ar^2 - bx^2 = 0 \\ x(\nu - cx^2) + \sigma r^2 = 0 \end{array}\right\} \quad \Rightarrow \quad ar^2 = \sigma a x(cx^2 - \nu) = \mu + x - bx^2. \tag{5.33}$$

The cubic equation for x, considering $\mu = 0$, has the root $x = 0$ (so $r = 0$), and the other roots (real or complex) are finite, away from the domain of validity of the normal form analysis, that assumes small values of (r, x, y). Therefore, there is another fixed point Q on the invariant plane $y = 0$ close to the origin. It is convenient to parametrise the fixed point with (x, ν) instead of (μ, ν):

$$Q: \ (r, x, y) = (\sqrt{\sigma x(cx^2 - \nu)}, x, 0), \quad \mu = x\big(\sigma a(cx^2 - \nu) - 1 + bx\big), \tag{5.34}$$

defined for (x, ν) values that fulfill $\sigma x(cx^2 - \nu) \geq 0$. For $x = 0$ ($\mu = 0$), $Q = O$, and for $x = \pm\sqrt{\nu/c}$ ($SP_\pm$), $Q = P_\pm$. Consequently, Q bifurcates from the already found fixed points O along $\mu = 0$ and from $P_\pm$ along $SP_\pm$. Q is a fixed point of the four-dimensional ODE (5.15) and also of the original map (5.3), because all the phases are constant (5.21):

$$Q_\phi: \ (A, B) = (\sqrt{\sigma x(cx^2 - \nu)}\mathrm{e}^{\mathrm{i}\phi}, x\mathrm{e}^{2\mathrm{i}\phi}). \tag{5.35}$$

In the four-dimensional problem, it is another pitchfork of revolution of the base state O, that in the three-dimensional ODE (5.19) reduces to a single point. This pitchfork of revolution happens on the line M_1 ($\mu = 0$), and in the fluid problem of the previous chapters corresponds to the B_1 mode. All the fixed points that have been found until the moment (O, $P_\pm$ and Q) are reflection symmetric.

The regions where Q exists ($\sigma x(cx^2 - \nu) \geq 0$) are bounded by the bifurcation lines $\mu = 0$ and SP. Close to the origin in parameter space (μ, ν), $\mathrm{sign}(x) = \mathrm{sign}(\mu)$, and we are supposing also $c > 0$. Therefore, for $\nu < 0$, Q exists iff $\sigma x > 0$, i.e. when $\sigma\mu > 0$; and inside the parabola SP, $cx^2 - \nu \geq 0$, so Q exists iff $\sigma\mu > 0$. Figure 5.4 shows the regions of existence of Q for $\sigma = \pm 1$. As in our problem the bifurcation $O \to Q$ for

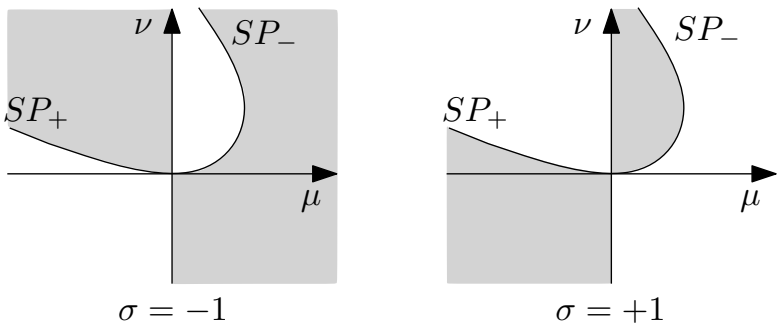

Figure 5.4: Regions of existence of the Q solution in grey, for the two values of σ.

$\nu < 0$ is supercritical, i.e. Q exists for $\mu > 0$, from now on $\sigma = -1$ will be supposed. There are two disconnected regions where Q exists. In the region originating near $\mu = 0$ and $\nu < 0$, $|A| = r = \sqrt{x\nu}$, $|B| = |x| \ll |A|$ close to bifurcation; thus, in this region we have a mode one ($|A|$) with a small contribution of mode two ($|B|$). This is what we have called mode B_1 in the fluid problem. In the region $\mu < 0$ and $\nu > 0$, close to the SP_+ line, we have $|A| = r \to 0$ approaching SP_+, while $|B| = |x|$ is finite, so Q is a mode two with a small contribution of mode one, a B_1-B_2 mixed mode, bifurcating from B_2.

The Jacobian matrix at Q is

$$J = \begin{pmatrix} -2ar^2 & r(1-2bx) & 0 \\ -2r & \nu - 3cx^2 & 0 \\ 0 & 0 & \nu - 2x - cx^2 \end{pmatrix}, \qquad r = \sqrt{x(\nu - cx^2)}. \tag{5.36}$$

The eigenvalues of Q are $\lambda_3 = \nu - 2x - cx^2$, and the roots of $\lambda^2 - 2p\lambda + q = 0$,

$$\lambda_\pm = p \pm \sqrt{p^2 - q}, \quad 2p = \nu - 2ar^2 - 3cx^2, \quad q = 2r^2\big(1 - 2bx + a(\nu - 3cx^2)\big). \tag{5.37}$$

The different bifurcations are:

1) $\lambda_3 = 0$, along the parabola

$$SBD: \ \nu = 2x + cx^2, \quad \mu = -x\big(1 - (2a+b)x\big), \quad r = \sqrt{2}|x|. \tag{5.38}$$

The other eigenvalues, at leading order in x are:

$$p = x + O(x^2), \quad q = 4x^2 + O(x^3), \quad \lambda_\pm = x(1 - \sqrt{3}\mathrm{i}) + O(x^2), \tag{5.39}$$

so the eigenvalues are complex and in the corresponding subspace, Q is stable for $x < 0$ and unstable for $x > 0$. As the eigenvector corresponding to λ_3 points in the y direction,

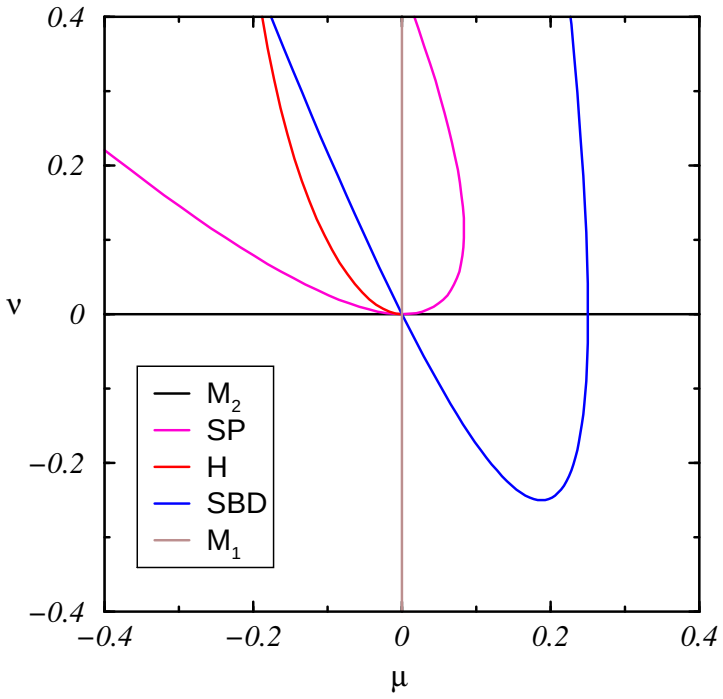

Figure 5.5: Bifurcation curves of the fixed points in the 3D system, for $a = 1$, $b = -3$ and $c = 4$.

this is a reflection-symmetry breaking bifurcation, and the bifurcated state moves away from the invariant planes.

2) Real bifurcation for $q = 0$, where one of the $\lambda_\pm$ is zero. The two cases $x = 0$, where Q bifurcates from O along $\mu = 0$, and $\nu = cx^2$, corresponding to Q bifurcating from $P_\pm$ along $SP_\pm$, have already been discussed. These bifurcations take place inside the invariant plane $y = 0$ and preserve the reflection symmetry.

3) Hopf bifurcation for $p = 0$, $q > 0$. From $p = 0$ and (5.34) we can parametrise the bifurcation curve in parameter space with x,

$$H: \ (\mu, \nu) = \frac{x}{1 - 2ax}\Big(cx(3 - 2ax), -1 + (b + 2a)x + 2a(c - b)x^2\Big), \tag{5.40}$$

and compute r and q:

$$r^2 = \frac{2cx^3}{1 - 2ax}, \quad q = 2r^2(1 - 2bx + 2a^2r^2). \tag{5.41}$$

The Hopf frequency is $\sqrt{q} = \sqrt{2}r = 2\sqrt{cx^3}$ at leading order. The Hopf bifurcation takes place into the invariant subspace (r, x) (5.36), so the resulting periodic solution So is contained into this plane, and it is reflection-symmetric.

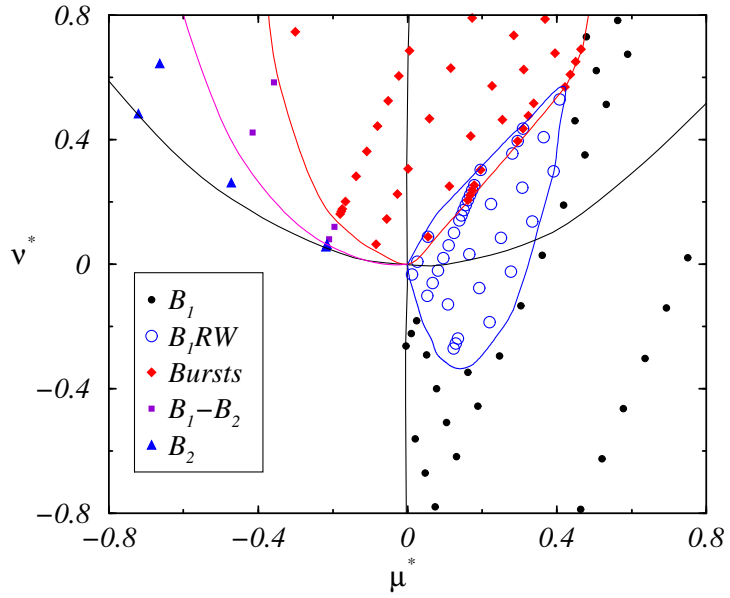

Figure 5.6: Families of bifurcated states near the bicritical point C_1. They are the same as in Figure 4.1, but the axis have been modified according to the affine transformation (5.42).

Figure 5.5 shows the bifurcation curves of the fixed points on the invariant plane $y = 0$, for the specified values of the parameters a, b and c. In order to compare the different regions in parameter space with the regions found in the fluid dynamics problem shown in Figure 4.1, we have made an affine transformation of this figure so that the bifurcation curves from the base state to the bifurcated states B_1 and B_2 have horizontal and vertical tangents at the codimension-two point, and moreover that the base state is stable in the third quadrant. The affine transformation is described by

$$\left.\begin{aligned} \mu^* &= -0.8400(St - St_c) + 0.05726(Re - Re_c) \\ \nu^* &= -0.5255(St - St_c) + 0.1617(Re - Re_c) \end{aligned}\right\}, \tag{5.42}$$

and the resulting regime diagram is shown in Figure 5.6. We should perform a non-linear coordinate transformation between (μ^*, ν^*) and (μ, ν) so that the bifurcation lines from the base state to B_1 and B_2 become the coordinate axis. However, the resemblance between Figures 5.6 and 5.5 is good enough for qualitative comparison. The normal form analysis captures up to now five of the bifurcation curves that have been obtained by direct numerical simulation of the Navier-Stokes equations. There remains to analyse the bifurcations of the drift solutions Dr and additional global bifurcations related to the bursting dynamics.

5.2.3 Fixed points outside the invariant planes

The exploration of the possible fixed points with $r > 0$ and $y > 0$ still remains:

$$\left.\begin{array}{c} \mu + x - ar^2 - b(x^2+y^2) = 0, \\ x\big(\nu - c(x^2+y^2)\big) + \sigma r^2 + 2y^2 = 0 \\ \nu - 2x - c(x^2+y^2) = 0 \end{array}\right\} \Rightarrow\ \nu - c(x^2+y^2) = 2x,\ 2x^2+2y^2 = -\sigma r^2, \quad (5.43)$$

so new fixed points are only possible when $\sigma = -1$. The new fixed point lies on a cone with vertex at the origin. It is obtained

$$Dr:\ \begin{cases} r = \sqrt{\dfrac{4\mu+2\nu}{4a+2b+c}}, \qquad x = \dfrac{(2a+b)\nu - c\mu}{4a+2b+c}, \\ y = \dfrac{1}{|4a+2b+c|}\sqrt{(4a+2b+c)(2\mu+\nu) - ((2a+b)\nu - c\mu)^2}. \end{cases} \quad (5.44)$$

From (5.21) we arrive at $\dot\theta = 0$ because $r^2 = 2(x^2+y^2)$; however, $\dot\phi = -y$ and $\dot\psi = -2y$, so it is a periodic solution of the 4D ODE, and a solution on an invariant circle of the 4D map. The frequency of the periodic solution is y, and for $y = 0$ it is zero, an infinite period bifurcation. When $y = 0$ the fixed point Dr coincides with Q along the parabola SBD (5.38). From the point of view of the 4D ODE (5.15), this is an infinite-period bifurcation breaking the reflection symmetry; the fixed points on the $SO(2)$ orbit (5.35) start a slow drift with frequency y along the group orbit, and at the bifurcation point the drift frequency is zero. As the reflection symmetry K_0 is broken, a couple of reflection-symmetry-related solutions, y and $-y$, drift in opposite directions. In summary, the fixed points Q (belonging to an $SO(2)$ orbit) undergo a symmetry-breaking reflection bifurcation resulting in a drifting periodic solution Dr along the bifurcation curve SBD.

Additional bifurcations of Dr can be analysed by looking at the eigenvalues of the Jacobian matrix of Dr,

$$J = \begin{pmatrix} -4a(x^2+y^2) & r(1-2bx) & -2bry \\ -2r & 2x(1-cx) & 2y(2-cx) \\ 0 & -2y(1+cx) & -2cy^2 \end{pmatrix}, \quad (5.45)$$

with r, x and y given by (5.44). The result is a cubic polynomial with coefficients that are very complicated functions of μ and ν, so any further analysis must be performed numerically.

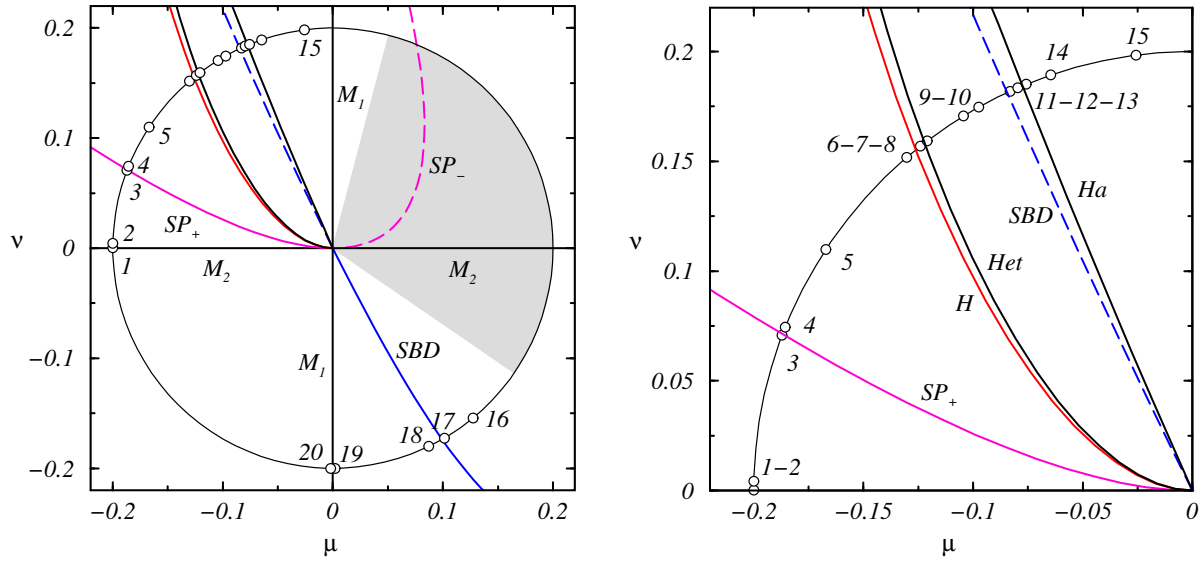

Figure 5.7: Bifurcation curves found in the 3D system, for $a = 1$, $b = -3$ and $c = 4$.

5.3 A numerical exploration of the 3D ODE

In order to analyse the sequence of bifurcations around the bicritical point, we have computed numerically the solution of the three-dimensional ODE (5.19) for the same parameter values as in Figure 5.5, $a = 1$, $b = -3$ and $c = 4$, and for bifurcation parameters (μ, ν) varying along a circumference of radius 0.2 around the origin that is is depicted in Figure 5.7. The same point $(r_0, x_0, y_0) = (0.1, 0.1, 0.1)$ has been taken as initial condition and is indicated in the subsequent phase portraits as a white disk, while the final point is indicated by a red disk. We have plotted the phase portraits corresponding to all the bifurcations that have been found; the symbols on the circumference in Figure 5.7 correspond to the different phase portraits considered.

Figure 5.8 shows the first two bifurcations obtained when increasing ν for $\mu < 0$. In Figure 5.8(a) and (b) we observe the bifurcation from the base state to mode two, $O \to P_+$, when crossing the M_2 bifurcation line $\nu = 0$, corresponding to the states labeled 1 and 2 in Figure 5.7. This bifurcation is closely followed by the bifurcation from the mode two solution to a mixed mode, $P_+ \to Q$, along the line SP_+, corresponding to the states labeled 3 and 4 in Figure 5.7. This two bifurcations are present in the fluid problem, and are the bifurcations from the base state to the B_2 pure mode and then to the mixed mode B_1-B_2. In this and subsequent plots we have drawn in blue the trajectory of the 3D ODE, and we have also portrayed its projections on the invariant planes $y = 0$ and $r = 0$ in green and red, respectively, in order to better appreciate the

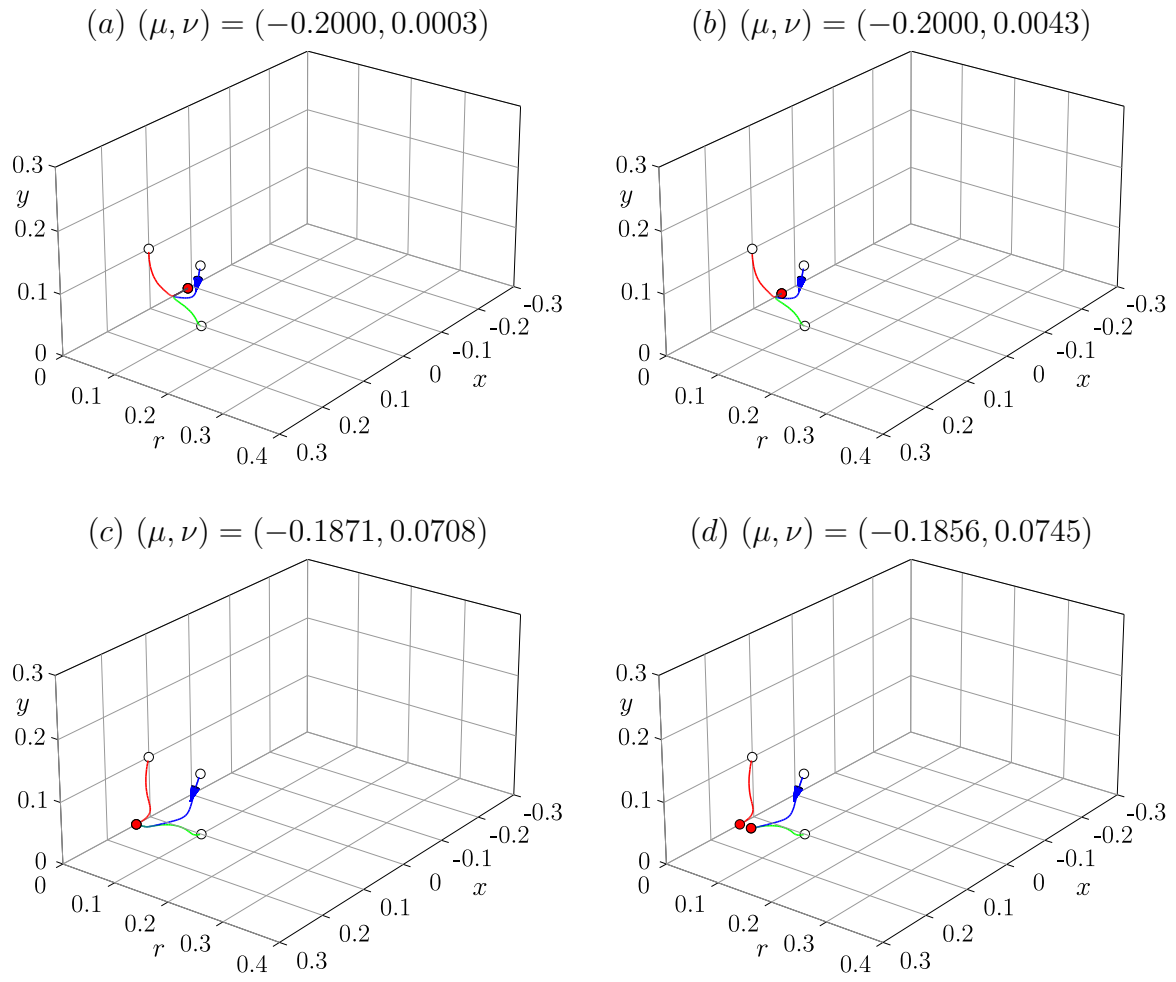

Figure 5.8: Phase portraits of the 3D system, for $a = 1$, $b = -3$ and $c = 4$. (a) and (b) shows the bifurcation $O \to P_+$ along the M_2 bifurcation line (states labeled 1 and 2 in Figure 5.7). (c) and (d) shows the bifurcation $P_+ \to Q$ along SP_+ (states 3 and 4 in Figure 5.7.

three-dimensional shape of the trajectory.

Figure 5.9 exhibits how the stable node Q becomes a stable focus (Figure 5.9(a) and (b), corresponding to the states 5 and 6 in Figure 5.7), that when crossing the bifurcation line H undergoes a Hopf bifurcation resulting in a periodic orbit, $Q \to So$, lying on the invariant plane $y = 0$ so that is is reflection-symmetric. So is shown in Figure 5.9(c), corresponding to the state 7 in Figure 5.7. This periodic orbit undergoes a heteroclinic collision with the unstable saddles P_+ and O. Since, O is connected with P_- with a heteroclinic orbit on the invariant line $r = y = 0$, and P_- is also connected with P_+ along the heteroclinic semicircle Hr discussed in Section §5.2.1, a complex heteroclinic cycle is formed involving the connection $P_+ \to O$ in the $y = 0$ invariant plane, the connection

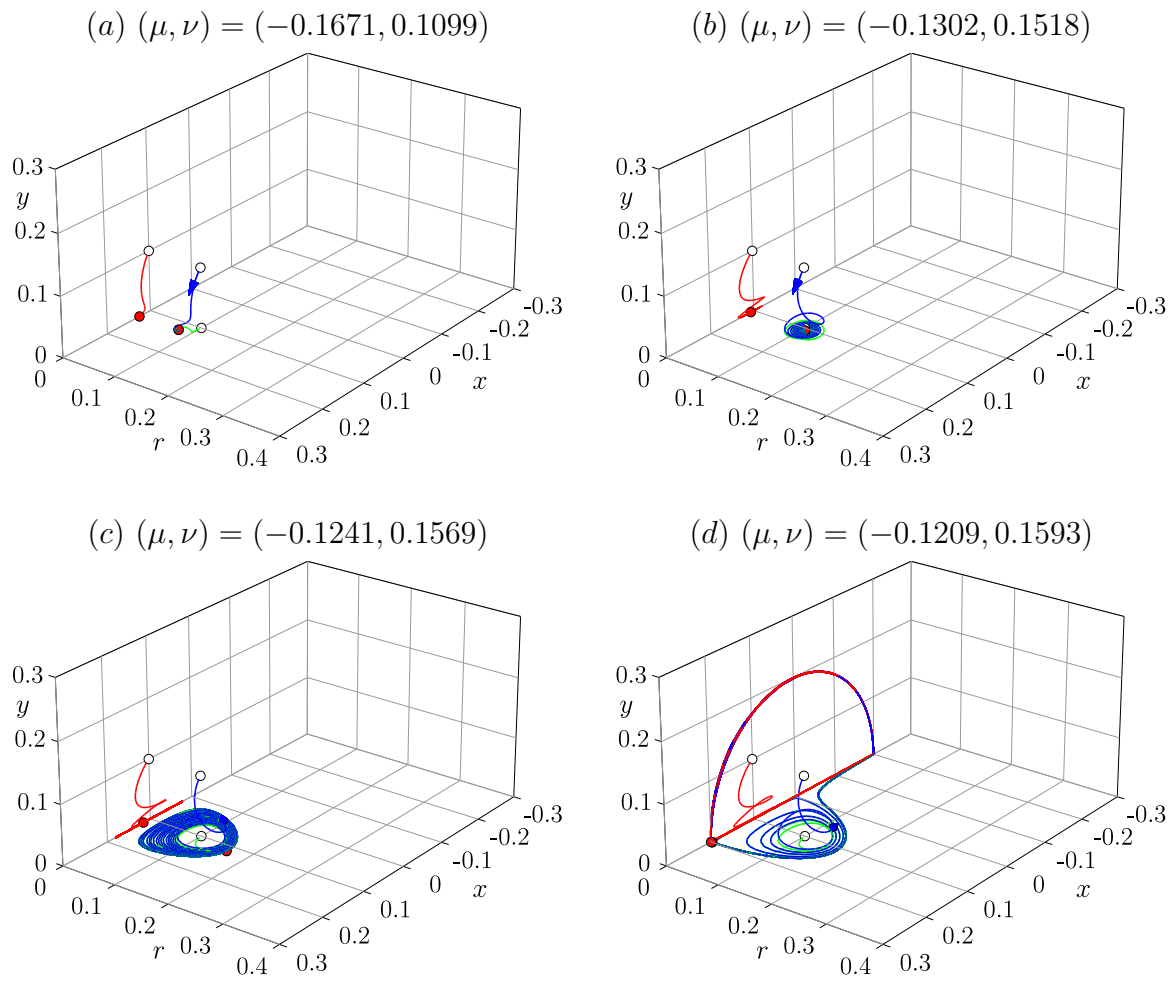

Figure 5.9: Phase portraits of the 3D system, for $a = 1$, $b = -3$ and $c = 4$. (b) and (c) shows the Hopf bifurcation $Q \to So$ along the curve H (states 6 and 7 in Figure 5.7). (d) shows the heteroclinic cycle $P_+ \to O \to P_- \to P_+$ formed when So collides with P_+ and O.

$O \to P_-$ on the invariant line $r = y = 0$, and the connection $P_- \to P_+$ in the $r = 0$ invariant plane. This heteroclinic cycle is illustrated in Figure 5.9(d), corresponding to the state 8 in Figure 5.7. This global bifurcation happens very close to the Hopf curve H, resulting in the bursting states observed in the numerical simulations. After the heteroclinic connection is broken, a large periodic orbit LAo (Large Asymmetric orbit) closely following the heteroclinic cycle is formed. As has been explained in Section §5.2.1, the proximity to the heteroclinic semicircle Hr is responsible for the jump in $\pi/2$ of the phase of the mode A amplitude. Therefore, in the four-dimensional system the orbit LAo is traversed four times before recovering the original phase. This orbit has broken the reflection symmetry because $y \neq 0$. As the Hopf bifurcation and the heteroclinic collision take place in a very small parameter range, we have not been able to observe

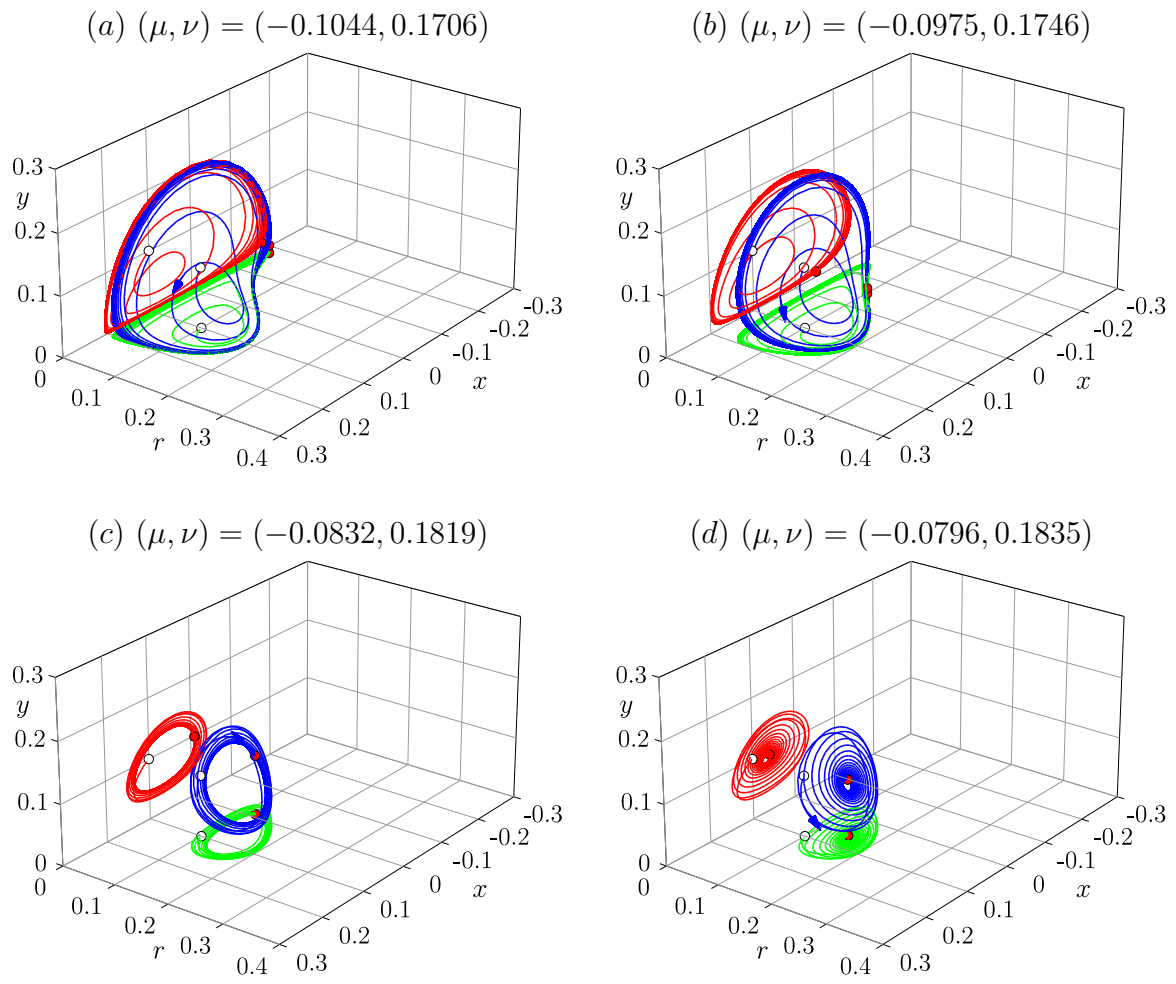

Figure 5.10: Phase portraits of the 3D system, for $a = 1$, $b = -3$ and $c = 4$. The phase portraits show the shrinking of the large asymmetric periodic orbit LAo formed in the heteroclinic collision described in Figure 5.9(d).

the periodic orbit in the full Navier-Stokes direct numerical simulations. In fact, due to the proximity to the codimension-two point, and the very large period of So because it is very close to the homoclinic collision, the necessary computations to find So would be extremely expensive.

Figure 5.10 shows the evolution of the LAo when moving away from the heteroclinic collision. The orbit becomes smaller in size, and very close to the SBD line undergoes a Hopf bifurcation, collapsing into a fixed point Dr, as can be seen in Figure 5.10(d) and Figure 5.11(a), corresponding to the states 12 and 13 in Figure 5.7. This fixed point of the 3D system is a drifting solution of the four-dimensional ODE, and therefore corresponds to solutions with two frequencies, lying in a two-torus, as a solution of the fluid problem. One of the frequencies is the forcing frequency, and the other one is a

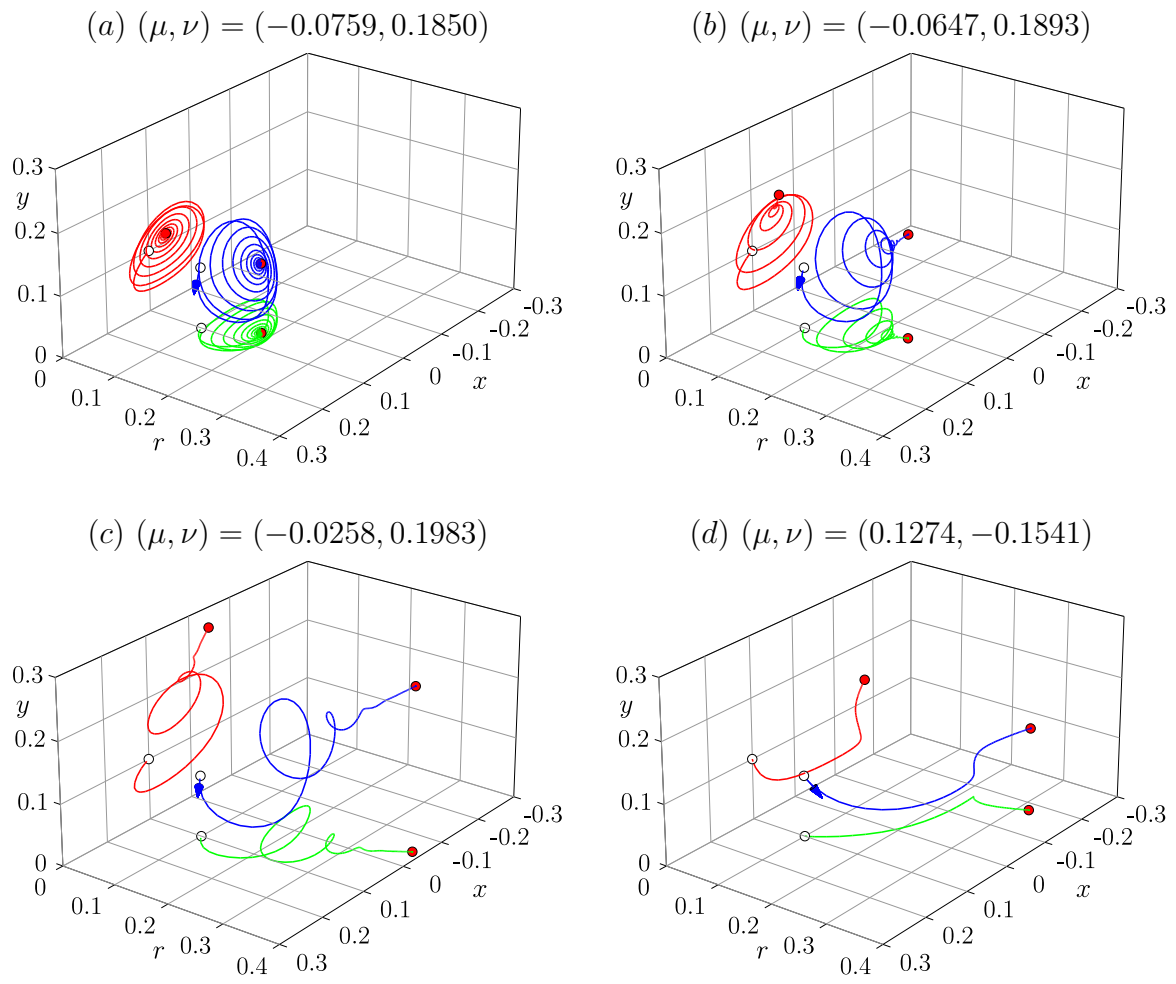

Figure 5.11: Phase portraits of the 3D system, for $a = 1$, $b = -3$ and $c = 4$. (a) shows the Hopf bifurcation $LAo \to Dr$ along the SBD curve (state 13 in Figure 5.7). (b), (c) and (d) illustrate how the Dr solution moves away from the origin in the grey region in Figure 5.7.

slow drift along the $SO(2)$-orbit of solutions. Therefore, the large asymmetric orbit LAo corresponds to a three-torus state in the Navier-Stokes equation.

Figure 5.11 shows the evolution of the drifting solution Dr that in fact moves away from the origin in the grey region in Figure 5.7. The normal form coordinates (r, x, y) become of order unity, suggesting that the dynamics in this region is poorly described by the normal form approach, and that in the real problem additional bifurcations are going to take place, as higher order terms in the normal form come into play. This is what happens in the fluid dynamics problem; in the grey region away from the codimension-two point new families of solutions have been found, displaying a complicated dynamics, described in the precedent chapter. This moving away of the Dr fixed point is illustrated

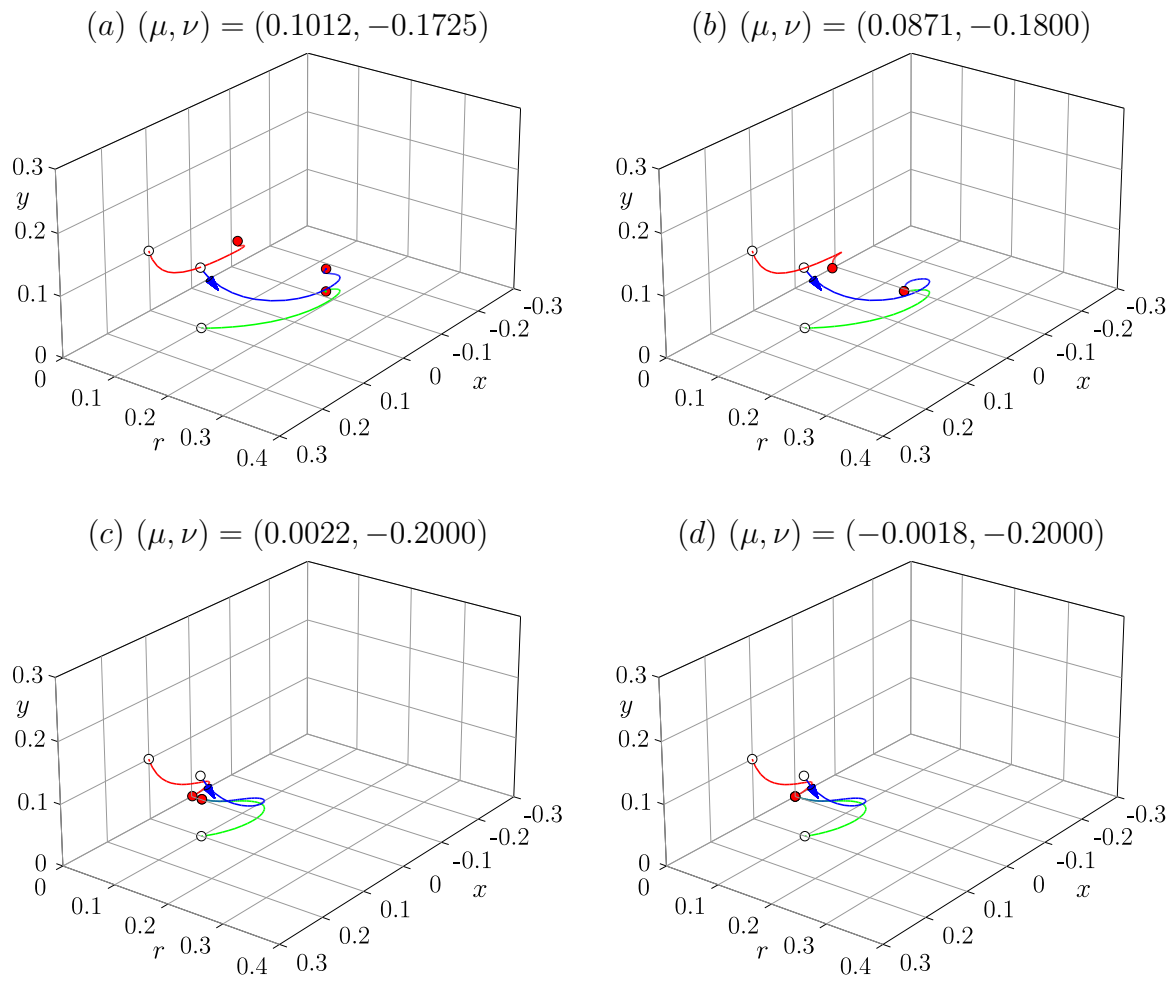

Figure 5.12: Phase portraits of the 3D system, for $a = 1$, $b = -3$ and $c = 4$. (a) and (b) shows the bifurcation $Dr \rightarrow Q$ along the SBD line (states labeled 17 and 18 in Figure 5.7). (c) and (d) shows the bifurcation $Q \rightarrow O$ along the line M_1 (states 19 and 20 in Figure 5.7.

in Figure 5.11(c) and (d) corresponding to the states 15 and 16 in Figure 5.7.

Figure 5.12 shows the last two simple bifurcations of fixed points that complete the trajectory around the codimension-two point in parameter space. One of them is the bifurcation from the drifting solution to the mode one solution, $Dr \rightarrow Q$, along the SBD line, illustrated in Figure 5.12(a) and (b), corresponding to the states 17 and 18 in Figure 5.7. And the last case is the bifurcation from the mode one solution into the base state, along the line M_1. This is shown in Figure 5.12(c) and (d), corresponding to the states 19 and 20 in Figure 5.7.

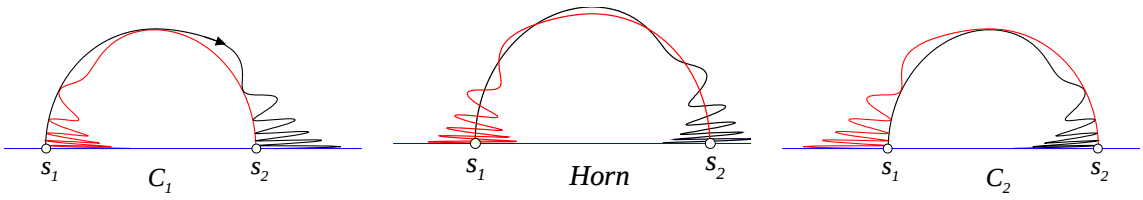

Figure 5.13: Transversal intersection and tangencies of the unstable manifold of s_1 and the stable manifold of s_2 resulting in a horn of complex dynamics.

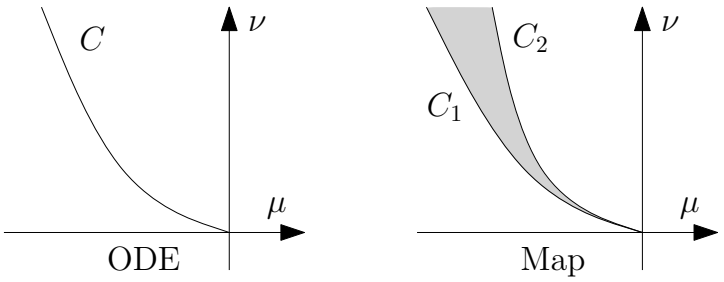

Figure 5.14: Heteroclinic bifurcation curve for the ODE and the corresponding horn shaped region for the map.

5.4 Considerations about the 4D ODE and the map normal form

The four-dimensional ODE (5.15) interpolating the map has been analysed in detail, following previous studies like Porter & Knobloch (2001), that studied the $1:2$ spatial resonance of ODEs with $O(2)$ symmetry. In our problem, the relevant normal form corresponds to a map with $O(2)$ symmetry and $1:2$ spatial resonance, so we should move back to the analysis of the map (5.3), and see how much of the previous analysis applies in the map scenario. Although the ODE (5.15) has been obtained from the map, it is an approximating interpolating ODE, up to third order in our problem. Consequently, the map obtained by integrating the ODE up to time $t = 1$ may differ from the original map in therms of order higher than three. We expect that most of the dynamics obtained close to the bifurcation point and in a neighbourhood of the base state in phase space will be present in the map, but small differences may appear when moving away from the origin. In particular, it is well known that the dynamics related to local bifurcations of fixed points and periodic orbits will remain, while the dynamics related to global bifurcations may undergo significant changes (see e.g. Kuznetsov, 2004).

Global bifurcation curves of the ODE involving homoclinic of heteroclinic collisions

of limit cycles typically become in the map a narrow region of complex dynamics. Generically, consider a heteroclinic orbit γ starting at a fixed point s_1 and ending in another fixed point s_2 in the ODE. For example, the heteroclinic loop $P_+ \to O \to P_- \to P_+$ shown in Figure 5.9(d) is made of three heteroclinic orbits joining three unstable fixed points. The orbit γ is simultaneously an unstable manifold of s_1 and a stable manifold of s_2. When the corresponding map is assumed, the orbits are discrete, and the unstable manifold of s_1 and the stable manifold of s_2 intersect transversally in the discrete heteroclinic orbit of the map. This transversal intersection begins and ends in two heteroclinic tangency curves which are the limiting curves of a narrow region with a horn shape in parameter space. Figure 5.13 shows the process of tangency and transversal intersection of the invariant manifolds, and Figure 5.14 shows the heteroclinic bifurcation curve for the ODE and the corresponding horn shaped region for the map in parameter space.

In a generic system, instead of a single bifurcation curve associated with the heteroclinic connection, there is a horn-shaped region about it. Inside the horn, the dynamics can be extremely complex, including an infinity of two-tori, solutions homoclinic and heteroclinic to both unstable fixed points, cascades of saddle-node and period-doubling bifurcations, and chaos. Other bifurcations may also result in qualitatively different dynamics. For example, the Hopf bifurcations in the ODE become Neimark-Sacker (NS) bifurcations for the map. And the Neimark-Sacker bifurcation is more complex than a Hopf bifurcation, because there are two frequencies at play; and when the ratio of the frequencies is a rational number with a small denominator, horns of complicated dynamics (involving saddle-nodes, period doublings and torus break-up) appear. Therefore a careful exploration of the map dynamics must be carried out, at least close to the heteroclinic and Hopf bifurcations (including the bifurcation Dr, which for the map involves also two frequencies).

5.5 Discussion

In this chapter, we have formulated a model based on dynamical system theory of the codimension-two bifurcation explored numerically by direct numerical simulation of the Navier-Stokes equations in the preceding chapter. As the flow is periodically forced, the normal form of the Poincaré map associated with strobing the flow at the forcing frequency, has been calculated. Instead of working directly with the map, that is really an awkward task, we can try to work with an equivalent continuous dynamical system. To this aim, we have obtained an interpolating ODE such that at the $t = 1$ approximates

the map to a desired order. The resulting ODE is the normal form of a $1:2$ spatial resonance with $O(2)$ symmetry. Following previous studies of this normal form, it has been possible to obtain a scenario that closely resembles our problem, and the exploration combining analytical and numerical tools has resulted very useful.

The results provided by the normal form fully agrees with the results of the precedent chapter, except in the grey region in Figure 5.7, where the normal form theory exhibits a drifting solution, while the Navier-Stokes direct simulations show a more complex interaction and coexistence between drifting and bursting solutions.

In order to complete the analysis in this chapter, there are several issues to pursue as an immediate continuation of the present work. For instance, determining the precise values of the parameters a, b and c of the normal form, by detailed quantitative (numerical) comparisons between the normal form and the simulations in the fluid problem. Furthermore, comprehensive numerical explorations looking for local and global bifurcations of the periodic solutions obtained from the normal form are necessary. In addition, it would be desirable to conduct detailed explorations of the normal form of the map, which is expected to differ with respect to the ODE normal form results in the regions where global bifurcations of limit cycles are present, in particular in the aforementioned grey regions where we have observed discrepancies between the ODE normal form and the Navier-Stokes results. Last but not least, the full description of all the different scenarios corresponding to the normal forms obtained, both for the ODE and the map, in order to help future research in problems with $O(2)$-equivariant $1:2$ resonances. Of course, things are not as simple as they seem, and other aspects of the problem may appear along the precedent analysis.

CHAPTER 6
VISCOELASTIC FLOW

In general terms, the research that has been conducted on fluid dynamics since the first experiments of Reynolds (1883) has provided the naive notion that the transitions in Newtonian flows are governed mainly by the Reynolds number. This non-dimensional number represents the ratio between inertial and viscous damping effects. Therefore, the typical scenario is that as inertia becomes more and more relevant, the flow suffers more and more instabilities that tend to increment its complexity. Of course, in some cases such as the plane Couette or the pipe Poiseuille, a direct transition to turbulence is *fait accompli*. Since viscoelastic fluids possess a very high viscosity, the Reynolds number is very small, so the inertial effects cannot be the instability agent. In fact, the elasticity associated to the polymers diluted in the fluid, is the mechanism that induces the transition in viscoelastic flows (Larson, 2000). Analogously to the Reynolds number, the so-called Weissenberg number, which accounts for the elasticity, is crucial in the destabilisation process in viscoelastic flows (Morozov & van Saarlos, 2007).

The case under study consists in a fluid confined in a cylindrical cavity whose lateral wall oscillates periodically in time, so the basic flow is invariant under the symmetry group $O(2) \times Z_2^{ST}$. The first symmetry, $O(2)$, is purely spatial, acts on the azimuthal direction, and is composed by all the rotations and reflections generated by the cylindrical configuration. The second one, Z_2^{ST}, is a spatial reflection about the middle of the cylinder after half the period forcing, thus being imposed by the sidewall frequency. The Newtonian scenario has been deeply analysed in Panades *et al.* (2011, 2013) and depending on the dimensionless group, St and Re, it has been observed how the inertia breaks the symmetry group in a variety of ways. For a viscoelastic fluid, the idea is similar but driving the instability through the elasticity parameters and analysing, if possible, the symmetry-breaking process.

The comparison with experimental work is always desirable, but as far as we are concerned there are no experiments being carried out with the exact setting that has been described. Nevertheless, some experimental research with a very large aspect ratio has been taking place for some years (Torralba *et al.*, 2005, 2007; Casanellas & Ortín, 2012*a*). In practical terms, the cylinder can be considered periodic in the axial direction and this periodicity introduces an additional symmetry: the flow remains invariant under translations in the axial direction. Furthermore, note that in this scenario the spatio-temporal symmetry changes because now the reflection applies to any plane with constant z. A theoretical analysis of the laminar oscillatory flow can be found in Casanellas & Ortín

(2012*b*). As Casanellas (2013) reports, after the occurrence of the first instability, some vortices enter the stage, so the translational symmetry breaks partially: the system is only invariant under some specific translations related with the periodicity of the vortices. Concerning the spatio-temporal symmetry, the infinite family of reflection planes is reduced to just a collection of them. Consequently, the symmetry group that emerges from the first bifurcation resembles $O(2) \times Z_2^{ST}$, so the analysis between the first bifurcations in our system and the secondary bifurcations of this experimental device might be intimately related.

This chapter has the following structure. In Section §6.1 the main features of the viscoelastic flow are described. Section §6.2 is devoted to the analysis of the spectral accuracy in terms of the flow parameters. In Section §6.3, evidences of elastic instability are tried to find. After showing the existance of an elastic instability, the artificial diffusion is introduced in an attempt of obtaining a stable state in Section §6.4. This chapter closes with Section §6.5, a discussion of the main results.

6.1 Basic state

As occurs in the Newtonian scenario, the basic state of an Oldroyd-B flow has to be also axisymmetric, time-periodic and synchronous with the sidewall oscillation. By means of using the Classical Oldroyd (CO) numerical scheme described in Section §2.2.2, the basic state of a dilute polymer solution for $(St, Re, We, \beta) = (1, 0.01, 0.01, 0.9)$ with $\Delta t = 10^{-2}$ is computed. Since Re and We are moderately small, a steady state is reached in a relatively small amount of time. The convergence of this state is displayed in Figure 6.1(a). As expected, the solution is clearly axisymmetric. Curiously, the axial coefficients are distributed in two bands composed by odd and even coefficients. The even band is several orders of magnitude greater than the other, which might imply that the energy is almost symmetric respect to the mid-plane $z = 0$. This result has nothing to do with the viscoelastic fluid because the same behaviour is observed for a Newtonian fluid with $(St, Re) = (1, 0.01)$. Therefore, the inertia and the elasticity are likely to be irrelevant in comparison with the viscosity, which dominates the dynamics. Taking into account the axisymmetry and the presumed pseudo-reflection in z, the most relevant contribution of the coefficients to the convergence of this state is plotted in Figure 6.1(b). The ratio between the leading coefficients and the ones in the tail for the radial and axial coordinates are $q_r \approx 2955$ and $q_z \approx 3752$, respectively; therefore the solution is accurate enough despite the aliasing at high values of n in both directions.

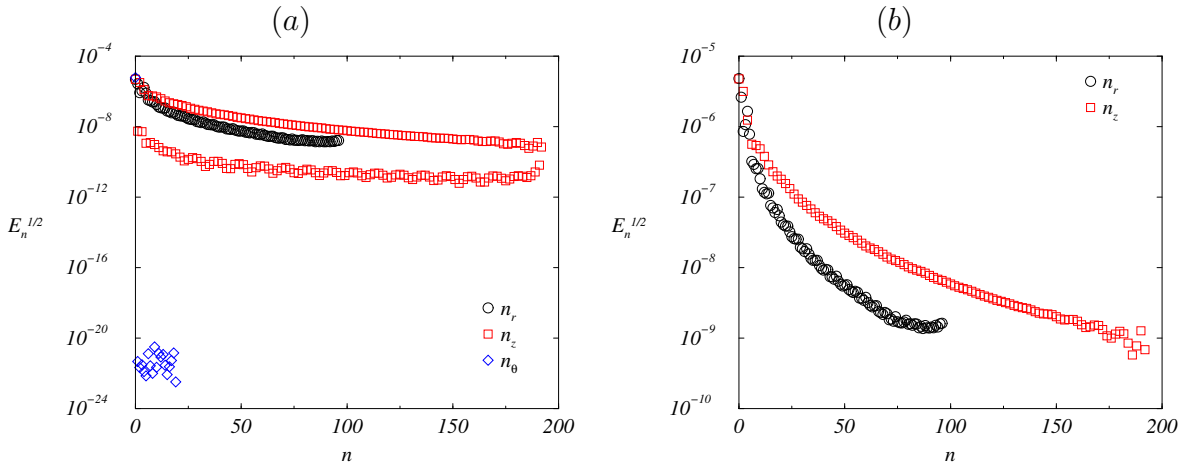

Figure 6.1: Chebyshev amplitudes of the suare root of the kinetic energy for the radial coeffcients n_r (circumferences) and axial coefficients n_z (squares), and Fourier modes of square root of the kinetic energy n_θ (diamonds), for the basic state of the viscoelastic flow at $(St, Re, We, \beta) = (1, 0.01, 0.01, 0.9)$ with $\Delta t = 10^{-2}$. (a) exhibits the contribution of all the coefficients, while (b) focuses the attention on the relevant ones.

In the manner done in Section §3.1, Figure 6.2 represents meridional planes of some useful magnitudes at a time t_0 and after advancing in time half of the period for the viscoelastic flow. The minima of these magnitudes correspond to integral multiples of the period and its half, because the flow and the sidewall are completely in-phase. Column (a) shows the contours of the kinetic energy, E, and serves to illustrate the statement of the previous paragraph: at first sight, this magnitude is almost symmetric respect to the $z = 0$ plane. The streamfunction displayed in Figure 6.2(b), shows a single roller occupying the whole cylinder throughout the forcing cycle. Since St and Re are small enough, these rollers have enough time to form and dissipate during each half of the forcing period. Columns (c) and (d) are used to demonstrate that the velocity field is invariant to the spatio-temporal symmetry H, eq. (2.28). In the current scenario, instead of using the azimuthal vorticity η, the non-zero velocity components have been used because the visualisations of η are really bothersome: almost neglectable in the whole domain and concentrated in a very small region near the junctions. This insignificant azimuthal vorticity is translated in a very small recirculation of the flow near the corners. Apparently, from the flow visualisations, this state possesses a reflection symmetry in z, but numeric data, such as the two bands in Figure 6.1(a), make evident that this solution is not symmetric at all and this curiosity is caused by the small forcing. Therefore, talking about this pseudo-symmetry is avoided intentionally from now on due to its lack of interest.

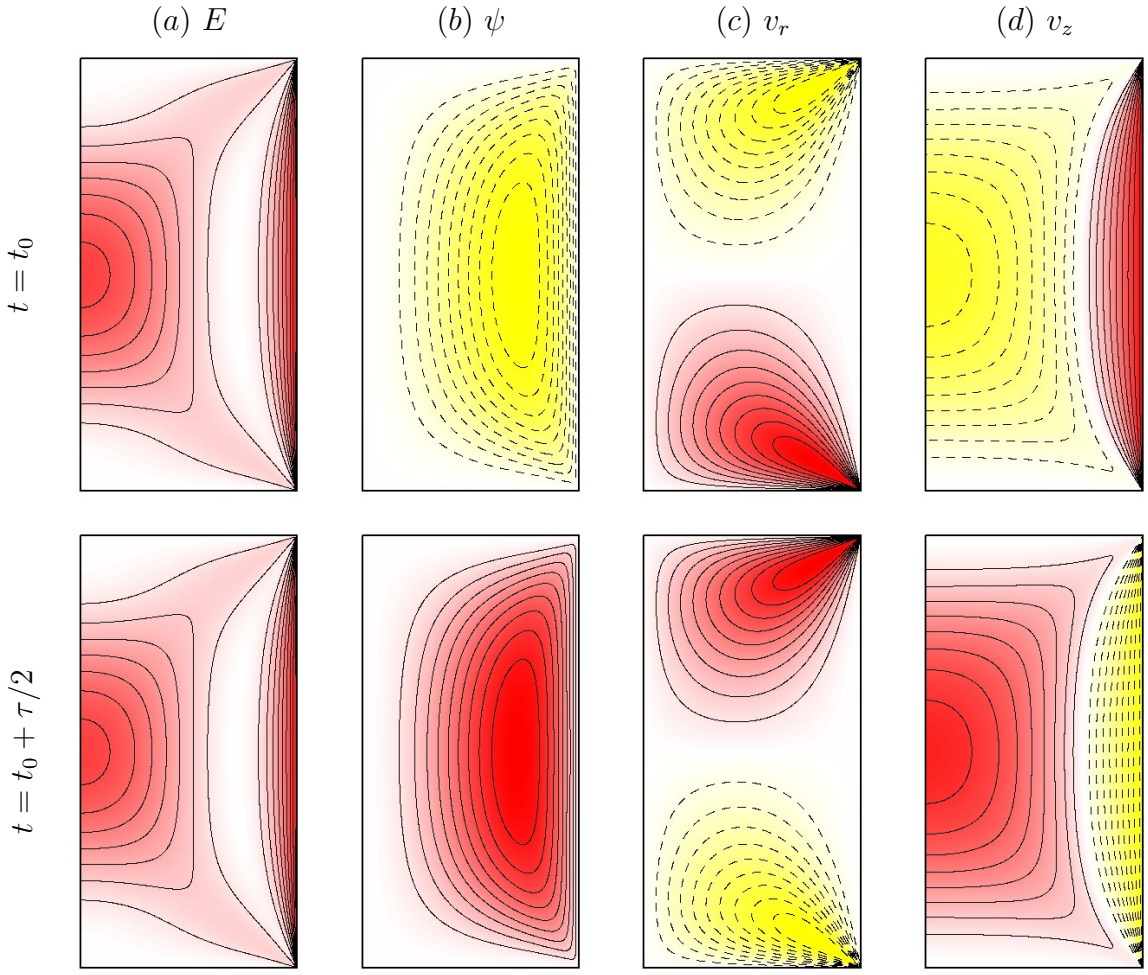

Figure 6.2: Contours of (a) kinetic energy E, (b) streamfunction ψ, (c) radial velocity v_r, and (d) axial velocity v_z of the basic state of a viscoelastic flow computed at $(St, Re, We, \beta) = (1, 0.01, 0.01, 0.9)$. Solid (dashed) contours are positive (negative); light/dark (yellow/red) colours correspond to negative/positive values. The initial time is $t_0 = \tau/3$ and has been selected where the magnitudes are most intense.

6.2 Spectral convergence

The solution displayed in the previous section, which is computed at $(St, Re, We, \beta) = (1, 0.01, 0.01, 0.9)$, is accurate enough in terms of spectral accuracy. Several authors (Sureshkumar & Beris, 1995; Fattal & Kupferman, 2005) have reported how numerical simulations of non-Newtonian flows begin to lose their numerical stability when the polymeric stress becomes rather large, the so-called High Weissenberg Number Problem (HWNP). Hence, the importance of studying the spectral convergence as a function of the flow parameters: the Stokes number is kept fixed at $St = 1$, while the other three

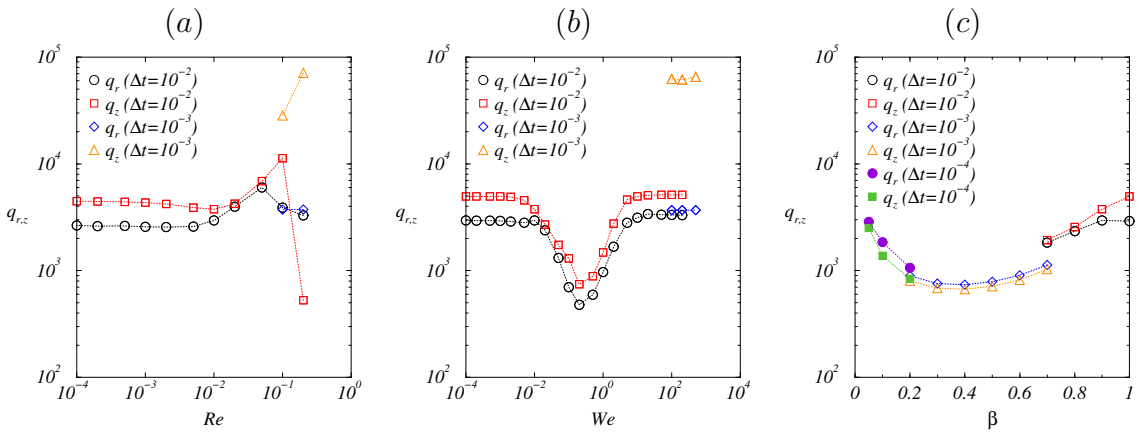

Figure 6.3: Spectral precision as a function of the non-dimensional parameters: (a) Re with $(St, We, \beta) = (1, 0.01, 0.9)$, (b) We with $(St, Re, \beta) = (1, 0.01, 0.9)$, and (c) β with $(St, Re, We) = (1, 0.01, 0.01)$.

are modified, one at a time (Figure 6.3). Mention that a Newtonian flow with the same Stokes number is linearly unstable to a synchronous B_2 mode for $Re > Re_c = 262.866$.

In Figure 6.3(a), the Reynolds number range is $Re \in [0.0001, 0.2]$, while $(St, We, \beta) = (1, 0.01, 0.9)$. With a time step of $\Delta t = 10^{-2}$, the accuracy in the radial direction is quite constant, whereas in the axial direction decreases dramatically at $Re = 0.2$. At higher Reynolds numbers, the simulations explode. By means of employing smaller time steps, $\Delta t = 10^{-3}$ and 10^{-4}, a higher precision is achieved in z, but the numerical breakdown persists. In all cases, the determinant of the conformation tensor becomes negative almost at the same time and this eventually leads the system to a numerical blow-up. Increasing the Reynolds number beyond $Re = 0.02$ might indicate that the advection of the flow is beginning to influence the dynamics and this is probably causing large gradients that induce numerical instabilities in the integration of $\mathbb{C}$. The presence of the advection is necessary, but its influence has to be neglectable to obtain purely viscoelastic instabilities. As a consequence, values of $Re > 0.02$ are avoided.

Figure 6.3(b) exhibits the variation of the spectral accuracy as a function of We with fixed Reynolds number and viscosity ratio, $(St, Re, \beta) = (1, 0.01, 0.9)$. Considering $\Delta t = 10^{-2}$, the accuracy in r and z does not suffer substantial variations except for $We \in [0.02, 2]$. These variations seem to be caused by an enhancement of the aliasing in the last coefficients. When the Weissenberg number is high enough, the dynamics need very long time scales to establish and, for $We > 200$, $\det(\mathbb{C})$ eventually becomes negative, thus causing numerical instabilities. By means of utilising $\Delta t = 10^{-3}$, the spectral accuracy improves remarkably in the axial direction and, with this time step,

the computations at even higher We are stable, but the *per se* slow dynamics need even much more time to settle. Since the advection is small enough, it is expected that for high We the system is likely to have entered the region where the elasticity of the polymers is relevant.

The variaton of the spectral accuracy in terms of β is displayed in Figure 6.3(c). In this case, $(St, Re, We) = (1, 0.01, 0.01)$. The accuracy decreases monotonically with β considering $\Delta t = 10^{-2}$. For $\beta < 0.7$, the simulations explode and the utilisation of smaller time steps is necessary. The integration results successful at first, but for $\beta < 0.2$ the numerical blow-up appears again. Employing even smaller time steps of $\Delta t = 10^{-3}$ solves the problem temporarily and the same problem appears again at even larger stages ($\beta < 0.05$). Furthermore, working with such small Δt is not feasible because elastic instabilities develop at large time scales and these simulations last an eternity. Decreasing β signifies increasing the concentration of polymers, thus getting really far away from the Newtonian case and escaping the definition of a dilute solution. Reducing the viscosity ratio might intensify the effects of the velocity gradients and the elasticity at the same time.

Consequently, in an attempt to find some evidences of elastic instability, some considerations about the parameters have to be kept in mind. The system has to be set in a frame where the viscosity dominates over the inertia, but with a non-zero velocity, so $Re = 0.01$ and $St = 1$ are chosen. In addition, the concentration of polymers difficults the integration and distances us from the Newtonian scenario. Hence, this magnitude is selected close to one, $\beta = 0.9$. Even though the system is different, the chance of finding resonance phenomena is slim because of the proximity of β to the unity (Casanellas & Ortín, 2012*b*). After fixing all these non-dimensional numbers, it is intended to destabilise the basic flow changing the Weissenberg number with $We > 1$, because this parameter is supposed to enhance the elasticity effects (Morozov & van Saarlos, 2007).

6.3 Elastic instability

As it has been mentioned in the previous section, the system might be entering the elastic regime for $We > 1$, so $(St, Re, We\beta) = (1, 0.01, 10, 0.9)$ is considered here. Figure 6.4 shows the time evolution of the kinetic and elastic energy of the axisymmetric mode. From Figure 6.4(a), E_0 clearly reaches a steady state very rapidly, while U_0 needs much more time, at least two more orders of magnitude to arrive Figure 6.4(b). Thus, the

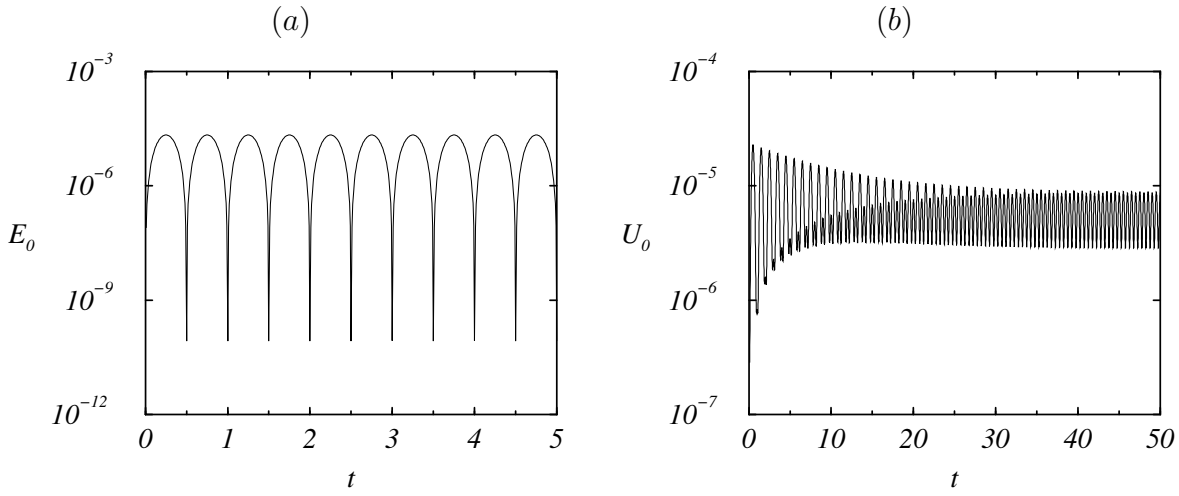

Figure 6.4: Time series of the (a) kinetic energy E_0 and (b) elastic energy U_0 of the axisymmetric Fourier mode $(St, Re, We, \beta) = (1, 0.01, 10, 0.9)$.

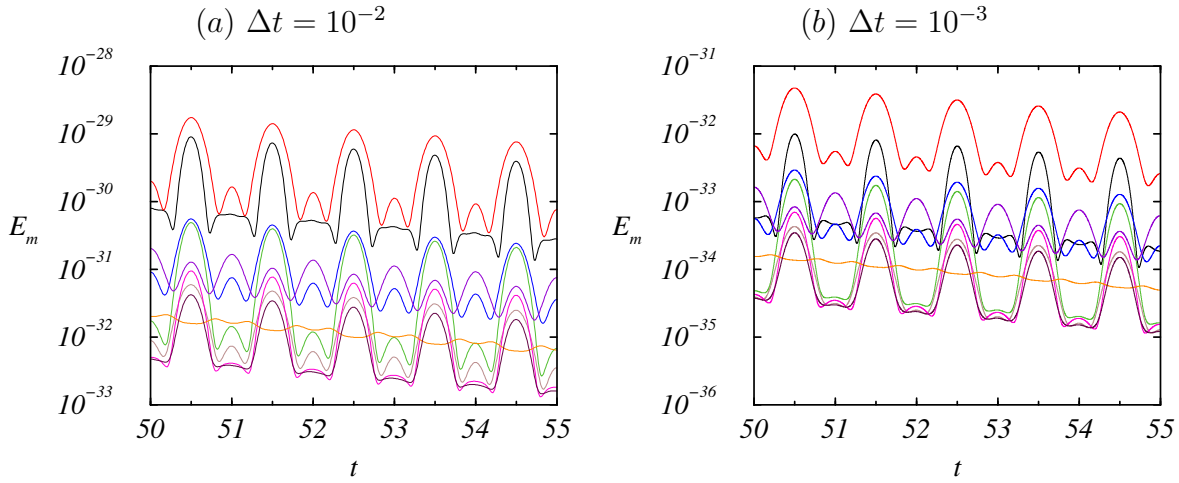

Figure 6.5: Time series of the kinetic energy of all the Fourier modes for an axisymmetric base state at $(St, Re, We, \beta) = (1, 0.01, 10, 0.9)$ considering different time steps Δt. The growth rates of the different modes are displayed in Table 6.1.

presence of the elasticity in the flow dynamics cannot be denied. Time steps of $\Delta t = 10^{-2}$ and 10^{-3} have been employed and the same steady states are achieved.

After obtaining the axisymmetric basic state, all the Fourier modes are perturbed at once introducing a small perturbation $\delta = 10^{-10}$ in their radial velocity components, as is explained in Section §2.4. By taking a glimpse to Figure 6.5, which shows the time evolution of the kinetic energy of the different modes, there is no doubt that the solution under consideration is linearly stable. This feature does not depend on the

Δt	10^{-2}	10^{-3}	Error (%)
σ_1	-0.2142	-0.2173	1.43
σ_2	-0.2002	-0.1963	1.99
σ_3	-0.2097	-0.2161	2.96
σ_4	-0.2033	-0.2006	1.35
σ_5	-0.2153	-0.2243	4.01
σ_6	-0.2074	-0.2058	0.78
σ_7	-0.2100	-0.2106	2.85
σ_8	-0.2283	-0.2284	0.04
σ_9	-0.2178	-0.2212	1.54

Table 6.1: Growth rates of the different Fourier modes exhibited at Figure 6.5 and the relative error between them.

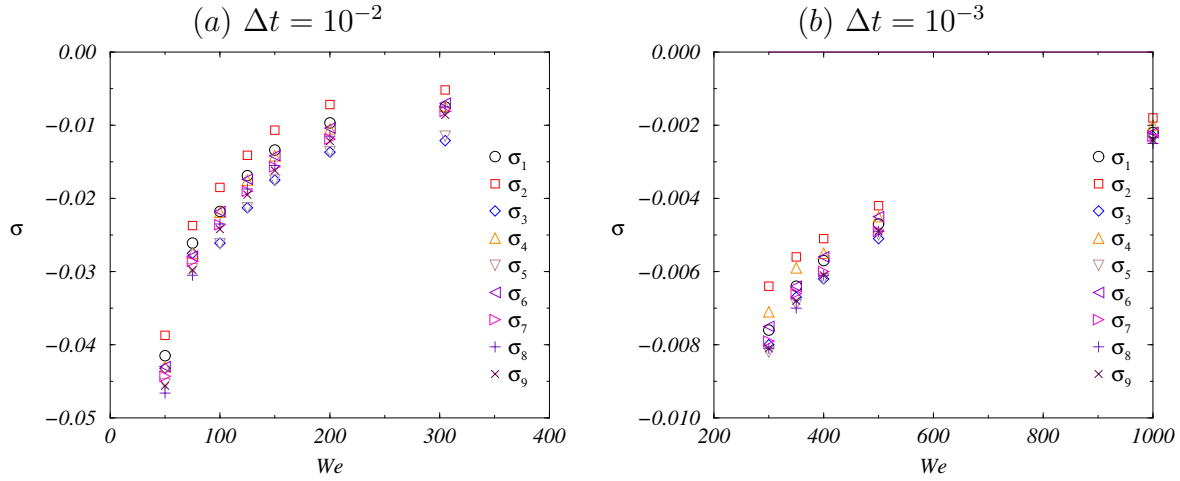

Figure 6.6: Growth rates of the Fourier modes as a function of We at $(St, Re, \beta) = (1, 0.01, 0.9)$ considering different time steps Δt.

time step and the growth rates of the different m Fourier modes, σ_m, are listed in Table 6.1. As occurs in the Newtonian scenario, the second Fourier mode is the least stable one. These growth rates, which are intimately related with the eigenvalues, seem to not depend substantially on Δt. In fact, assuming that the measure with $\Delta t = 10^{-3}$ is the most accurate, the relative error between them can be easily computed, thus yielding a maximum error of about 4%. The fact that σ_m are so close, translates in a contiuous eigenspectrum, which is typical from hyperbolic equations, as the Oldroyd-B equation is (Sureshkumar & Beris, 1995; Chokshi & Kumaran, 2009).

As a consequence, by means of increasing the Weissenberg number, the growth rates should increment too. Keeping in mind the Newtonian flow, in case that the basic flow becomes unstable at a finite We, the least stable σ_m ought to become positive, thus

indicating the first mode that bifurcates from the axisymmetric state. Figure 6.6(a) shows the growth rates of the different Fourier modes as a function of We considering $(St, Re, \beta) = (1, 0.01, 0.9)$ and computed with $\Delta t = 10^{-2}$. All the Fourier modes tend te become unstable when We is incremented and the leading mode is still the second one. Unfortunately, the computations explode beyond $We = 325$, thus rendering the presumably interesting regions inaccesible with the time step considered. In this context, Figure 6.6(b) is completely equivalent to (a) but a smaller time step is used to explore the regions that were unreachable. Apparently, the critical value cannot be estimated in a simple way and it seems to be necessary to go to even higher We. Note that the computational cost of working with such small time steps and the large dynamics developed because of We, forces us to think in another direction because there is the possibility that the system might be always linearly stable, as occurs in the Newtonian plane Couette and pipe Poiseuille flow (Schmid & Henningson, 2001; Drazin, 2002).

In this case, the transition ought to be subcritical and by means of employing higher perturbations, the basic flow should become unstable at some point due to the non-linear interactions of the different modes. Thus, perturbations ranging from $\delta = 10^{-9}$ to $\delta = 10^{-3}$ are introduced to a basic flow with $(St, Re, We, \beta) = (1, 0.01, 10, 0.9)$ and $\Delta t = 10^{-3}$. The result is that for $\delta = 10^{-3}$ the simulations begin to explode after some time steps, whilst for $\delta = 10^{-4}$ they are stable, very similarly to Figure 6.5. This process is refined introducing perturbations comprised between the two values in another series of computations and the main findings are displayed in Figure 6.7. Perturbing with $\delta = 7.5 \cdot 10^{-4}$, Figure 6.7($a$), results in almost the usual linear decay to the basic state. Increasing the amplitude of the perturbation to $\delta = 7.9 \cdot 10^{-4}$, Figure 6.7($b$), yields the base state after a strange transient. Apparently, the first Fourier mode (black) excites the remaining ones, but this is not sufficient to destabilise the basic flow. Nevertheless, a slightly larger perturbation, $\delta = 8 \cdot 10^{-4}$ in Figure 6.7(c), provides enough strength to the excitation of the first Fourier mode to make the system unstable. All the Fourier modes begin to grow in a non-linear fashion and, eventually, a numerical breakdown occurs when they become of the same order as the axisymmetric mode, which is roughly speaking the same of Figure 6.4(a), and after the determinant becomes positive. This feature indicates the possibility that there is no such thing as a saturation process. For even higher amplitudes, $\delta = 8.7 \cdot 10^{-4}$ in Figure 6.7(d), not only the first Fourier mode is initially unstable, but others, such as the second one (red), which has the highest energy of all, begin to grow from the start and the simulations explode after some forcing periods due to the inability to saturate.

As is mentioned for parallel shear flows in Morozov & van Saarlos (2007), once the

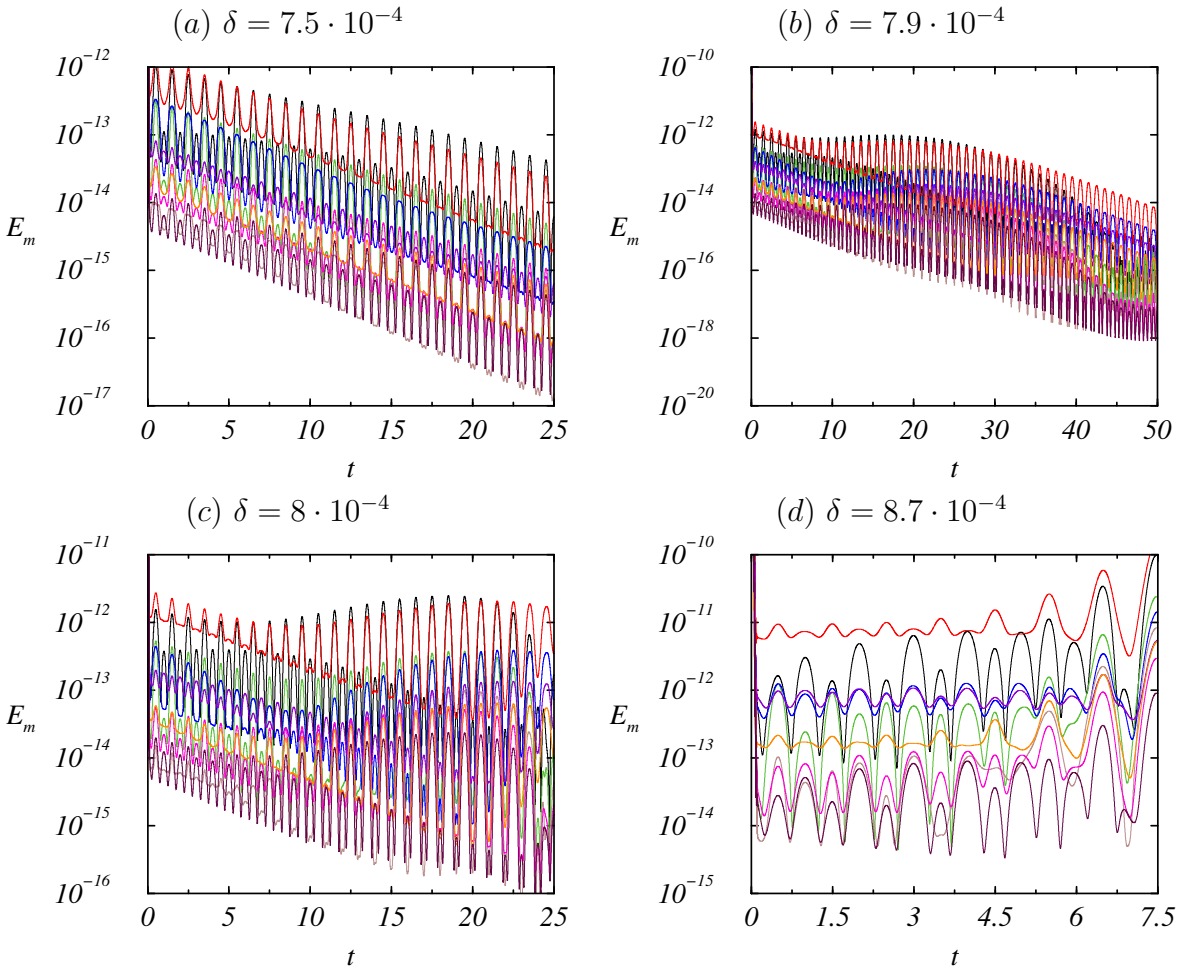

Figure 6.7: Time series of the Fourier modes at $(St, Re, We, \beta) = (1, 0.01, 10, 0.9)$ with $\Delta t = 10^{-3}$ considering different perturbations δ.

amplitudes of the perturbations are large enough, the perturbations will grow even larger due to the non-linear interactions between them. This reasoning is applicable here too, and it would be very helpful if we could obtain an estimate for the critical amplitude that drives the finite-amplitude instability. Note that the initial value of the kinetic energy $E_{m,i}$ from which every Fourier mode begins to grow or decrease is achieved in a relatively short scale, less than a forcing period, and $E_{m,i}$ might be closely related with the mechanism that triggers the instability. At first sight, there seems to be two ways for the Fourier modes to become unstable: interplaying with other modes and/or through the self-interaction. When comparing both mechanisms, the cooperative effects between modes give the impression to appear at smaller energies, as can be observed in Figure 6.7(c) and (d). For the sake of comparison and in order to corroborate the previous statement, it is necessary to perturb only one Fourier mode that has no interactions with

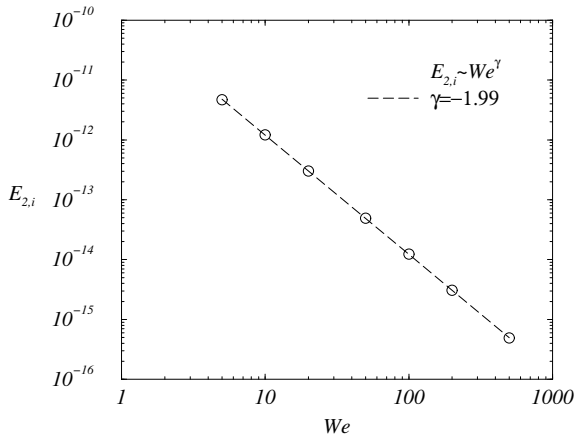

Figure 6.8: Initial kinetic energy $E_{2,i}$ for different Weissenberg numbers We at $(St, Re, \beta) = (1, 0.01, 0.9)$ with $\Delta t = 10^{-3}$.

others, such as is the case of $m = 5$. In this scenario, the estimation of a critical value E_{5,i_C} is possible and the result is that $E_{5,i_C} \in [2.01 \cdot 10^{-12}, 3.17 \cdot 10^{-12}]$. In contrast, when there is cooperativity between modes, the maximum energies in Figures 6.7(b) and (c), which correspond to $m = 2$, might trigger the instability, and have a value of $E_{2,i} = 9.68 \cdot 10^{-13}$ and $1.21 \cdot 10^{-12}$, respectively. Consequently, the interval described by these values contains the minimum energy that is necessary to destabilise the basic state. This energy cannot be understood as critical value in the usual sense, because they need the assistance of the other modes. The sequence sketched in Figures 6.7(a)-(d), plus this qualitative analysis in terms of the initial kinetic energies, reinforces the idea that the strong cooperation between modes is crucial in the process.

The emerging picture suggests the absence of a precise Fourier number guiding the instability process and the idea that there might be a rapid transition to a fully developed turbulent state when the flow becomes unstable. Furthermore, the fact that the perturbations seem to be unable to saturate, maybe are a sign that there is no stable finite-amplitude branch of solutions. This is exactly what Morozov & van Saarlos (2007) claim in their study of viscoelastic parallel shear flows. In addition, they stated that the threshold in this kind of flows undergoing a subcritical instability, has to decrease as $1/We^2$ for sufficiently large We. Therefore, based on this surmise, the next step is the application of different perturbations to flows with different Weissenberg numbers and note down the minimum value of the energy that is needed to trigger the transition. In other words, the same exact procedure described in the previous paragraph is repeated for $We \in [5, 500]$.

Figure 6.8 displays the approximate minimum energy that destabilises the basic flow

as a function of the Weissenberg number. For instance, for $We = 10$, it corresponds to a second mode with initial energy $E_{2,i} = 1.21 \cdot 10^{-12}$. The second mode always possesses the largest $E_{m,i}$ in the whole range, and $E_{2,i}$ decreases with We because as the Weissenberg number increases. it becomes easier to surpass the critical amplitude that separates decaying and growing amplitudes. After fitting the data with a power law, it is infered that $E_{2,i} \sim We^{\gamma}$ with $\gamma = -1.99 \approx 2$. The idea is that for a range of $E_{2,i}$ below the dashed line, the system returns to the axisymmetric state. For slightly higher initial perturbations of the second mode, the second mode is stable at first, but after some time it becomes unstable, as occurs in Figure 6.7(c). At even higher values, the analogous behaviour depicted in Figure 6.7(d) is observed: the perturbations are so high that the Fourier modes grow non-linearly from the beginning because of their self-interactions and, after some time, the cooperative effects take control.

In contrast with the Newtonian scenario, it has not been possible to obtain any stable state, besides, of course, the axisymmetric flow. Apparently, the system is always linearly stable, but there seems to be a subcritical transition for a large enough perturbation. These perturbations never saturate, so there seems to be no such thing as a stable branch or, perhaps, there is still the possibility to jump into the stable branch for We very close to the saddle-node point, as is suggested in Morozov & van Saarlos (2005) for plane Couette viscoelastic flows. Morozov & van Saarlos (2007) stated that the threshold in viscoelastic parallel shear flows undergoing a subcritical instability, should decrease as $1/We^2$ for sufficiently large We. Actually, the same power law is recovered, although the cylinder is finite and has the two lids. It has been constantly manifested (Pakdel & McKinley, 1996; Morozov & van Saarlos, 2007) that the curvature of the streamlines in combination with the polymeric forces induce the elastic instability. Due to the cylinder lids, in the case under study the streamlines are always curved, as can be observed in the streamfunction of Figure 6.2(b). This curvature is probably responsible for the numerical blow-ups explained in the former section, but once the basic state is reached, the effect of this curvature as a destabilising factor should be irrelevant. Nevertheless, when the axisymmetric flow is perturbed in the azimuthal direction beyond a critical amplitude, the distortion of the streamlines makes the polymers stretch, thus creating the mechanism that induces the elastic instability. As a result, when the elastic instability achieves the breaking into θ, all the Fourier mode are excited almost at the same time without any apparent saturation.

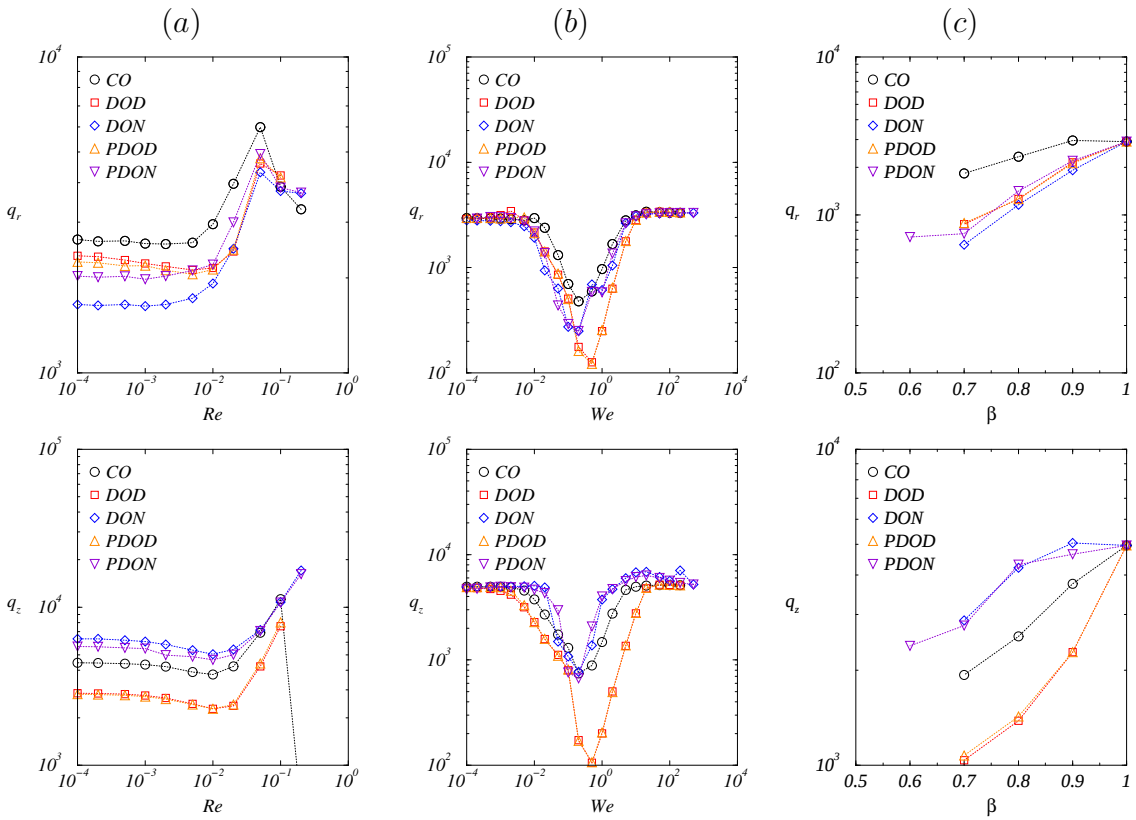

Figure 6.9: Spectral precision in the radial q_r and axial q_z direction for the different numerical schemes as a function of the non-dimensional parameters: (a) Re with $(St, We, \beta, \kappa) = (1, 0.01, 0.9, 10^{-4})$, (b) We with $(St, Re, \beta, \kappa) = (1, 0.01, 0.91, 0^{-4})$, and (c) β with $(St, Re, We, \kappa) = (1, 0.01, 0.01, 10^{-4})$. The time step is set to $\Delta t = 10^{-2}$ in all cases.

6.4 Diffusive models

There are some strong evidences suggesting that the system is always linearly stable and can suffer a subcritical instability depending on the perturbation. The strong non-linearities of the perturbations make the system unstable. In canonical Newtonian shear flows, the generic transition scenario is characterised by a sudden transient non-modal growth of the perturbation superseded by either a relaminarisation or eventual transition to turbulent regimes. According to our computations, modal instabilities associated with a precise wavenumber have not been identified. However, it is unclear whether the flow reaches a saturated non-linear regime before an eventual transition. In an attempt to stabilise the numerical simulations of viscoelastic flows, it is common practice to include a diffusive term κ in the constitutive equation (Sureshkumar & Beris, 1995)

As has been described in Section §2.2, we have developed four numerical schemes

that introduce κ in the computations: Diffusive Oldroyd Dirichlet (DOD), Diffusive Oldroyd Neumann (DON), Purely Diffusive Oldroyd Dirichlet (PDOD), and Purely Diffusive Oldroyd Neumann (PDON). Recall that the purely diffusive models consider the diffusivity of the conformation tensor from the beginning, while the diffusive ones perform an explicit update of $\mathbb{C}$ and later introduce the diffusivity to gain stability. In Section §6.2, the spectral accuracy of the basic states in terms of the different parameters has been analysed. Figure 6.9 goes in the same direction but contrasting the results of the diffusive models with a small diffusivity ($\kappa = 10^{-4}$) and the Classical Oldroyd (CO).

Column (a) in Figure 6.9, exhibits q_r and q_z as a function of Re by keeping fixed the remaining parameters, $(St, We, \beta, \kappa) = (1, 0.01, 0.9, 10^{-4})$. with $\Delta t = 10^{-2}$. In comparison with CO, the numerical schemes that employ Dirichlet boundary conditions (DOD and PDOD) possess less acuracy and explode at smaller Re. In contrast, DON and PDON allow us to explore the same regions as CO with a less dramatic decrease in q_r and q_z for $Re = 0.2$. Nevertheless, they are less acurate in r, but more precise in z

In terms of changing We and fixing the other parameters, to the common values of $(St, Re, \beta, \kappa) = (1, 0.01, 0.9, 10^{-4})$ and $\Delta t = 10^{-2}$, column (b) of Figure 6.9, it is observed the same severe decrease in accuracy that has been already mentioned for Figure 6.3(b). Concerning the regions of high Weissenberg number, which are the intereseting ones, there is no much difference between CO, DOD and PDOD. However, the numerical schemes that use Neumann boundary conditions (DON and PDON), are much more stable and precise than the other three.

The analysis of the accuracy as a function of the viscous ratio is performed for the sake of completeness, $(St, Re, We, \kappa) = (1, 0.01, 0.01, 10^{-4})$. Apparently, PDON is stable where the others breakdown ($\beta < 0.7$). In addition, DOD and PDOD are always less precise than CO, while the comparison of precisions between the remaining depends on the finite direction: DON and PDON are more accurate than CO in the axial direction, but the opposite in the radial coordinate.

The main conclusions that can be extracted from this analysis is that the two numerical schemes that use the explicit update of $\mathbb{C}$ as Dirichlet boundary conditions (DOD and PDOD) are always less precise than the usual Oldroyd-B equation (CO). They are stable for the same ranges of parameters, with the exception of $Re = 0.2$. There is the possibility that the discontinuous boundary conditions are the source of all these problems. On the other side of the coin, there are the Neumann-based schemes (DON and PDOD). Generally, they are more accurate in z than in r and can arrive to We and β unatteinable for the CO.

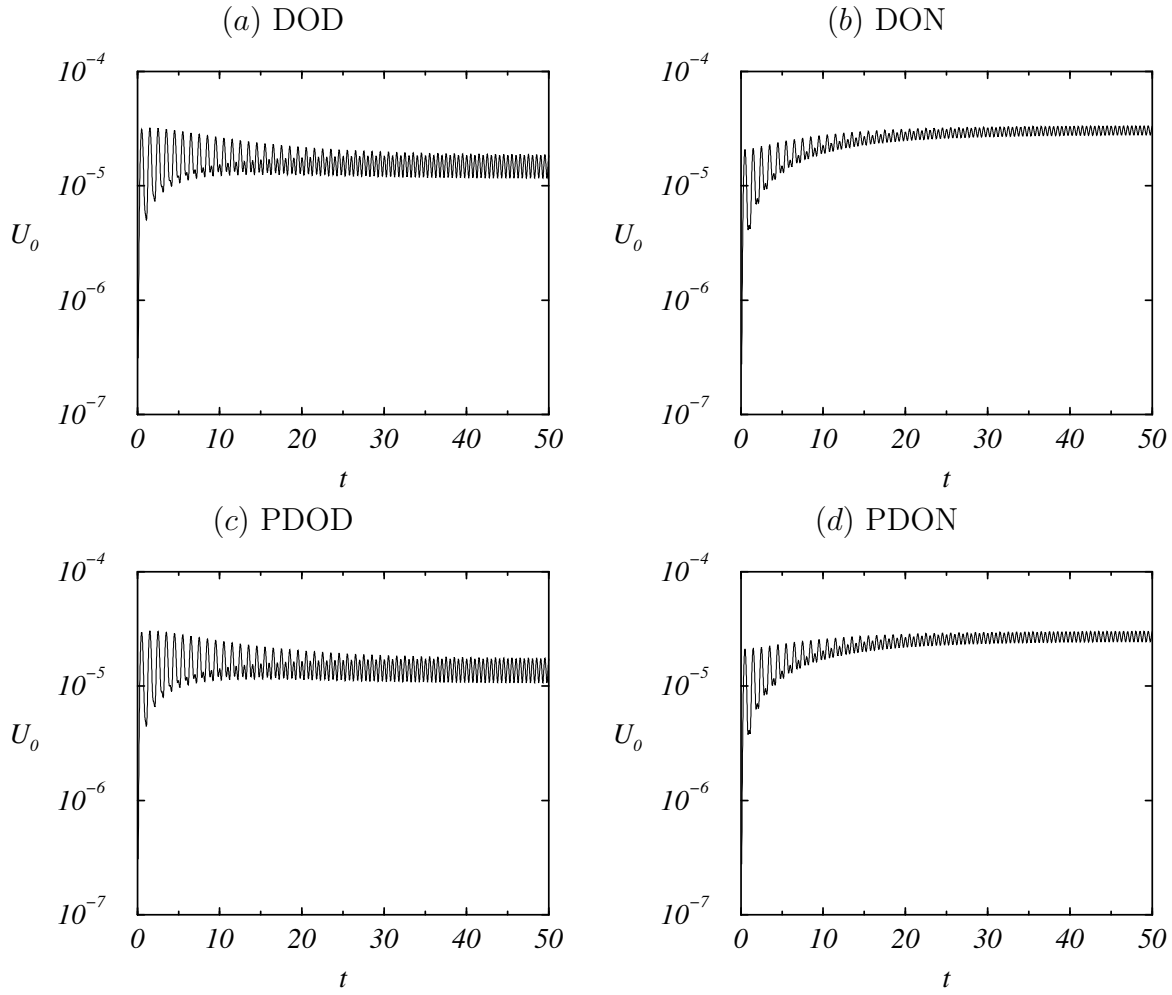

Figure 6.10: Time series of the elastic energy U_0 of the axisymmetric Fourier mode at $(St, Re, We, \beta, \kappa) = (1, 0.01, 10, 0.9, 10^{-4})$ with $\Delta t = 10^{-3}$ for the different numerical schemes.

Recall that introducing κ is just an artifact to try to stabilise the simulations. Therefore, it is important to keep the flow dynamics as unaltered as possible (Thomas *et al.*, 2006, 2009). For this reason, the equivalent flow of the previous section is again under study with a small κ, $(St, Re, We, \beta, \kappa) = (1, 0.01, 10, 0.9, 10^{-4})$. Time steps of $\Delta t = 10^{-2}$ and 10^{-3} have been employed without any remarkable changes. The diffusivity of the conformation tensor does not alter substantially the kinematic energy in any case: E_0 is the same as the one in Figure 6.4(a) with the same average value, $\langle E_0 \rangle = 1.12 \cdot 10^{-5}$. However, the dynamics that spread from the polymers, characterised by Figure 6.4(b), vary in a relevant manner (Figure 6.10). The process towards saturation is almost the same in DOD and PDON, Figure 6.10(a) and (c), and is quite similar to CO: after a first excitation, the elastic energy relaxes to the steady state. Observe that

Δt	10^{-2}	10^{-3}	Error (%)
σ_1	-0.2035	-0.2033	0.10
σ_2	-0.2047	-0.2040	0.35
σ_3	-0.1968	-0.2017	2.43
σ_4	-0.2009	-0.2037	1.37
σ_5	-0.1999	-0.2042	2.11
σ_6	-0.2033	-0.2061	1.36
σ_7	-0.2045	-0.2071	1.26
σ_8	-0.2057	-0.2086	1.39
σ_9	-0.2080	-0.2088	0.38

Table 6.2: Growth rates of the different Fourier modes after perturbing an axisymmetric base state at $(St, Re, We, \beta, \kappa) = (1, 0.01, 10, 0.9, 10^{-4})$ with $\delta = 10^{-10}$ employing different time steps with the DOD scheme, and the relative error between them

the steady state of Figure 6.4(b) has an average value of $\langle U_0 \rangle = 5.85 \cdot 10^{-6}$, while in the Dirichlet-based schemes this value is at least a factor two higher: $\langle U_0 \rangle_{\mathrm{DOD}} = 1.50 \cdot 10^{-5}$ and $\langle U_0 \rangle_{\mathrm{PDOD}} = 1.38 \cdot 10^{-5}$. Nevertheless, the process in DON and PDON is much more different: the first excitation does not decay and the elastic energy U_0 results in a rather high value in comparison with the others, Figure 6.10(b) and (d). In this case, $\langle U_0 \rangle_{\mathrm{DON}} = 2.97 \cdot 10^{-5}$ and $\langle U_0 \rangle_{\mathrm{PDON}} = 2.68 \cdot 10^{-5}$. Notice that the differences between the diffusive schemes with their respective purely diffusive cases are minimal. As a matter of fact, the introduction of a small κ preserves somehow the dynamics towards equilibrium in DOD and PDOD respect CO, but the numerics suffer some variations; in the case of DON and PDON, the dynamics and the numerical values are very different.

In fact, incorporating a small diffusivity in the constitituve equation modifies the flow strongly and the choice of the boundary conditions is crucial. For this reason, the numerical schemes that employ Neumann boundary conditions (DON and PDON) are rejected, whereas the ones that use the explicit update of $\mathbb{C}$ (DOD and PDOD) seem to be more convenient. Since both of them behave in a very similar way, DOD is preferred because by taking a look at the literature, it is observed that similar algorithms are utilised by different authors (Sureshkumar & Beris (1995); Atalik & Keunings (2002)). As it is done in the previous section, let us perturb an axisymmetric flow at $(St, Re, We, \beta, \kappa) = (1, 0.01, 10, 0.9, 10^{-4})$ with a small perturbation $\delta = 10^{-10}$. The result of applying this perturbation is perfectly compatible with the decay of all the Fourier modes of Figure 6.5. The growth rates of the different modes are listed in Table 6.2 and changing the time step does not affect appreciably σ_m; the maximum discrepancy is provided by the maximum relative error of the measurements and is about the 2% . Apparently, the $m = 3$ Fourier mode is the least stable one and the values of σ_m are

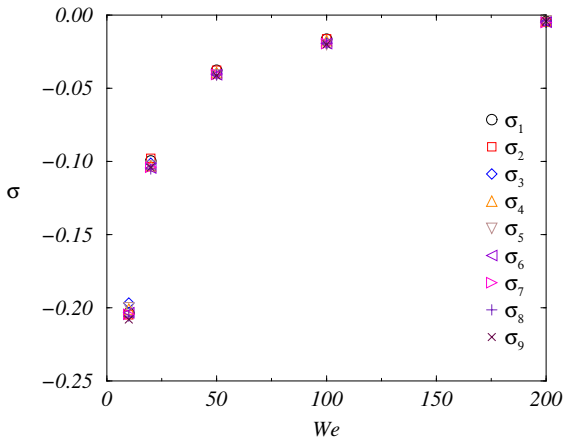

Figure 6.11: Growth rates of the Fourier modes as a function of We at $(St, Re, \beta, \kappa) = (1, 0.01, 0.9, 10^{-4})$ considering a time step of $\Delta t = 10^{-2}$.

very close, in contrast with the CO scenario (Table 6.1).

Once again, by means of increasing the Weissenberg number, the growth rates tend to become more and more unstable (Figure 6.11). However, some remarkably high We have been achieved considering $(St, Re, \beta, \kappa) = (1, 0.01, 0.9, 10^{-4})$ with $\Delta t = 10^{-2}$ and the basic flow does not become unstable. As a consequence, the axisymmetric state might be always linearly stable, the same scenario sketched in the former section.

As a consequence, the amplitude of the perturbation has to be increased in order destabilise the basic flow, the same procedure that has been done in Section §6.3. The main findings are presented in Figure 6.12. Introducing a small perturbation of $\delta = 7 \cdot 10^{-4}$, Figure 6.12(a), yields a clear linear decay of all the Fourier modes. By means of incrementing the amplitude to $\delta = 7.3 \cdot 10^{-3}$, Figure 6.12($b$), the linear trend is distorted because of a small bump introduced by the second mode (red), and later on the usual decay is recovered. Presumably, the $m = 2$ mode excites the even Fourier modes, but this is not enough to make the axisymmetric flow unstable. However, imposing a little bit larger perturbation, $\delta = 7.4 \cdot 10^{-3}$ in Figure 6.12(c), causes dramatic changes in the dynamics: the excitation of the second Fourier mode, which is also followed by all the even ones, is strong enough to excite all the remaining modes, headed by the $m = 1$ mode (black). The modes begin to interact non-linearly and these perturbations never cease their growth, until acquiring energies of similar order as the axisymmetric mode. For higher amplitudes, $\delta = 8 \cdot 10^{-4}$ in Figure 6.12(d), the same process occurs in a much smaller time scale. Following the prescriptions of the previous section, the critical amplitude that is able to destabilise the basic flow has to be comprised between the maximum initial energies of Figures 6.12(b) and (c), $E_{2,i} = 4.89 \cdot 10^{-12}$ and $E_{2,i} =$

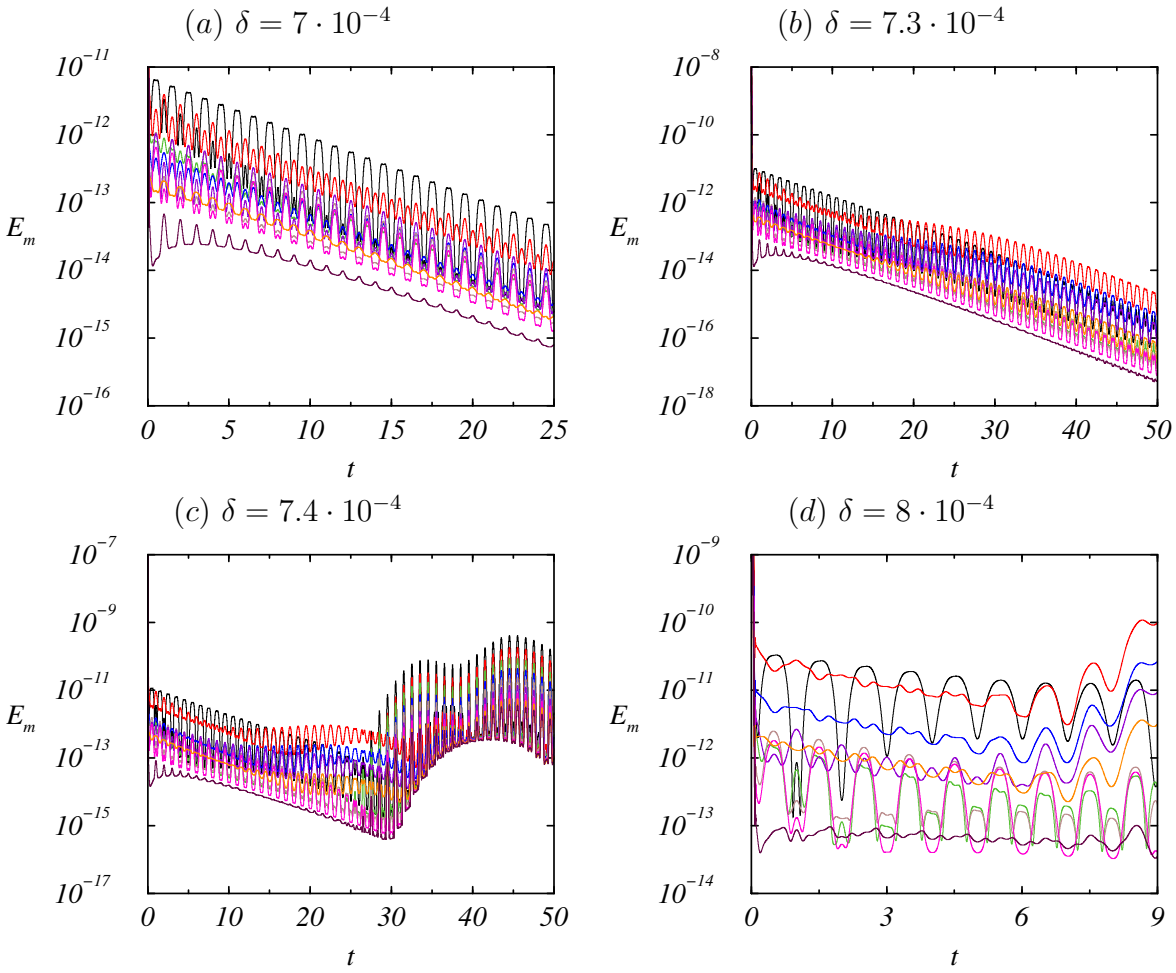

Figure 6.12: Time series of the Fourier modes employing the DOD scheme for $(St, Re, We, \beta, \kappa) = (1, 0.01, 10, 0.9, 10^{-4})$ with $\Delta t = 10^{-3}$ considering different perturbations δ.

$6.49 \cdot 10^{-12}$, respectively. Therefore, the diffusive term κ produces a stabilising effect on the perturbed flow because higher perturbations are necessary to exceed the threshold and destabilise the basic flow, in comparison with the usual Oldroyd-B equation. Using the PDOD numerical scheme, the same results are obtained with some minor changes in the numbers. The same conclusions expressed in the last paragraph of Section §6.3 seem applicable here too.

6.5 Discussion

A dilute polymer solution described by the Oldroyd-B equation is the most closely related viscoelastic material to a Newtonian fluid. Nevertheless, these polymers change the

flow properties and the instabilities mechanisms enormously. This precept is also valid in the case under, a dilute polymeric solution enclosed in a cylinder whose lateral sidewall oscillates harmonically. In particular, the Newtonian flow with $St = 1$ is unstable to a synchronous B_2 mode at a finite critical Reynolds number, meanwhile the equivalent viscoelastic scenario is characterised by undergoing a subcritical finite-amplitude instability for small Reynolds numbers.

Once the amplitudes of the perturbations are strong enough, the non-linear interactions are enhanced and are capable of destabilising the axisymmetric basic state. Consequently, there is not a precise Fourier mode leading the process, in contrast with the Newtonian case. As a matter of fact, we have provided a semi-quantitative measure of the critical amplitude that enables the instability, and this magnitude shows a power-law dependence with the Weissenberg number of the form $1/We^2$. These perturbations never saturate, independently of We. This might indicate that there is no such thing as a stable branch of solutions for such high We. Another possibility is that this hypothetical branch only exists for Weissenberg numbers very close to the saddle-node value. In an attempt to stabilise the perturbed flow, an artificial diffusivity is inserted in the constitutive equation and different boundary conditions are used. Whatever the case, the Neumann-based schemes change completely the dynamics, meanwhile the ones that utilise Dirichlet boundary conditions are almost equivalent to the former case with just an increase in the critical amplitude because the diffusivity acts as a stabiliser. Although our computations are consistent with Newtonian subcritical phenomena and the arguments developed in Morozov & van Saarlos (2007), the results that have been obtained should be confirmed in the future with alternative methodologies.

The transition scenario clearly resembles the typical one of the plane Couette and pipe Poiseuille, because the basic state is always linearly stable. These solutions include stationary and travelling-wave solutions that are unstable and disconnected from the basic state. For this reason, it seems a good idea to use similar techniques, such as Newton-based solvers, instead of the usual time integration to obtain travelling-wave states, as Roland *et al.* (2010) do for pipe flows. In fact, Kaptan *et al.* (2010) used these kind of methods to simulate successfully a non-Newtonian fluid in a cylindrical cavity whose top lid is under rotation.

What was supposed to be a natural extension of the Newtonian scenario, has become a tremendous challenge. Since one of the initial interests was the comparison with some experimental work with a large height-to-radius ratio cylinder, the cylindrical cavity should be abandoned and replaced in the first place by a periodic cylinder. Atalik &

Keunings (2004) have studied the same system but with a planar geometry and have obtained some interesting results with the Giesekus and Johnson-Segelman equations. Actually, surpassing the Oldroyd-B model is an upgrade that has to be kept in mind for future studies.

CHAPTER 7
CONCLUSIONS AND FUTURE PERSPECTIVES

Fully unraveling the emergence of spatio-temporal complexity and the origin of turbulence in fluid dynamics, represent the ultimate goal of scholars that devote their efforts to this discipline. For this reason, researchers in the past century considered what were supposed to be simple problems to tackle this question. Among these, there is the study of wakes past a cylinder and the subsequent flow regimes. The transition from the von Kármán vortex street to turbulent wakes made of a superposition of large-scale coherent structures and incoherent motion on much smaller spatial scales, is still under study. In order to discern the cascade towards chaos, an oscillatory cylindrical cavity is proposed here as a subject of study because the same symmetry group, $O(2) \times Z_2^{ST}$, is present and seems more appropriate than other periodically forced cavity flows.

In order to solve the incompressible Navier-Stokes equations of a Newtonian fluid enclosed in a cylindrical cavity that is forced periodically in the axial direction, an efficient and accurate pseudospectral code has been adapted. This code, which is based on spectral-projection methods formulated in terms of primitive variables, has been the indispensable intrument to attain the main results of Chapters 3 and 4.

The basic state is axisymmetric, time-periodic and synchronous with the forcing. The linear stability analysis has revealed that this two-dimensional flow is able to become three-dimensional via the three different types of bifurcations reported for systems with the same symmetry group. Curiously, it has been observed a striking similarity between the marginal curve of the driven rectangular cavity and the one obtained in our case. The bifurcating modes might be synchronous or quasiperiodic, depending on the flow parameters. Synchronous modes preserve (B_1 and B_2) or break (A_2) the spatio-temporal symmetry, meanwhile quasiperiodic modes always break it because of the presence of the additional period, of course. The temporal evolution of axisymmetric states that are linearly unstable to these bifurcating modes, result in the non-linear saturated states of synchronous or quasiperiodic nature. As occurred in other periodically forced cavity flows, the modulated rotating waves MRW_1 are the only quasiperiodic stable solutions. Nonetheless, these synchronous and quasiperiodic states have been obtained for the first time in curved geometries. Truth is that resorting to simulations on a proper subspace was necessary in the annular geometry because of the strong competition of the modes.

Furthermore, the marginal stability curve has exposed the existence of three codimension-two points where two modes bifurcate simultaneously. The first bicritical point C_1 where

the two synchronous modes that preserve the spatio-temporal coincide, has been analysed carefully. Close to C_1, a B_1-B_2 mixed mode is obtained from the bifurcation of a pure B_2 state and the resulting solution is synchronous. The obtaining of this kind of solutions is somehow predictable, but the appearance of the rotating wave B_1RW and bursting solutions, which have an additional period, is more than remarkable. Although systems with the pure $1:2$ modal resonance exhibit analogous solutions, states with these properties have never been found in periodically forced systems. Away from C_1, there are other families of solutions that apparently are unrelated with this point and help to understand the transition to chaos. The pulsating solution B_1QP and the asymmetric bursts look like intermediate states before reaching chaos. The latter might stem from the asymmetric B_1-B_2 mixed modes and their occurrence might come from the distant MRW_1 branch of solutions. In contrast with other periodically forced cavities, a detailed examination of the transition to some chaotic states by means of a series of secondary bifurcations, has been possible. However, in order to complement the picture, it would be desirable to explore the remaining codimension-two points.

In addition, a first analysis of C_1 from the theoretical dynamical system perspective has been addressed. Systems with a pure $1:2$ modal resonance have been modeled employing continuous dynamical systems. Due to the forcing, a Poincaré map associated with strobing the flow at the frequency has been obtained. In order to be capable of performing an analysis, an interpolating ODE that approximates the map has been achieved, thus resulting in the normal form of the $1:2$ spatial resonance with $O(2)$ symmetry. As this issue has been examined before, the previous studies are a great asset in our problem. The combination of analytical calculations and numerical methods, are able to capture the main characteristics of the solutions obtained close to C_1 and provide a relatively good agreement with the bifurcation curves. It is clear that there are several open questions regarding the complete description of the normal form, but we would like to emphasise the preliminary character of these explorations. Of course, the normal form of the other codimension-two point has been found, but an analysis similar to the one that has been discussed still remains.

As can be observed, Newtonian fluids enclosed in a periodically driven cylindrical cavity offer a very rich dynamics and there are still many unresolved issues. Despite this fact, a new line of research has been commenced at the end of the thesis: the substitution of the Newtonian flow by another of viscoelastic character. To this end, a variety of numerical schemes mainly based on the Newtonian code have been programmed to simulate a dilute polymer solution (Oldroyd-B fluid) in our system. As a matter of fact, it seems that the polymers alter the properties and the instability mechanisms of the

flow critically. The highly hyperbolic nature of the equations tends to cause numerical instabilities, as well as a clustering of the growth rates of the different modes. Introducing perturbations of different amplitudes in the viscoelastic basic flow, provides the idea that the base state is only unstable if the initial perturbations are strong enough. The non-linear interactions are amplified and all the modes lead the transition in this case. The minimum perturbation that is able to destabilise the basic state shows a power-law dependence of the form $1/We^2$. At first sight, this transition recalls the scenarios of plane Couette and pipe Poiseuille flows, despite having a dependence with $1/Re$. With this argument, we think that using the same techniques might produce fruitful results to tackle this problem. However, if we are interested in comparing with the experimental work that is being conducted with very large aspect ratio cylinders, the most reasonable option will be the removal of the lids. Last but no least, employing more realistic models for viscoelastic fluids (FENE-P, Giesekus or Johnson-Segelman) has to be considered for future studies.

APPENDIX A

CYLINDRICAL COORDINATES

This appendix is devoted to write down in cylindrical coordinates all the terms that appear in the incompresible Navier-Stokes equations:

$$\nabla \cdot \mathbf{u} = 0, \tag{A.1a}$$

$$\partial_t \mathbf{u} + \mathbf{u} \cdot \nabla \mathbf{u} = -\nabla p + \nabla^2 \mathbf{u}, \tag{A.1b}$$

and constitutive equations for an Oldroyd-B viscoelastic fluid:

$$\nabla \cdot \mathbf{u} = 0, \tag{A.2a}$$

$$\partial_t \mathbf{u} + \mathbf{u} \cdot \nabla \mathbf{u} = -\nabla p + \frac{1}{Re}\left((1-\beta)\,\nabla \cdot \mathbb{T} + \beta \nabla^2 \mathbf{u}\right), \tag{A.2b}$$

$$\mathbb{T} = \frac{\mathbb{C} - \mathbb{I}}{We}, \tag{A.2c}$$

$$\partial_t \mathbb{C} + \mathbf{u} \cdot \nabla \mathbb{C} - \mathbb{C} \cdot \nabla \mathbf{u} - (\nabla \mathbf{u})^\dagger \cdot \mathbb{C} = -\frac{\mathbb{C} - \mathbb{I}}{We} + \left[\kappa \nabla^2 \mathbb{C}\right]. \tag{A.2d}$$

Consider a scalar, the kinematic pressure p. Then, a generic vector in cylindrical coordinates, the velocity $\mathbf{u}$, is expressed as

$$\mathbf{u} = u_r\,\mathbf{e_r} + u_\theta\,\mathbf{e}_\theta + u_z\,\mathbf{e_z} = u\,\mathbf{e_r} + v\,\mathbf{e}_\theta + w\,\mathbf{e_z}, \tag{A.3}$$

and a second-order tensor, the conformation tensor $\mathbb{C}$, is

$$\begin{aligned}\mathbb{C} = {} & C_{rr}\,\mathbf{e_r}\otimes\mathbf{e_r} + C_{r\theta}\,\mathbf{e_r}\otimes\mathbf{e}_\theta + C_{rz}\,\mathbf{e_r}\otimes\mathbf{e_z} + \\ & + C_{\theta r}\,\mathbf{e}_\theta\otimes\mathbf{e_r} + C_{\theta\theta}\,\mathbf{e}_\theta\otimes\mathbf{e}_\theta + C_{\theta z}\,\mathbf{e}_\theta\otimes\mathbf{e_z} + \\ & + C_{zr}\,\mathbf{e_z}\otimes\mathbf{e_r} + C_{z\theta}\,\mathbf{e_z}\otimes\mathbf{e}_\theta + C_{zz}\,\mathbf{e_z}\otimes\mathbf{e_z}.\end{aligned} \tag{A.4}$$

Since $\mathbb{C}$ is symmetric, this tensor can be written as follows:

$$\mathbb{C} = C_{rr}\,\mathbf{e_r}\otimes\mathbf{e_r} + C_{r\theta}\,\{\mathbf{e_r}\mathbf{e}_\theta\} + C_{rz}\,\{\mathbf{e_r}\mathbf{e_z}\} + C_{\theta\theta}\,\mathbf{e}_\theta\otimes\mathbf{e}_\theta + C_{\theta z}\,\{\mathbf{e}_\theta\mathbf{e_z}\} + C_{zz}\,\mathbf{e_z}\otimes\mathbf{e_z}, \tag{A.5}$$

where $\{\mathbf{e_i}\mathbf{e_j}\} = \mathbf{e_i}\otimes\mathbf{e_j} + \mathbf{e_j}\otimes\mathbf{e_i}$.

The divergence of a vector is a scalar

$$\nabla \cdot \mathbf{u} = \left(\partial_r + \frac{1}{r}\right) u_r + \frac{1}{r}\partial_\theta u_\theta + \partial_z u_z, \tag{A.6}$$

while the divergence of a symmetric second-order tensor results in a vector

$$\begin{aligned}\nabla\cdot\mathbb{C} = &\left(\partial_r C_{rr} + \frac{C_{rr}}{r} + \frac{1}{r}\partial_\theta C_{r\theta} - \frac{C_{\theta\theta}}{r} + \partial_z C_{rz}\right)\mathbf{e_r} + \\ &+ \left(\partial_r C_{r\theta} + \frac{2C_{r\theta}}{r} + \frac{1}{r}\partial_\theta C_{\theta\theta} + \partial_z C_{\theta z}\right)\mathbf{e}_\theta + \\ &+ \left(\partial_r C_{rz} + \frac{C_{rz}}{r} + \frac{1}{r}\partial_\theta C_{\theta z} + \partial_z C_{zz}\right)\mathbf{e_z}.\end{aligned} \tag{A.7}$$

The gradient of a scalar is a vector

$$\nabla p = \partial_r p\,\mathbf{e_r} + \frac{1}{r}\partial_\theta p\,\mathbf{e}_\theta + \partial_z p\,\mathbf{e_z}. \tag{A.8}$$

The gradient of a vector results in a second-order tensor

$$\begin{aligned}\nabla\mathbf{u} = &\,\partial_r u_r\,\mathbf{e_r}\otimes\mathbf{e_r} + \partial_r u_\theta\,\mathbf{e_r}\otimes\mathbf{e}_\theta + \partial_r u_z\,\mathbf{e_r}\otimes\mathbf{e_z} + \\ &+ \frac{1}{r}\left(\partial_\theta u_r - u_\theta\right)\,\mathbf{e}_\theta\otimes\mathbf{e_r} + \frac{1}{r}\left(\partial_\theta u_\theta + u_r\right)\,\mathbf{e}_\theta\otimes\mathbf{e}_\theta + \frac{1}{r}\partial_\theta u_z\,\mathbf{e}_\theta\otimes\mathbf{e_z} + \\ &+ \partial_z u_r\,\mathbf{e_z}\otimes\mathbf{e_r} + \partial_z u_\theta\,\mathbf{e_z}\otimes\mathbf{e}_\theta + \partial_z u_z\,\mathbf{e_z}\otimes\mathbf{e_z},\end{aligned} \tag{A.9}$$

meanwhile the gradient of a symmetric second-order tensor is one of third-order:

$$\begin{aligned}\nabla\mathbb{C} = &\,\partial_r C_{rr}\,\mathbf{e_r}\otimes\mathbf{e_r}\otimes\mathbf{e_r} + \partial_r C_{r\theta}\,\mathbf{e_r}\otimes\mathbf{e_r}\otimes\mathbf{e}_\theta + \partial_r C_{rz}\,\mathbf{e_r}\otimes\mathbf{e_r}\otimes\mathbf{e_z} + \\ &+ \partial_r C_{r\theta}\,\mathbf{e_r}\otimes\mathbf{e}_\theta\otimes\mathbf{e_r} + \partial_r C_{\theta\theta}\,\mathbf{e_r}\otimes\mathbf{e}_\theta\otimes\mathbf{e}_\theta + \partial_r C_{\theta z}\,\mathbf{e_r}\otimes\mathbf{e}_\theta\otimes\mathbf{e_z} + \\ &+ \partial_r C_{rz}\,\mathbf{e_r}\otimes\mathbf{e_z}\otimes\mathbf{e_r} + \partial_r C_{\theta z}\,\mathbf{e_r}\otimes\mathbf{e_z}\otimes\mathbf{e}_\theta + \partial_r C_{zz}\,\mathbf{e_r}\otimes\mathbf{e_z}\otimes\mathbf{e_z} + \\ &+ \frac{1}{r}\left(\partial_\theta C_{rr} - 2C_{r\theta}\right)\mathbf{e}_\theta\otimes\mathbf{e_r}\otimes\mathbf{e_r} + \frac{1}{r}\left(\partial_\theta C_{r\theta} + C_{rr} - C_{\theta\theta}\right)\mathbf{e}_\theta\otimes\mathbf{e_r}\otimes\mathbf{e}_\theta + \\ &+ \frac{1}{r}\left(\partial_\theta C_{rz} - C_{\theta z}\right)\mathbf{e}_\theta\otimes\mathbf{e_r}\otimes\mathbf{e_z} + \frac{1}{r}\left(\partial_\theta C_{r\theta} + C_{rr} - C_{\theta\theta}\right)\mathbf{e}_\theta\otimes\mathbf{e}_\theta\otimes\mathbf{e_r} + \\ &+ \frac{1}{r}\left(\partial_\theta C_{\theta\theta} + 2C_{r\theta}\right)\mathbf{e}_\theta\otimes\mathbf{e}_\theta\otimes\mathbf{e}_\theta + \frac{1}{r}\left(\partial_\theta C_{\theta z} + C_{rz}\right)\mathbf{e}_\theta\otimes\mathbf{e}_\theta\otimes\mathbf{e_z} + \\ &+ \frac{1}{r}\left(\partial_\theta C_{rz} - C_{\theta z}\right)\mathbf{e}_\theta\otimes\mathbf{e_z}\otimes\mathbf{e_r} + \frac{1}{r}\left(\partial_\theta C_{\theta z} + C_{rz}\right)\mathbf{e}_\theta\otimes\mathbf{e_z}\otimes\mathbf{e}_\theta + \\ &+ \frac{1}{r}\partial_\theta C_{zz}\,\mathbf{e}_\theta\otimes\mathbf{e_z}\otimes\mathbf{e_z} + \\ &+ \partial_z C_{rr}\,\mathbf{e_z}\otimes\mathbf{e_r}\otimes\mathbf{e_r} + \partial_z C_{r\theta}\,\mathbf{e_z}\otimes\mathbf{e_r}\otimes\mathbf{e}_\theta + \partial_z C_{rz}\,\mathbf{e_z}\otimes\mathbf{e_r}\otimes\mathbf{e_z} + \\ &+ \partial_z C_{r\theta}\,\mathbf{e_z}\otimes\mathbf{e}_\theta\otimes\mathbf{e_r} + \partial_z C_{\theta\theta}\,\mathbf{e_z}\otimes\mathbf{e}_\theta\otimes\mathbf{e}_\theta + \partial_z C_{\theta z}\,\mathbf{e_z}\otimes\mathbf{e}_\theta\otimes\mathbf{e_z} + \\ &+ \partial_z C_{rz}\,\mathbf{e_z}\otimes\mathbf{e_z}\otimes\mathbf{e_r} + \partial_z C_{\theta z}\,\mathbf{e_z}\otimes\mathbf{e_z}\otimes\mathbf{e}_\theta + \partial_z C_{zz}\,\mathbf{e_z}\otimes\mathbf{e_z}\otimes\mathbf{e_z}.\end{aligned} \tag{A.10}$$

Thus, the non-linear term of the Navier-Stokes equations is:

$$\begin{aligned}\mathbf{N}(\mathbf{u}) = \mathbf{u}\cdot\nabla\mathbf{u} = &\left(u_r\partial_r u_r + \frac{u_\theta}{r}\left(\partial_\theta u_r - u_\theta\right) + u_z\partial_z u_r\right)\mathbf{e_r} + \\ &+ \left(u_r\partial_r u_\theta + \frac{u_\theta}{r}\left(\partial_\theta u_\theta + u_r\right) + u_z\partial_z u_\theta\right)\mathbf{e}_\theta + \\ &+ \left(u_r\partial_r u_z + \frac{u_\theta}{r}\partial_\theta u_z + u_z\partial_z u_z\right)\mathbf{e_z}.\end{aligned} \tag{A.11}$$

The non-linear term for the constituve equations of a viscoelastic fluid is computed term by term

$$
\begin{aligned}
\mathbb{C}\cdot(\nabla\mathbf{u}) = &\left(C_{rr}\partial_r u_r + \frac{C_{r\theta}}{r}\left(\partial_\theta u_r - u_\theta\right) + C_{rz}\partial_z u_r\right)\mathbf{e_r}\otimes\mathbf{e_r} + \\
&+\left(C_{rr}\partial_r u_\theta + \frac{C_{r\theta}}{r}\left(\partial_\theta u_\theta + u_r\right) + C_{rz}\partial_z u_\theta\right)\mathbf{e_r}\otimes\mathbf{e}_\theta + \\
&+\left(C_{rr}\partial_r u_z + \frac{C_{r\theta}}{r}\partial_\theta u_z + C_{rz}\partial_z u_z\right)\mathbf{e_r}\otimes\mathbf{e_z} + \\
&+\left(C_{r\theta}\partial_r u_r + \frac{C_{\theta\theta}}{r}\left(\partial_\theta u_r - u_\theta\right) + C_{\theta z}\partial_z u_r\right)\mathbf{e}_\theta\otimes\mathbf{e_r} + \\
&+\left(C_{r\theta}\partial_r u_\theta + \frac{C_{\theta\theta}}{r}\left(\partial_\theta u_\theta + u_r\right) + C_{\theta z}\partial_z u_\theta\right)\mathbf{e}_\theta\otimes\mathbf{e}_\theta + \\
&+\left(C_{r\theta}\partial_r u_z + \frac{C_{\theta\theta}}{r}\partial_\theta u_z + C_{\theta z}\partial_z u_z\right)\mathbf{e}_\theta\otimes\mathbf{e_z} + \\
&+\left(C_{rz}\partial_r u_r + \frac{C_{\theta z}}{r}\left(\partial_\theta u_r - u_\theta\right) + C_{zz}\partial_z u_r\right)\mathbf{e_z}\otimes\mathbf{e_r} + \\
&+\left(C_{rz}\partial_r u_\theta + \frac{C_{\theta z}}{r}\left(\partial_\theta u_\theta + u_r\right) + C_{zz}\partial_z u_\theta\right)\mathbf{e_z}\otimes\mathbf{e}_\theta + \\
&+\left(C_{rz}\partial_r u_z + \frac{C_{\theta z}}{r}\partial_\theta u_z + C_{zz}\partial_z u_z\right)\mathbf{e_z}\otimes\mathbf{e_z},
\end{aligned}
\tag{A.12}
$$

$$
\begin{aligned}
(\nabla\mathbf{u})^\dagger\cdot\mathbb{C} = &\left(C_{rr}\partial_r u_r + \frac{C_{r\theta}}{r}\left(\partial_\theta u_r - u_\theta\right) + C_{rz}\partial_z u_r\right)\mathbf{e_r}\otimes\mathbf{e_r} + \\
&+\left(C_{r\theta}\partial_r u_r + \frac{C_{\theta\theta}}{r}\left(\partial_\theta u_r - u_\theta\right) + C_{\theta z}\partial_z u_r\right)\mathbf{e_r}\otimes\mathbf{e}_\theta + \\
&+\left(C_{rz}\partial_r u_r + \frac{C_{\theta z}}{r}\left(\partial_\theta u_r - u_\theta\right) + C_{zz}\partial_z u_r\right)\mathbf{e_r}\otimes\mathbf{e_z} + \\
&+\left(C_{rr}\partial_r u_\theta + \frac{C_{r\theta}}{r}\left(\partial_\theta u_\theta + u_r\right) + C_{rz}\partial_z u_\theta\right)\mathbf{e}_\theta\otimes\mathbf{e_r} + \\
&+\left(C_{r\theta}\partial_r u_\theta + \frac{C_{\theta\theta}}{r}\left(\partial_\theta u_\theta + u_r\right) + C_{\theta z}\partial_z u_\theta\right)\mathbf{e}_\theta\otimes\mathbf{e}_\theta + \\
&+\left(C_{rz}\partial_r u_\theta + \frac{C_{\theta z}}{r}\left(\partial_\theta u_\theta + u_r\right) + C_{zz}\partial_z u_\theta\right)\mathbf{e}_\theta\otimes\mathbf{e_z} + \\
&+\left(C_{rr}\partial_r u_z + \frac{C_{r\theta}}{r}\partial_\theta u_z + C_{rz}\partial_z u_z\right)\mathbf{e_z}\otimes\mathbf{e_r} + \\
&+\left(C_{r\theta}\partial_r u_z + \frac{C_{\theta\theta}}{r}\partial_\theta u_z + C_{\theta z}\partial_z u_z\right)\mathbf{e_z}\otimes\mathbf{e}_\theta + \\
&+\left(C_{rz}\partial_r u_z + \frac{C_{\theta z}}{r}\partial_\theta u_z + C_{zz}\partial_z u_z\right)\mathbf{e_z}\otimes\mathbf{e_z},
\end{aligned}
\tag{A.13}
$$

$$
\begin{aligned}
\mathbf{u}\cdot\nabla\mathbb{C} = &\left(u_r\partial_r C_{rr} + \frac{u_\theta}{r}\left(\partial_\theta C_{rr} - 2C_{r\theta}\right) + u_z\partial_z C_{rr}\right)\mathbf{e_r}\otimes\mathbf{e_r} + \\
&+\left(u_r\partial_r C_{r\theta} + \frac{u_\theta}{r}\left(\partial_\theta C_{r\theta} + C_{rr} - C_{\theta\theta}\right) + u_z\partial_z C_{r\theta}\right)\{\mathbf{e_r}\mathbf{e}_\theta\} + \\
&+\left(u_r\partial_r C_{rz} + \frac{u_\theta}{r}\left(\partial_\theta C_{rz} - C_{\theta z}\right) + u_z\partial_z C_{rz}\right)\{\mathbf{e_r}\mathbf{e_z}\} + \\
&+\left(u_r\partial_r C_{\theta\theta} + \frac{u_\theta}{r}\left(\partial_\theta C_{\theta\theta} + 2C_{r\theta}\right) + u_z\partial_z C_{\theta\theta}\right)\mathbf{e}_\theta\otimes\mathbf{e}_\theta + \\
&+\left(u_r\partial_r C_{\theta z} + \frac{u_\theta}{r}\left(\partial_\theta C_{\theta z} + C_{rz}\right) + u_z\partial_z C_{\theta z}\right)\{\mathbf{e}_\theta\mathbf{e_z}\} + \\
&+\left(u_r\partial_r C_{zz} + \frac{u_\theta}{r}\partial_\theta C_{zz} + u_z\partial_z C_{zz}\right)\mathbf{e_z}\otimes\mathbf{e_z}.
\end{aligned}
\tag{A.14}
$$

Therefore, the non-linear term that involves the conformation tensor and the velocity is:

$$
\begin{aligned}
&\mathbb{N}\left(\mathbf{u},\mathbb{C}\right) = \mathbf{v}\cdot\nabla\mathbb{C} - \mathbb{C}\cdot\nabla\mathbf{v} - \left(\nabla\mathbf{v}\right)^\dagger\cdot\mathbb{C} = \\
&=\Bigg(v_r\partial_r C_{rr} + \frac{v_\theta}{r}\partial_\theta C_{rr} + v_z\partial_z C_{rr} - 2C_{rr}\partial_r v_r - \frac{2C_{r\theta}}{r}\partial_\theta v_r - \\
&- 2C_{rz}\partial_z v_r\Bigg)\mathbf{e_r}\otimes\mathbf{e_r} + \\
&+\left(v_r\partial_r C_{r\theta} + \frac{v_\theta}{r}\partial_\theta C_{r\theta} + v_z\partial_z C_{r\theta} - C_{rr}\left(\partial_r v_\theta - \frac{v_\theta}{r}\right) - \right. \\
&\left. - C_{r\theta}\left(\frac{1}{r}\left(\partial_\theta v_\theta + v_r\right) + \partial_r v_r\right) - C_{rz}\partial_z v_\theta - \frac{C_{\theta\theta}}{r}\partial_\theta v_r - C_{\theta z}\partial_z v_r\right)\{\mathbf{e_r}\mathbf{e}_\theta\} + \\
&+\Bigg(v_r\partial_r C_{rz} + \frac{v_\theta}{r}\partial_\theta C_{rz} + v_z\partial_z C_{rz} - C_{rr}\partial_r v_z - \frac{C_{r\theta}}{r}\partial_\theta v_z - C_{rz}\left(\partial_z v_z + \partial_r v_r\right) - \\
&- \frac{C_{\theta z}}{r}\partial_\theta v_r - C_{zz}\partial_z v_r\Bigg)\{\mathbf{e_r}\mathbf{e_z}\} + \\
&+\Bigg(v_r\partial_r C_{\theta\theta} + \frac{v_\theta}{r}\partial_\theta C_{\theta\theta} + v_z\partial_z C_{\theta\theta} - 2C_{r\theta}\left(\partial_r v_\theta - \frac{v_\theta}{r}\right) - \frac{2C_{\theta\theta}}{r}\left(\partial_\theta v_\theta + v_r\right) - \\
&- 2C_{\theta z}\partial_z v_\theta\Bigg)\mathbf{e}_\theta\otimes\mathbf{e}_\theta + \\
&+\Bigg(v_r\partial_r C_{\theta z} + \frac{v_\theta}{r}\partial_\theta C_{\theta z} + v_z\partial_z C_{\theta z} - C_{r\theta}\partial_r v_z - C_{rz}\left(\partial_r v_\theta - \frac{v_\theta}{r}\right) - \frac{C_{\theta\theta}}{r}\partial_\theta v_z - \\
&- C_{\theta z}\left(\frac{1}{r}\left(\partial_\theta v_\theta + v_r\right) + \partial_z v_z\right) - C_{zz}\partial_z v_\theta\Bigg)\{\mathbf{e}_\theta\mathbf{e_z}\} + \\
&+\left(v_r\partial_r C_{zz} + \frac{v_\theta}{r}\partial_\theta C_{zz} + v_z\partial_z C_{zz} - 2C_{rz}\partial_r v_z - \frac{2C_{\theta z}}{r}\partial_\theta v_z - 2C_{zz}\partial_z v_z\right)\mathbf{e_z}\otimes\mathbf{e_z}.
\end{aligned}
\tag{A.15}
$$

The rotational of a vector is the vorticity:

$$
\nabla\times\mathbf{u} = \left(\frac{1}{r}\partial_\theta u_z - \partial_z u_\theta\right)\mathbf{e_r} + \left(\partial_z u_r - \partial_r u_z\right)\mathbf{e}_\theta + \left(\partial_r u_\theta + \frac{u_\theta}{r} - \frac{1}{r}\partial_\theta u_r\right)\mathbf{e_z}, \tag{A.16}
$$

and its rotational is:

$$\begin{aligned}\nabla\times\nabla\times\mathbf{u} = &\left(-\frac{1}{r^2}\partial^2_{\theta\theta}u_r - \partial^2_{zz}u_r + \frac{1}{r^2}\partial_\theta u_\theta + \frac{1}{r}\partial^2_{\theta r}u_\theta + \partial^2_{zr}u_z\right)\mathbf{e_r}+\\ &+\left(\frac{1}{r}\partial^2_{r\theta}u_r - \frac{1}{r^2}\partial_\theta u_r - \partial^2_{zz}u_\theta - \partial^2_{rr}u_\theta - \frac{1}{r}\partial_r u_\theta + \frac{u_\theta}{r^2} + \frac{1}{r}\partial^2_{z\theta}u_z\right)\mathbf{e}_\theta+\\ &+\left(\frac{1}{r}\partial_z u_r + \partial^2_{rz}u_r + \frac{1}{r}\partial^2_{\theta z}u_\theta - \frac{1}{r}\partial_r u_z - \partial^2_{rr}u_z - \frac{1}{r^2}\partial^2_{\theta\theta}u_z\right)\mathbf{e_z}.\end{aligned} \tag{A.17}$$

The laplacian of a scalar is

$$\nabla^2 p = \Delta p = \partial^2_{rr}p + \frac{1}{r}\partial_r p + \frac{1}{r^2}\partial^2_{\theta\theta}p + \partial^2_{zz}p, \tag{A.18}$$

where:

$$\Delta = \partial^2_{rr} + \frac{1}{r}\partial_r + \frac{1}{r^2}\partial^2_{\theta\theta} + \partial^2_{zz}. \tag{A.19}$$

Thus, the laplacian of a vector is

$$\begin{aligned}\nabla^2\mathbf{u} = &\left(\Delta u_r - \frac{u_r}{r^2} - \frac{2}{r^2}\partial_\theta u_\theta\right)\mathbf{e_r}+\\ &+\left(\Delta u_\theta - \frac{u_\theta}{r^2} + \frac{2}{r^2}\partial_\theta u_r\right)\mathbf{e}_\theta+\\ &+\Delta u_z\,\mathbf{e_z},\end{aligned} \tag{A.20}$$

whilst the laplacian of a second-order symmetric tensor is

$$\begin{aligned}\nabla^2\mathbb{C} = &\left(\Delta C_{rr} - \frac{4}{r^2}\partial_\theta C_{r\theta} - \frac{2}{r^2}(C_{rr} - C_{\theta\theta})\right)\mathbf{e_r}\otimes\mathbf{e_r}+\\ &+\left(\Delta C_{r\theta} + \frac{2}{r^2}\partial_\theta(C_{rr} - C_{\theta\theta}) - \frac{4}{r^2}C_{r\theta}\right)\{\mathbf{e_r}\mathbf{e}_\theta\}+\\ &+\left(\Delta C_{rz} - \frac{2}{r^2}\partial_\theta C_{\theta z} - \frac{1}{r^2}C_{rz}\right)\{\mathbf{e_r}\mathbf{e_z}\}+\\ &+\left(\Delta C_{\theta\theta} + \frac{4}{r^2}\partial_\theta C_{r\theta} + \frac{2}{r^2}(C_{rr} - C_{\theta\theta})\right)\mathbf{e}_\theta\otimes\mathbf{e}_\theta+\\ &+\left(\Delta C_{\theta z} + \frac{2}{r^2}\partial_\theta C_{rz} - \frac{1}{r^2}C_{\theta z}\right)\{\mathbf{e}_\theta\mathbf{e_z}\}+\\ &+\Delta C_{zz}\mathbf{e_z}\otimes\mathbf{e_z}.\end{aligned} \tag{A.21}$$

The laplacian operators couple different components of vectors and tensors, in each case. Appropriate linear combinations decouple the different components. For a vector field, the combination is:

$$u_\alpha = u_r - \mathrm{i}u_\theta = u - \mathrm{i}v, \tag{A.22a}$$

$$u_\beta = u_r + \mathrm{i}u_\theta = u + \mathrm{i}v, \tag{A.22b}$$

and the usual components can be computed afterwards by means of:

$$u_r = u = \frac{1}{2}\left(u_\alpha + u_\beta\right), \tag{A.23a}$$

$$u_\theta = v = \frac{\mathrm{i}}{2}\left(u_\alpha - u_\beta\right). \tag{A.23b}$$

For a second-order symmetric tensor field, the combination is:

$$C_{\alpha\beta} = C_{rr} + C_{\theta\theta}, \tag{A.24a}$$

$$C_{\alpha\alpha} = \frac{1}{2}\left(C_{rr} - C_{\theta\theta} - 2\mathrm{i}C_{r\theta}\right), \tag{A.24b}$$

$$C_{\beta\beta} = \frac{1}{2}\left(C_{rr} - C_{\theta\theta} + 2\mathrm{i}C_{r\theta}\right), \tag{A.24c}$$

$$C_{\alpha z} = C_{rz} - \mathrm{i}C_{\theta z}, \tag{A.24d}$$

$$C_{\beta z} = C_{rz} + \mathrm{i}C_{\theta z}, \tag{A.24e}$$

and the physical components are obtained employing the following expressions:

$$C_{rr} = \frac{1}{2}\left(C_{\alpha\beta} + C_{\alpha\alpha} + C_{\beta\beta}\right), \tag{A.25a}$$

$$C_{\theta\theta} = \frac{1}{2}\left(C_{\alpha\beta} - C_{\alpha\alpha} - C_{\beta\beta}\right), \tag{A.25b}$$

$$C_{r\theta} = \frac{\mathrm{i}}{2}\left(C_{\alpha\alpha} - C_{\beta\beta}\right), \tag{A.25c}$$

$$C_{rz} = \frac{1}{2}\left(C_{\alpha z} + C_{\beta z}\right), \tag{A.25d}$$

$$C_{\theta z} = \frac{\mathrm{i}}{2}\left(C_{\alpha z} - C_{\beta z}\right). \tag{A.25e}$$

APPENDIX B

NORMAL FORMS

A normal form is a low-dimensional system with a polynomial expression that is able to describe the dynamics of a full non-linear system in the neighbourhood of a bifurcation. As a matter of fact, normal forms can provide us with a clear and simple method to capture the dynamics of our system. Following the method of Iooss & Adelmeyer (1998), the derivation and application of normal forms of codimension-one bifurcations in systems with the $O(2)\times Z_2^{ST}$ symmetry group have been done in Marques *et al.* (2004). This work can be extended straightforwardly to the codimension-one bifurcations of our scenario but additional calculations are necessary for the normal forms of the three codimension-two points. Our intention is to obtain the normal form for each bifurcation, associated with the half-period-flip map $\mathcal{H}$, and then the corresponding normal form for the Poincaré map $\mathcal{P}=\mathcal{H}^2$ is easily achieved.

B.1 Codimension-two bifurcation point $\mathcal{F}_2^+$ and $\mathcal{F}_2^+$ with spatial ressonance $1:2$

In the first codimension-two point, the synchronous modes B_1 and B_2 bifurcate simultaneously. There is a pair of eigenfunctions associated with B_1, with eigenvalues $+1$, and amplitudes A and $\overline{A}$. The normal form for a $\mathcal{F}_2^+$ bifurcation is (see Marques *et al.*, 2004, sections §4.1 and §5.1)

$$\mathcal{H}: A\mapsto A\big(1+P(|A|^2,\mu)\big), \tag{B.1}$$

where P is a real polynomial and μ the bifurcation parameter. Up to and including third order terms in A and the small bifurcation parameter, the normal form is

$$\mathcal{H}:\ A\mapsto A(1+\mu-a|A|^2), \tag{B.2}$$

where $\mu, a\in\mathbb{R}$. The action of the symmetries and the linearised half-period-flip map on $(A,\overline{A})$ is

$$R_\alpha A=\mathrm{e}^{\mathrm{i}m\alpha}A,\qquad K_0A=\overline{A},\qquad L_HA=A, \tag{B.3}$$

where the exponent m indicates that the bifurcating eigenfunctions have broken the $SO(2)$ symmetry, but are still invariant under rotations of $\alpha=2\pi/m$. All the operators are real, and their action on the complex conjugate is obtained using $\mathcal{O}_p\overline{A}=\overline{\mathcal{O}_pA}$. The action of K_β can be obtained from $K_\beta=R_\beta K_0R_{-\beta}$: $K_\beta A=\mathrm{e}^{2\mathrm{i}m\beta}\overline{A}$.

In the codimension-two point where two $\mathcal{F}_2^+$ modes bifurcate simultaneously, we have two complex amplitudes (A, B), corresponding to exponents m and n respectively. In our problem, $(m, n) = (1, 2)$, corresponding to the B_1 and B_2 modes. The action of the symmetries and the linearised half-period-flip map on $X = (A, B, \overline{A}, \overline{B})$ is

$$R_\alpha(A, B) = (\mathrm{e}^{\mathrm{i}m\alpha}A, \mathrm{e}^{\mathrm{i}n\alpha}B), \quad K_0(A, B) = (\overline{A}, \overline{B}), \quad L_H(A, B) = (A, B). \tag{B.4}$$

The space-time symmetry L_H acts as the identity on A and B, so it does not impose any condition on the normal form, which possesses the structure

$$\mathcal{H} : \begin{cases} A \mapsto A + P_1(A, B, \overline{A}, \overline{B},), \\ B \mapsto B + P_2(A, B, \overline{A}, \overline{B}), \end{cases} \tag{B.5}$$

and the complex conjugate equations for $\overline{A}$ and $\overline{B}$. Introducing $P = (P_1, P_2, \overline{P_1}, \overline{P_2})$, the conditions the normal form $P(X)$ satisfies are given by

$$R_\alpha P(X) = P(R_\alpha X), \qquad K_0 P(X) = P(K_0 X), \qquad L_H P(X) = P(L_H X). \tag{B.6}$$

The expansion of these conditions read

$$P_1(\mathrm{e}^{\mathrm{i}m\alpha}A, \mathrm{e}^{\mathrm{i}n\alpha}B, \mathrm{e}^{-\mathrm{i}m\alpha}\overline{A}, \mathrm{e}^{-\mathrm{i}n\alpha}\overline{B}) = \mathrm{e}^{\mathrm{i}m\alpha}P_1(A, B, \overline{A}, \overline{B}), \tag{B.7}$$

$$P_2(\mathrm{e}^{\mathrm{i}m\alpha}A, \mathrm{e}^{\mathrm{i}n\alpha}B, \mathrm{e}^{-\mathrm{i}m\alpha}\overline{A}, \mathrm{e}^{-\mathrm{i}n\alpha}\overline{B}) = \mathrm{e}^{\mathrm{i}n\alpha}P_2(A, B, \overline{A}, \overline{B}), \tag{B.8}$$

$$P_1(\overline{A}, \overline{B}, A, B) = \overline{P_1(A, B, \overline{A}, \overline{B})}, \tag{B.9}$$

$$P_2(\overline{A}, \overline{B}, A, B) = \overline{P_2(A, B, \overline{A}, \overline{B})}. \tag{B.10}$$

The last two equations say that P_1 and P_2 are real polynomials. Applying the first two relations to a monomial of the form $A^p B^q \overline{A}^r \overline{B}^s$ in P_1 and P_2, the result is

$$\begin{aligned} P_1 : &\quad m(p - r - 1) = n(s - q), \\ P_2 : &\quad m(p - r) = n(s - q + 1). \end{aligned} \tag{B.11}$$

where $p, q, r, s \in \mathbb{N}_0$. Equation (B.11) for P_1 gives $p = r + 1 + jn$, $s = q + jm$, $j \in \mathbb{Z}$ and the form of the monomial is $A(A^n\overline{B}^m)^j|A|^{2r}|B|^{2q}$. In our particular case, where there is a spatial ressonance $1 : 2$, $A(A^2\overline{B})^j|A|^{2r}|B|^{2q}$ for $j \geq 0$ and $\overline{A}B(\overline{A}^2B)^j|A|^{2m}|B|^{2q}$ for $j < 0$. Treating P_2 similarly, the form of the monomial is $A^2(A^2\overline{B})^j|A|^{2r}|B|^{2q}$ for $j \geq 0$ and $B(\overline{A}^2B)^j|A|^{2r}|B|^{2q}$ for $j < 0$. The resulting polynomials are

$$\begin{aligned} P_1(A, B, \overline{A}, \overline{B}) =& A\, P_{11}(|A|^2, |B|^2, A^2\overline{B}) + \overline{A}B\, P_{12}(|A|^2, |B|^2, \overline{A}^2B), \\ P_2(A, B, \overline{A}, \overline{B}) =& B\, P_{21}(|A|^2, |B|^2, \overline{A}^2B) + A^2\, P_{22}(|A|^2, |B|^2, A^2\overline{B}), \end{aligned} \tag{B.12}$$

where all of them are real in their arguments. Therefore, the normal form is

$$\mathcal{H}: \begin{cases} A \mapsto A\big(1 + P_{11}(|A|^2, |B|^2, A^2\overline{B})\big) + \overline{A}B\, P_{12}(|A|^2, |B|^2, \overline{A}^2 B), \\ B \mapsto B\big(1 + P_{21}(|A|^2, |B|^2, \overline{A}^2 B)\big) + A^2\, P_{22}(|A|^2, |B|^2, A^2\overline{B}). \end{cases} \tag{B.13}$$

Up to and including third order terms and small bifurcation parameters, the normal form becomes

$$\mathcal{H}: \begin{cases} A \mapsto A(1 + \mu + a_1|A|^2 + b_1|B|^2) + c_1\overline{A}B, \\ B \mapsto B(1 + \nu + a_2|A|^2 + b_2|B|^2) + c_2A^2, \end{cases} \tag{B.14}$$

where the bifurcation parameters and the coefficients $\mu, \nu, a_i, b_i, c_i \in \mathbb{R}$. The Poincaré map normal form, $\mathcal{P} = \mathcal{H}^2$ has exactly the same form, but with different values of the parameters and coefficients.

B.1.1 Hypernormal form

By assuming the non-degeneracy condition $c_1c_2 \neq 0$, additional simplifications in the normal form are possible. The resulting map is called the hypernormal form (Algaba *et al.*, 1998; Murdock, 2004). Let us consider a second order coordinate transformation

$$P = A + d\overline{A}B, \quad Q = B + eA^2, \quad \text{with inverse} \tag{B.15}$$

$$A = P(1 + de|P|^2 + d^2|Q|^2) - d\overline{P}Q, \quad B = Q(1 + 2de|P|^2) - eP^2, \tag{B.16}$$

that does not change the second order terms and do not introduce new terms in the normal form, but changes the coefficients of the third order terms. The map (B.14) in the new coordinates is

$$P \mapsto P\Big(1 + \mu + (a_1 + dc_2 - ec_1)|P|^2 + b_1|Q|^2\Big) + c_1\overline{P}Q, \tag{B.17}$$

$$Q \mapsto Q\Big(1 + \nu + (a_2 + 2ec_1 - 2dc_2)|P|^2 + b_2|Q|^2\Big) + c_2P^2. \tag{B.18}$$

As d and e appear in the same combination $dc_2 - ec_1$, only one of the cubic terms in (B.14) can be simplified. The simplification will be postponed for the moment.

Additional simplifications can be introduced into the normal form (B.14) by rescaling the amplitudes A and B: given a map $x_i \mapsto f_i(x_1, \ldots, x_n)$, $i = 1, \ldots, n$, it can be rescaled $y_i = k_ix_i$, and

$$y_i \mapsto k_if_i(x_1, \ldots, x_n) = k_if_i(y_1/k_1, \ldots, y_n/k_n) = \tilde{f}_i(y_1, \ldots, y_n). \tag{B.19}$$

Applying this method to (B.14) results in the same expression with different coefficients:

$$\tilde{a}_i = \frac{a_i}{k_1^2}, \quad \tilde{b}_i = \frac{b_i}{k_2^2}, \quad i = 1, 2; \quad \tilde{c}_1 = \frac{c_1}{k_2}, \quad \tilde{c}_2 = \frac{c_2 k_2}{k_1^2}. \tag{B.20}$$

As all coefficients are real, the case k_i real is the only under consideration. Assuming the non-degeneracy condition $c_1 c_2 \neq 0$, and choosing $k_1 = \sqrt{|c_1 c_2|}$, $k_2 = c_1$ and $\sigma = \text{sign}(c_1 c_2)$, we arrive at the hipernormal form (with $\tilde{}$ suppressed for convenience)

$$\mathcal{P} : \begin{cases} A \mapsto A(1 + \mu + a_1|A|^2 + b_1|B|^2) + \overline{A}B, \\ B \mapsto B(1 + \nu + a_2|A|^2 + b_2|B|^2) + \sigma A^2, \end{cases} \tag{B.21}$$

where the bifurcation parameters μ, ν and the coefficients a_1, b_1, b_2 are all real. Close to the codimension-two point $\mu = \nu = 0$, the bifurcations corresponding to B_1 and B_2 are non-degenerate and supercritical, so we expect $a_1 < 0$ and $b_2 < 0$.

B.2 Codimension-two bifurcation point $\mathcal{F}_2^+$ and $\mathcal{F}_4^C$ with spatial ressonance $1:2$

In the second codimension-two point, the synchronous mode B_2 and the quasiperiodic mode MRW_1 bifurcate at the same time. All the considerations for the B_2 mode commented in the former section are applied here straightforwardly. Concerning to the quasiperiodic mode, there are two pairs of eigenfunctions associated with MRW_1, whose complex eigenvalues are $\mathrm{e}^{\pm \mathrm{i}\theta/2}$ with θ being an arbitrary angle, and amplitudes B, C, $\overline{B}$ and $\overline{C}$. The normal form for a $\mathcal{F}_4^C$ bifurcation is (see Marques *et al.*, 2004, sections §4.2 and §5.3)

$$\mathcal{H} : \begin{cases} B \mapsto B\big(\mathrm{e}^{\mathrm{i}\theta/2} + Q(|B|^2, |C|^2, \nu)\big), \\ C \mapsto C\big(\mathrm{e}^{\mathrm{i}\theta/2} + Q(|C|^2, |B|^2, \nu)\big), \end{cases} \tag{B.22}$$

where Q is a complex polynomial and ν the bifurcation parameter. Up to and including third order terms in B and C and the small bifurcation parameter, the normal form is

$$\mathcal{H} : \begin{cases} B \mapsto B(\mathrm{e}^{\mathrm{i}\theta/2} + \nu + b|B|^2 + c|C|^2), \\ C \mapsto C(\mathrm{e}^{\mathrm{i}\theta/2} + \nu + b|C|^2 + c|B|^2), \end{cases} \tag{B.23}$$

where $\nu, b, c \in \mathbb{C}$. The action of the symmetries and the linearised half-period-flip map on $(B, C, \overline{B}, \overline{C})$ is

$$R_\alpha(B, C, \overline{B}, \overline{C}) = (\mathrm{e}^{\mathrm{i}n\alpha}B, \mathrm{e}^{-\mathrm{i}n\alpha}C, \mathrm{e}^{-\mathrm{i}n\alpha}\overline{B}, \mathrm{e}^{\mathrm{i}n\alpha}\overline{C}), \tag{B.24a}$$

$$K_\beta(B, C, \overline{B}, \overline{C}) = (C, B, \overline{C}, \overline{B}), \tag{B.24b}$$

$$L_H(B, C, \overline{B}, \overline{C}) = (\mathrm{e}^{\mathrm{i}\theta/2}B, \mathrm{e}^{\mathrm{i}\theta/2}C, \mathrm{e}^{-\mathrm{i}\theta/2}\overline{B}, \mathrm{e}^{-\mathrm{i}\theta/2}\overline{C}), \tag{B.24c}$$

where $n = 1$. Therefore, the action of the symmetries and the linearised half-period-flip map on $X = (A, B, C, \overline{A}, \overline{B}, \overline{C})$ is

$$R_\alpha(A, B, C, \overline{A}, \overline{B}, \overline{C}) = (\mathrm{e}^{\mathrm{i}m\alpha}A, \mathrm{e}^{\mathrm{i}n\alpha}B, \mathrm{e}^{-\mathrm{i}n\alpha}C, \mathrm{e}^{-\mathrm{i}m\alpha}\overline{A}, \mathrm{e}^{-\mathrm{i}n\alpha}\overline{B}, \mathrm{e}^{\mathrm{i}n\alpha}\overline{C}), \tag{B.25a}$$

$$K_\beta(A, B, C, \overline{A}, \overline{B}, \overline{C}) = (\overline{A}, C, B, A, \overline{C}, \overline{B}), \tag{B.25b}$$

$$L_H(A, B, C, \overline{A}, \overline{B}, \overline{C}) = (A, \mathrm{e}^{\mathrm{i}\theta/2}B, \mathrm{e}^{\mathrm{i}\theta/2}C, \overline{A}, \mathrm{e}^{-\mathrm{i}\theta/2}\overline{B}, \mathrm{e}^{-\mathrm{i}\theta/2}\overline{C}). \tag{B.25c}$$

The action of the space-time symmetry L_H is no longer the identity and introduces some conditions over the normal form, which has the structure

$$\mathcal{H} : \begin{cases} A \mapsto A + Q_1(A, B, C, \overline{A}, \overline{B}, \overline{C}), \\ B \mapsto B\mathrm{e}^{\mathrm{i}\theta/2} + Q_2(A, B, C, \overline{A}, \overline{B}, \overline{C}), \\ C \mapsto C\mathrm{e}^{\mathrm{i}\theta/2} + Q_3(A, B, C, \overline{A}, \overline{B}, \overline{C}), \end{cases} \tag{B.26}$$

and the complex conjugate equations for $\overline{A}$, $\overline{B}$ and $\overline{C}$. Here, all the Q_i are complex polynomials. Introducing $Q = (Q_1, Q_2, Q_3, \overline{Q}_1, \overline{Q}_2, \overline{Q}_3)$, the conditions the normal form $Q(X)$ satisfies are given by

$$R_\alpha Q(X) = Q(R_\alpha X), \qquad K_\beta Q(X) = Q(K_\beta X), \qquad L_H Q(X) = Q(L_H X). \tag{B.27}$$

Expanding these expressions, they become

$$\mathrm{e}^{\mathrm{i}m\alpha}Q_1(A, B, C, \overline{A}, \overline{B}, \overline{C}) = Q_1(\mathrm{e}^{\mathrm{i}m\alpha}A, \mathrm{e}^{\mathrm{i}n\alpha}B, \mathrm{e}^{-\mathrm{i}n\alpha}C, \mathrm{e}^{-\mathrm{i}m\alpha}\overline{A}, \mathrm{e}^{-\mathrm{i}n\alpha}\overline{B}, \mathrm{e}^{\mathrm{i}n\alpha}\overline{C}), \tag{B.28a}$$

$$\overline{Q_1(A, B, C, \overline{A}, \overline{B}, \overline{C})} = Q_1(\overline{A}, C, B, A, \overline{C}, \overline{B}), \tag{B.28b}$$

$$Q_1(A, B, C, \overline{A}, \overline{B}, \overline{C}) = Q_1(A, \mathrm{e}^{\mathrm{i}\theta/2}B, \mathrm{e}^{\mathrm{i}\theta/2}C, \overline{A}, \mathrm{e}^{-\mathrm{i}\theta/2}\overline{B}, \mathrm{e}^{-\mathrm{i}\theta/2}\overline{C}), \tag{B.28c}$$

$$\mathrm{e}^{\mathrm{i}n\alpha}Q_2(A, B, C, \overline{A}, \overline{B}, \overline{C}) = Q_2(\mathrm{e}^{\mathrm{i}m\alpha}A, \mathrm{e}^{\mathrm{i}n\alpha}B, \mathrm{e}^{-\mathrm{i}n\alpha}C, \mathrm{e}^{-\mathrm{i}m\alpha}\overline{A}, \mathrm{e}^{-\mathrm{i}n\alpha}\overline{B}, \mathrm{e}^{\mathrm{i}n\alpha}\overline{C}), \tag{B.28d}$$

$$Q_3(A, B, C, \overline{A}, \overline{B}, \overline{C}) = Q_2(\overline{A}, C, B, A, \overline{C}, \overline{B}), \tag{B.28e}$$

$$\mathrm{e}^{\mathrm{i}\theta/2}Q_2(A, B, C, \overline{A}, \overline{B}, \overline{C}) = Q_2(A, \mathrm{e}^{\mathrm{i}\theta/2}B, \mathrm{e}^{\mathrm{i}\theta/2}C, \overline{A}, \mathrm{e}^{-\mathrm{i}\theta/2}\overline{B}, \mathrm{e}^{-\mathrm{i}\theta/2}\overline{C}), \tag{B.28f}$$

$$\mathrm{e}^{-\mathrm{i}n\alpha}Q_3(A, B, C, \overline{A}, \overline{B}, \overline{C}) = Q_3(\mathrm{e}^{\mathrm{i}m\alpha}A, \mathrm{e}^{\mathrm{i}n\alpha}B, \mathrm{e}^{-\mathrm{i}n\alpha}C, \mathrm{e}^{-\mathrm{i}m\alpha}\overline{A}, \mathrm{e}^{-\mathrm{i}n\alpha}\overline{B}, \mathrm{e}^{\mathrm{i}n\alpha}\overline{C}), \tag{B.28g}$$

$$Q_2(A, B, C, \overline{A}, \overline{B}, \overline{C}) = Q_3(\overline{A}, C, B, A, \overline{C}, \overline{B}), \tag{B.28h}$$

$$\mathrm{e}^{\mathrm{i}\theta/2}Q_3(A, B, C, \overline{A}, \overline{B}, \overline{C}) = Q_3(A, \mathrm{e}^{\mathrm{i}\theta/2}B, \mathrm{e}^{\mathrm{i}\theta/2}C, \overline{A}, \mathrm{e}^{-\mathrm{i}\theta/2}\overline{B}, \mathrm{e}^{-\mathrm{i}\theta/2}\overline{C}). \tag{B.28i}$$

These relations have to be applied again to a polynomial of the form $A^p B^q C^r \overline{A}^s \overline{B}^t \overline{C}^u$, where $p, q, r, s, t, u \in \mathbb{N}_0$.

For Q_1 and assuming $\theta/(2\pi) \notin \mathbb{Q}$, (B.28a) and (B.28c) result in two constrains for the exponents:

$$m(p - s - 1) = n(r - u + t - q), \qquad r - u = t - q, \tag{B.29}$$

and there are two scenarios to be considered, $r-u \geq 0$ or $r-u < 0$.

Case 1: $r-u = t-q = v \geq 0$. Then, $m(p-s-1) = 2nv$ and considering $w = \gcd(m, 2n)$ the greatest common divisor of m and $2n$: $m = jw$, $2n = kw$ and $\gcd(j,k) = 1$, so they do not have any common factor. For instance, for $m = 2$ and $n = 1$, $w = 2$ and $j = k = 1$ are obtained. Therefore, from $j(p-s-1) = kv$ it follows $p-s-1 = kl$ with $v = jl$ for some integer $l \geq 0$. The exponents of the monomial satisfy

$$p = s + kl + 1, \quad r = u + jl, \quad t = q + jl, \tag{B.30}$$

where $q, s, u, l \in \mathbb{N}_0$ and $j, k \in \mathbb{N}$. The monomial is $A|A|^{2s}|B|^{2q}|C|^{2u}\big(A^k(\overline{B}C)^j\big)^l$. Grouping all these monomials together, the contribution to Q_1 is

$$AQ_{11}\big(|A|^2, |B|^2, |C|^2, A^k(\overline{B}C)^j\big), \tag{B.31}$$

where Q_{11} is an arbitrary complex polynomial.

Case 2: $r-u = t-q = -v$, $v > 0$. Then, $m(s-p+1) = 2nv$; let $w = \gcd(m, 2n)$, $m = jw$, $2n = kw$ and $\gcd(j,k) = 1$ as before. From $j(s-p+1) = kv$ it follows $s-p+1 = kl'$ and $v = jl'$. But $l' > 0$ because $v > 0$, so $l' = l+1$, with $l \geq 0$ and the exponents of the monomial fulfill

$$q = t + jl + j, \quad s = p + kl + k - 1, \quad u = r + jl + j, \tag{B.32}$$

where $p, r, t, l \in \mathbb{N}_0$ and $j, k \in \mathbb{N}$. The monomial is $\overline{A}^{k-1}(B\overline{C})^j|A|^{2p}|B|^{2t}|C|^{2r}\big(\overline{A}^k(B\overline{C})^j\big)^l$. Gathering all these monomials, the following contribution to Q_1 is procured

$$\overline{A}^{k-1}(B\overline{C})^j Q_{12}\big(|A|^2, |B|^2, |C|^2, \overline{A}^k(B\overline{C})^j\big), \tag{B.33}$$

where Q_{12} is another arbitrary complex polynomial.

The normal form Q_1 is the sum of the contributions (B.31) and (B.33), and the last remaining condition (B.28b) must be satisfied. This results in

$$\overline{Q_{11}\big(|A|^2, |B|^2, |C|^2, A^k(\overline{B}C)^j\big)} = Q_{11}\big(|A|^2, |C|^2, |B|^2, \overline{A}^k(B\overline{C})^j\big), \tag{B.34a}$$

$$\overline{Q_{12}\big(|A|^2, |B|^2, |C|^2, \overline{A}^k(B\overline{C})^j\big)} = Q_{12}\big(|A|^2, |C|^2, |B|^2, A^k(\overline{B}C)^j\big). \tag{B.34b}$$

Conditions (B.34) ascertain a relationship between the monomials of the form $|B|^{2q}|C|^{2r}$ and $|B|^{2r}|C|^{2q}$, without any contribution of all other factors, yielding combinations of the form

$$|A|^{2p}\big(\alpha|B|^{2q}|C|^{2r} + \overline{\alpha}|B|^{2r}|C|^{2q}\big)\big(A^k(\overline{B}C)^j\big)^l \quad \text{for } Q_{11}, \tag{B.35a}$$

$$|A|^{2p}\big(\alpha|B|^{2q}|C|^{2r} + \overline{\alpha}|B|^{2r}|C|^{2q}\big)\big(\overline{A}^k(B\overline{C})^j\big)^l \quad \text{for } Q_{12}. \tag{B.35b}$$

The final expression for Q_1 is

$$Q_1(A,B,C,\overline{A},\overline{B},\overline{C}) = AQ_{11}\big(|A|^2,|B|^2,|C|^2,A^k(\overline{B}C)^j\big)+ \\ +\overline{A}^{k-1}(B\overline{C})^jQ_{12}\big(|A|^2,|B|^2,|C|^2,\overline{A}^k(B\overline{C})^j\big), \quad \text{(B.36)}$$

where Q_{11} and Q_{12} are complex polynomials with monomials gathered as mentioned in (B.35).

Equations (B.28e) and (B.28h) are identical, and provide Q_3 once Q_2 is known. Therefore, determining Q_2 is the only remaining part. Keeping in mind the same considerations made with Q_1, (B.28d) and (B.28f) result in two constrains for the exponents of the polynomial

$$m(p-s) = n(r-u+t-q+1), \qquad r-u = t-q+1, \quad \text{(B.37)}$$

and once again two cases have to be tackled, $r-u>0$ or $r-u\leq 0$.

Case 1: $r-u=t-q+1=v+1$, $v\geq 0$. Introducing j and k as before, $j(p-s)=k(v+1)$, so $p-s=kl'$ and $v+1=jl'$. But $l'>0$ because $v\geq 0$, so $l'=l+1$, $l\geq 0$ and the exponents of the monomial satisfy

$$p = s+kl+k, \quad r = u+jl+j, \quad t = q+jl+j-1, \quad \text{(B.38)}$$

where $q,s,u,l\in\mathbb{N}_0$ and $j,k\in\mathbb{N}$. The monomial is $A^k\overline{B}^{j-1}C^j|A|^{2s}|B|^{2q}|C|^{2u}\big(A^k(\overline{B}C)^j\big)^l$. After grouping all these monomials together, the following contribution to Q_2 is obtained:

$$A^k\overline{B}^{j-1}C^j\,Q_{22}\big(|A|^2,|B|^2,|C|^2,A^k(\overline{B}C)^j\big), \quad \text{(B.39)}$$

where Q_{22} is an arbitrary complex polynomial.

Case 2: $r-u=t-q+1=-v, v\geq 0$. With the same procedure, $j(s-p)=kv$ is procured, so $s-p=kl$ and $v=jl$, $l\geq 0$ and the exponents of the monomial satisfy

$$q = t+jl+1, \quad s = p+kl, \quad u = r+jl, \quad \text{(B.40)}$$

where $p,r,t,l\in\mathbb{N}_0$ and $j,k\in\mathbb{N}$. The monomial is $B|A|^{2p}|B|^{2t}|C|^{2r}\big(\overline{A}^k(B\overline{C})^j\big)^l$ and gathering together all these monomials the following contribution to Q_2 is achieved:

$$B\,Q_{21}\big(|A|^2,|B|^2,|C|^2,\overline{A}^k(B\overline{C})^j\big), \quad \text{(B.41)}$$

where Q_{21} is an arbitrary complex polynomial.

Summing up the contributions (B.39) and (B.41), and using (B.28e), the final expressions for Q_2 and Q_3 are

$$\begin{aligned} Q_2(A,B,C,\overline{A},\overline{B},\overline{C}) = {} & B\,Q_{21}\big(|A|^2,|B|^2,|C|^2,\overline{A}^{\,k}(B\overline{C})^j\big)+ \\ & + A^k\overline{B}^{\,j-1}C^j\,Q_{22}\big(|A|^2,|B|^2,|C|^2,A^k(\overline{B}C)^j\big), \qquad \text{(B.42)} \\ Q_3(A,B,C,\overline{A},\overline{B},\overline{C}) = {} & C\,Q_{21}\big(|A|^2,|C|^2,|B|^2,A^k(\overline{B}C)^j\big)+ \\ & + \overline{A}^k B^j\overline{C}^{\,j-1}\,Q_{22}\big(|A|^2,|C|^2,|B|^2,\overline{A}^{\,k}(B\overline{C})^j\big), \qquad \text{(B.43)} \end{aligned}$$

where Q_2 and Q_3 are arbitrary complex polynomials.

Curiously, the apparently more general expressions

$$Q_{ii'}\big(|A|^2,|B|^2,|C|^2,A^k(\overline{B}C)^j,\overline{A}^{\,k}(B\overline{C})^j\big) \qquad \text{(B.44)}$$

in (B.36, B.42, B.43) also satisfy (B.28). Nevertheless, the five arguments in (B.44) are not independent, and verify

$$A^k(\overline{B}C)^j\ \cdot\ \overline{A}^{\,k}(B\overline{C})^j = |A|^{2k}|B|^{2j}|C|^{2j}, \qquad \text{(B.45)}$$

$$A\ \cdot\ \overline{A}^{\,k}(B\overline{C})^j = \overline{A}^{\,k-1}(B\overline{C})^j\ \cdot\ |A|^2 \qquad \text{(B.46)}$$

$$\overline{A}^{\,k-1}(B\overline{C})^j\ \cdot\ A^k(\overline{B}C)^j = A\ \cdot\ |A|^{2k-2}|B|^{2j}|C|^{2j}, \qquad \text{(B.47)}$$

$$B\ \cdot\ A^k(\overline{B}C)^j = A^k\overline{B}^{\,j-1}C^j\ \cdot\ |B|^2 \qquad \text{(B.48)}$$

$$A^k\overline{B}^{\,j-1}C^j\ \cdot\ \overline{A}^{\,k}(B\overline{C})^j = B\ \cdot\ |A|^{2k}|B|^{2j-2}|C|^{2j}, \qquad \text{(B.49)}$$

$$C\ \cdot\ \overline{A}^{\,k}(B\overline{C})^j = \overline{A}^{\,k}B^j\,\overline{C}^{\,j-1}\ \cdot\ |C|^2 \qquad \text{(B.50)}$$

$$\overline{A}^{\,k}B^j\,\overline{C}^{\,j-1}\ \cdot\ A^k(\overline{B}C)^j = C\ \cdot\ |A|^{2k}|B|^{2j}|C|^{2j-2}. \qquad \text{(B.51)}$$

By means of employing (B.45), all monomials in $Q_{ii'}$ can be eliminated with simultaneous powers of $A^k(\overline{B}C)^j$ and $\overline{A}^{\,k}(B\overline{C})^j$. Then, by using (B.46) and (B.47) all monomials containing $\overline{A}^{\,k}(B\overline{C})^j$ can be transferred from Q_{11} to Q_{12}, the same for the ones that possess $A^k(\overline{B}C)^j$ from Q_{12} to Q_{11}. Considering now the case in Q_2 and by means of utilising (B.48) and (B.49), all monomials possessing $A^k(\overline{B}C)^j$ can be moved from Q_{21} to Q_{22}, and all monomials that contain $\overline{A}^{\,k}(B\overline{C})^j$ from Q_{22} to Q_{21}. At last, in Q_3, employing (B.50) and (B.51), all monomials that include $\overline{A}^{\,k}(B\overline{C})^j$ can be transferred from Q_{21} to Q_{22}, and all monomials possessing $A^k(\overline{B}C)^j$ from Q_{22} to Q_{21}. Thus, B.36, B.42, B.43 are recovered. In these expressions the polynomials in the normal form are uniquely determined, while in the apparently more general form (B.44) there seem to be many different ways to express the polynomials, and the unicity is lost.

Turning back to our particular case, where $m = 2$ and $n = 1$, so $j = k = 1$, and the

polynomials are

$$Q_1 = A\,Q_{11}\big(|A|^2,|B|^2,|C|^2,A\overline{B}C\big) + B\overline{C}\,Q_{12}\big(|A|^2,|B|^2,|C|^2,\overline{A}B\overline{C}\big), \tag{B.52}$$

$$Q_2 = B\,Q_{21}\big(|A|^2,|B|^2,|C|^2,\overline{A}B\overline{C}\big) + AC\,Q_{22}\big(|A|^2,|B|^2,|C|^2,A\overline{B}C\big), \tag{B.53}$$

$$Q_3 = C\,Q_{21}\big(|A|^2,|C|^2,|B|^2,A\overline{B}C\big) + \overline{A}B\,Q_{22}\big(|A|^2,|C|^2,|B|^2,\overline{A}B\overline{C}\big). \tag{B.54}$$

Up to and including third order terms and small bifurcation parameters, the normal form can be written as

$$\mathcal{H}:\begin{cases} A \mapsto A\big(1+\mu-a|A|^2-e|B|^2-\overline{e}|C|^2\big)+dB\overline{C},\\ B \mapsto B\big(\mathrm{e}^{\mathrm{i}\theta/2}+\nu-f|A|^2-b|B|^2-c|C|^2\big)+gAC,\\ C \mapsto C\big(\mathrm{e}^{\mathrm{i}\theta/2}+\nu-f|A|^2-b|C|^2-c|B|^2\big)+g\overline{A}B, \end{cases} \tag{B.55}$$

where $\mu, a, d \in \mathbb{R}$, whilst $\nu, b, c, e, f, g \in \mathbb{C}$. The Poincaré map normal form, $\mathcal{P} = \mathcal{H}^2$ has exactly the same expression with another parameters and coefficients, given by

$$\begin{gathered} \tilde{\theta} = 2\theta, \quad \tilde{\mu} = \mu(2+\mu), \quad \tilde{a} = 2a(1+\mu), \quad \tilde{e} = 2e(1+\mu) - d\overline{g}(\mathrm{e}^{\mathrm{i}\theta/2}+\nu),\\ \tilde{d} = d(1+\mu+|\mathrm{e}^{\mathrm{i}\theta/2}+\nu|^2), \quad \tilde{\nu} = \nu(2\mathrm{e}^{\mathrm{i}\theta/2}+\nu), \quad \tilde{f} = 2f(\mathrm{e}^{\mathrm{i}\theta/2}+\nu) - g^2(1+\mu),\\ \tilde{b} = 2b(\mathrm{e}^{\mathrm{i}\theta/2}+\nu), \quad \tilde{c} = (2c-dg)(\mathrm{e}^{\mathrm{i}\theta/2}+\nu), \quad \tilde{g} = g(2+\mu)(\mathrm{e}^{\mathrm{i}\theta/2}+\nu). \end{gathered} \tag{B.56}$$

Additional simplifications can be performed into the normal form (B.55) by rescaling the amplitudes A, B and C utilising the rescaling method of the previous section. Applying (B.19) to (B.55), with complex k_i, results in the same expression but with different coefficients:

$$\begin{gathered} \tilde{a} = \frac{a}{|k_1|^2},\ \tilde{b} = \frac{b}{|k_2|^2} = \frac{b}{|k_3|^2},\ \tilde{c} = \frac{c}{|k_2|^2} = \frac{c}{|k_3|^2},\ \tilde{d} = \frac{k_1 d}{k_2\overline{k}_3},\\ \tilde{e} = \frac{e}{|k_2|^2} = \frac{e}{|k_3|^2},\ \tilde{f} = \frac{f}{|k_1|^2},\ \tilde{g} = \frac{k_2 g}{k_1 k_3} = \frac{k_3 g}{\overline{k}_1 k_2}. \end{gathered} \tag{B.57}$$

These equations impose some restrictions on the k_i scaling factors, in order to preserve the structure of the normal form. Using $k_i = r_i\mathrm{e}^{\mathrm{i}\alpha_i}$ and replacing in the former equations, the following expressions are achieved

$$\mathrm{e}^{\mathrm{i}(\alpha_1-\alpha_2+\alpha_3)} = \pm 1 = s, \quad \frac{k_1}{k_2\overline{k}_3} = \frac{s r_1}{r_2^2}, \quad \frac{k_2}{k_1 k_3} = \frac{k_3}{\overline{k}_1 k_2} = \frac{s}{r_1}. \tag{B.58}$$

All transformation factors in (B.57) are real, and using complex k_i do not make any improvement at all. At last, the coefficients become

$$\tilde{a} = \frac{a}{r_1^2},\ \tilde{b} = \frac{b}{r_2^2},\ \tilde{c} = \frac{c}{r_2^2},\ \tilde{d} = \frac{s r_1 d}{r_2^2},\ \tilde{e} = \frac{e}{r_2^2},\ \tilde{f} = \frac{f}{r_1^2},\ \tilde{g} = \frac{sg}{r_1}. \tag{B.59}$$

From now on, the tilde is omitted for the sake of simplicity. Supposing that close to the codimension-two point $\mu = \nu = 0$, the bifurcation corresponding to B_2 is non-degenerate, then $a \neq 0$, and it is always possible to choose the scaling factor r_1 so that a is ± 1. In the case under consideration B_2 bifurcates supercritically, so $a = 1$ is taken in (B.55). If $d \neq 0$, it is always possible by choosing r_2 and s appropriatelly, to take $d = 1$, and there are no more degrees of freedom to use for simplifying the normal form (B.55). With these values, the hypernormal form is procured

$$\mathcal{P} : \begin{cases} A \mapsto A\big(1 + \mu - |A|^2 - e|B|^2 - \overline{e}|C|^2\big) + B\overline{C}, \\ B \mapsto B\big(\mathrm{e}^{\mathrm{i}\theta/2} + \nu - f|A|^2 - b|B|^2 - c|C|^2\big) + gAC, \\ C \mapsto C\big(\mathrm{e}^{\mathrm{i}\theta/2} + \nu - f|A|^2 - b|C|^2 - c|B|^2\big) + g\overline{A}B, \end{cases} \tag{B.60}$$

where $\mu \in \mathbb{R}$ and $\nu, b, c, e, f, g \in \mathbb{C}$.

B.3 Codimension-two point $\mathcal{F}_4^C$ and $\mathcal{F}_2^-$ with spatial ressonance 1 : 2

In the last codimension-two point, the synchronous mode A_2 and the quasiperiodic mode MRW_1 bifurcate simultaneously. There is a pair of eigenfunctions associated with A_2, with eigenvalues -1, and amplitudes A and $\overline{A}$. The normal form for a $\mathcal{F}_2^-$ bifurcation is (see Marques *et al.*, 2004, sections §4.1 and §5.2)

$$\mathcal{H} : A \mapsto A\big(-1 + R(|A|^2, \mu)\big), \tag{B.61}$$

where R is a real polynomial and μ the bifurcation parameter. Up to and including third order terms in A and the small bifurcation parameter, the normal form is

$$\mathcal{H} : \ A \mapsto A(-1 - \mu + a|A|^2), \tag{B.62}$$

where $\mu, a \in \mathbb{R}$. The action of the symmetries and the linearised half-period-flip map on $(A, \overline{A})$ is

$$R_\alpha(A, \overline{A}) = (\mathrm{e}^{\mathrm{i}m\alpha}A, \mathrm{e}^{-\mathrm{i}m\alpha}\overline{A}), \tag{B.63a}$$

$$K_\beta(A, \overline{A}) = (\overline{A}, A), \tag{B.63b}$$

$$L_H(A, \overline{A}) = (-A, -\overline{A}), \tag{B.63c}$$

where $m = 2$ because the A_2 mode is being analised. All the considerations for the quasiperiodic $MRW1$ mode commented in the previous section are also used here. The

action of the symmetries and the linearised half-period-flip map on $X = (A, B, C, \overline{A}, \overline{B}, \overline{C})$ is

$$R_\alpha(A, B, C, \overline{A}, \overline{B}, \overline{C}) = (\mathrm{e}^{\mathrm{i}m\alpha}A, \mathrm{e}^{\mathrm{i}n\alpha}B, \mathrm{e}^{-\mathrm{i}n\alpha}C, \mathrm{e}^{-\mathrm{i}m\alpha}\overline{A}, \mathrm{e}^{-\mathrm{i}n\alpha}\overline{B}, \mathrm{e}^{\mathrm{i}n\alpha}\overline{C}), \tag{B.64a}$$

$$K_\beta(A, B, C, \overline{A}, \overline{B}, \overline{C}) = (\overline{A}, C, B, A, \overline{C}, \overline{B}), \tag{B.64b}$$

$$L_H(A, B, C, \overline{A}, \overline{B}, \overline{C}) = (-A, \mathrm{e}^{\mathrm{i}\theta/2}B, \mathrm{e}^{\mathrm{i}\theta/2}C, -\overline{A}, \mathrm{e}^{-\mathrm{i}\theta/2}\overline{B}, \mathrm{e}^{-\mathrm{i}\theta/2}\overline{C}). \tag{B.64c}$$

The action of the space-time symmetry L_H is no longer the identity and introduces some conditions over the normal form, which has the structure

$$\mathcal{H} : \begin{cases} A \mapsto -A + R_1(A, B, C, \overline{A}, \overline{B}, \overline{C}), \\ B \mapsto B\mathrm{e}^{\mathrm{i}\theta/2} + R_2(A, B, C, \overline{A}, \overline{B}, \overline{C}), \\ C \mapsto C\mathrm{e}^{\mathrm{i}\theta/2} + R_3(A, B, C, \overline{A}, \overline{B}, \overline{C}), \end{cases} \tag{B.65}$$

and the complex conjugate equations for $\overline{A}$, $\overline{B}$ and $\overline{C}$. Here, all the R_i are complex polynomials. Introducing $R = (R_1, R_2, R_3, \overline{R}_1, \overline{R}_2, \overline{R}_3)$, the conditions the normal form $R(X)$ fulfill are provided by

$$R_\alpha R(X) = R(R_\alpha X), \qquad K_\beta R(X) = R(K_\beta X), \qquad L_H R(X) = R(L_H X). \tag{B.66}$$

Expanding these expressions, they become

$$\mathrm{e}^{\mathrm{i}m\alpha}R_1(A, B, C, \overline{A}, \overline{B}, \overline{C}) = R_1(\mathrm{e}^{\mathrm{i}m\alpha}A, \mathrm{e}^{\mathrm{i}n\alpha}B, \mathrm{e}^{-\mathrm{i}n\alpha}C, \mathrm{e}^{-\mathrm{i}m\alpha}\overline{A}, \mathrm{e}^{-\mathrm{i}n\alpha}\overline{B}, \mathrm{e}^{\mathrm{i}n\alpha}\overline{C}), \tag{B.67a}$$

$$\overline{R_1(A, B, C, \overline{A}, \overline{B}, \overline{C})} = R_1(\overline{A}, C, B, A, \overline{C}, \overline{B}), \tag{B.67b}$$

$$-R_1(A, B, C, \overline{A}, \overline{B}, \overline{C}) = R_1(-A, \mathrm{e}^{\mathrm{i}\theta/2}B, \mathrm{e}^{\mathrm{i}\theta/2}C, -\overline{A}, \mathrm{e}^{-\mathrm{i}\theta/2}\overline{B}, \mathrm{e}^{-\mathrm{i}\theta/2}\overline{C}), \tag{B.67c}$$

$$\mathrm{e}^{\mathrm{i}n\alpha}R_2(A, B, C, \overline{A}, \overline{B}, \overline{C}) = R_2(\mathrm{e}^{\mathrm{i}m\alpha}A, \mathrm{e}^{\mathrm{i}n\alpha}B, \mathrm{e}^{-\mathrm{i}n\alpha}C, \mathrm{e}^{-\mathrm{i}m\alpha}\overline{A}, \mathrm{e}^{-\mathrm{i}n\alpha}\overline{B}, \mathrm{e}^{\mathrm{i}n\alpha}\overline{C}), \tag{B.67d}$$

$$R_3(A, B, C, \overline{A}, \overline{B}, \overline{C}) = R_2(\overline{A}, C, B, A, \overline{C}, \overline{B}), \tag{B.67e}$$

$$\mathrm{e}^{\mathrm{i}\theta/2}R_2(A, B, C, \overline{A}, \overline{B}, \overline{C}) = R_2(-A, \mathrm{e}^{\mathrm{i}\theta/2}B, \mathrm{e}^{\mathrm{i}\theta/2}C, -\overline{A}, \mathrm{e}^{-\mathrm{i}\theta/2}\overline{B}, \mathrm{e}^{-\mathrm{i}\theta/2}\overline{C}), \tag{B.67f}$$

$$\mathrm{e}^{-\mathrm{i}n\alpha}R_3(A, B, C, \overline{A}, \overline{B}, \overline{C}) = R_3(\mathrm{e}^{\mathrm{i}m\alpha}A, \mathrm{e}^{\mathrm{i}n\alpha}B, \mathrm{e}^{-\mathrm{i}n\alpha}C, \mathrm{e}^{-\mathrm{i}m\alpha}\overline{A}, \mathrm{e}^{-\mathrm{i}n\alpha}\overline{B}, \mathrm{e}^{\mathrm{i}n\alpha}\overline{C}), \tag{B.67g}$$

$$R_2(A, B, C, \overline{A}, \overline{B}, \overline{C}) = R_3(\overline{A}, C, B, A, \overline{C}, \overline{B}), \tag{B.67h}$$

$$\mathrm{e}^{\mathrm{i}\theta/2}R_3(A, B, C, \overline{A}, \overline{B}, \overline{C}) = R_3(-A, \mathrm{e}^{\mathrm{i}\theta/2}B, \mathrm{e}^{\mathrm{i}\theta/2}C, -\overline{A}, \mathrm{e}^{-\mathrm{i}\theta/2}\overline{B}, \mathrm{e}^{-\mathrm{i}\theta/2}\overline{C}). \tag{B.67i}$$

These relations have to be applied once again to a polynomial of the form $A^p B^q C^r \overline{A}^s \overline{B}^t \overline{C}^u$, where $p, q, r, s, t, u \in \mathbb{N}_0$.

For R_1 and assuming $\theta/(2\pi) \notin \mathbb{Q}$, (B.67a) and (B.67c) result in the same pair of constrains found in the previous section and an additional condition:

$$m(p - s - 1) = n(r - u + t - q), \qquad r - u = t - q, \qquad p + s = \text{odd}, \tag{B.68}$$

so the same results are valid here too, but in the latter stage the last condition will be taken into account.

Case 1: $r-u=t-q=v\geq 0$. The exponents of the monomial satisfy

$$p=s+kl+1,\quad r=u+jl,\quad t=q+jl,\quad kl=\text{even} \tag{B.69}$$

where $q,s,u,l\in\mathbb{N}_0$ and $j,k\in\mathbb{N}$. The monomial is $A|A|^{2s}|B|^{2q}|C|^{2u}\big(A^k(\overline{B}C)^j\big)^l$, as expected, and there is a subtlety related with the last condition. Since $k=1$, l is forced to be even, so $l\to 2l$ and the contribution to R_1 is

$$AR_{11}\big(|A|^2,|B|^2,|C|^2,A^{2k}(\overline{B}C)^{2j}\big), \tag{B.70}$$

where R_{11} is an arbitrary complex polynomial.

Case 2: $r-u=t-q=-v$, $v>0$. The exponents of the monomial fulfill

$$q=t+jl+j,\quad s=p+kl+k-1,\quad u=r+jl+j,\quad k(l+1)=\text{even} \tag{B.71}$$

where $p,r,t,l\in\mathbb{N}_0$ and $j,k\in\mathbb{N}$. The monomial is $\overline{A}^{k-1}(B\overline{C})^j|A|^{2p}|B|^{2t}|C|^{2r}\big(\overline{A}^k(B\overline{C})^j\big)^l$ again. In our case, $k=1$, thus l must be odd, $l\to 2l+1$ can be considered and contributes to R_1 with

$$\overline{A}^{2k-1}(B\overline{C})^{2j}R_{12}\big(|A|^2,|B|^2,|C|^2,\overline{A}^{2k}(B\overline{C})^{2j}\big), \tag{B.72}$$

where R_{12} is an arbitrary complex polynomial.

The normal form R_1 is the sum of the contributions (B.70) and (B.72), and the last remaining condition (B.67b) must be fulfilled. This results in

$$\overline{R_{11}\big(|A|^2,|B|^2,|C|^2,A^{2k}(\overline{B}C)^{2j}\big)}=R_{11}\big(|A|^2,|C|^2,|B|^2,\overline{A}^{2k}(B\overline{C})^{2j}\big), \tag{B.73a}$$

$$\overline{R_{12}\big(|A|^2,|B|^2,|C|^2,\overline{A}^{2k}(B\overline{C})^{2j}\big)}=R_{12}\big(|A|^2,|C|^2,|B|^2,A^{2k}(\overline{B}C)^{2j}\big). \tag{B.73b}$$

Conditions (B.73) establishes the same relationship between the monomials found in the previous section, thus giving combinations of the form

$$|A|^{2p}\big(\alpha|B|^{2q}|C|^{2r}+\overline{\alpha}|B|^{2r}|C|^{2q}\big)\big(A^{2k}(\overline{B}C)^{2j}\big)^l\quad\text{for } R_{11}, \tag{B.74a}$$

$$|A|^{2p}\big(\alpha|B|^{2q}|C|^{2r}+\overline{\alpha}|B|^{2r}|C|^{2q}\big)\big(\overline{A}^{2k}(B\overline{C})^{2j}\big)^l\quad\text{for } R_{12}. \tag{B.74b}$$

At last, the expression for R_1 is

$$\begin{aligned}R_1(A,B,C,\overline{A},\overline{B},\overline{C})=AR_{11}\big(|A|^2,|B|^2,|C|^2,A^{2k}(\overline{B}C)^{2j}\big)+\\+\overline{A}^{2k-1}(B\overline{C})^{2j}R_{12}\big(|A|^2,|B|^2,|C|^2,\overline{A}^{2k}(B\overline{C})^{2j}\big),\end{aligned} \tag{B.75}$$

where R_{11} and R_{12} are complex polynomials with monomials grouped as mentioned in (B.74).

As occurred in the former section, equations (B.67e) and (B.67h) are identical, and provide us with Q_3 once Q_2 is known. Considering (B.67d) and (B.67f), the same two constrains for the exponents of the polynomial and another condition are obteined

$$m(p-s) = n(r-u+t-q+1), \qquad r-u = t-q+1, \qquad p+s = \text{even}. \tag{B.76}$$

As a consequence, the same results can be used here too, but taking into account the latter condition. Once again, two cases have to be studied separately, $r-u > 0$ or $r-u \leq 0$.

Case 1: $r-u = t-q+1 = v+1$, $v \geq 0$. The exponents satisfy

$$p = s+kl+k, \quad r = u+jl+j, \quad t = q+jl+j-1, \quad k(l+1) = \text{even} \tag{B.77}$$

where $q, s, u, l \in \mathbb{N}_0$ and $j, k \in \mathbb{N}$. The monomial is $A^k\overline{B}^{\,j-1}C^j|A|^{2s}|B|^{2q}|C|^{2u}\big(A^k(\overline{B}C)^j\big)^l$ again. Considering the fact that in our case $k=1$, l is forced to be odd and $l \to 2l+1$ can be considered. Therefore, its contribution to R_2 is

$$A^{2k}\overline{B}^{\,2j-1}C^{2j}\, R_{22}\big(|A|^2, |B|^2, |C|^2, A^{2k}(\overline{B}C)^{2j}\big), \tag{B.78}$$

where R_{22} is an arbitrary complex polynomial.

Case 2: $r-u = t-q+1 = -v$, $v \geq 0$. The exponents of the monomial fulfill

$$q = t+jl+1, \quad s = p+kl, \quad u = r+jl, \quad kl = \text{even} \tag{B.79}$$

where $p, r, t, l \in \mathbb{N}_0$ and $j, k \in \mathbb{N}$. The monomial is $B|A|^{2p}|B|^{2t}|C|^{2r}\big(\overline{A}^{\,k}(B\overline{C})^j\big)^l$. Since $k=1$, l has to be even, so $l \to 2l$. Grouping together all these monomials, the contribution to R_2 becomes:

$$B\, R_{21}\big(|A|^2, |B|^2, |C|^2, \overline{A}^{\,2k}(B\overline{C})^{2j}\big), \tag{B.80}$$

where R_{21} is an arbitrary complex polynomial.

Summing up the contributions (B.78) and (B.80), and employing (B.67e), the final expressions for the remaining polynomials, R_2 and R_3 are

$$\begin{aligned} R_2(A,B,C,\overline{A},\overline{B},\overline{C}) = {} & B\, R_{21}\big(|A|^2, |B|^2, |C|^2, \overline{A}^{\,2k}(B\overline{C})^{2j}\big) + \\ & + A^{2k}\overline{B}^{\,2j-1}C^{2j}\, R_{22}\big(|A|^2, |B|^2, |C|^2, A^{2k}(\overline{B}C)^{2j}\big), \end{aligned} \tag{B.81}$$

$$\begin{aligned} R_3(A,B,C,\overline{A},\overline{B},\overline{C}) = {} & C\, R_{21}\big(|A|^2, |C|^2, |B|^2, A^{2k}(\overline{B}C)^{2j}\big) + \\ & + \overline{A}^{\,2k}B^{2j}\overline{C}^{\,2j-1}\, R_{22}\big(|A|^2, |C|^2, |B|^2, \overline{A}^{\,2k}(B\overline{C})^{2j}\big), \end{aligned} \tag{B.82}$$

where R_2 and R_3 are arbitrary complex polynomials.

Similarly to the previous section, the apparently more general expressions

$$R_{ii'}\big(|A|^2,|B|^2,|C|^2,A^{2k}(\overline{B}C)^{2j},\overline{A}^{\,2k}(B\overline{C})^{2j}\big) \tag{B.83}$$

in (B.75, B.81, B.82) also satisfy (B.67). The five arguments in (B.83) have a clear dependence, and verify similar expressions to the ones of the previous section (equations B.45-B.51), thus possessing analogous properties. However, treating this question exhaustively does not provide any novelty at all.

Regarding the case where $m = 2$ and $n = 1$, so $j = k = 1$, the polynomial are

$$R_1 = A\,R_{11}\big(|A|^2,|B|^2,|C|^2,(A\overline{B}C)^2\big) + \overline{A}(B\overline{C})^2\,R_{12}\big(|A|^2,|B|^2,|C|^2,(\overline{A}B\overline{C})^2\big), \tag{B.84}$$

$$R_2 = B\,R_{21}\big(|A|^2,|B|^2,|C|^2,(\overline{A}B\overline{C})^2\big) + \overline{B}(AC)^2\,R_{22}\big(|A|^2,|B|^2,|C|^2,(A\overline{B}C)^2\big), \tag{B.85}$$

$$R_3 = C\,R_{21}\big(|A|^2,|C|^2,|B|^2,(A\overline{B}C)^2\big) + \overline{C}(\overline{A}B)^2\,R_{22}\big(|A|^2,|C|^2,|B|^2,(\overline{A}B\overline{C})^2\big). \tag{B.86}$$

Up to and including third order terms and small bifurcation parameters, the normal form can be written as

$$\mathcal{H}:\begin{cases} A\mapsto A\big(-1-\mu+a|A|^2-d|B|^2-\overline{d}|C|^2\big),\\ B\mapsto B\big(\mathrm{e}^{\mathrm{i}\theta/2}+\nu-e|A|^2-b|B|^2-c|C|^2\big),\\ C\mapsto C\big(\mathrm{e}^{\mathrm{i}\theta/2}+\nu-e|A|^2-b|C|^2-c|B|^2\big),\end{cases} \tag{B.87}$$

where $\mu, a \in \mathbb{R}$, whilst $\nu, b, c, d, e \in \mathbb{C}$. Due to the A_2 mode, the Poincaré map normal form, $\mathcal{P} = \mathcal{H}^2$ has a different expression,

$$\mathcal{P}:\begin{cases} A\mapsto A\big(1+\tilde{\mu}-\tilde{a}|A|^2+\tilde{d}|B|^2+\overline{\tilde{d}}|C|^2\big),\\ B\mapsto B\big(\mathrm{e}^{\mathrm{i}\tilde{\theta}/2}+\nu-\tilde{e}|A|^2-\tilde{b}|B|^2-\tilde{c}|C|^2\big),\\ C\mapsto C\big(\mathrm{e}^{\mathrm{i}\tilde{\theta}/2}+\nu-\tilde{e}|A|^2-\tilde{b}|C|^2-\tilde{c}|B|^2\big),\end{cases} \tag{B.88}$$

and the relation between the parameters is:

$$\begin{aligned}\tilde{\theta}=2\theta,\quad \tilde{\mu}=\mu(2+\mu),\quad \tilde{a}=2a(1+\mu),\quad \tilde{d}=2d(1+\mu),\quad \tilde{\nu}=\nu(2\mathrm{e}^{\mathrm{i}\theta/2}+\nu),\\ \tilde{e}=2e(\mathrm{e}^{\mathrm{i}\theta/2}+\nu),\quad \tilde{b}=2b(\mathrm{e}^{\mathrm{i}\theta/2}+\nu),\quad \tilde{c}=2c(\mathrm{e}^{\mathrm{i}\theta/2}+\nu).\end{aligned} \tag{B.89}$$

Further simplifications can be obtained proceeding exactly in the same way as it was done previously. From now on, the tilde is omitted for the sake of simplicity. Assuming that close to the codimension-two point $\mu = \nu = 0$, the bifurcation corresponding to A_2 is non-degenerate, then $a \neq 0$, and it is always possible to choose the scaling factor that

makes $a = \pm 1$. As before, the $+$ $(-)$ sign corresponds to a supercritical (subcritical) bifurcation. Since A_2 bifurcates supercritically, $a = 1$ is considered. Unfortunately, there are no more possible simplifications. With these, the hypernormal form is

$$\mathcal{P} : \begin{cases} A \mapsto A\big(1 + \mu - |A|^2 + d|B|^2 + \overline{d}|C|^2\big), \\ B \mapsto B\big(\mathrm{e}^{\mathrm{i}\theta/2} + \nu - e|A|^2 - b|B|^2 - c|C|^2\big), \\ C \mapsto C\big(\mathrm{e}^{\mathrm{i}\theta/2} + \nu - e|A|^2 - b|C|^2 - c|B|^2\big), \end{cases} \tag{B.90}$$

where $\mu \in \mathbb{R}$ and $\nu, b, c, d, e \in \mathbb{C}$.

BIBLIOGRAPHY

Algaba, A., Freire, E. & Gamero, E. 1998 Hypernormal form for the Hopf-zero bifurcation. *Int. J. Bif. Chaos* **8** (10), 1857–1887.

Allen, J. J. & Lopez, J. M. 2007 Transition processes for junction vortex flow. *J. Fluid Mech.* **585**, 457–467.

Armbruster, D., Guckenheimer, J. & Holmes, P. 1988 Heteroclinic cycles and modulated travelling waves in systems with O(2) symmetry. *Physica D* **29**, 257–282.

Ascher, U. M., Ruuth, S. J. & Wetton, B. T. R. 1995 Implicit-explicit methods for time-dependant partial differential equations. *SIAM J. on Numer. Anal.* **32**, 797–823.

Atalik, K. & Keunings, R. 2002 Non-linear temporal stability analysis of viscoelastic plane channel flows using a fully-specral method. *J. Non-Newtonian Fluid Mech.* **102**, 299–319.

Atalik, K. & Keunings, R. 2004 On the occurrence of even harmonics in the shear stress response of viscoelastic fluids in large amplitude oscillatory shear. *J. Non-Newtonian Fluid Mech.* **122**, 107–116.

Avila, M., Belisle, M. J., Lopez, J. M., Marques, F. & Saric, W. S. 2008 Mode competition in modulated Taylor-Couette flow. *J. Fluid Mech.* **601**, 381–406.

Avila, M., Marques, F., Lopez, J. M. & Meseguer, A. 2007 Stability control and catastrophic transition in a forced Taylor-Couette system. *J. Fluid Mech.* **590**, 471–496.

Balci, N., Thomases, B., Renardy, M. & R, D. C. 2011 Symmetric factorization of the conformation tensor in viscoelastic fluid models. *J. Non-Newtonian Fluid Mech.* **166**, 546–553.

Barkley, D. & Henderson, R. D. 1996 Three–dimensional Floquet stability analysis of the wake of a circular cylinder. *J. Fluid Mech.* **322**, 215–241.

Barkley, D., Tuckerman, L. S. & Golubitsky, M. 2000 Bifurcation theory for three-dimensional flow in the wake of a circular cylinder. *Phys. Rev. E* **61**, 5247–5252.

Batchelor, G. K. 1967 *An introduction to Fluid Mechanics*. Cambridge University Press.

Bird, R. B., Armstrong, R. C. & Hassager, O. 1987 *Dynamics of Polymeric Liquids*. Birkhäuser.

Blackburn, H. M. & Lopez, J. M. 2003*a* On three-dimensional quasiperiodic Floquet instabilities of two-dimensional bluff body wakes. *Phys. Fluids* **15** (8), L57–L60.

Blackburn, H. M. & Lopez, J. M. 2003*b* The onset of three-dimensional standing and modulated travelling waves in a periodically driven cavity flow. *J. Fluid Mech.* **497**, 289–317.

Blackburn, H. M. & Lopez, J. M. 2011 Modulated waves in a periodically driven annular cavity. *J. Fluid Mech.* **667**, 336–357.

Blackburn, H. M., Marques, F. & Lopez, J. M. 2005 Symmetry breaking of two-dimensional time-periodic wakes. *J. Fluid Mech.* **522**, 395–411.

Blackburn, H. M. & Sheard, G. J. 2010 On quasiperiodic and subharmonic Floquet wake instabilities. *Phys. Fluids* **22**, 031701.

Boronski, P. & Tuckerman, L. 2007 Poloidal-toroidal decomposition in a finite cylinder. I: Influence matrices for the magnetohydrodynamic equations. *J. Comput. Phys.* **227**, 1523–1543.

Boyd, J. P. 2000 *Chebyshev and Fourier Spectral Methods*, 2nd edn. DOVER Publications, Inc.

Casanellas, L. 2013 *Oscillatory pipe flow of wormlike micellar solutions*. Ph.D. Thesis, Universitat de Barcelona.

Casanellas, L. & Ortín, J. 2012*a* Experiments on the laminar oscillatory flow of wormlike micellar solutions. *Rheol. Acta* **51**, 545–557.

Casanellas, L. & Ortín, J. 2012*b* Laminar oscillatory flow of Maxwell and Oldroyd-B fluids: Theoretical analysis. *J. Non-Newtonian Fluid Mech.* **166**, 1315–1326.

Chokshi, P. & Kumaran, V. 2009 Stability of the plane shear flow of dilute polymeric solutions. *Phys. Fluids* **21**, 014109.

Chossat, P. & Lauterbach, R. 2000 *Methods in Equivariant Bifurcations and Dynamical Systems*. World Scientific.

Crawford, J. D. & Knobloch, E. 1991 Symmetry and symmetry-breaking bifurcations in fluid dynamics. *Annu. Rev. Fluid Mech.* **23**, 341–387.

Dangelmayr, G. 1986 Steady-state mode interactions in the presence of O(2)-symmetry. *Dynamics and Stability of Systems* **1** (2), 159–185.

Do, Y., Lopez, J. M. & Marques, F. 2010 Optimal harmonic response in a confined Bödewadt boundary layer flow. *Phys. Rev. E* **82**, 036301.

Drazin, P. G. 2002 *An introduction to Fluid Mechanics*. Introduction to hydrodynamic stability.

Echebarría, B., Krmpotić, D. & Pérez-García, C. 1997 Resonant interactions in Bénard-Marangoni convection in cylindrical containers. *Physica D* **99**, 487–502.

Eckmann, J.-P. 1981 Roads to turbulence in dissipative dynamical systems. *Rev. Mod. Phys.* **54**, 643–656.

Fattal, R. & Kupferman, R. 2005 Time-dependent simulation of viscoelastic flows at high Weissenberg number using the log-conformation representation. *J. Non-Newtonian Fluid Mech.* **126**, 23–37.

Fornberg, B. 1998 Calculation of weights in finite difference formulas. *SIAM Rev.* **40** (3), 685–691.

Goldstein, H. F., Knobloch, E., Mercader, I. & Net, M. 1998 Convection in a rotating cylinder. Part 1. Linear theory for moderate Prandtl numbers. *J. Fluid Mech.* **248**, 583–604.

Golubitsky, M., Stewart, I. & Schaeffer, D. G. 1988 *Singularities and Groups in Bifurcation Theory, vol. II*. Springer.

Guermond, J., Minev, P. & Shen, J. 2006 An overview of projection methods for incompressible flows. *Comp. Meth. Appl. Mech. & Engng* **195**, 6011–6045.

Guyon, E., Hulin, J. P., Petit, L. & Mitescu, C. D. 2001 *Physical Hydrodynamics*. Oxford University Press.

Hughes, S. & Randriamampianina, A. 1998 An improved projection scheme applied to pseudospectral methods for the incompressible Navier-Stokes equations. *Intnl J. Num. Meth. Fluids* **28**, 501–521.

Iooss, G. & Adelmeyer, M. 1998 *Topics in Bifurcation Theory and Applications*, 2nd edn. World Scientific.

Julien, S., Lasheras, J. & Chomaz, J.-M. 2003 Three-dimensional instability and vorticity patterns in the wake of a flat plate. *J. Fluid Mech.* **479**, 155–189.

Kaptan, Y., Ecder, A. & Atalik, K. 2010 Rotating-surface-driven non-Newtonian flow in a cylindrical enclosure. *Korea-Australia Rheol. J.* **22**, 265–272.

Karniadakis, G. E., Israeli, M. & Orszag, S. A. 1991 High-order splitting methods for the incompressible Navier-Stokes equations. *J. Comput. Phys.* **97**, 414–443.

Kuznetsov, Y. A. 2004 *Elements of Applied Bifurcation Theory*, 3rd edn. Springer.

Kuznetsov, Y. A., Meijer, H. G. E. & van Veen, L. 2004 The fold-flip bifurcation. *Int. J. Bif. Chaos* **14** (7), 2253–2282.

Lamb, J. S. W. 1996 Local bifurcations in k-symmetric dynamical systems. *Nonlinearity* **9**, 537–557.

Lamb, J. S. W. & Melbourne, I. 1999 Bifurcation from discrete rotating waves. *Arch. Ration. Mech. An.* **149**, 229–270.

Larson, R. G. 1999 *The structure and rheology of complex fluids*. John Wiley and Sons.

Larson, R. G. 2000 Turbulence without inertia. *Nature* **405**, 27.

Lasheras, J. C. & Meiburg, E. 1990 Three-dimensional vorticity modes in the wake of a flat plate. *Phys. Fluids A* **5**, 371–380.

Leung, J. J. F., Hirsa, A. H., Blackburn, H. M., Marques, F. & Lopez, J. M. 2005 Three-dimensional modes in a periodically driven elongated cavity. *Phys. Rev. E* **71**, 026305.

Leweke, T. & Provansal, M. 1995 The flow behind rings: bluff body wakes without end effects. *J. Fluid Mech.* **280**, 265–310.

Lopez, J. M. & Hirsa, A. 2001 Oscillatory driven cavity with an air/water interface and an insoluble monolayer: Surface viscosity effects. *J. Colloid Interface Sci.* **242**, 1–5.

Lopez, J. M. & Marques, F. 2000 Dynamics of 3-tori in a periodically forced Navier-Stokes flow. *Phys. Rev. Lett.* **85**, 972–975.

Lopez, J. M. & Marques, F. 2009 Centrifugal effects in rotating convection: nonlinear dynamics. *J. Fluid Mech.* **628**, 269–297.

Lopez, J. M., Marques, F., Mercader, I. & Batiste, O. 2007 Onset of convection in a moderate aspect-ratio rotating cylinder: Eckhaus-Benjamin-Feir instability. *J. Fluid Mech.* **590**, 187–208.

Lopez, J. M., Marques, F., Rubio, A. M. & Avila, M. 2009 Crossflow instability of finite Bödewadt flows: transients and spiral waves. *Phys. Fluids* **21**, 114107.

Lopez, J. M., Marques, F. & Shen, J. 2002 An efficient spectral-projection method for the Navier-Stokes equations in cylindrical geometries II. Three dimensional cases. *J. Comput. Phys.* **176**, 384–401.

Lopez, J. M. & Shen, J. 1998 An efficient spectral-projection method for the Navier–Stokes equations in cylindrical geometries I. Axisymmetric cases. *J. Comput. Phys.* **139**, 308–326.

Marques, F. & Lopez, J. M. 1997 Taylor-Couette flow with axial oscillations of the inner cylinder: Floquet analysis of the basic flow. *J. Fluid Mech.* **348**, 153–175.

Marques, F. & Lopez, J. M. 2000 Spatial and temporal resonances in a periodically forced extended system. *Physica D* **136**, 340–352.

Marques, F., Lopez, J. M. & Blackburn, H. M. 2004 Bifurcations in systems with Z_2 spatio-temporal and $O(2)$ spatial symmetry. *Physica D* **189**, 247–276.

Marques, F., Mellibovsky, F. & Meseguer, A. 2013 Fold-pitchfork bifurcation for maps with z_2 symmetry in pipe flow. *PRE* **submitted**.

Marques, F., Mercader, I., Batiste, O. & Lopez, J. M. 2007 Centrifugal effects in rotating convection: Axisymmetric states and three-dimensional instabilities,. *J. Fluid Mech.* **580**, 303–318.

Marques, F., Net, M., Masseguer, J. M. & Mercader, I. 1993 Thermal convection in vertical cylinders. a method based on potentials. *Comp. Meth. Appl. Mech. & Engng* **110**, 157–169.

Meiburg, E. & Lasheras, J. C. 1988 Experimental and numerical investigation of the three-dimensional transition in plane wakes. *J. Fluid Mech.* **190**, 1–37.

Mercader, I., Alonso, A. & Batiste, O. 2008 Spatio-temporal dynamics near the onset of convection for binary mixtures in cylindrical containers. *Phys. Rev. E* **77**, 036313.

Mercader, I., Batiste, O. & Alonso, A. 2010 An efficient spectral code for incompressible flows in cylindrical geometries. *Computers & Fluids* **39**, 215–224.

Mercader, I., Net, M. & Falqués, A. 1991 Spectral methods for high order equations. *Comp. Meth. Appl. Mech. & Engng* **91**, 1245–1251.

Mercader, I., Prat, J. & Knobloch, E. 2001 The 1:2 mode interaction in Rayleigh-Benard convection with weakly broken midplane symmetry. *Int. J. Bif. Chaos* **11** (1), 27–41.

Mercader, I., Prat, J. & Knobloch, E. 2002 Robust heteroclinic cycles in two-dimensional Rayleigh-Bénard convection without Boussinesq symmetry. *Int. J. Bif. Chaos* **12**, 2501–2522.

Morozov, A. N. & van Saarlos, W. 2005 Subcritical finite-amplitude solutions in plane Couette flow of visco-elastic fluids. *Phys. Rev. Lett.* **95**, 024501.

Morozov, A. N. & van Saarlos, W. 2007 An introductory essay on subcritical instabilities and the transition to turbulence in visco-elastic shear flows. *Physics Reports* **447**, 112–143.

Murdock, J. 2004 Hypernormal form theory: foundations and algorithms. *Journal of Differential Equations* **205**, 424–465.

Nore, C., Tuckerman, L. S., Daube, O. & Xin, S. 2003 The 1:2 mode interaction in exactly counter-rotating von Kármán swirling flow. *J. Fluid Mech.* **477**, 51–88.

Pakdel, P. & McKinley, G. H. 1996 Elastic instability and curved streamlines. *Phys. Rev. Lett.* **77**, 2459.

Panades, C., Marques, F. & Lopez, J. M. 2011 Transitions to three-dimensional flows in a cylinder driven by oscillations of the sidewall. *J. Fluid Mech.* **681**, 193–204.

Panades, C., Marques, F. & Meseguer, A. 2013 Mode competition in cylindrical flows driven by sidewall oscillations. *Phys. Rev. E* **87**, 043001.

Perry, A. E., Chong, M. S. & Lim, T. T. 1982 The vortex-shedding process behind two-dimensional bluff bodies. *J. Fluid Mech.* **116**, 77–90.

Porter, J. & Knobloch, E. 2001 New type of complex dynamics in the 1:2 spatial resonance. *Physica D* **159** (3-4), 125–154.

Priymak, V. G. & Miyazaki, T. 1998 Accurate navier-stokes investigation of transitional and turbulent flows in a circular pipe. *J. Comput. Phys.* **142**, 370–411.

Proctor, M. R. E. & Jones, C. A. 1988 The interaction of two spatially resonant patterns in thermal convection. part 1. exact 1:2 resonance. *J. Fluid Mech.* **188**, 301–335.

Reynolds, O. 1883 An experimental investigation of the circumstances which determine whether the motion of water shall be direct or sinuous, and the law of resistance in parallel channels. *Phil. Trans. Roy. Soc. Lond. A* **174**, 935–982.

Robichaux, J., Balachandar, S. & Vanka, S. P. 1999 Three-dimensional Floquet instability of the wake of a square cylinder. *Phys. Fluids* **11**, 560–578.

Roland, N., Plaut, E. & Nouar, C. 2010 Petrov-Galerkin computation of nonlinear waves in pipe flow of shear-thinning fluids: first theoretical evidences for a delayed transition. *Computers & Fluids* **39**, 1733–1743.

Rubio, A., Lopez, J. M. & Marques, F. 2010 Onset of Küppers-Lortz-like dynamics in finite rotating thermal convection. *J. Fluid Mech.* **644**, 337–357.

Schlichting, H. & Kestin, J. 1979 *Boundary-Layer Theory*, seventh edn. McGraw-Hill.

Schmid, P. J. & Henningson, D. 2001 *Stability and transition in shear flows*. Springer.

Sheard, G. J., Thompson, M. C. & Hourigan, K. 2004 From spheres to circular cylinders: non-axisymmetric transitions in the flow past rings. *J. Fluid Mech.* **506**, 45–78.

Strogatz, S. 1994 *Nonlinear Dynamics and Chaos*. MA: Addison-Wesley, Reading.

Sureshkumar, R. & Beris, A. N. 1995 Effect of artificial stress diffusivity on the stability of numerical calculations and the flow dynamics of time-dependent viscoelastic flows. *J. Non-Newtonian Fluid Mech.* **60**, 53–80.

Thomas, D. G., Al-Mubaiyedh, U. A., Sureshkumar, R. & Khomami, B. 2006 Time-dependent simulations of non-axisymmetric patterns in Taylor-Couette flow of dilute polymer solutions. *J. Non-Newtonian Fluid Mech.* **138**, 111–133.

Thomas, D. G., Khomami, B. & Sureshkumar, R. 2009 Nonlinear dynamics of viscoelastic Taylor-Couette flow: effect of elasticity on pattern selection, molecular conformation and drag. *J. Fluid Mech.* **620**, 353–382.

Torralba, M., Castrejón-Pita, A. A., Hernández, G., Huelsz, G., del Río, J. A. & Ortín, J. 2007 Instabilities in the oscillatory flow of a complex fluid. *Phys. Rev. E* **72**, 056307.

Torralba, M., Castrejón-Pita, J. R., Castrejón-Pita, A. A., Huelsz, G., del Río, J. A. & Ortín, J. 2005 Measurements of the bulk and interficial velocity profiles in oscillating Newtonian and Maxwellian fluids. *Phys. Rev. E* **72**, 016308.

Trefethen, L. N. 2000 *Spectral Methods in Matlab*. SIAM.

Vogel, M. J., Hirsa, A. H. & Lopez, J. M. 2003 Spatio-temporal dynamics of a periodically driven cavity flow. *J. Fluid Mech.* **478**, 197–226.

Williamson, C. H. K. 1988 The existence of two stages in the transition to three-dimensionality of a circular cylinder wake. *Phys. Fluids* **31** (11), 3165–3168.

Williamson, C. H. K. 1996 Three-dimensional wake transition. *J. Fluid Mech.* **328**, 345–407.

Zhao, S. & Yedlin, M. J. 1994 A new iterative Chebyshev spectral method for solving the elliptic equation $\nabla \cdot (\sigma \nabla u) = f$. *J. Comput. Phys.* **113**, 215–223.